Real Time Cosmology with Extragalactic Proper Motions: The Secular Aberration Drift and Evolution of Large-Scale Structure

by

A. E. Truebenbach

B.A., Wesleyan University, 2012

M.S., University of Colorado Boulder, 2015

A thesis submitted to the

Faculty of the Graduate School of the

University of Colorado in partial fulfillment

of the requirements for the degree of

Doctor of Philosophy

Department of Astrophysical and Planetary Sciences

2018

This thesis entitled:
Real Time Cosmology with Extragalactic Proper Motions: The Secular Aberration Drift and Evolution of Large-Scale Structure
written by A. E. Truebenbach
has been approved for the Department of Astrophysical and Planetary Sciences

Prof. Jeremy Darling

Prof. Julie Comerford

Prof. David Brain

Prof. Nils Halverson

Prof. Alysia Marino

Date

The final copy of this thesis has been examined by the signatories, and we find that both the content and the form meet acceptable presentation standards of scholarly work in the above mentioned discipline.

Truebenbach, A. E. (Ph.D., Astrophysical and Planetary Sciences)

Real Time Cosmology with Extragalactic Proper Motions: The Secular Aberration Drift and Evolution of Large-Scale Structure

Thesis directed by Prof. Jeremy Darling

We present the VLBA Extragalactic Proper Motion Catalog, a catalog of extragalactic proper motions created using archival VLBI data and our own VLBA astrometry. The catalog contains 713 proper motions, with average uncertainties of ~ 24 μas yr^{-1}, including 40 new or improved proper motion measurements using relative astrometry with the VLBA. We detect the secular aberration drift – the apparent motion of extragalactic objects caused by the Solar System's acceleration around the Galactic Center – at 6.3 sigma significance with an amplitude of 1.69 ± 0.27 μas yr^{-1} and an apex consistent with the Galactic Center (275.2 ± 10.0 deg, -29.4 ± 8.8 deg). Our dipole model detects the aberration drift at a higher significance than some previous studies (e.g., Titov & Lambert 2013), but at a lower amplitude than expected or previously measured. We then use the correlated relative proper motions of extragalactic objects to place upper limits on the average velocity of galaxies caused by the mass distribution of large-scale structure (e.g., Quercellini et al. 2009; Darling 2013). Pairs of small-separation objects that are in gravitationally interacting structures, such as virialized clusters, will show a net decrease in angular separation (> -15 μas yr^{-1}) as they move toward each other, while pairs of large-separation objects that are gravitationally non-interacting and move with the Hubble expansion will show no net change in angular separation. With our catalog, we place a 3 sigma limit on the average rate of convergence of large-scale structure of > -17.4 μas yr^{-1} for extragalactic objects within 100 comoving Mpc of each other. We also confirm that large-separation objects (> 800 comoving Mpc) move with the Hubble flow to within ~ 2.3 μas yr^{-1}. Finally, we predict that *Gaia* end-of-mission proper motions will be able to detect the mass distribution of large-scale structure

on length scales < 50 Mpc at a significance of $> 9.8\sigma$. This future detection will allow a test of the shape of the theoretical mass power spectrum without a reliance on precise distance measurements.

Acknowledgements

First and foremost, I'd like to thank my advisor, Jeremy Darling. He invited me to work with him before I even arrived at CU and has supported me through six years of countless paper revisions, last-minute meeting requests, and proposal deadlines. Thank you for giving me the freedom to create my own work, but providing guidance when I needed it most.

Thank you to my thesis committee, David Brain, Nils Halverson, Julie Comerford, and Alysia Marino for your advice and feedback. John Stocke, who could not be on my committee because he was having fun in retirement, also deserves thanks for his support and mentorship over the years. I'd also like to thank David Gordon from the NASA Goddard Space Flight Center for providing me with an early copy of the 2017a global solution, and Amy Mioduszewski from the NRAO for answering my endless questions about AIPS.

The road to my PhD was much longer and harder than I ever would have guessed, but the support and friendship of a truly awesome collection of people made the journey fun. These people include, Briana Ingermann, my first and best friend in Boulder, Matteo Crismani, who taught me to forget about work and have fun, Becky Nevin, my astro sister, Morgan Rehnberg, the best homework partner ever, and Connor White and Kayla Zelm, my ski buddies. There are too many other classmates and friends to list here, but all of you made these last six years the best of my life so far.

Finally, my fiancé, Bowen McDougal, deserves the most credit for getting me through this entire process. Thank you for reminding me to relax and not take everything so seriously. This dissertation wouldn't have been possible without your unwavering support.

Contents

Chapter

Tables

Table

Figures

Figure

Chapter 1

Introduction

In this chapter, I provide the scientific background on which my thesis work is based. In Section 1.1, I introduce the observation technique of radio interferometry, which is currently the only way to measure high-precision extragalactic proper motions (pending the release of *Gaia* proper motions; Gaia Collaboration et al. 2016). I use archival radio interferometric observations as the basis for the VLBA Extragalactic Catalog and conduct my own observations to add additional proper motions to the final catalog (Chapters 2 and 3, respectively). In Section 1.2, I present the technique of using vector spherical harmonics to model global proper motion signals. This technique can be used to measure the secular aberration drift (modeled as a curl-free dipole; Chapter 4) and primordial gravitational waves (modeled as a quadrupole). Next, in Section 1.3, I summarize current research on the evolution of large-scale structure. Then, I introduce the technique of using relative proper motions, binned by comoving separation, to detect and measure this global cosmological effect. Finally, I present my thesis work in the context of the background and previous work described in this chapter and outline the following chapters in Section 1.4. I assume $H_0 = 70$ km s^{-1} Mpc^{-1} and a flat cosmology with $\Omega_\Lambda = 0.73$ and $\Omega_M = 0.27$.

1.1 Radio Interferometry

A radio interferometer is a series of radio antennae that are used together to create a single telescope with a synthetic aperture of a diameter equal to the largest physical

separation of antennae. Although interferometry is a technique that can be implemented at any wavelength, historically, it was only practical at radio wavelengths where the frequency of signal arrival times are low enough to be digitally processed. The first radio interferometer was built in the 1940s and since then the number of interferometers has grown to include the Karl G. Jansky Very Large Array (VLA), the Multi-Element Radio Linked Interferometer Network (MERLIN), the Atacama Large Millimeter Array (ALMA), the Very Long Baseline Array (VLBA), and the Australia Telescope Compact Array (ATCA).

A large synthetic telescope is created from an array of radio antennae using the arrival times of radiation from a distant source. For a distant source in direction $\vec{s}$ and two radio antennae separated by a vector baseline $\vec{b}$, the light will have to travel an extra distance $\vec{L}$ to the more distant antenna, $\vec{L} = \vec{b} \cdot \vec{s}$, which corresponds to an arrival time difference of

$$\tau_g = \frac{\vec{b} \cdot \vec{s}}{c}, \tag{1.1}$$

where c is the speed of light. The time difference, τ_g, is called the geometric delay. See Figure 1.1 for an illustration of these equations. Note that $\vec{s}$ is the same at both antennae because the source is assumed to be in the far-field.

If we represent light as an electric field with an infinitely small bandwidth, then we can write the temporal dependence of the field as

$$E_\nu(t) = A\cos(2\pi\nu t + \phi), \tag{1.2}$$

where A is the amplitude of the wave, ν is the frequency, and ϕ is the phase. Then, because the light is treated as a wave, a geometric delay between two antennae will cause a phase difference in the signal received at both antennae –

$$\phi = 2\pi\frac{\vec{b} \cdot \vec{s}}{\lambda} = 2\pi\nu\tau_g, \tag{1.3}$$

where λ is the wavelength of the radiation. Thus, the signal (or voltage) at antennas 1 and 2 can be expressed as

$$V_1 = v_1\cos[2\pi\nu(t - \tau_g)], \tag{1.4}$$

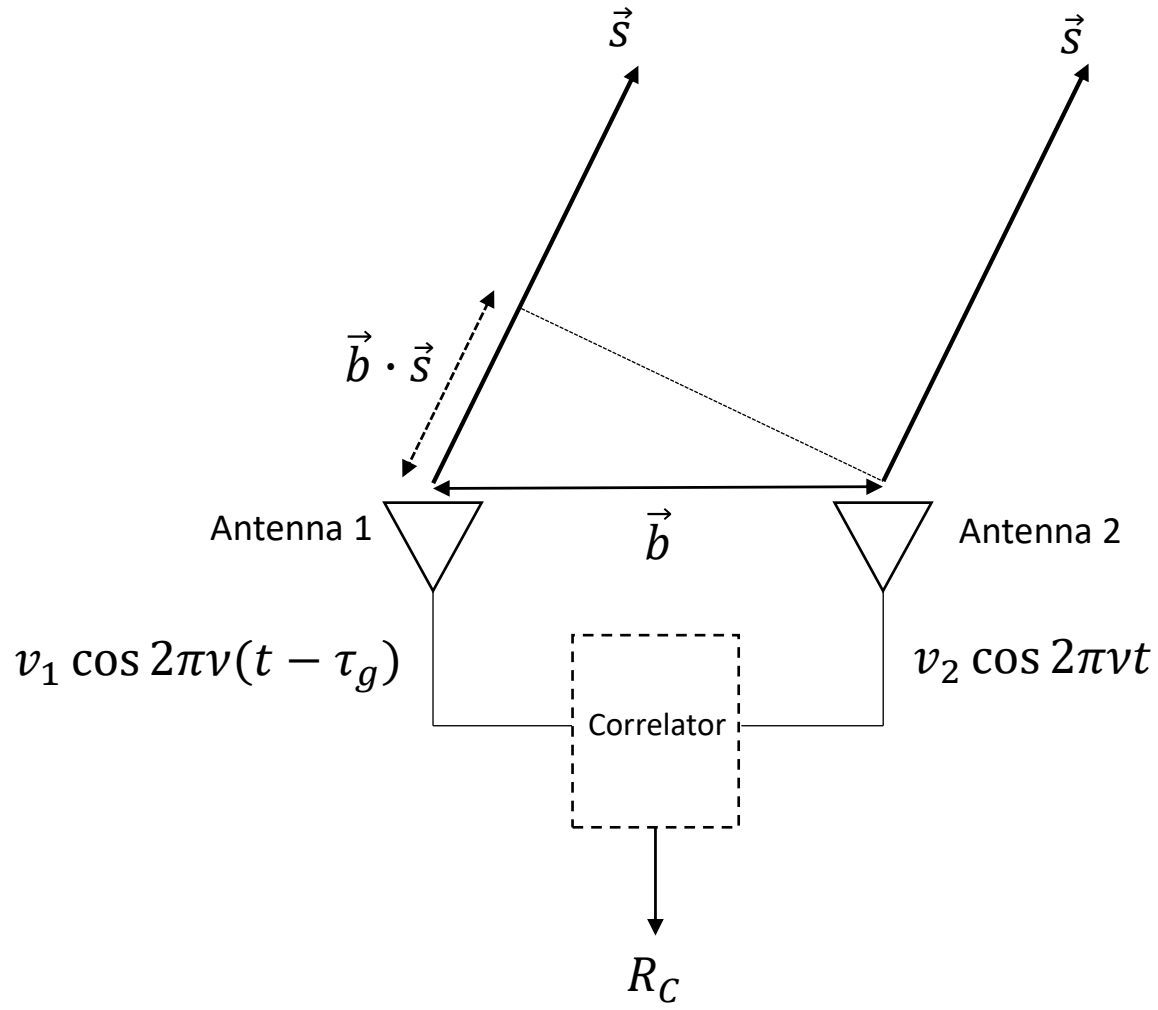

Figure 1.1 A schematic of the signals received from two antennae separated by a baseline, $\vec{b}$, observing a distant source in direction $\vec{s}$. See Equations 1.1 – 1.6 for a description of the variables.

and

$$V_2 = v_2 \cos(2\pi\nu t), \tag{1.5}$$

where v_1 and v_2 are the voltage amplitudes at each antenna. After the signal is received at both antennae, the signals are multiplied together and averaged in a correlator. The correlator output power is then

$$R_C = v_1 v_2 \cos(2\pi\nu\tau_g). \tag{1.6}$$

Note that all $\cos(t)$ terms are removed when the correlator averages the signals in time.

The above equations include many simplifications and assumptions, most notably the assumptions that the source is point-like, the antennae are perfect receivers with no loss, and that the bandwidth is infinitely small. Additionally, it is difficult to see how any source properties can be obtained from the above equations. To address these issues, we rewrite the correlator power amplitude for a small area of the sky as

$$v_1 v_2 = \mathcal{A}(\vec{s}) I(\vec{s}) \Delta\nu \; d\Omega, \tag{1.7}$$

where $\mathcal{A}(\vec{s})$ is the antenna response in direction $\vec{s}$ (assumed to be the same for all antennae), $I(\vec{s})$ is the specific intensity of the source in direction $\vec{s}$, $\Delta\nu$ is the bandwidth, and $d\Omega$ is the incremental solid angle. Then, the correlator power can be rewritten as

$$R_C = \Delta\nu \int_S \mathcal{A}(\vec{s}) I(\vec{s}) \cos(2\pi\nu\tau_g) \; d\Omega \tag{1.8}$$

(Thompson 1999). The integral is taken over the entire surface S of the celestial sphere (4π steradians), but in practice the integrand usually is negligible outside of the finite dimensions of the radio source. This equation assumes that the bandwidth is sufficiently small that there are no variations in $\mathcal{A}(\vec{s})$ and $I(\vec{s})$ with ν and that the source is spatially incoherent so that $I(\vec{s})$ from different points in the source are uncorrelated. In essence, R_C measures the interference pattern of the radiation received by the two antennae, where the cosine term describes the shape of the interference pattern. In radio interferometry, the peaks in the interference pattern are referred to as "fringes."

In reality, bandwidths have a finite size and it is incorrect to assume that $\mathcal{A}(\vec{s})$ and $I(\vec{s})$ are constant over the observed bandwidth. For a rectangular frequency bandpass centered at ν_0 and with a width $\Delta\nu$, the correlator power is

$$R_C = \int_{\nu_0-\Delta\nu/2}^{\nu_0+\Delta\nu/2} \int_S \mathcal{A}(\vec{s},\nu) I(\vec{s},\nu) \cos(2\pi\nu\tau_g)\ d\Omega\ d\nu. \tag{1.9}$$

For illustrative purposes, if we assume again that $\mathcal{A}(\vec{s})$ and $I(\vec{s})$ are constant over $\Delta\nu$, Equation 1.9 reduces to

$$R_C = \Delta\nu \int_S \mathcal{A}(\vec{s}) I(\vec{s})\ \frac{\sin \pi\Delta\nu\tau_g}{\pi\Delta\nu\tau_g} \cos(2\pi\nu_0\tau_g)\ d\Omega. \tag{1.10}$$

Thus, for a rectangular bandpass, the fringes are modulated by a sinc-function envelope. The full R_C is only measured when the source is in a direction normal to the baseline ($\tau_g = 0$). To ensure that the full correlator power is recorded throughout the observations, an instrumental time delay is added to each baseline so that $\tau_g = 0$ for all baselines. This delay is later removed during calibration (see Section 3.2, Step 7).

Finally, the correlator response, R_C, is not sufficient to completely recover $I(\vec{s})$. If we express the angular distribution of the source specific intensity as a sum of even and odd functions, then Equation 1.8 will only recover the even portion of $I(\vec{s})$ because the odd portion multiplied by cosine will integrate to zero –

$$\int_S \mathcal{A}(\vec{s}) I_O(\vec{s}) \cos(2\pi\nu\tau_g)\ d\Omega = 0, \tag{1.11}$$

where $I_O(\vec{s})$ is the odd portion of the specific intensity. To fully recover the specific intensity, a "sine correlator" is created by inserting a 90 degree phase shift into one of the signal paths before correlating the signal from two antennae –

$$R_S = \Delta\nu \int_S \mathcal{A}(\vec{s}) I(\vec{s}) \sin(2\pi\nu\tau_g)\ d\Omega. \tag{1.12}$$

The two correlator outputs, R_C and R_S, are combined to form the complex visibility,

$$\mathcal{V}(\vec{b}) = R_C - iR_s = \Delta\nu \int_S \mathcal{A}(\vec{s}) I(\vec{s}) e^{-2\pi i\nu\tau_g}\ d\Omega. \tag{1.13}$$

From Equation 1.13, we see that $I(\vec{s})$ is the Fourier transform of $\mathcal{V}(\vec{b})$, modulo the antenna response. The ultimate goal of all subsequent data reductions and measurements is to determine $I(\vec{s})$ and $\vec{s}$ from the measured $\mathcal{V}(\vec{b})$. For astrometry in particular, only $\vec{s}$, the position of the source, is needed. In principle, $\vec{s}$ can be measured by comparing τ_g from all antennae (Eqn. 1.1) without a need to determine $I(\vec{s})$ or remove the effects of antenna response and bandwidth. However, there are many other sources of delay that can contribute to the total delay measured by the antennae and can confuse the recovery of τ_g. In the following subsection, I will describe the most common sources of delay. In Chapter 3, I describe several additional sources of delay and discuss the methods for recovering the desired geometric delay, τ_g.

1.1.1 Sources of Delay

The total phase delay between two antennae can be described as

$$\phi_T = \nu(\tau_g + \tau_n) + \phi_d + \phi_\nu \tag{1.14}$$

(Fomalont 1999), where

- τ_g is the geometric time delay due to the difference in path length traveled by the signal before it reaches the antennae (Fig. 1.1). This delay is independent of frequency because it is assumed the signal travels in a vacuum. τ_g is the quantity that we ultimately aim to recover from the measurements in order to determine the source position.

- τ_n is the non-dispersive delay and contains additional contributions to the total phase delay that are *not* frequency dependent. Sources of non-dispersive delay include tropospheric refraction, timing errors between antennae, instrumental delay, and various time delays introduced by the antennae systems or correlator, such as cable stretching.

- ϕ_d is the dispersive delay and contains phase changes that are a non-linear function of frequency. Dispersive delays include ionospheric refraction and frequency dependent delays from the antennae systems.

- ϕ_ν is the visibility phase due to source structure. Astrometric observations are typically restricted to point-like objects, where the visibility phase is zero.

The Earth's atmosphere contributes to both τ_n and ϕ_d. The troposphere refracts light through a dry layer ($\sim$ 6 km thick) and a variable wet layer ($\sim$ 2 km thick), causing a non-dispersive delay. Refraction causes a decrease in light propagation speed, which equates to a time delay of $\sim$ 8 ns at the zenith (Fomalont & Perley 1999). The excess propagation path can be approximated as

$$L = 0.228 P_{tot} + 6.3w, \tag{1.15}$$

where L is the total zenith excess path in cm, P_{tot} is the ground-level pressure in millibars, and w is the vertical column of water-vapor content in cm (Fomalont & Perley 1999). Because L depends strongly on the troposphere's water-vapor content, which is highly dependent on weather conditions, the total pressure, water-vapor partial pressure, and temperature must be monitored throughout the observations.

The ionosphere also refracts light, causing an excess path length (in meters) of

$$L_i = -40\nu^{-2}N_e \tag{1.16}$$

at the zenith, where ν is the frequency in GHz and N_e is the electron column density in units of 10^{18} m^{-2} (Fomalont & Perley 1999). The excess path length is negative because the ionosphere advances the phase with respect to a wave in a vacuum. The ionosphere refraction is strongly dependent on frequency and therefore contributes to the dispersive delay. The electron column density varies by a factor of five between day and night and varies over the course of the year with the solar activity cycle and incidence angle. Thus, the excess path length must be calculated for each observing window using dual-frequency

satellite transmissions. At 8.3 GHz and a typical daytime electron column density of 3×10^{17} m^{-2}, the path length decrease is ~ 0.2 m, or 0.7 ns. The ionosphere also alters the plane of polarization of light, which can have a significant effect on observations of strongly polarized light.

For connected arrays where the antennae observe approximately the same atmosphere, removing the atmospheric delays is not strictly necessary because all antennae will experience roughly the same delay from the same portion of atmosphere. However, for long baseline arrays where the antennae are separated by hundreds of kilometers (or for observations at high frequencies), estimating the atmospheric delays at each antenna is crucial to recovering τ_g from the measured correlator power. In addition, each antenna in a long baseline array observes the object at a different elevation. Because both ionosphere and troposphere delays scale with the elevation angle Z as $\sec(Z)$, inaccuracies in the models of troposphere water-vapor partial pressure and ionosphere electron column density as a function of sky position can cause large phase delays between antennae that observe the target at different elevations (Walker 1999). Therefore, for long baseline arrays, it is important that atmospheric delays are correctly modeled and removed from the observed phase delay.

Because of the significant effect the atmosphere can have on the observed phase delay for long baseline interferometers, high precision astrometry measurements often require measurements of the atmospheric delay that are more accurate than the models and measurements described above. For these cases, geodetic blocks are observed before, after, and sometimes during the observations (e.g., Reid & Brunthaler 2004). Geodetic blocks are approximately 45 minute long observations of ~ 20 strong extragalactic radio sources at a range on elevations, including low elevations less than 10 degrees where the tropospheric delay is greatest (Walker 2000). These observations are used to calculate the tropospheric delay directly from the observed atmospheric conditions during the science observations, rather than from models. The measured delay from the geodetic blocks relates to the tropospheric

delay as

$$\tau = \tau_c + \frac{\tau_a}{\sin(Z)}, \tag{1.17}$$

where τ_c is the delay from clock error between the antennae and τ_a is the tropospheric delay. Reduction step 11 in Section 3.2, describes the process of measuring atmospheric delay from geodetic blocks in more detail.

In general, many of the sources of delay can be removed by referencing the observed source phases to a second source, known as the phase reference. Typically, the phase reference is a bright object that is near the target on the sky (usually < 10 degrees) and the target and phase reference are observed in an alternating cadence so that the time between target and phase reference observations is small (typically ~ 1 minute). If the excess delays vary on a time scale longer than the switching time and vary across the sky on an scale larger than the angular separation of the sources, then we can assume that the target and phase reference experience the same delay. Thus, the relative phase delay of the two sources will only contain the difference in τ_g. If the position (and, equivalently, τ_g) is well known for the phase reference, then τ_g of the target can be directly measured from the relative phase delay of the target and phase reference.

For most observations, it is reasonable to assume that the excess delay is constant between the target and phase reference. However, for high precision astrometry, the small differences in phase delay between the target and phase reference cannot be ignored. In this case, the target and phase reference delays should be calculated separately and then any minor remaining phase delays can be accounted for through phase referencing. This is the process that we describe in Chapter 3.

1.1.2 Extragalactic Proper Motions

Using high precision astrometry from VLBI observations, one can derive the proper motions of extragalactic objects. Extragalactic radio sources have been observed since the

1970s, either to study radio jets or, for apparently stationary objects, as fixed point sources to measure the Earth's orientation and monitor the terrestrial and celestial reference frames. However, improved VLBI astrometry and continued observations of extragalactic radio objects shows that the apparently stationary objects are *not* fixed over human timescales and have proper motions on the order of microarcseconds to milliarcseconds (e.g., Eubanks 1997; Gwinn et al. 1997; Feissel & Gontier 2000).

Extragalactic proper motions are a combination of intrinsic apparent proper motions that are specific to each individual source and uncorrelated between objects (e.g., radio jets), correlated proper motions from cosmological effects (e.g., Gwinn et al. 1997; Quercellini et al. 2009; Nusser et al. 2012; Darling 2013), and apparent proper motions from observer-induced signatures such as the secular aberration drift (e.g., Fanselow 1983; Bastian 1995; Eubanks et al. 1995; Sovers et al. 1998; Mignard 2002; Kovalevsky 2003; Kopeikin & Makarov 2006; Titov et al. 2011; Titov & Lambert 2013; Xu et al. 2012, 2013). Extragalactic proper motions typically have large uncertainties of tens of μas yr^{-1} (e.g., Titov & Lambert 2013; Truebenbach & Darling 2017) that are much larger than the predicted cosmological proper motions ($\lessapprox$ 15 μas yr^{-1}; see Section 1.3.1). Therefore, studies using extragalactic proper motions to measure correlated cosmological and observer-induced effects are challenged by both noise from the randomly-oriented, intrinsic apparent proper motions of the objects and large proper motion uncertainties. In the remainder of this Chapter, I describe several methods used to statistically detect these small correlated signals, including the secular aberration drift, primordial gravitational waves, and the relative peculiar transverse velocities caused by the matter density of large-scale structure.

1.2 Vector Spherical Harmonics

Global extragalactic proper motion signals can be expressed as a spherical vector field. Following Mignard & Klioner (2012), one can characterize the vector field as a sum of a series of vector spherical harmonics (VSH). The VSHs are split into spheroidal and toroidal

functions that resemble electric and magnetic fields, respectively, and that together form an orthogonal set of basis functions:

$$\vec{S}_{lm} = \frac{1}{\sqrt{(l(l+1)}}\ \vec{\nabla} Y_{lm} = \vec{u} \times \vec{T}_{lm}, \tag{1.18}$$

$$\vec{T}_{lm} = \frac{-1}{\sqrt{(l(l+1)}}\ \vec{u} \times \vec{\nabla} Y_{lm} = -\vec{u} \times \vec{S}_{lm}, \tag{1.19}$$

where $\vec{u}$ is the radial unit vector and Y_{lm} is the spherical harmonic function of degree l and order m. The spheroidal and toroidal functions can be expressed in equatorial coordinates as

$$\vec{S}_{lm}(\alpha, \delta) = \frac{1}{\sqrt{l(l+1)}} \left[\frac{1}{\cos\delta} \frac{\partial Y_{lm}}{\partial \alpha} \vec{e}_\alpha + \frac{\partial Y_{lm}}{\partial \delta} \vec{e}_\delta \right] \tag{1.20}$$

and

$$\vec{T}_{lm}(\alpha, \delta) = \frac{1}{\sqrt{l(l+1)}} \left[\frac{\partial Y_{lm}}{\partial \delta} \vec{e}_\alpha - \frac{1}{\cos\delta} \frac{\partial Y_{lm}}{\partial \alpha} \vec{e}_\delta \right], \tag{1.21}$$

respectively, where $\vec{e}_\alpha$ and $\vec{e}_\delta$ are the unit vectors along the right ascension and declination axes, which are both orthogonal to $\vec{u}$.

As with scalar spherical harmonics, where any scalar function on the surface of a sphere can be expressed as a linear combination of scalar spherical harmonics, any vector field $\vec{V}(\alpha, \delta)$ on the surface of a sphere can by expressed as a linear combination of VSHs:

$$\vec{V}(\alpha, \delta)) = \sum_{l=1}^{\infty} \sum_{m=-l}^{l} (s_{lm} \vec{S}_{lm} + t_{lm} \vec{T}_{lm}), \tag{1.22}$$

where s_{lm} and t_{lm} are complex coefficients describing the magnitude of the spheroidal and toroidal orders, respectively. Using the standard definitions of Y_{lm} and the associated Legendre functions (see Mignard & Klioner 2012 for sign convention), the first two orders ($l < 3$) for a real vector field can be expressed as follows:

$$\vec{V}_{E1}(\alpha, \delta) = \frac{1}{2}\sqrt{\frac{3}{\pi}} \left(s_{11}^{Re} \sin\alpha + s_{11}^{Im} \cos\alpha \right) \hat{e}_\alpha + \frac{1}{2}\sqrt{\frac{3}{\pi}} \Bigg(s_{10} \sqrt{\frac{1}{2}} \cos\delta + s_{11}^{Re} \cos\alpha \sin\delta - s_{11}^{Im} \sin\alpha \sin\delta \Bigg) \hat{e}_\delta, \tag{1.23}$$

$$\vec{V}_{B1}(\alpha,\delta) = \frac{1}{2}\sqrt{\frac{3}{\pi}}\left(t_{10}\sqrt{\frac{1}{2}}\cos\delta + t_{11}^{Re}\cos\alpha\sin\delta - t_{11}^{Im}\sin\alpha\sin\delta\right)\hat{e}_\alpha + \frac{1}{2}\sqrt{\frac{3}{\pi}}\Bigg(-t_{11}^{Re}\sin\alpha - t_{11}^{Im}\cos\alpha\Bigg)\hat{e}_\delta, \quad (1.24)$$

$$\vec{V}_{E2}(\alpha,\delta) = \frac{1}{2}\sqrt{\frac{5}{\pi}}\left(s_{21}^{Re}\sin\alpha\sin\delta + s_{21}^{Im}\cos\alpha\sin\delta - s_{22}^{Re}\sin 2\alpha\cos\delta - s_{22}^{Im}\cos 2\alpha\cos\delta\right)\hat{e}_\alpha + \frac{1}{2}\sqrt{\frac{5}{\pi}}\Bigg(s_{20}\frac{1}{2}\sqrt{\frac{3}{2}}\sin 2\delta - s_{21}^{Re}\cos\alpha\cos 2\delta + s_{21}^{Im}\sin\alpha\cos 2\delta - s_{22}^{Re}\frac{1}{2}\cos 2\alpha\sin 2\delta + s_{22}^{Im}\frac{1}{2}\sin 2\alpha\sin 2\delta\Bigg)\hat{e}_\delta, \quad (1.25)$$

and

$$\vec{V}_{M2}(\alpha,\delta) = \frac{1}{2}\sqrt{\frac{5}{\pi}}\Bigg(t_{20}\frac{1}{2}\sqrt{\frac{3}{2}}\sin 2\delta - t_{21}^{Re}\cos\alpha\cos 2\delta + t_{21}^{Im}\sin\alpha\cos 2\delta - t_{22}^{Re}\frac{1}{2}\cos 2\alpha\sin 2\delta + t_{22}^{Im}\frac{1}{2}\sin 2\alpha\sin 2\delta\Bigg)\hat{e}_\alpha + \frac{1}{2}\sqrt{\frac{5}{\pi}}\Bigg(-t_{21}^{Re}\sin\alpha\sin\delta - t_{21}^{Im}\cos\alpha\sin\delta + t_{22}^{Re}\sin 2\alpha\cos\delta + t_{22}^{Im}\cos 2\alpha\cos\delta\Bigg)\hat{e}_\delta, \quad (1.26)$$

where $\vec{V}_E$ and $\vec{V}_B$ are the spheroidal and toroidal portions of the vector field, respectively, and s_{lm} and t_{lm} have been rewritten in polar form. In this form, the s_{lm} and t_{lm} coefficients are all real numbers.

1.2.1 The Secular Aberration Drift

One global extragalactic proper motion signal that can be represented as a spherical harmonic vector field is the secular aberration drift. The secular aberration drift is the apparent motion of extragalactic objects caused by the barycenter's acceleration towards the Galactic center. The observed signal can be modeled as a curl-free dipole (Eqn. 1.23) with

an apex at the Galactic center (266.4°, -28.9°). Using proper motions of masers associated with young massive stars, Reid et al. (2009) created a model of the Galactic plane to measure that the Solar System is 8.4 ± 0.6 kpc from the Galactic center and has a barycentric circular rotation speed of 254 ± 16 km s^{-1}. This yields an acceleration of 0.79 ± 0.11 cm s^{-1} yr^{-1} and a dipole amplitude of 5.40 ± 0.78 μas yr^{-1}.

Although the secular aberration drift signal is small compared to typical extragalactic proper motions, it is important that it be well measured. The International Celestial Reference System (ICRS) is defined based on the positions of a set of extragalactic objects, which are assumed to have a net null proper motion (McCarthy & Petit 2004). Although some extragalactic objects now have measured proper motions, these motions are, in general, randomly oriented, thereby making the ICRS assumption essentially correct. The ICRS is defined using a least-squares parameter estimation, so randomly oriented proper motions will have little effect on the fit outcome. On the other hand, the secular aberration drift imparts a global dipole signal to all observed extragalactic proper motions. Because this motion is correlated, it may systematically influence the ICRS axes (Bastian 1995; Eubanks et al. 1995; Gwinn et al. 1997; Sovers et al. 1998; Kovalevsky 2003; MacMillan 2005; Kopeikin & Makarov 2006; Titov 2010). If the secular aberration drift is not accounted for during definition of the ICRS axes, then the ICRS is only a quasi-inertial reference system (Hofmann-Wellenhof et al. 2003), rather than the preferred inertial reference system. The current realization of the ICRS, the Second International Celestial Reference Frame (ICRF2; IERS Technical Note No. 35 2009), finds significant systematic effects on the order of 50 μas when the ICRF2 is compared with seven catalogs created from the same data but from different analysis centers and with different software packages. Additionally, they find that the reported source position uncertainties in the catalog are too small and must be scaled by 95% for declination and 88% for Right Ascension in order to be a true reflection of the position uncertainties (IERS Technical Note No. 35 2009). Titov (2010) suggests that a portion of the systematic uncertainties and unaccounted for position uncertainties is due to the secular aberration

drift.

There are two main methods of measuring the secular aberration drift. The first treats the positions of all extragalactic radio sources as non-fixed: they can change every 24 hours when solving for the ICRS (see Chapter 2). With this approach, a coordinate time-series is created for each radio source, from which proper motions are calculated. Then, a spherical and toroidal dipole (Eqns. 1.23 and 1.24) can be simultaneously fit to the proper motions to measure the secular aberration drift. This approach was first realized by Gwinn et al. (1997) and has been more recently used by Titov & Lambert (2013) to measure a solar acceleration of 0.93 ± 0.11 cm s^{-1} yr^{-1}; equivalent to a spheroidal dipole amplitude of 6.4 ± 1.1 μas yr^{-1} pointed towards $(266 \pm 7°, -26 \pm 7°)$ in equatorial coordinates and a toroidal component with amplitude 1.9 ± 0.8 μas yr^{-1}. We also use the time-series approach to measure the secular aberration drift in Chapter 4.

The second method to measure the secular aberration drift is to directly solve for the three-dimensional solar acceleration vector and the ICRS axes simultaneously. This approach was initially realized by MacMillan (2005) and Titov (2009) and later used by Xu et al. (2013) to find a solar acceleration vector of $(.74 \pm 0.05, 0.02 \pm 0.06, 0.40 \pm 0.05)$ cm s^{-1} yr^{-1} in Galactic Cartesian coordinates, which is equivalent to a dipole with an amplitude of 5.8 ± 0.3 μas yr^{-1} pointed towards $(243.0°, -11.5°)$ in equatorial coordinates.

All of these measurements of the secular aberration drift, including our measurement in Truebenbach & Darling (2017) and Chapter 4, show that the aberration drift is a significant effect that has a measurable effect on extragalactic proper motions. Because the solar acceleration is currently not removed from ICRS calculations, we must remove it after the fact from our extragalactic proper motions before measuring any cosmological effects. To illustrate, the predicted relative proper motion for objects in a gravitationally-bound, static structure that is receding with the Hubble flow is -15 μas yr^{-1} (Sec. 1.3.1), while the secular aberration drift adds an apparent dipole signal with a predicted amplitude of 5.40 ± 0.78 μas yr^{-1}. Both effects are of a similar order of magnitude, thereby demonstrating

that the aberration drift must be removed from the proper motions before attempting to measure equally large cosmological effects.

1.2.2 Primordial Gravitational Waves

A second global extragalactic proper motion signal that can be represented as a spherical harmonic vector field are the oscillations in space-time driven by primordial gravitational waves. Primordial gravitational waves are created by temperature anisotropies during inflation and cause angular deflection of light that creates an apparent global quadrupole signal (e.g., Braginsky et al. 1990; Book & Flanagan 2011). The gravitational wave background can also be detected through other methods – e.g., pulsar timing (Backer & Hellings 1986) and CMB polarization (Polnarev 1985) – but extragalactic proper motions are able to measure or constrain the background over a much larger frequency range than pulsar timing or CMB polarization, $H_0 \lesssim f \lesssim 1$ yr^{-1} ($10^{-18} \lesssim f \lesssim 10^{-8}$ Hz; Book & Flanagan 2011).

The discovery of the cosmic microwave background (CMB; Penzias & Wilson 1965) provided confirmation of the hot big bang (Dicke et al. 1965) and spurred questions about the isotropy and temperature of the background. The temperature anisotropies of the CMB were detected by the Cosmic Background Explorer (COBE; Smoot et al. 1990) and confirmed the Big Bang paradigm (Smoot et al. 1992). The creation of the "standard" cosmological model and the modification of the model to include dark energy followed (ΛCDM; Riess et al. 1998). Inflationary cosmology extended the standard model to offer solutions for a number of puzzles including the entropy, flatness, and smoothness problems (e.g., Brout et al. 1978; Starobinsky 1980; Sato 1981). According to the inflationary model, the CMB temperature anisotropies originated as quantum fluctuations that were stretched by inflationary expansion (e.g., Mukhanov & Chibisov 1981; Hawking 1982; Starobinsky 1982; Mukhanov 1985). However, the inflationary paradigm requires large extrapolation from the well-tested physical regimes of the modern Universe to the highly curved space-time of the early Universe, with energies near 10^{16} GeV and time scales less than 10^{-32} s (BICEP2 Collaboration et al.

2014). Therefore, a more direct test of inflation is needed to both confirm this model and to measure its energy scale.

Primordial gravitational waves can provide such a test. As the quantum fluctuations of the primordial Universe are stretched by inflation, gravitational waves are generated by the anisotropic stretching of space-time. Theory predicts that the background produced by these stochastic gravitational waves has a characteristic spectral shape (e.g., Grishchuk 1975; Rubakov et al. 1982; Krauss & Wilczek 2014). Although this signal is too weak to be detected by modern instruments, there are several methods to detect the imprint of the signal on the CMB (BICEP2 Collaboration et al. 2014). Just as density perturbations in the early Universe are seen as temperature anisotropies in the CMB, gravitational waves stretch the space-time metric and introduce both local and global quadrupole anisotropies on the CMB. The anisotropic stretching of space-time by the gravitational wave background can be seen as a shift in location of a quasar or other extragalactic object (Gwinn et al. 1997), as well as a delay/advance in the arrival of a pulsar signal (Backer & Hellings 1986). Lastly, because a gravitational wave can be described as a tensor perturbation, they imprint a unique B-mode polarization on the CMB (e.g., Polnarev 1985; Seljak 1997).

The growth of large-scale structure, clusters, and galaxies can be described as scalar density perturbations that grow linearly with time from the initial density anisotropies seen in the CMB. As light is scattered off of the surface of last scattering, the CMB density perturbations lead to a net E-mode polarization of the light. Similarly, gravitational waves can be described as tensor perturbations that grow from early Universe anisotropies (Dodelson 2003). Because the perturbations are tensor rather than scalar, they introduce a quadrupole signal to the anisotropies of the CMB, which is seen as an E- and B-mode polarization. Unlike light plane waves, which are rotationally symmetric and therefore produce only E-mode polarization, gravitational waves are perturbations of the space-time metric and have no rotational symmetry, allowing the production of both E- and B-mode polarization (Dodelson 2003). Thus, the detection and measurement of the B-mode polarization of

the CMB has been a popular proposed avenue for detecting primordial gravitational waves and consequently confirming the inflationary model (e.g., BICEP2 Collaboration et al. 2014; Kim & Trippe 2016). Although B-mode polarization from gravitational waves has not yet been detected, limits on the gravitational wave background have been published by many teams. The background is typically presented either as r, the tensor-to-scalar ratio – i.e., the strength of gravitational wave perturbations relative to scalar density perturbations – or as Ω_{gw}, the energy density due to gravitational waves relative to the critical density of the Universe. In the frequency range $10^{-17} - 10^{-16}$ Hz, BICEP2/Keck joint analysis found $r < 0.07$ at a 95% confidence level (Ade et al. 2016) – i.e., $\Omega_{gw}h^2 < 10^{-14}$ (Pagano et al. 2016). At smaller scales corresponding to frequencies $\sim 10^2$ Hz, the cross-correlation between the LIGO and VIRGO detectors found $\Omega_{gw}h^2 < 2.6 \times 10^{-6}$ (Aasi et al. 2014). Unfortunately, a definitive detection of gravitational wave B-mode polarization has been obscured by B-mode polarization produced by dust in our own galaxy – intergalactic dust grains align with the Galactic magnetic fields and produce linear polarization in both E- and B-modes (Hildebrand et al. 1999). To detect the B-mode polarization from gravitational waves, either larger angular scales must be examined to average out the small-scale variations in interstellar dust polarization (Efstathiou & Gratton 2009), or more data with lower noise at a variety of frequencies must be obtained to model and remove dust contribution (BICEP2/Keck and Planck Collaborations et al. 2015).

Another proposed method of detecting gravitational waves is pulsar timing. As a gravitational wave passes between the Earth and a pulsar, space-time will be stretched/compressed, causing a change in the pulsar period (Detweiler 1979). Because of the high precision with which we can measure pulsar periods, pulsar timing enables the detection of ultra-long period ($\sim 5 - 10$ years) gravitational waves of dimensionless strain amplitudes $\geq 10^{-15}$ (Kelley et al. 2017). However, changes in pulsar timing can also be caused by systematic errors, including errors in atomic time standards or locations of planetary ephemeris, or even noise from the pulsar itself (Ransom 2013). These errors can be mitigated by using an array of

pulsars – the quadrupolar nature of gravitational waves creates a correlated delay based on the angular separation of pulsar pairs (Hellings & Downs 1983). There are many pulsar timing arrays currently taking measurements, including the North American Nanohertz Observatory for Gravitational Waves (NANOGrav; Demorest et al. 2013), the European Pulsar Timing Array (EPTA; van Haasteren et al. 2011), and the Parkes Pulsar Timing Array (PPTA; Manchester et al. 2013). The EPTA has constrained the gravitational wave background to $\Omega_{gw}h^2 < 1.1 \times 10^{-9}$ at 2.8 nHz (Lentati et al. 2015).

One of the limitations of pulsar timing is that detections are limited by the span of observations; the gravitational wavelength must be less than the observing period for the pulsar period to noticeably change (Backer & Hellings 1986). Detection of gravitational waves by B-mode polarization of the CMB is similarly limited by the observed frequencies used to measure the CMB. Extragalactic proper motions, on the other hand, can detect all waves with frequencies less than the observing frequencies (roughly down to the horizon scale, $H_0 \sim 10^{-18}$ Hz; Pyne et al. 1996) and are independent of both the spectrum of the waves and the source of the gravitational radiation (Gwinn et al. 1997). A light ray propagating through a gravitational wave background will be deflected by the stretched space-time at an angle of order the gravitational wave strain amplitude (Book & Flanagan 2011), giving the emitting object an apparent proper motion. However, because many extragalactic objects also have their own intrinsic proper motions (when measured at radio wavelengths), an array of sources must be used to find a correlated deflection. Book & Flanagan (2011) show that the gravitational wave background energy density is related to the correlated proper motions of extragalactic objects, μ, as $\Omega_{gw} \sim \langle\mu^2\rangle/(NH_0^2)$, where N is the number of proper motions observed. These correlated proper motions will have a quadrupolar signal with equal power E- and B-modes that can be modeled as a VSH quadrupole using Equations 1.25 and 1.26. The modeled quadrupole can potentially measure or constrain the gravitational wave background over ten decades in frequency, $10^{-18} - 10^{-8}$ Hz, depending on the timespan over which proper motions are derived.

Several limits on the gravitational wave background have been measured using extragalactic proper motions, including $\Omega_{gw}h^2 < 0.11$ for $f < 2 \times 10^{-9}$ Hz at 95% confidence (Gwinn et al. 1997) and $\Omega_{gw}h^2 < 0.0042$ for $f < 10^{-9}$ Hz (Titov et al. 2011). Most recently, we obtained a 95% confidence limit using the catalog presented in this thesis (Truebenbach & Darling 2017) of $\Omega_{gw}h^2 < 0.0031$ for $f \lesssim 10^{-9}$ Hz (Darling et al. 2018 submitted). We also combined the VLBA proper motion catalog with the first *Gaia* data release (Gaia Collaboration et al. 2016) to add an additional position epoch to the extragalactic proper motions. With this *Gaia*-VLBA catalog, we found $\Omega_{gw}h^2 < 0.005$ for the same frequency range (Darling et al. 2018 submitted). Finally, we predict the end-of-mission gravitational wave background limit detectable by *Gaia* of $\Omega_{gw}h^2 \lesssim 2 \times 10^{-4}$ using the Paine et al. (2018 submitted) *Gaia*-WISE extragalactic proper motion catalog, which includes estimated *Gaia* end-of-mission proper motion uncertainties for $\sim 5 \times 10^5$ extragalactic objects.

1.2.3 Anisotropy

The isotropy of Hubble expansion can also be tested with extragalactic proper motions and vector spherical harmonics. The isotropy of expansion is well constrained for the early Universe (Ade et al. 2016). However, "cold spots" in the CMB suggest that there may be local deviations from isotropy (Cruz et al. 2005). Although inflation in the early Universe efficiently smooths major anisotropies, dark energy with anisotropic pressure can drive late-time anisotropic expansion in the present, dark energy-dominated Universe (Battye & Moss 2006; Chimento & Forte 2006; Koivisto & Mota 2008a,b; Cooray et al. 2010). One test of anisotropic expansion is through extragalactic proper motions. If expansion is anisotropic, extragalactic objects will appear to stream towards regions of faster expansion and away from regions of slower expansion. The proper motion vector field will, to first order, contain a curl-free quadrupole signal (Fontanini et al. 2009; Quercellini et al. 2009; Titov 2009).

Anisotropic, homogeneous expansion can be described by a Bianchi I model solution

to the Friedmann equations –

$$ds^2 = -dt^2 + a^2(t)dx^2 + b^2(t)dy^2 + c^2(t)dz^2, \tag{1.27}$$

where $a(t)$, $b(t)$, and $c(t)$ are three separate scale factors for spatial directions x, y, and z, respectively (e.g., Quercellini et al. 2009; Fontanini et al. 2009). These three different expansion rates will produce a shearing velocity field where the shear can be characterized by the fractional deviation from the current average Hubble expansion (H_0),

$$\Sigma_i = \frac{H_{i,0}}{H_0} - 1, \tag{1.28}$$

where $i = x$, y, or z (Darling 2014). Using the Titov & Lambert (2013) proper motion catalog of 429 radio sources, Darling (2014) fit an anisotropy model to the proper motion vector field to measure any potential deviations from isotropic Hubble expansion. The Hubble expansion was found to be isotropic to 7% in the best-constrained direction. More recently, Paine et al. (2018 submitted) used the *Gaia*-WISE extragalactic proper motion catalog to predict the extent to which *Gaia* will be able to constrain the isotropy of Hubble expansion. Using 1000 randomly generated anisotropy models, Paine et al. (2018 submitted) find that *Gaia*-WISE active galactic nuclei (AGN) will be able to constrain the anisotropy of the Hubble expansion to $\sim 2\%$.

1.3 The Evolution of Large-Scale Structure

The modern standard model of cosmology is a spatially flat, expanding Universe dominated by cold dark matter and a cosmological constant. Small matter density perturbations in the primordial Universe drive the initial gravitational collapse of matter and dark matter into overdensities, which give rise to the formation of large-scale structure (LSS), clusters, and galaxies (e.g., Blumenthal et al. 1984) through a hierarchical process. The overall process and cosmological parameters that govern the process are, in general, well constrained (e.g., Hu & White 1996a; Hu & White 1996b; Hu et al. 1997; Riess et al. 2001; Peiris et al.

2003; Moodley et al. 2004; Planck Collaboration et al. 2016a). However, the exact values of the parameters remain somewhat uncertain, including the baryon and neutrino density (e.g., Eisenstein & Hu 1999; Eisenstein et al. 2005), the Hubble constant (e.g., Eisenstein et al. 2005; Riess et al. 2011; Planck Collaboration et al. 2016b; Zhang et al. 2017), the tensor-to-scalar ratio (e.g., Planck Collaboration et al. 2016c), and the spatial curvature (e.g., Eisenstein et al. 2005; Planck Collaboration et al. 2016d).

The current distribution of LSS provides a means to test many of the less certain cosmological parameters by comparing the observed LSS to that predicted by cosmological simulations. Most commonly, maps of LSS are created using the sky distribution of visible galaxies with redshift as a proxy for distance (e.g., de Lapparent et al. 1986; York et al. 2000; Gott et al. 2005). However, these maps rely on the assumption that light and visible matter trace the overall mass distribution. In general, it is reasonable to assume that galaxies form at the peaks of matter (Kaiser 1984), but a bias model (e.g., Bardeen et al. 1986; Coles 1993; Fry 1996; Tegmark & Peebles 1998) is still required to translate the observed LSS to the matter distributions generated by cosmological simulations.

Galaxy line-of-sight peculiar velocities are an alternate means to track the mass distribution that does not require a translation between light and total mass because peculiar velocities of galaxies are directly caused by the density distribution. Additionally, velocity surveys can probe more distant structures than redshift surveys because objects' velocities can be influenced by distant objects that are outside the range of the survey (e.g., Doumler et al. 2013; Tully et al. 2014). The major drawback of line-of-sight velocity surveys to detect matter distribution is that small uncertainties in a galaxy's distance can translate to large velocity uncertainties. Therefore, large samples of galaxy velocities and distances are needed to statistically detect an average mass density distribution (Tully et al. 2014).

Both methods of mapping LSS produce similar mass distributions (e.g., Strauss et al. 1992; Dekel et al. 1993; Kitaura et al. 2012; Courtois et al. 2012), which is a good confirmation of the standard model of LSS evolution through hierarchical growth and gravitational

instability. However, both methods require redshifts or other model-dependent distance measures to either spatially place the galaxies or to translate spectroscopic line shifts to peculiar velocities. Therefore, another method that is independent of the "distance ladder" and other distance models is needed to provide an independent test of the model of LSS evolution.

1.3.1 Pairwise Proper Motion

Extragalactic proper motions can be used to test models of LSS evolution without a reliance on the "distance ladder." Like line-of-sight peculiar velocities, proper motions directly probe the mass density distribution and do not require any assumptions about the relative abundances of visible matter and dark matter. As the Universe expands, both line-of-sight velocities and proper motions will contain peculiar motion from gravitational interactions. However, line-of-sight velocities require an independent distance measure to differentiate Hubble expansion and peculiar velocity. On the other hand, orthogonal proper motions across the line of sight - including gravitationally-bound structures decoupled from the Hubble flow - are separable from the Hubble expansion because no proper motion will occur in a homogeneous expansion (Nusser et al. 2012; Darling 2013).

The majority of extragalactic proper motions are measured using radio-loud quasars because they have high radio flux densities, radio interferometry allows high astrometric precision through large, globe-spanning synthetic apertures, and quasar cores are often point-like at radio frequencies. However, in addition to proper motion caused by cosmological effects, quasars also have intrinsic proper motions, predominantly due to the motion of plasma in relativistic jets produced by the quasars (e.g., Bridle & Perley 1984; Fey et al. 1997). These intrinsic proper motions are random in orientation on the sky. To separate intrinsic proper motions from cosmological proper motions, we use the relative proper motions of "pairs" of quasars (Darling 2013). The intrinsic proper motions of two quasars are uncorrelated, whereas LSS growth will display a *correlated* signal in close separation pairs along the pair axis. With a large enough sample size and a long enough observing period, the noise caused

by intrinsic motions can be reduced enough to detect the correlated proper motion caused by the mass distribution of LSS.

For a "pair" of extragalactic objects[1] , the angular separation of the objects is defined as

$$\sin\theta = \frac{l}{D_A}, \tag{1.29}$$

where l is the proper length separating the objects and D_A is the angular diameter distance. Then, the relative proper motion of the two objects along a great circle, $\dot{\theta}$, is the fractional change in their angular separations –

$$\frac{\dot{\theta}}{\sin\theta} = \frac{-\dot{D_A}}{D_A} + \frac{\dot{l}}{l} = \frac{-H(z)}{1+z} + \frac{\dot{l}}{l}, \tag{1.30}$$

where

$$H(z) = H_0\sqrt{\Omega_{M,0}(1+z)^3 + \Omega_\Lambda}, \tag{1.31}$$

and $\dot{l}$ is the change in proper length (Darling 2013). See Figure 1.3.1 for a schematic of Equation 1.30.

If the pair of extragalactic objects are far enough apart that they do not interact gravitationally, then

$$\frac{\dot{l}}{l} = \frac{H(z)}{1+z}, \tag{1.32}$$

because the space between the objects expands with the Hubble expansion. Combining this equation and Equation 1.30 gives $\dot{\theta} = 0$ – no proper motion is expected for objects comoving with a homogeneously expanding Universe. On the other hand, if the pair are part of a static structure (e.g., two quasars in the same virialized cluster) then $\dot{l}/l = 0$ and the pair will appear to converge as they move away from us with the Hubble flow. For a static structure at $z = 0$, the apparent convergence of a pair can be approximated as ~ 15 μas yr^{-1}. The majority of extragalactic pairs have large physical separations and will show the null signal expected for gravitationally non-interacting objects entrained in the Hubble flow.

[1] "Pair" signifies any two randomly selected objects and does not denote any association between the two objects.

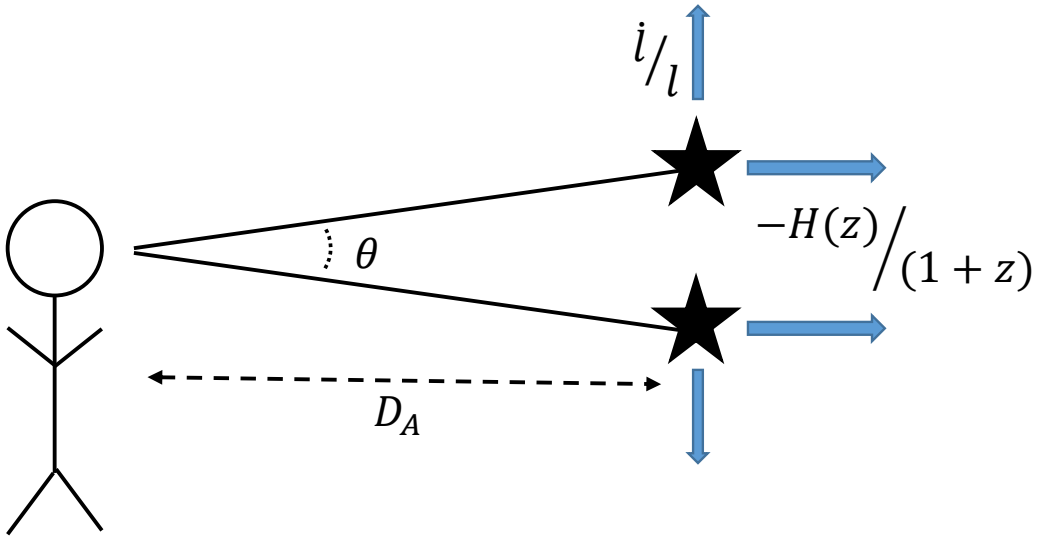

Figure 1.2 Schematic showing the relative change in angular separation for two extragalactic objects, represented as stars. For simplicity, it is assumed that both objects have the same angular diameter distance, D_A. See Equation 1.30 for an explanation of the variables.

However, pairs with close physical separations ($\lesssim 50$ Mpc, comoving) are expected to show relative proper motion that is a combination of the two signals; the pair will both appear to converge as they move away from us with the Hubble flow and they will have relative proper motion determined by their gravitational interaction with their local mass density distribution. Therefore, the majority of pairs are expected to have a total relative proper motion that is less than the ~ 15 μas yr^{-1} signal predicted for static structures.

1.4 Summary of the Following Thesis Work

In this Chapter, I have described several correlated, global signals that can be measured or constrained using extragalactic proper motions, including the secular aberration drift, primordial gravitational waves, the anisotropy of expansion, and the evolution of large-scale structure. The secular aberration drift can only be measured with proper motions, and primordial graviataional waves, although constrained through other methods, have not been detected by any technique. For these signals, extragalactic proper motions are a crucial detection method that can make significant contributions to these fields. In contrast, anisotropy and the evolution of large-scale structure can be measured through other techniques. However, extragalactic proper motions provide an alternative method of study that provides an important verification of results that rely on models or assumptions (e.g., the assumption of a "distance ladder" for measurements of the distribution of large-scale structure). An independent measurement of these cosmological processes provides not only confirmation of existing paradigms, but further support for the models and theories from which those paradigms are made.

The primary complication of using extragalactic proper motions to measure cosmological signals are the large intrinsic proper motions exhibited by many extragalactic objects at radio wavelengths. The average radio object has a proper motion of ~ 14 μas yr^{-1} and statistically significant proper motions can range between $\sim 1-1000$ μas yr^{-1} (Truebenbach & Darling 2017). Additionally, typical proper motions have uncertainties of tens of μas yr^{-1}

(e.g., Titov & Lambert 2013; Truebenbach & Darling 2017). In contrast, the secular aberration drift is predicted to have an amplitude of 5.40 μas yr^{-1} (derived from Reid et al. 2009) and the apparent relative proper motion of pairs of extragalactic objects is expected to be less than ~ 15 μas yr^{-1}. Therefore, these small cosmological signals can only by separated from large intrinsic proper motions with large sample sizes and statistical methods that are not biased by large, highly significant intrinsic proper motions.

In this thesis, I make improvements in both the sample size of available extragalactic proper motions and the statistical methods used to detect small, correlated signals underlying the large, randomly-oriented distribution of intrinsic proper motions. In Chapter 2, I describe the archival VLBI data that I used to calculate the majority of the extragalactic proper motions. I developed a new method of calculating proper motions from the data that produces proper motions that are less influenced by outlier position measurements and that have lower uncertainties than those found by previous studies using the same data (e.g., Titov & Lambert 2013). In this chapter, I also present 10 new redshift measurements, which are used in a later chapter to study relative peculiar transverse velocities caused by the mass distribution of LSS.

In Chapter 3, I expand the sample of available extragalactic proper motions with new VLBA astrometry observations. I developed an observing plan and reduction process that minimizes the resulting proper motion uncertainties. Additionally, I created an automated self-calibration pipeline that can quickly produce VLBA images without sacrificing resolution or accuracy. Unlike the majority of astrometric archival data (e.g., IERS Technical Note No. 35 2009), which are reduced in bulk, I deal with each object individually and produce more precise astrometry.

Chapter 4 presents the new extragalactic proper motion catalog created from the archival data and new observations described in Chapters 2 and 3. Then, I use the proper motion catalog to measure the secular aberration drift. To measure the small secular aberration drift signal from a sample dominated by large intrinsic proper motions, previous studies

used a priori knowledge of the expected signal to clip their data (e.g., Titov et al. 2011; Titov & Lambert 2013). In this Chapter, I describe a new method that does not make any assumptions about the expected signal and is less influenced by significant intrinsic proper motions than previously used fitting techniques.

Chapter 5 uses the extragalactic proper motion catalog to measure the average pairwise proper motions of extragalactic objects as a function of comoving separation. Again, I focus on extracting the small cosmological signal from the intrinsic proper motions with a fitting algorithm that is insensitive to significant outliers and a clipping method that removes pairs whose relative velocities are dominated by jets or other non-cosmological phenomena. I also compare the extracted signal to the signal predicted from a theoretical mass power spectrum through a transverse, peculiar velocity two-point correlation function. Finally, I create a simulated *Gaia* catalog with predicted end-of-mission proper motion uncertainties to estimate the significance at which *Gaia* proper motions will be able to measure the relative peculiar transverse velocities of extragalactic objects caused by the mass distribution of LSS.

To conclude, in Chapter 6 I summarize the presented thesis work and discuss future improvements to extragalactic proper motions with both existing and proposed radio interferometers and with *Gaia*.

Chapter 2

Catalog Creation and Optical Redshifts

We conducted our measurements of the secular aberration drift and evolution of large-scale structure primarily with archival VLBI data. By using existing data that spans more than 30 years, we are able to detect small extragalactic proper motions of ~ 1 μas yr^{-1} without requiring that the observations be overly precise. The precision of the proper motions is dominated by the total monitoring length, rather than the precision of the astrometry at each epoch. In this chapter, I introduce the archival VLBI data used to create the majority of the extragalactic proper motion catalog and describe the process for deriving proper motions from the available coordinate time-series. I calculated 680 proper motions from the coordinate time-series, with average uncertainties of ~ 24 μas yr^{-1}. In addition, we found that 8% of our final catalog did not have redshifts. But, in order to use extragalactic proper motions for cosmological studies, we require redshifts. In particular, redshifts are needed to measure the physical separation between objects as part of our measurement of the Hubble expansion and collapse of large-scale structure. In the second half of this chapter, I describe the optical spectroscopic observations at Apache Point Observatory and Gemini North Observatory that I conducted to measure 10 new quasar redshifts.

This chapter reproduces Sections 2 and 3 from Truebenbach & Darling (2017). Reproduced with permission of the AAS.

2.1 Catalog Creation

We created our catalog of extragalactic radio proper motions using the 2017a Goddard VLBI global solution [1] (e.g., IERS Technical Note No. 35 2009). The global solution uses group delays and radio wave arrival times of a series of distant compact radio sources (typically quasars) to simultaneously solve for both a terrestrial and celestial reference frame using the fitting program CALC/SOLVE[2] . Earth orientation parameters are also solved for after each 24-hour session.

The 2017a solution is computed from more than 30 years of dual-band VLBI observations – 1979 August 3 to 2017 March 27 – and uses a total of 5696 diurnal sessions and greater than 10^7 measurements of group delays. All session with durations of 18 hours and longer and source elevations higher than 5° were used in the fitting process. No net translation and rotation constraints were applied to the positions and velocities of all stations except for stations near Chile and Japan. The recent earthquakes in 2010 and 2011, respectively, caused non-linear motions for nearby stations, which are modeled using post-seismic deformation models (Altamimi et al. 2016). Atmospheric gradient delays were modeled following MacMillan (1995) and MacMillan & Ma (1997) and the troposphere zenith delay was calculated using logged pressure and temperature (e.g., Saastamoinen 1972)[3] .

In addition to the 2017a global solution, an astrometric time-series of 4618 extragalactic radio sources is also produced by Goddard[4] . Instead of treating the radio source positions as global parameters, which are assumed to be constant with time, the positions are incrementally treated as local parameters and are estimated once for each 24-hour session. Five separate solutions are combined to create the final 2017a time series. In the first solution, the positions of all 295 ICRF2 defining sources are global parameters and are tied to their

[1] https://gemini.gsfc.nasa.gov/solutions/2017_astro/2017a_ts.html

[2] https://lupus.gsfc.nasa.gov/software_calc_solve.htm

[3] See https://gemini.gsfc.nasa.gov/solutions/2016a/gsf2016a.eops.txt for further details on initial parameters and assumptions

[4] See https://gemini.gsfc.nasa.gov/solutions/2017_astro/2017a_ts.html

ICRF2 positions with a a no-net-rotation (NNR) constraint, while the positions of all other sources are solved for at each session. In the second solution, the NNR constraint is removed for a quarter of the defining sources (every fourth source in RA) and the positions of this quarter are treated as local parameters and are solved for at each session. In the third, fourth, and fifth solutions, the next successive quarter of the defining sources are treated as local parameters. By incrementally treating all source positions as local parameters, the positions are allowed to vary between sessions and a coordinate time-series can be constructed. Then, we can fit a trend line to the coordinate vs. epoch for each source and solve for each source's proper motion.

During the creation of the solutions, a NNR constraint is applied to fix the ICRS axes (IERS Technical Note No. 35 2009). This constraint is needed to remove degeneracy when solving for local parameters of each 24-hour observing session. However, Titov (2010) argues that a tight NNR constraint can remove systemic proper motions from the final catalog. To mitigate this effect, the NNR constraint is loosened during the creation of the Goddard 2017a coordinate time series. By creating five separate solutions where only a portion of the sources are required to satisfy the NNR constraint in each solution, all source positions are allowed to rotate with respect to the ICRS axes, while still enabling a non-degenerate local solution.

We fit a line to each coordinate time series (right ascension and declination) for each radio source using an analytical least-squares parameter estimation. If we assume each source has a constant proper motion (this is a reasonable approximation for most extragalactic sources, with a few exceptions discussed below), then we can solve for the proper motion, μ, by minimizing the χ^2 statistic,

$$S = \sum_{i=1}^{N} \frac{(r_i - \theta_0 - \mu t_i)^2}{\sigma_{r_i}^2} \tag{2.1}$$

where r_i is the celestial position of the source at time t_i, σ_{r_i} is the uncertainty of the source position, and θ_0 is the y-intercept of the line – a physically meaningless quantity in this

application. Because the fitting model is linear, we can directly solve for μ and θ_0 –

$$\mu = \frac{s\ s_{tr} - s_t\ s_r}{\Delta}, \tag{2.2}$$

and

$$\theta_0 = \frac{s_{t^2}\ s_r - s_t\ s_{tr}}{\Delta}, \tag{2.3}$$

where

$$s = \sum_{i=1}^{N} \frac{1}{\sigma_{r_i}^2}, \tag{2.4}$$

$$s_t = \sum_{i=1}^{N} \frac{t_i}{\sigma_{r_i}^2}, \tag{2.5}$$

$$s_r = \sum_{i=1}^{N} \frac{r_i}{\sigma_{r_i}^2}, \tag{2.6}$$

$$s_{t^2} = \sum_{i=1}^{N} \frac{t_i^2}{\sigma_{r_i}^2}, \tag{2.7}$$

$$s_{tr} = \sum_{i=1}^{N} \frac{t_i\ r_i}{\sigma_{r_i}^2}, \tag{2.8}$$

and

$$\Delta = s\ s_{t^2} - s_t^2. \tag{2.9}$$

We solved for proper motions separately in right ascension and declination – r in the above equations is thus α or δ, respectively. Proper motions in right ascension, and their associated uncertainties, are corrected for declination. We excluded all sources that had been observed for less than 10 years or for fewer than 10 sessions. We also excluded sessions from before 1990 because fewer antennas and fewer monitored radio sources made VLBI data taken before this time less accurate (e.g., Gontier et al. 2001; Malkin 2004; Feissel-Vernier et al. 2004; Lambert & Gontier 2009; Titov et al. 2011). We also removed the 39 "special handling" sources from ICRF2 (IERS Technical Note No. 35 2009). These sources show significant position instability in either right ascension and/or declination, indicating that their proper motion is largely from relativistic radio jets, rather than from the global effects

we hope to measure. Thus, the inclusion of these sources in our catalog would impede our goal of detecting small, correlated proper motions.

There is a large variation in the uncertainties of individual positions within many of the time series. Additionally, some of these positions with high uncertainties are separated from the other measurements by a large gap in time, thereby giving them a disproportionately large influence on the resulting proper motion fit. To assess the influence of individual measurements on each fit and to better estimate the uncertainty of the fits, we employed 500 iterations of a bootstrap re-sampling on each time series. The reported proper motions in our catalog are the median of the bootstrap distribution. The proper motion uncertainties are calculated from the variance of the distribution using

$$\sigma_\mu^2 = \frac{1}{N-1} \sum_i^N (\mu_i - \bar{\mu})^2 \tag{2.10}$$

where $\bar{\mu}$ is the mean of the distribution, μ_i is the proper motion for an individual bootstrap iteration, and N is the total number of bootstrap iterations.

2.2 Optical Redshifts

When available, we include redshifts in our catalog. Although not necessary for measurement of the secular aberration drift, redshifts are crucial for measurement of many of the cosmological effects described in Section 4.2. The majority of the redshifts were obtained from the 2017 May 31 version of the Optical Characteristic of Astrometric Radio Sources (OCARS; Malkin 2016) Catalog. This catalog contains known redshifts and optical or infrared magnitudes of radio sources observed in astrometric and geodetic VLBI observations. These source characteristics are primarily obtained from the NASA/IPAC Extragalactic Database[5] (NED) or the SIMBAD Astronomical Database[6] (Wenger et al. 2000). About 8% of our proper motion catalog is either missing redshifts or the redshifts are listed as "questionable" in OCARS.

[5] https://ned.ipac.caltech.edu
[6] simbad.u-strasbg.fr/simbad/

We observed 28 catalog objects with either no redshift or a "questionable" OCARS redshift at the Apache Point Observatory (APO) 3.5m telescope and/or at Gemini North to increase the fraction of our proper motion catalog that is usable in cosmological studies. Table 2.1 lists the observed objects and their measured redshifts. Ultimately, we measured 10 redshifts, ranging from $z = 0.21 - 2.86$. For cases where no redshift was determined, many of the spectra showed no significant emission or absorption lines. In a few cases, the only detectable lines were consistent with the local standard of rest ($z = 0$), even though we expect all of our catalog objects to be extragalactic. With only foreground, Galactic absorption features present, we were unable to measure optical redshifts for these extragalactic radio sources. These objects have a redshift of "Galactic" in Table 2.1. The spectroscopic observations are described below.

Table 2.1. Optical Redshifts Measured at Apache Point Observatory / Gemini North

IVS Name	Mag	Filter	z	Obs.
0017+200	20.6	V	···	APO
0019+058	18.8	V	2.86 ± 0.02	APO
0056-001	17.1	V	0.719 ± 0.001	APO
0106+138	19.0	V	1.697 ± 0.005	APO
0159+723	19.2	V	Galactic	APO
0253+033	18.0	V	···	APO
0300+470	16.6	V	···	APO
0302+625	···	···	Galactic	APO
0420+417	19.2	R	···	Gemini
0422+004	16.5	V	0.268^a	NED
0426+273	19.6	R	···	APO
0459+135	20.5	V	0.35 ± 0.01	APO
0529+483	19.9	V	···	APO
1013+127	18.6	V	···	APO
1147+245	15.7	V	0.209 ± 0.001	APO
1444+313	15.0	r	Galactic	APO
1506+591	18.9	V	0.310 ± 0.004	APO
1525+610	19.9	G	0.2456 ± 0.0007	APO
1717+178	19.9	V	0.14^b	NED
1754+155	17.2	R	2.06 ± 0.04	APO
1823+689	19.0	R	2.143 ± 0.001	APO

2.2.1 Apache Point Observatory

We conducted observations on the 3.5m telescope at Apache Point Observatory from 2015 April 18 to 2016 June 30. We used the Dual Imaging Spectrograph (DIS) with a 1.5″ slit and two gratings centered at 4400 Å and 7500 Å with linear dispersions of 1.83 Å pixel^{-1} and 2.31 Å pixel^{-1}, respectively. The final spectra have spatial resolution of 0.162″ pixel^{-1}. We observed each target for a total of between $\sim$ 15 and 75 minutes, depending on the target's optical magnitude.

We reduced the data using the Image Reduction and Analysis Facility (IRAF) package. The images were overscan corrected, trimmed, bias subtracted, flat fielded, wavelength calibrated, and background sky subtracted. Then we median stacked the reduced images for each source and extracted a one-dimensional final spectrum. For objects where a flux calibrator was observed on the same night, we flux calibrated the reduced, extracted spectra using the IRAF model of the calibrator's flux density and a mean extinction curve measured at Apache Point[7] . Figure 2.2.2 shows the final, one-dimensional spectra taken at APO. The measured redshifts and key lines used to determine those redshifts are listed on the plots. In the rest of this subsection, we discuss each spectrum individually.

0017+200 No emission or absorption lines were detected for this object. Additionally, the continuum on the blue CCD had too low of a signal-to-noise ratio (SNR) to extract. Together these factors prevent us from determining a redshift.

0019+058 We find $z = 2.86$ based on three AGN emission lines – O I, C II, and C IV. There is also a prominent emission line at $\sim$ 5700 Å that coincides with a sky emission line. It is likely that this line is an artifact of incomplete sky subtraction. There is a scatter of $10 - 30$ Å in the line identifications at $z = 2.86$. This equates to a redshift uncertainty of $\sigma_z = 0.2$. OCARS gives this object a lower limit of $z > 0.64$, which is in good agreement with our measurement.

[7] http://www.apo.nmsu.edu/arc35m/Instruments/DIS/images/apoextinct.dat

Table 2.1 (cont'd)

IVS Name	Mag	Filter	z	Obs.
2013+163	17.3	R	Galactic	APO
2021+317	19.0	R	···	Gemini
2051+745	20.4	V	0.92 ± 0.01	APO
2225+033	17.5	V	···	APO
2315+032	20.4	R	···	APO
2319+444	20.7	R	···	APO

Note. — Columns from left to right: (a) The IVS name of the target, (b) the magnitude of the object from OCARS, (c) the optical filter in which the magnitude was measured, (d) the redshift of the object if a measurement was possible, and (e) the observatory where the object was observed (both objects observed at Gemini were first observed at APO). An ellipsis for the redshift indicates that no redshift was measured. A redshift of "Galactic" indicates that only Galactic ($z = 0$) lines were detected, even though we expect all catalog objects to be extragalactic. We were unable to measure optical redshifts for these extragalactic radio sources. For all of our redshift observations, we also include the associated uncertainty based on the scatter in the line identifications. The two redshifts listed without uncertainties were obtained from the literature, where no uncertainties were provided.

[a]Shaw et al. (2013)

[b]Sowards-Emmerd et al. (2005)

0056-001 We find $z = 0.719$ based on several emission lines, including H γ, H β and [O III]. The scatter is < 6 Å , which equates to $\sigma_z = 0.001$. After we observed this object at Apache Point, OCARS added a new redshift for this object – $z = 0.719$. Our measurements match this redshift exactly.

0106+138 We find $z = 1.697$ from several emission lines shown in Figure 2.2.2. The scatter is $3 - 7$ Å , which equates to $\sigma_z = 0.005$. This is in good agreement with the redshift measured by SDSS: $z = 1.7005 \pm 0.0003$ (Alam et al. 2015).

0159+723 There are several objects in our sample where only local standard of rest ($z = 0$) absorption lines were detected. 0159+723 is an example of one of these. It shows no emission lines and has many $z = 0$ absorption lines (Na I, Mg I, Ca II, etc.). Without the detection of any extragalactic lines, we cannot measure a redshift for this extragalactic radio source.

0253+033 This object has many deep, broad absorption and/or emission lines. However, none of the typical AGN lines can explain all of the detected features. This object has a photometric redshift of $z = 0.4$ in the Million Quasars (Milliquas) catalog[8] (Flesch 2015), but we are unable to confirm this redshift with our spectrum. The line profiles are similar to those seen in broad absorption line (BAL) quasars (e.g., Hazard et al. 1984; Foltz et al. 1987; Weymann et al. 1991), suggesting that some of the lines may be blended and are confusing the identification of line centers. This object is classified as a BL Lacertae object (BL Lac) by D'Abrusco et al. (2014) based on its WISE colors, although the strength of the detected lines in our spectrum casts this classification into doubt. Further study of this object is needed to measure a redshift.

0300+470 No emission or absorption lines were detected for this object. It has a tentative redshift of $z = 0.475$ in NED from Hughes et al. (1992), but the original paper shows that this object is a BL Lac who was assigned the mean redshift of all known BL Lacs in lieu of an actual redshift. Without any detected lines or a measured redshift from

[8] http://quasars.org/milliquas.htm

previous studies, we cannot assign this object a redshift.

0302+625 This object's spectrum only contains Galactic absorption lines. A few of the detected absorption lines are marked in the plot – notably, the Balmer series. We are unable to measure a redshift for this object because no extragalactic lines are detected.

0420+417 This object shows no significant emission or absorption lines. Additionally, the continuum is not detected on the blue CCD and has a low SNR on the red CCD. Because of these two factors, we selected this object for additional observation on Gemini North. These observations are discussed in Section 2.2.2.

0422+004 In the literature, Shaw et al. (2013) find $z = 0.268$ based on Ca II H & K and G-band absorption lines (no uncertainty is given on the redshift). We do not detect these lines – or any other significant lines – in our spectrum, but the continuum SNR is much lower. Based on the spectrum provided in Shaw et al. (2013), we accept their redshift of $z = 0.268$ for inclusion in our catalog.

0426+245 There are three emission lines detected for this object. From these lines, we find two possible redshifts, both of which only fit two of the three lines. The first option is $z = 0.59$ based on the [O III] doublet. The scatter for this option is ~ 4 Å ($\sigma_z = 0.001$). The second option is $z = 3.12$ based on C IV and C III] (using the first half of the doublet at 7900 Å). The scatter for this option is ~ 7 Å ($\sigma_z = 0.003$). Because neither of these redshifts can explain all three emission lines, we cannot assign a redshift to this object. A higher SNR spectrum is needed to detect additional lines and determine the correct redshift.

0459+135 We find $z = 0.35$ using four lines – Hβ, He II, Hδ, and [Ne V]. It is possible that Hα is also present, but lies in the noisy red end of the spectrum at ≈ 8860 Å. There is an overall scatter of $\sim 20 - 40$ Å in the line identifications at $z = 0.35$. This equates to a redshift uncertainty of $\sigma_z = 0.01$.

0529+483 This object is a blazar and has a redshift of $z = 1.162$ from Halpern et al. (2003). This redshift is based on a single line detection, which the authors identified as Mg II (2798 Å). No other information is given about their redshift determination, but it is likely

they assumed this line is Mg II because it is one of the most common optical emission line seen in blazars. We also detect this line in our spectrum, but no other lines are significantly detected. Without any other lines, we are unable to measure a statistically viable redshift, despite the conclusions of Halpern et al. (2003). Their redshift determination, although possible, should be regarded as tentative and is therefore not included in our catalog.

1013+127 This object has a redshift in NED of $z = 0.463$, but no references are given. An additional literature search revealed no potential sources for the redshift identification. A spectrum is available in SDSS (Alam et al. 2015), from which their algorithms measured a tentative redshift of $z = 3.0140 \pm 0.0005$. However, examination of the SDSS spectrum shows no clear emission or absorption lines on which to base their measurement. There are also no clear lines in our APO spectrum, nor any indication of non-significant lines that support either reported redshift. Therefore, we conclude that no reliable redshift can be determined for this object from the available data.

1147+245 This object has a redshift in NED of $z = 0.2$, but no references are given. There is also a spectrum in SDSS with a redshift of $z = 3.9 \pm 9.0$ (Alam et al. 2015). The SDSS spectrum shows no statistically significant lines, which, combined with the large redshift uncertainty, leads us to disregard this redshift. Based on our APO spectrum, we find a redshift of $z = 0.209 \pm 0.001$ using a cluster of three lines identified as Hα flanked by the [N II] doublet. This is in good agreement with the NED redshift. The large bump at ~ 4000 Å is an artifact of flux calibration that can be seen to a lesser extent in other spectra (e.g., 0529+483 and 1013+127).

1444+313 This object's spectrum only contains Galactic absorption lines. A few of the detected absorption lines are marked in the plot. We cannot measure a redshift for this object without any detected extragalactic lines.

1506+591 We find $z = 0.310$ using seven AGN emission lines, shown in Figure 2.2.2. There is a scatter of $\sim 6 - 20$ Å in the expected line locations. This equates to a redshift uncertainty of $\sigma_z = 0.004$.

1525+610 We find $z = 0.2456$ from four AGN emission lines. Only the long wavelength halves of the [N II] and [O III] doublets are visible, but it is assumed that the other half of each is lost in the surrounding noise. There is a scatter of $3 - 5$ Å , indicating $\sigma_z = 0.0007$. The emission line at 7540 Å is an artifact from background subtraction.

1717+178 No significant emission lines are detected for this object. OCARS gives this object a "tentative" redshift of $z = 0.137$ from an observation by Sowards-Emmerd et al. (2005). This redshift is based on the Ca II H & K doublet and Mg I absorptions lines. We do not detect any of these lines, but examination of the higher SNR spectrum in Sowards-Emmerd et al. (2005) confirms their redshift. Thus, we use $z = 0.137$ in our catalog. No uncertainty was given in the source paper.

1754+155 We find $z = 2.06$ from O I, N IV], O III], and Fe II. There is a scatter of ~ 50 Å, indicating $\sigma_z = 0.04$. This spectrum is also well fit by $z = 0.05 \pm 0.02$ where the lines from blue to red are [O II], H γ, H β, and H α. However, images of this object in the National Geographic Society - Palomar Observatory Sky Atlas (POSS-I), AllWISE (Cutri et al. 2013), and VLA observations at 1.45 and 43.3 GHz[9] all show a point-like object. A quasar at $z = 0.05$ should be near enough for the host galaxy to be resolved in at least one of these wavelength regimes. Thus, we conclude that $z = 2.06 \pm 0.04$ is the most likely redshift.

1823+689 We find $z = 2.143$ from Ly α and C IV emission lines. The sudden decrease in continuum flux leftward of Ly α may indicate the beginning of the Lyman α forest, but it is too close to the edge of the spectrum (where the CCD sensitivity also decreases) to make a definitive statement. There is a scatter of 2 Å between the two lines, which equates to a redshift uncertainty of $\sigma_z = 0.001$.

2013+163 This object's spectrum only contains Galactic absorption lines. A few of the detected absorption lines are marked in the plot. We cannot measure a redshift for this extragalactic object because no extragalactic lines are detected.

2021+317 This object shows no significant emission or absorption lines. Addition-

[9] http://archive.nrao.edu/nvas/

ally, the continuum is not detected on the blue CCD and has a low SNR on the red CCD. Because of these two factors, this object was selected for additional observation on Gemini North. These observations are discussed in Section 2.2.2.

2051+745 We find $z = 0.92$ from Fe II and [O II]. The Fe II feature is very broad (FWHM $\sim$ 100 Å) and has no clear peak. This is a good fit for the large group of Fe II emission lines present at $\sim$ 2600 Å (rest wavelength) for some quasars. Because the Fe II feature is several blended lines, we are unable to use the line scatter to estimate the redshift uncertainty. Instead, we use the FWHM of the [O II] feature – $\sim$ 50 Å – to estimate a redshift uncertainty of $\sigma_z = 0.01$.

2225+003 This object shows no significant absorption or emission lines. It has a flagged redshift of $z = 3.823 \pm 0.001$ as measured by the SDSS BOSS survey (Dawson et al. 2013). This redshift is based primarily on Ly α in absorption and C IV, He II, and C III] in emission, none of which are strong lines in the SDSS spectrum. In the APO spectrum, the absorption feature is non-significantly detected and none of the other lines are visible. With only one low SNR absorption feature and a weak SDSS redshift, we cannot assign this source a reliable redshift. Note that the strong emission line at 5581 Å is a sky line.

2315+032 This object shows no significant lines and the continuum was not detected on the blue CCD. We are unable to measure a redshift.

2319+444 There is only one significant emission line in this spectrum. The object has a redshift in NED of $z = 1.31$ (Xu & Han 2014), but the original paper gives no previous source or additional data to support this redshift. There are no common AGN lines that correspond with the detected line at this redshift, nor are there any other low SNR lines to support the redshift. Additionally, if we try other redshifts where the significant emission line corresponds with common AGN lines, there are no other low SNR lines to add validity to any of these redshifts. With only one reliable emission line, we cannot assign a redshift to this object.

2.2.2 Gemini North

Several of the objects observed at Apace Point Observatory showed weak continua and no significant emission or absorption lines. We chose two of these objects (0420+417 and 2021+317) for additional observations with the Gemini Multi-Object Spectrograph – North (GMOS-N; Hook et al. 2004) at Gemini North Observatory[10] . 2021+317 was observed in 2016 on June 26 and June 28, while 0420+417 was observed in 2016 on November 8 and November 26. We observed both objects with a $1''$ slit and two grating setups: the B600 grating with no filter and the R400 grating with a OG515 filter to prevent order overlap (gratings centered at 4880 and 7640 Å, respectively). We used 2×2 binning, which, combined with the grating setup, resulted in final spectra with linear dispersions of 0.9 Å pixel^{-1} and 1.4 Å pixel^{-1} and wavelength coverage of 3500 Å − 6250 Å and 6250 Å − 9000 Å, respectively. Sixteen exposures of 632 seconds each were taken for both objects – eight for each grating.

To reduce the Gemini North observations, we used the Gemini IRAF package; a package written specifically for reducing Gemini observations[11] . The reduction process is the same as for the images taken at Apache Point Observatory – the images were overscan corrected, trimmed, bias subtracted, flat fielded, wavelength calibrated, and background subtracted. Then we extracted a one-dimensional science spectrum from each reduced image, median stacked the extracted spectra, and flux calibrated the resulting final spectra.

Figure 2.2 shows the reduced spectra from the Gemini North observations. Neither object has any significant emission or absorption lines and no redshift was measured for either. The only visible lines in the spectra are due to sky absorption, cosmic rays, and artifacts from the chip gaps. Several of these lines are marked in the figure. Although the spectra are flux calibrated, the flux calibrator was observed on a different night and under different weather conditions than the targets, which were also observed on four separate

[10] Program ID GN-2016B-Q-81
[11] http://www.gemini.edu/sciops/data-and-results/processing-software

nights. For precise flux calibration, the calibrator should be observed on the same night and in a similar part of the sky as the target to ensure that the atmosphere equally affects both spectra. Because this was not done, there are discontinuities in the final continua from the variations in atmospheric conditions on the four nights on which the targets were observed.

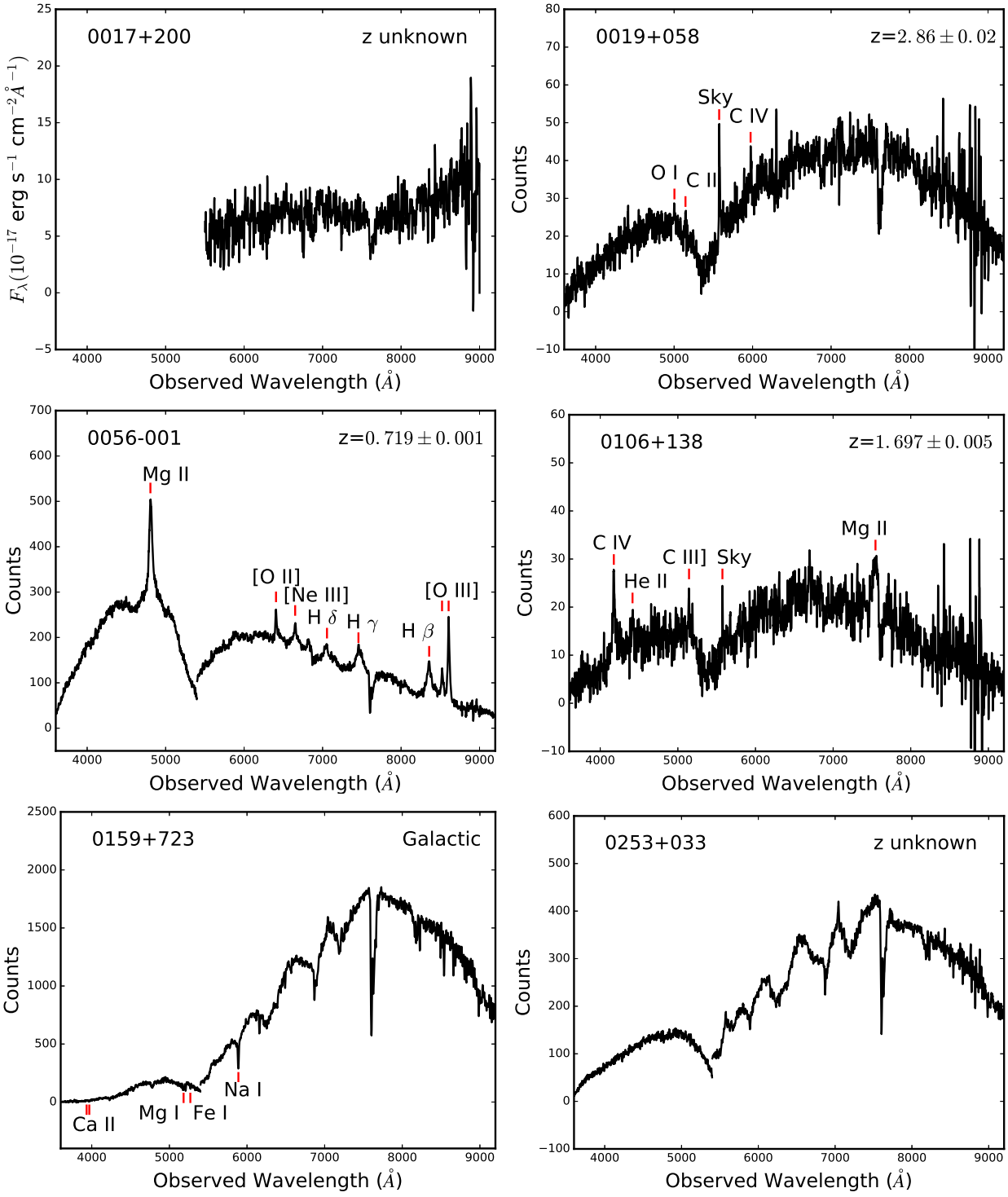
0017+200
z unknown
$F_\lambda(10^{-17}$ erg s^{-1} cm^{-2} Å$^{-1})$
Observed Wavelength (Å)
0019+058
z=2.86±0.02
Sky
C IV
O I
C II
Counts
Observed Wavelength (Å)
0056-001
z=0.719±0.001
Mg II
[O II]
[Ne III]
H δ
H γ
H β
[O III]
Counts
Observed Wavelength (Å)
0106+138
z=1.697±0.005
C IV
He II
C III]
Sky
Mg II
Counts
Observed Wavelength (Å)
0159+723
Galactic
Ca II
Mg I
Fe I
Na I
Counts
Observed Wavelength (Å)
0253+033
z unknown
Counts
Observed Wavelength (Å)

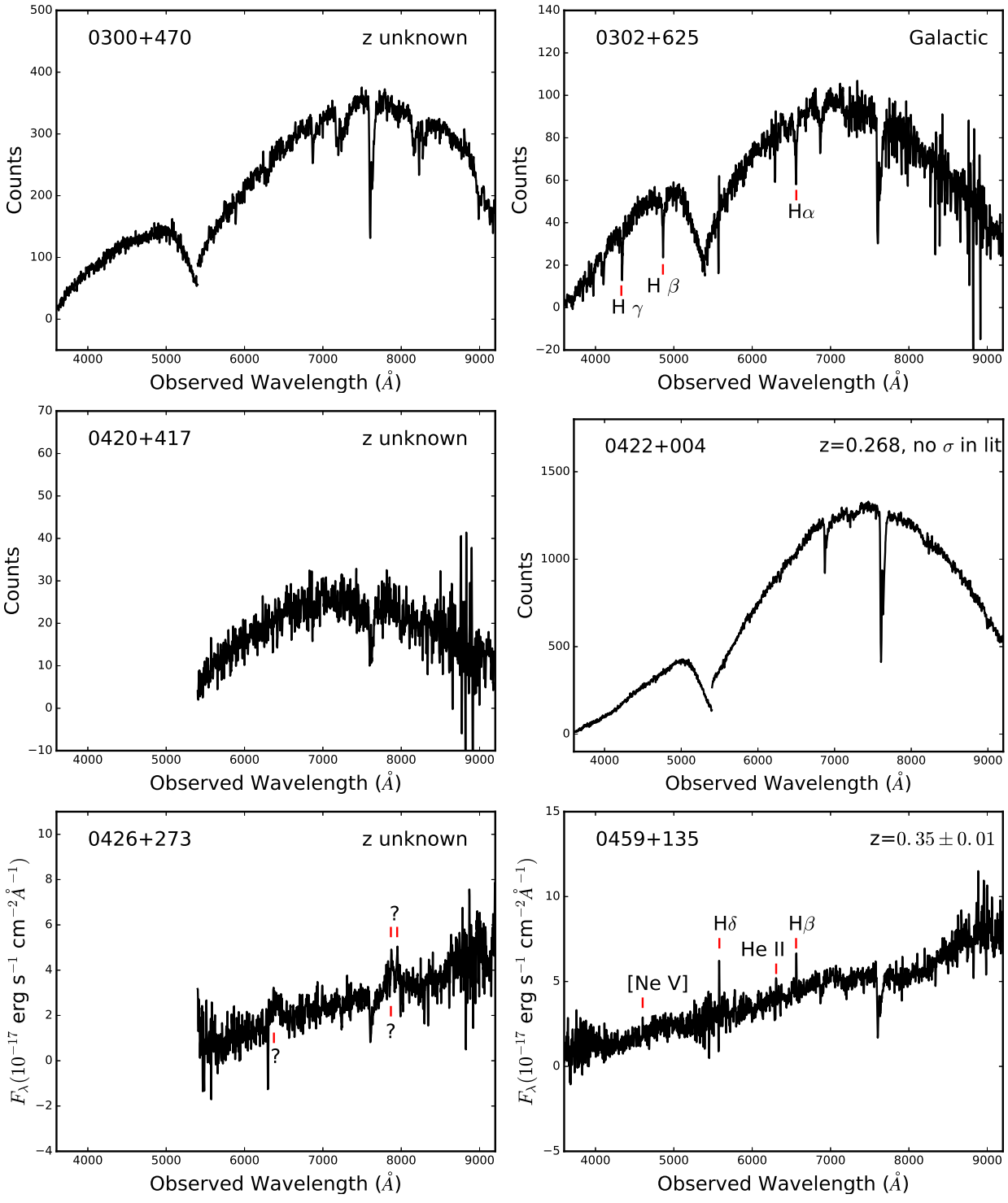
0300+470
z unknown
Counts
Observed Wavelength (Å)
0302+625
Galactic
Hα
H β
H γ
0420+417
z unknown
0422+004
z=0.268, no σ in lit
0426+273
z unknown
?
?
?
$F_\lambda(10^{-17}$ erg s^{-1} cm^{-2}Å$^{-1})$
0459+135
$z=0.35\pm0.01$
Hδ
Hβ
He II
[Ne V]

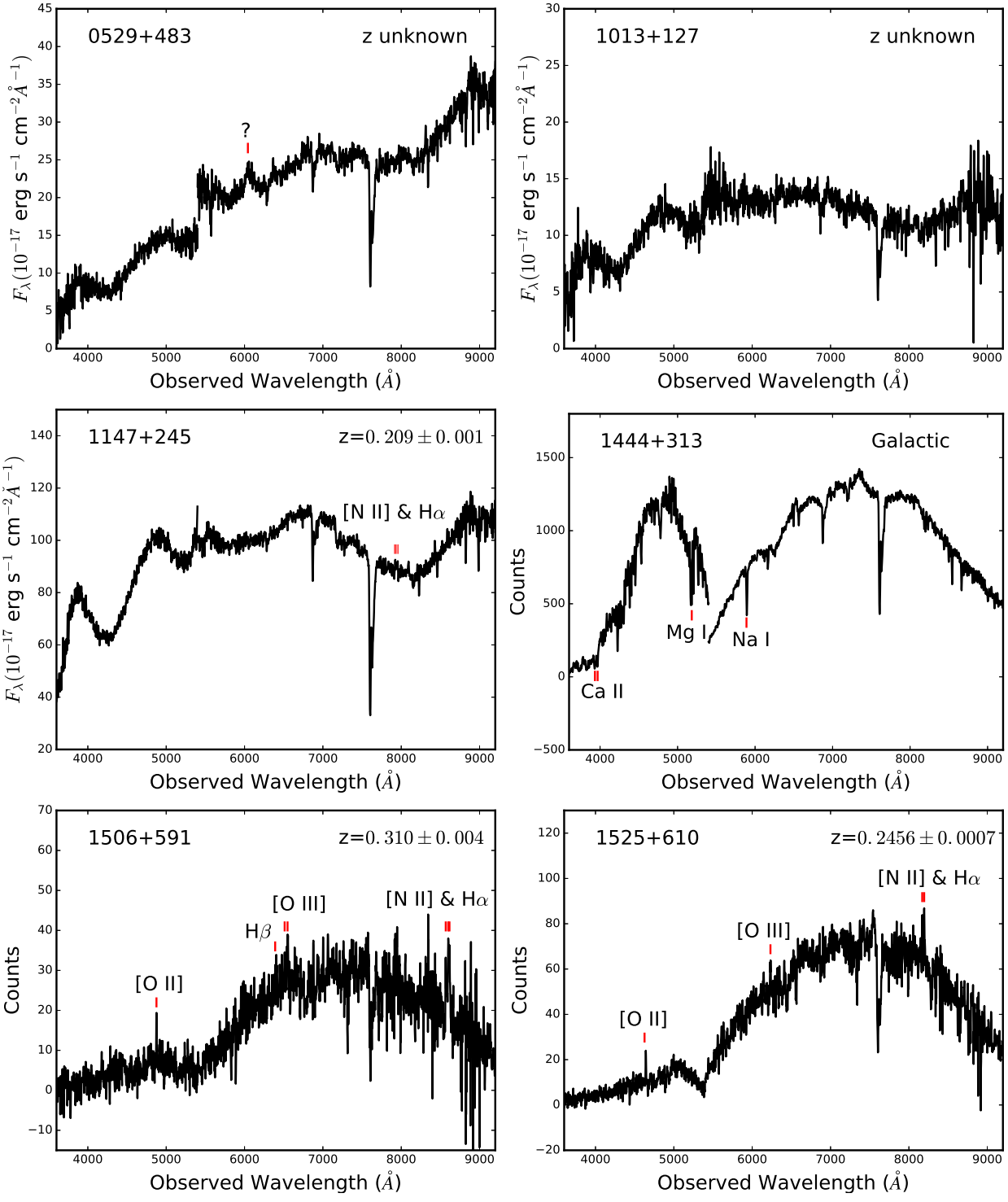
0529+483
z unknown
?
1013+127
z unknown
1147+245
z=0.209±0.001
[N II] & Hα
1444+313
Galactic
Mg I
Na I
Ca II
1506+591
z=0.310±0.004
[O III]
Hβ
[N II] & Hα
[O II]
1525+610
z=0.2456±0.0007
[N II] & Hα
[O III]
[O II]
Observed Wavelength (Å)
Counts

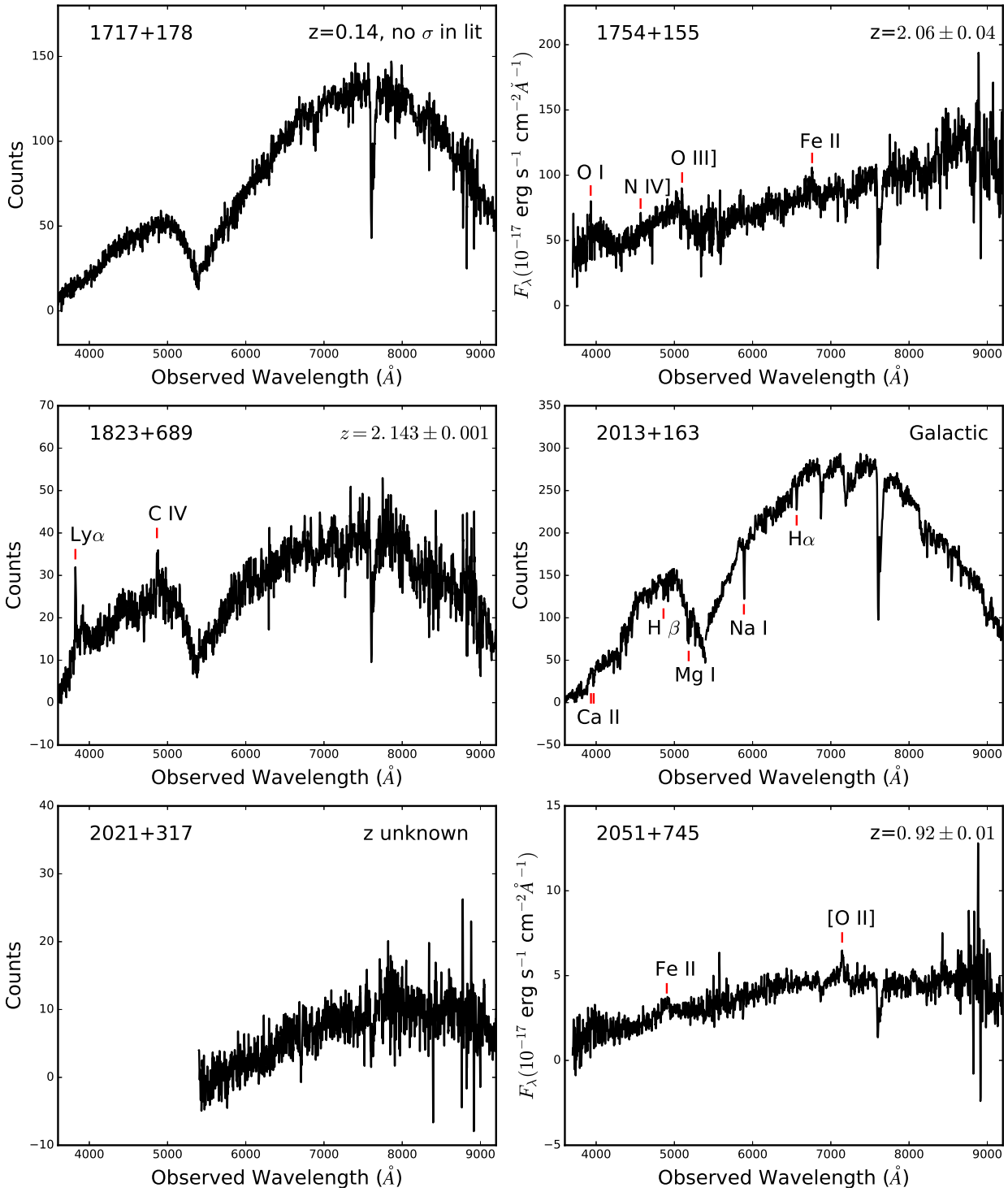
1717+178
z=0.14, no σ in lit
Counts
Observed Wavelength (Å)
1754+155
z=2.06±0.04
O I
N IV]
O III]
Fe II
$F_\lambda(10^{-17}$ erg s^{-1} cm^{-2}Å$^{-1})$
Observed Wavelength (Å)
1823+689
$z = 2.143 \pm 0.001$
Lyα
C IV
Counts
Observed Wavelength (Å)
2013+163
Galactic
Hα
H β
Na I
Mg I
Ca II
Counts
Observed Wavelength (Å)
2021+317
z unknown
Counts
Observed Wavelength (Å)
2051+745
z=0.92±0.01
[O II]
Fe II
$F_\lambda(10^{-17}$ erg s^{-1} cm^{-2}Å$^{-1})$
Observed Wavelength (Å)

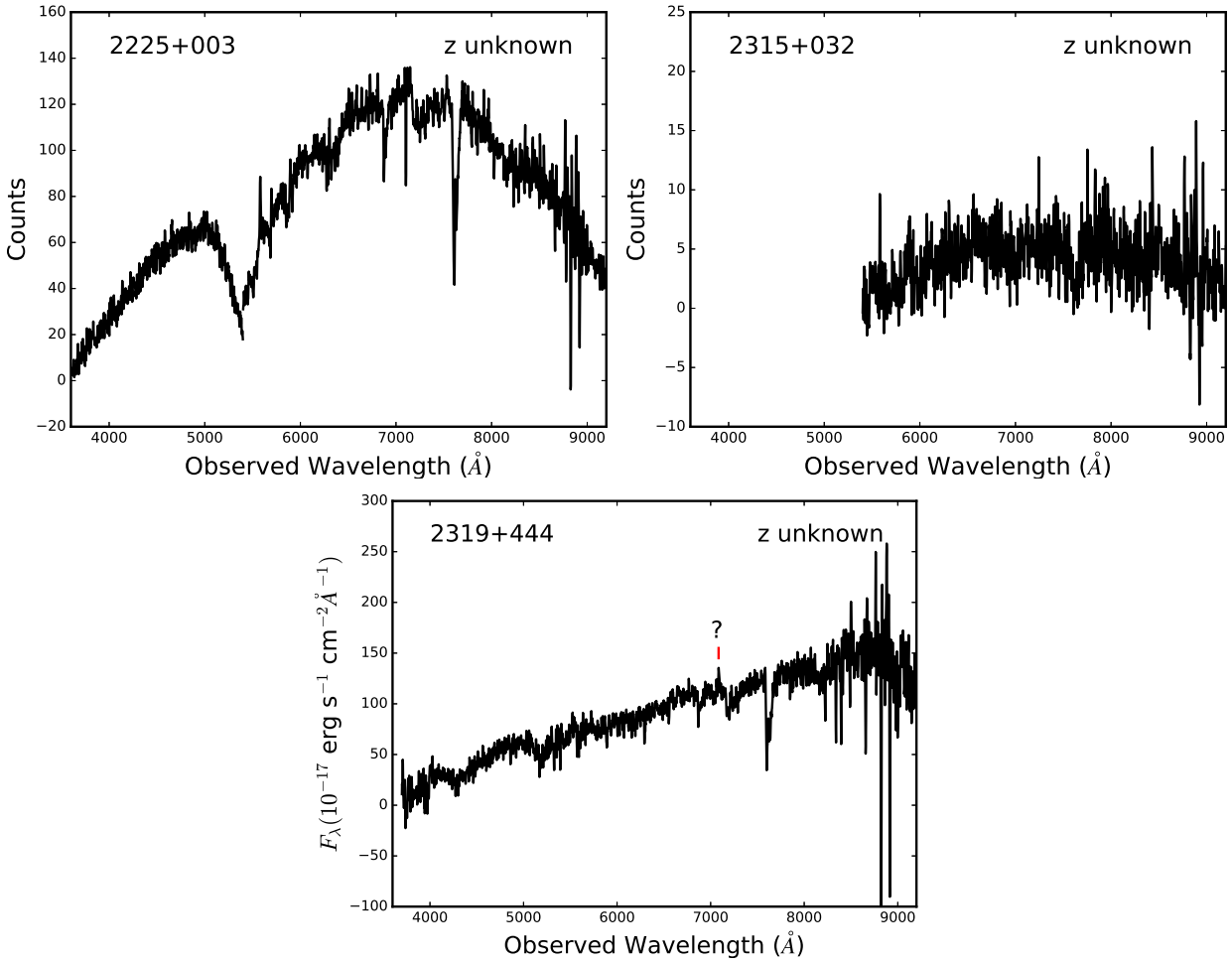

Figure 2.1 Calibrated, one-dimensional spectra obtained from APO. All spectra are smoothed by a 3 Å wide boxcar. Some of the spectra lack flux calibration, as indicated by the y-axis label. In the spectra without flux calibration, there is a large dip at $\sim$ 5500 Å due to the sensitivity falloff at the edges of the red and blue CCDs. For objects where only the red half of the spectrum is plotted, the blue continuum was not significantly detected and could therefore not be extracted from the final image. Detected lines and the best-fit identifications are shown in each plot, along with their redshift. There are also two night sky absorption features visible in all plots at 6866 Å and $\sim$ 7600 Å . For all of our redshifts, we determine the uncertainty based on the scatter in the line identifications. The two redshifts listed without uncertainties were obtained from the literature, where no uncertainties were provided. Objects labeled "Galactic" have only Galactic ($z = 0$) lines detected. Without any detected extragalactic lines, we cannot measure redshifts for these objects.

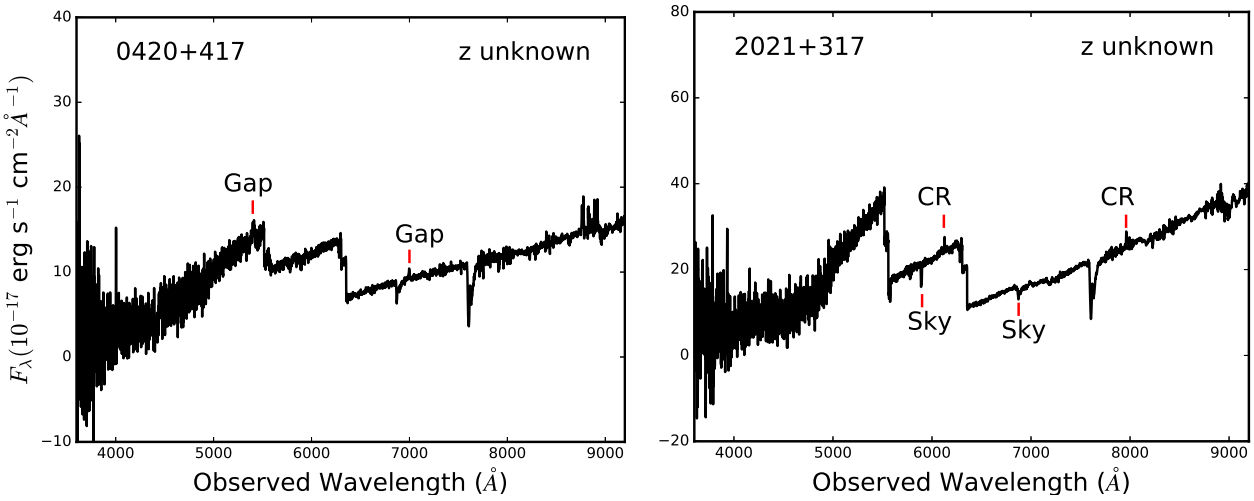

Figure 2.2 Flux calibrated spectra obtained from Gemini North. Jumps in the continua are not real and are due to inexact flux calibration. Several sky absorption features, cosmic rays, and artifacts from the chip gaps are marked in the plots. The night sky absorption feature at ~ 7600 Å is also visible in both spectra.

Chapter 3

VLBA Precision Astrometry

Although several studies to measure global proper motion signals have been conducted using only archival VLBI proper motions (e.g., Titov & Lambert 2013; Darling 2013; Titov & Lambert 2016), we found that the sample size was insufficient to significantly detect the net convergence of large-scale structure for close separation pairs. Using 507 radio proper motions with redshifts, Darling (2013) found an average relative proper motion of 8.3 ± 14.9 μas yr^{-1} for pairs separated by < 200 Mpc comoving, which is consistent with both pure Hubble expansion and the predicted convergence of gravitationally-bound, static structures.

In this chapter, I describe a set of VLBA observations I conducted to increase the number of small-separation (< 200 Mpc comoving) pairs in our catalog. I observed 42 radio sources and from those calculated 33 new proper motions and increased the precision of 7 existing proper motions. Because the measurement of large-scale structure evolution is made from *relative* proper motions, I selected targets that are in close-separation pairs with objects with existing proper motions. By using the known source as a phase reference, I am able to directly measure the relative proper motion of the target without the complicating factor of obtaining absolute astrometric measurements.

Section 3.1 is a more detailed expansion of Section 4 from Truebenbach & Darling (2017) – it includes a new description of the selection criteria for my two VLBA observing campaigns. Sections 3.2 and 3.3 are new sections describing my AIPS reduction process, including an automated self-calibration pipeline I created to rapidly calibrate my observa-

tions and a description of how the proper motion measurements are derived from VLBA astrometry (Section 3.3). Reproduced section is with permission of the AAS.

3.1 VLBA Observations

In addition to the coordinate time series we obtained from the Goddard VLBI global solution, we also conducted our own astrometric observations to add position epochs to existing object time series – thereby either improving existing proper motion measurements or enabling the measurement of new proper motions. We observed 42 radio sources with the Very Long Baseline Array (VLBA) in X-band (3.6 cm / 8.3 GHz). Our targets had all been previously observed by VLBI but lacked a recent observing epoch with high astrometric precision with which to derive proper motions. The VLBA observations were conducted in two campaigns from 2015 September to 2016 January and 2016 October to November. The target selection for the two campaigns differed slightly based on our evolving science goals. In the first campaign, we selected 15 bright compact radio sources that are within 200 Mpc (comoving) of ICRF2 defining sources (IERS Technical Note No. 35 2009). We used the defining sources as phase references for the targets and used their positions relative to the targets to calculate the absolute positions of the targets. In this campaign, we only used targets in close separation pairs with defining sources because defining sources tend to have highly accurate positions, which leads to more accurate absolute positions from our astrometry. For targets with large angular separations from their phase reference ($\theta > 2^\circ$), we also included another bright radio source as a second phase reference. All targets are within 5° angular separation of their ICRF2 defining source partner to reduce phase differences introduced by atmospheric variations between the two locations, are at declinations $> -35^\circ$, and have known redshifts.

In the second campaign, we expanded our target selection criteria to include a wider range of targets so that our final sample of close separation radio pairs would roughly double in size and contain a larger fraction of objects with high precision proper motions. We

observed 27 sources that are within 150 Mpc (comoving) of a radio source with known proper motion. We loosened the selection criteria to include all sources with known proper motions because we found that restricting our search to targets in close separation with ICRF2 defining sources limited the sample size to less than 10 objects. Like the first campaign, twenty of our targets have been observed by the VLBI a handful of times but lack a recent observing epoch with which to measure a proper motion. To further increase our sample size, seven of our targets are well known galaxies that have been observed many times by VLBI. However, they had not been observed in at least a year (often > 4 years) and never with an astrometric precision of ~ 1 μas. By including these targets, we hope to increase the precision of their proper motion measurements and, in turn, to increase the precision of an average relative proper motion measurement between close-separation objects (see Chapter 5). Additionally, we restricted our sample to targets with declinations $> -10^{\circ}$ because we found in the first campaign that lower declination objects did not get sufficient uv-coverage for high precision astrometry. Like the first campaign, we used the close-separation radio source with known proper motion as a phase reference and restricted our sample to targets with measured redshifts.

For both campaigns, we also observed a third nearby object as a second phase reference for most targets. Because extragalactic proper motions are often small ($\sim 1-10$ μas yr^{-1}), we were concerned that small atmospheric variations between the target and its phase reference could significantly affect the relative astrometry. To mitigate this, we observed a second phase reference for targets with large angular separations from their phase references ($\theta > 5^{\circ}$). During data reduction, we reduced some of the target observations twice; once with their close-separation companion source as the phase reference and once with the third source as the phase reference. We used the results from this second reduction to ensure that tropospheric delay errors between the target and its companion did not significantly affect our final astrometric measurements. In all cases, the resulting positions were in statistical agreement.

Our instrument setup was the same for both campaigns. We observed with 8 evenly spaced baseband channels of 32 MHz each, all with left circular polarization, that spanned a total frequency range of 288 MHz. Each channel contained 64 spectral channels. Each target was observed in 1 minute intervals with a total on-target integration time of 3 – 10 minutes per session, depending on the source flux density. We used 2 bit sampling at the Nyquist rate and an aggregate bit rate of 1024 megabits $\sec^{-1}$. To maximize the signal-to-noise ratio (SNR), which directly correlates with the resulting astrometric uncertainty, all of our observations used at least nine out of ten VLBA antennas. The longest baseline, Mauna Kea to St. Croix, was always used in our observations to maximize angular resolution.

We included 45 minute geodetic blocks before and after each observing session to improve measurement of phase errors induced by the troposphere. For the geodetic blocks, we used a similar setup to our main observations, but with more widely spaced baseband channels in order to better model the tropospheric delay as a function of frequency (total span of 480 MHz). Additionally, we repeated each observing session within 3 – 24 days so that each target is observed twice within a month and the final astrometric measurements are based on two independent observations. Previous VLBA astrometric campaigns (e.g., Reid & Brunthaler 2004) have found that a second set of observations can increase astrometric precision by $\sqrt{2}$ and provide an important verification of the astrometry. The period between repeated observations must be long enough that weather conditions are not correlated (> 3 days) but short enough that the proper motions of the quasars are negligible (< 24 days). For all targets, the astrometry obtained from the two separate observations were in statistical agreement.

3.2 Data Reduction

We reduced the VLBA data using a series of tasks from the Astronomical Image Processing System (AIPS; Associated Universities 1999) designed specifically for VLBA data, with some alterations to increase astrometric precision. The reduction process and tasks

used to reduce VLBA data differ from those used for the VLA, ALMA, and other connected arrays primarily because the delays are calibrated for each antenna rather than for each baseline. For smaller arrays such as the VLA and ALMA, all antennas observe approximately the same atmosphere, thereby allowing each baseline to be calibrated separately. Baseline-based calibration is overall preferable because one can directly calibrate the delays between each antenna – the delays are the final desired result, so this reduction technique is the most straight-forward. However, for long-baseline interferometry, it is no longer correct to assume that all antennas are observing the same atmosphere. Therefore, the phases of each antenna are calibrated separately and then the delays for each baseline are derived from the calibrated phases. The disadvantage of this approach is that one antenna must be chosen as the reference antenna. The reference antenna is assumed to have zero phase throughout the observations and the delays are all calculated relative to the reference antenna. Because only *relative* delays are found in antenna-based calibration, only relative positions can be derived from VLBA observations. To calculate absolute astrometry from relative positions, another source with known position must be used as a phase reference throughout the observations. This technique is discussed in more detail below.

The following steps outline our VLBA calibration process.

(1) Import the visibilities into AIPS using `FITLD`. An initial calibration table is created with the uncalibrated phases sampled at 0.1 minutes. The sampling interval dictates how frequently the phases are calibrated. The interval must be long enough that the calibration tables are not unmanageably large, but short enough that the shortest fringe is well sampled.

(2) Apply basic ionospheric corrections to the data using `VLBATECR`. Ionospheric models of electron content for the observation time period are obtained from NASA's crustal dynamics data interchange system (CDDIS; Noll 2010). The models are used to calculate ionospheric Faraday rotation and, from this, the dispersive delay introduced

by the ionosphere at each antenna.

(3) Correct the phases for the earth orientation at each antenna using `VLBAEOPS`. When the phases are correlated, the VLBA correlator uses the best available earth orientation parameters (EOPs). However, new EOPs may have been calculated in between correlation and user calibration. This procedure checks the current EOPs calculated by GSFC as part of their global solution and adjusts the phases as necessary.

(4) Scale the data to correct for digital offsets in the sampling and correlation using `VLBACCOR`. When the spectrum is correlated, the correlator assumes the values of various parameters of the samplers (e.g., the sampling rate). However, these parameters are not exactly known and incorrect assumptions by the correlator lead to amplitude errors. This step corrects these errors by scaling the data for each antenna as a function of time so that the average amplitude over all channels of the autocorrelation for each source is unity (Walker 2014).

(5) Correct the phases for parallactic angle effects using `VLBAPANG`. As the alt-az mounted antennas track a source across the sky, the source will appear to rotate with respect to the feed horns, causing a phase offset. This processing step removes this effect using the input position of the source and the measured altitude of the antennas.

(6) Remove all scans of sources with elevations $< 10^{\circ}$ because the SNR on these scans is too low for strong fringes to be detected. This clipping is done for all antennas because fringes will be fit for all antennas in step 13.

(7) Model and remove the instrumental delay using `VLBAMPCL`. Because the source is observed over a finite bandwidth, the received fringes are modulated by a sinc-function envelope as a function of the geometric delay between two antennas (τ_g; Thompson 1999). Thus, the full amplitude of the source is observed only when the source is in a direction normal to the baseline; $\tau_g = 0$. To ensure that the full source amplitude is

always being recorded, an instrumental time delay is added to each baseline prior to correlation to make it appear as though $\tau_g = 0$ for all baselines. However, this technique introduces an artificial phase slope into the visibilities that must be removed prior to fitting the bandpass. Otherwise, the slope will be interpreted as a real signal caused by the shape of the bandpass. The instrumental delays are modeled by fitting the phase rate for a scan of a calibrator source that is well detected by all antennas. We observed a strong fringe calibrator source at the beginning, middle, and end of my science observations for this purpose. The phase rate is assumed to be constant with time and is removed from all scans.

(8) Make a bandpass model to scale the amplitudes and phases as a function of frequency using `VLBABPSS`. This procedure applies the calibrations from the previous steps to a calibrator source and models the bandpass shape across each baseband as the remaining variation in amplitude. Modeling and correcting for the bandpass shape is important because it removes the frequency dependence of source amplitude and phase that is introduced by the observing system. We use the same fringe calibrator source from the previous step to calibrate the bandpass because it is selected to have a high SNR and is observed periodically throughout the science observations.

(9) Re-scale the amplitudes after correcting for the bandpass model and apply a-priori amplitude corrections with `VLBAAMP`. After applying the bandpass model, the average amplitude over all channels of the autocorrelations may no longer by unity. This procedure first re-scales the amplitudes so the average amplitude is again unity. Then, the procedure converts the amplitudes into physical flux densities using the measured antenna gains and system temperatures. Briefly, the cross-correlation amplitudes are multiplied by $\frac{T_1 \times T_2}{g_1 \times g_2}$, the system temperatures of each baseline divided by the gains of each baseline (Walker 2014). The gains and system temperatures are measured by the correlator and then scaled to flux density using the Perley &

Butler (2013) flux density scale.

These flux densities are only rough estimates and should not be used as reliable measurements. For more accurate flux calibration, one would use an additional task such as `SETJY`, which scales the flux densities using an observation of an unresolved or well-modeled source with known flux density as a function of frequency. Absolute flux measurements are unnecessary for this work so we did not observe a flux calibrator.

(10) Examine each source's amplitude and phase on each baseline as a function of time with `EDITR`. Flag any major outliers. If the outliers are in the calibrators used in the previous steps, redo any previous calibration after applying the flags. In most cases, nothing is flagged in this step – it often takes several rounds of self-calibration to reveal bad data. The majority of data in need of flagging is already automatically flagged during data-gathering and correlation. Typical reasons for automatic flagging include an antenna that was still slewing to the source, an antenna that was late to start recording data, and various mechanical errors including synthesizer malfunctions and pointing errors.

(11) Calibrate the geodetic visibilities.

(a) Repeat steps 1 – 4 for the geodetic observations.

(b) Skip steps 5 and 6, which correct for parallactic angle and flag low elevation scans. The purpose of the geodetic observations is to create an improved model of the troposphere as a function of frequency and elevation. Thus, it is important to have scans from all elevations, including $< 10°$. Additionally, because we are only interested in the troposphere delays from the geodetic sources and not their true shapes and structures, it is unnecessary to correct for parallactic angle.

(c) Repeat step 7 – model and remove the instrumental delay. Because the tropo-

sphere conditions can vary during the observations, we observed geodetic blocks roughly every four hours (often at the beginning and end of the science observations). These blocks are reduced together and the troposphere delays during the science observations are interpolated from the models calculated during the geodetic blocks. However, the instrumental delay also changes with time. To account for this variation, this step is performed for each geodetic block separately. We use a scan of a well-detected source from each block that is at high elevation on all antennas to model the phase slope caused by the instrumental delay. Then we correct each geodetic block for the derived instrumental phase and recombine the corrected blocks into a single calibration file.

(d) Solve for the multi-band delay (MBD) using `FRING`. If one assumes that all of the geodetic sources are point-like and at phase center – on average, this is a good approximation for ICRF sources – then the only remaining relative phase slope for each source after the above calibrations should be due to clock error and / or tropospheric delay. As a first step towards calculating the tropospheric delays, `FRING` finds the relative phase slopes as a function of time, frequency, and source elevation and converts these slopes into multi-band delays. On average, the delays are on the order of $\sim 10 - 100$ ps, with delays up to 2 ns at low elevations.

(e) Solve for the zenith tropospheric delay using `DELZN`. This task assumes that the multi-band delay calculated in the previous step is a combination of clock error and tropospheric delay; MBD = Clock(t) + Atmo(t) / sin(elevation). The zenith atmospheric delay is found as a function of time by fitting a polynomial to the MBDs found by `FRING`.

(12) Apply the tropospheric delays found from the geodetic blocks to the science data using `CLCOR`. This task converts the tropospheric delay to a phase correction for each

source using the source's elevation, frequency range, and observation time. It also calculates phase corrections due to clock errors, which were also modeled with the geodetic blocks.

(13) Perform a global fringe fit using `FRING`. Even after removing all of the phase errors described in the previous steps, there will still be some frequency and time dependent phase variations that were not correctly removed during calibration. This task solves for any remaining time variable delays and rates for each station and removes them from the data. This is essentially the first iteration of self-calibration where the phases and amplitudes of each source are adjusted to match an assumed source model (in this step, the sources are assumed to be point sources) with the addition that the phase slopes are also adjusted. This step is typically only needed for long baseline interferometers and not needed for connected interferometers because the clock and troposphere errors between antennas for VLBI arrays are much larger.

(14) Smooth the data using `SNSMO`. First, the fringe phase as a function of time (the fringe rate) and delays for each antenna are clipped using a median window function. Fringe rates that deviate from the window median (we used a window width of 1 hour) by 100 mHz and single-band delays that deviate by 100 ns are clipped. Then the rates and delays are smoothed using the same median window function with a width of 1 hour. Fringe rates and delays are expected to vary smoothly over intervals of several hours so a large smoothing window is acceptable. Overall, the changes to our data from smoothing are minor. This step is primarily included to ensure that there are no large outliers in fringe rate as a function of time because outliers can cause spurious phase winding when the observations are phase referenced in the next steps.

(15) Average the phase-reference source using `SPLIT`. To increase the SNR of our observations, we average together the 64 sub-band channels in each baseband channel. It is

also possible to further increase the SNR by averaging together all baseband channels but this has the potential to decrease the final image RMS. At the 8.3 GHz frequency range, quasars typically have a strong amplitude-frequency dependence caused by synchrotron radiation. Therefore, because the amplitude may vary across the total bandwidth, self-calibration for each individual baseband will be more accurate if it is done separately and then averaged into a final, single image.

(16) Self-calibrate the phase-reference. See Section 3.2.1 for a description of self-calibration.

(17) Apply the calibrated phases from the phase-reference to the target source and to the phase-reference using `TACOP` and `CLCAL`. Once the phases and amplitudes of the phase-reference source have been sufficiently calibrated through self-calibration, we apply these phase and amplitude adjustments to the target source and to the original phase-reference visibilities. Typically, this step is referred to as "phase-referencing." Phase-referencing subtracts the phase-reference delays from the target delays to create a *relative* observation of the target source. This is often used to remove time- and location-dependent delay errors that are not accounted for when performing basic calibrations using a dedicated calibrator source. However, these time- and location-dependent delay errors are also corrected through self-calibration so this aspect of phase-referencing is of limited use for our reduction strategy. The primary use of phase-referencing for this application is that by creating a relative image of the target source, we can make accurate relative astrometry measurements. To this end, we first self-calibrate the phase-reference visibilities to create a high dynamic range set of observations for the phase-reference. We then use the self-calibrated phase-reference visibilities to phase reference the target source. It is important to first self-calibrate the phase-reference so that the main delay difference between the target and phase-reference is due to the physical separation between the two sources and not time- and location-dependent differences.

After phase-referencing the target, we self-calibrate both the target and the phase-reference using the new corrected visibilities from the initial self-calibration of the phase-reference. We include a second self-calibration of the phase-reference so that the final images of the target and the phase-reference both have as much calibration in common as possible. By reducing both objects in the same manner, we eliminate any potential position difference between the two that is caused by calibration error. This overall strategy of self-calibrating the phase-reference and then self-calibrating the target and re-self-calibrating the phase-reference are summarized in this step and steps 18 – 21.

(18) Average the target with `SPLIT`. This is done in the same manner as step 15.

(19) Self-calibrate the target source.

(20) Average the phase-reference source with `SPLIT`. Use the corrected visibilities from the initial self-calibration of the phase-reference source.

(21) Self-calibrate the phase-reference source.

3.2.1 Self-Calibration

Self-calibration is an iterative process in which the phases and amplitudes of a source are adjusted based on an assumed model of the source, a calibrated image is produced from the adjusted visibilities, and then the image is used as a model to further adjust the source phases and amplitudes. This process is repeated until the calibrations converge to a stable model. Self-calibration is required for producing VLBA images, unlike VLA images where self-calibration is an optional step to improve the final dynamic range. As discussed in step 13 and Section 1.1, long baseline interferometers have much larger phase errors than connected arrays due to the independent conditions affecting each individual antenna. Even with the first iteration of self-calibration done during fringe fitting in step 13, reliable images

cannot be produced without several more iterations for each source. Because no source is truly unresolved when observed with the VLBA, the assumption of a point source during global fringe fitting is rarely accurate. Through several iterations of self-calibration, a more realistic source model can be determined and a higher signal-to-noise image can be produced.

Self-calibration is particularly important for our goals because we require final images with SNR > 425 for a beam size of ~ 0.85 mas to obtain measurements with astrometric precision better than 1 μas. Based on our observing setup and integration times, we estimate a typical thermal noise of $\sim 0.1 - 0.2$ mJy/beam. Using between $30 - 400$ rounds of self-calibration, depending on the object, we achieve sky noise levels of a similar magnitude to the thermal noise, enabling final images with SNRs between $\sim 300 - 2500$. However, self-calibration is a labor-intensive process and the time required to manually calibrate all of our objects was unfeasible. Several automated self-calibration procedures exist but they are designed for producing images for large surveys and do not allow the step-by-step adjustments for individual objects required to reach our desired SNR. Therefore, we wrote a new AIPS procedure to automate 30 iterations of self-calibration at a time. By restricting the number of automatic iterations to 30, we can adjust the calibration through clipping and CLEAN box resizing (see step 3 below) with enough frequency to ensure that an accurate, high dynamic range image is produced within a reasonable amount of time. In the following steps, we outline the self-calibration process used in the new procedure.

(1) Adjust the phases of the source by assuming a point-source model using `CALIB`. To increase the accuracy of this initial model, we assume that the source has a peak amplitude equal to the measured total flux density of the source from previous observations at 3.6 cm.

(2) Using the initial calibrations from `CALIB`, create a raw image convolved with the beam image (a dirty image) by Fourier transforming the visibilities with `IMAGR`. The dirty image is used to measure the sky noise of the image for step 3. For all images,

we use a pixel size of 0.09 mas per pixel. The angular size of the primary beam is $\approx \lambda/B$ where λ is the observing wavelength and B is the longest baseline. For these observations, the wavelength is 3.6 cm and the longest baseline is typically ~ 8600 km, resulting in a primary beam of ~ 0.9 mas. To ensure that the centroids of point sources can be found with high precision, we chose the image pixel size so that there are ~ 10 pixels across the primary beam. Each image is 512×512 pixels so that any extended structure associated with the source is included. Additionally, we use uniform weighting when creating the images. Uniform weighting equally weights all visibilities when creating the final, deconvolved image, which increases the angular resolution of the final image. High angular resolution correlates with precise centroid measurements from the final image, which is the ultimate goal of these observations.

(3) Create a CLEANed image of the source using `IMAGR`. CLEANing is an iterative algorithm devised by Högbom (1974) that creates a model of the beam and removes effects of that beam from the final image through deconvolution. `IMAGR` uses the Clark CLEAN algorithm (Clark 1980), which creates a model of the source emission within a user-defined CLEAN box and produces a CLEANed image by combining the source model with the residual sky noise, convolved by the beam image. To avoid over-CLEANing the image and creating false sources, we only CLEAN a small area around the source (typically a rectangle of ~ 30 – 40 pixels (3 – 4 beams) per side) and CLEAN until the maximum pixel value in the residual image is equal to the sky noise in the dirty image (measured in the previous step). For VLBA observations, the dirty image sky noise is high, typically $15-100$ mJy for our data. Thus, cleaning to this level is a very shallow initial CLEAN.

(4) Measure the sky RMS of the CLEANed image. This RMS is used as the new CLEANing limit.

(5) Adjust the phases of the source using the CLEANed image as the source model

with `CALIB`. For this second run of `CALIB`, use the initial visibilities from before self-calibration. In later runs of `CALIB`, we use the most recent self-calibrated visibilities and further adjust them based on the updated source model. But the initial phase adjustments from step 1 are likely to be incorrect because a point-source model was assumed, which is rarely the true shape of VLBA sources. Therefore, we use the bad assumption of a point source in order to create an initial CLEANed image but then disregard those calibrations as soon as a more accurate source model is obtained.

(6) Using the new calibrations from the previous step, create a new CLEANed image. Use the sky RMS measured in step 4 as the new CLEANing limit.

(7) Measure the sky RMS of the CLEANed image.

(8) Adjust the phases of the calibrated visibilities from step 5 using the new CLEANed image from step 6 as the source model.

For the rest of self-calibration, the procedure repeats steps 6 – 8 until the sky RMS of the CLEANed image stops decreasing. During the first 9 rounds of self-calibration (steps 6 – 8 are considered one round), the procedure gradually CLEANs to deeper levels. For example, after five rounds, it stops CLEANing to the sky RMS and begins CLEANing to five times the theoretical thermal noise. It continues to decrease this CLEANing level until, after 9 rounds, it CLEANs to the theoretical thermal noise for all future rounds. Similarly, as a more accurate source model is gradually created, the SNR restrictions on `CALIB` are increased. Initially, phase solutions based on the assumed source model with SNR < 3 are rejected, but after 4 rounds, this is increased to SNR < 5. We find that an initial lower SNR requirement increases the chance of a successful first few rounds of self-calibration when the phases have higher noise levels (typically $\sim 5 - 10^{\circ}$ rms). Finally, after 15 rounds of self-calibration, the procedure begins to adjust both the phases and amplitudes to match the source model. For the first 15 rounds, only the phases are adjusted to avoid the addition of

any false flux into the final image while the source model is still not accurate.

Figure 3.1 shows the final CLEANed and self-calibrated images of the observed radio sources. The images have an average sky RMS of 0.5 mJy beam^{-1} and a SNR of $\sim$ 2200 (based on the integrated flux of the object and the sky RMS). We separately calibrated and imaged both epochs for each source to serve as a check of the calibration process. The images show that the final image of all sources are relatively unchanged between epochs. Similar images were also produced for each phase-reference source.

3.3 Proper Motion Measurement

After producing a final, CLEANed image for both the target and its phase reference, we found the centroid of each object by fitting a two-dimensional gaussian to the main component of each reduced image. Although some of the objects have extended structure that is not well-fit by a single gaussian (e.g., 2208-373 in Fig. 3.1), we assumed all objects were point-like in order to be consistent with previous position measurements; in the GSFC solution, they assume that all sources are point-like without extended structure (IERS Technical Note No. 35 2009). The majority of ICRF2 sources used in the GSFC solution are either symmetric or nearly so, thereby allowing them to be modeled as point-like. For those sources with non-symmetrical structure, it is assumed that the structure is constant with time so the phase-center position will be effectively constant even if this position does not reflect the true center of the object. There are 39 "special handling" sources that are found to have significant structure or brightness variations over time (IERS Technical Note No. 35 2009). These sources are not treated as point-like and their positions are calculated separately for each epoch. We exclude these sources from the catalog because their proper motions are dominated by intrinsic proper motions that significantly obscure global signals such as the secular aberration drift and the evolution of large-scale structure.

There are several accepted ways to determine the centroid of a radio source observed by an interferometer. The simplest is to find the location of the brightest pixel in the

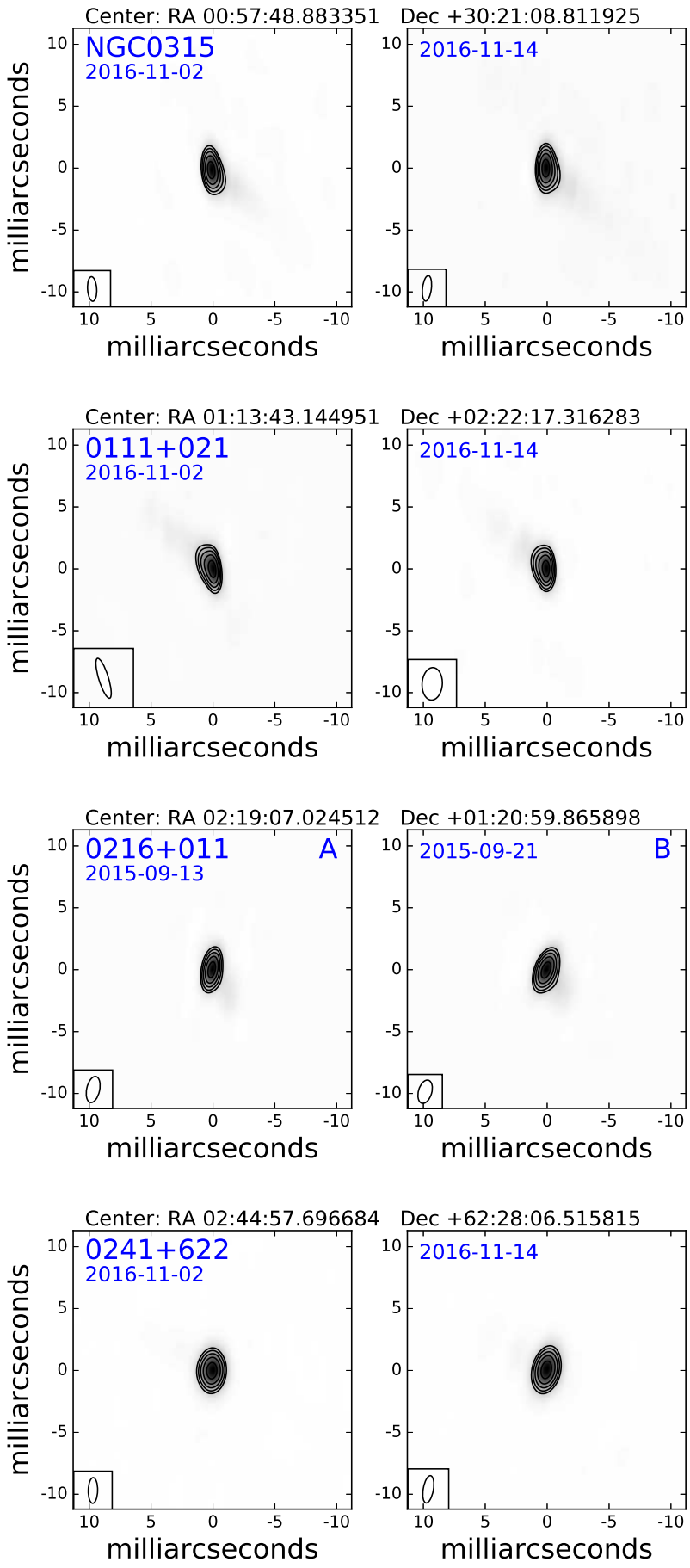
Center: RA 00:57:48.883351 Dec +30:21:08.811925
NGC0315
2016-11-02
2016-11-14
Center: RA 01:13:43.144951 Dec +02:22:17.316283
0111+021
2016-11-02
2016-11-14
Center: RA 02:19:07.024512 Dec +01:20:59.865898
0216+011 A
2015-09-13
2015-09-21 B
Center: RA 02:44:57.696684 Dec +62:28:06.515815
0241+622
2016-11-02
2016-11-14
milliarcseconds
10
5
0
-5
-10

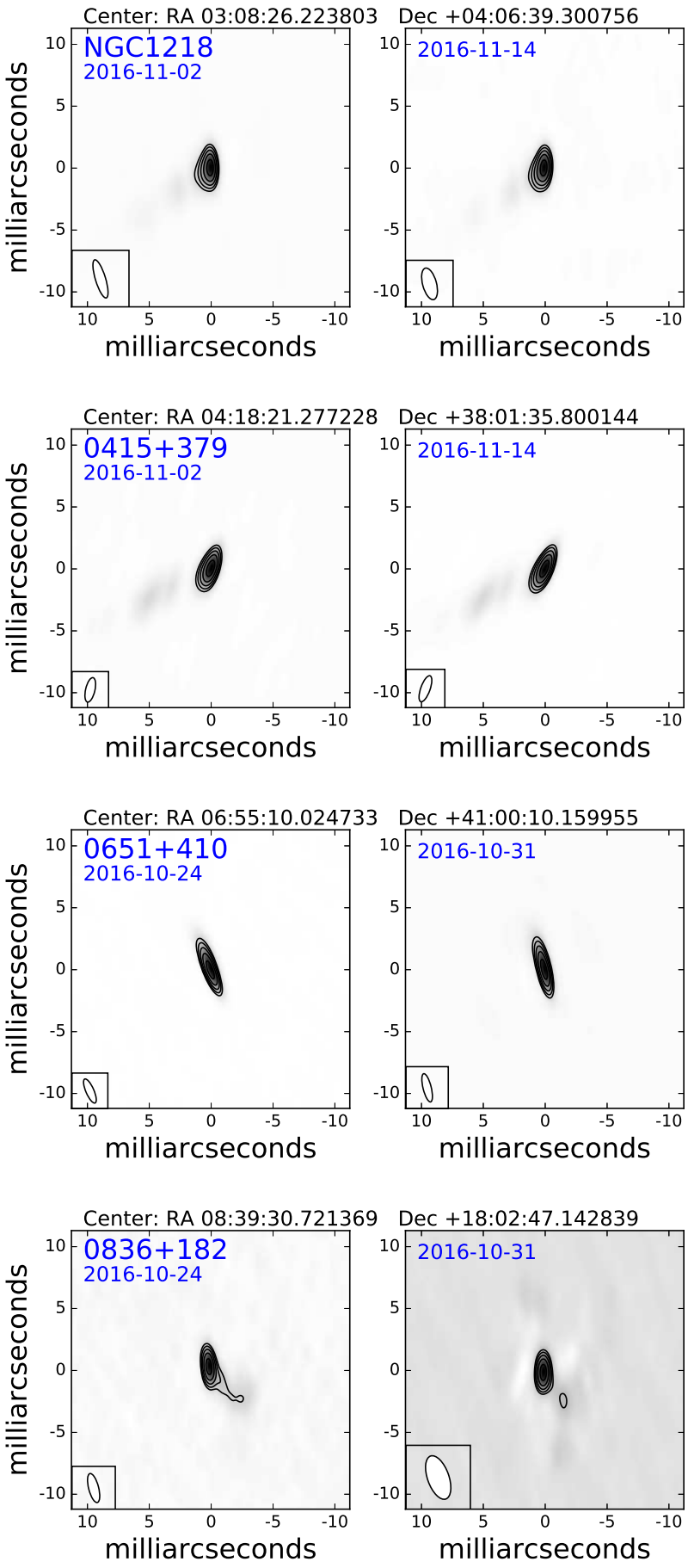
Center: RA 03:08:26.223803 Dec +04:06:39.300756
NGC1218
2016-11-02
2016-11-14
Center: RA 04:18:21.277228 Dec +38:01:35.800144
0415+379
2016-11-02
2016-11-14
Center: RA 06:55:10.024733 Dec +41:00:10.159955
0651+410
2016-10-24
2016-10-31
Center: RA 08:39:30.721369 Dec +18:02:47.142839
0836+182
2016-10-24
2016-10-31
milliarcseconds
10
5
0
-5
-10

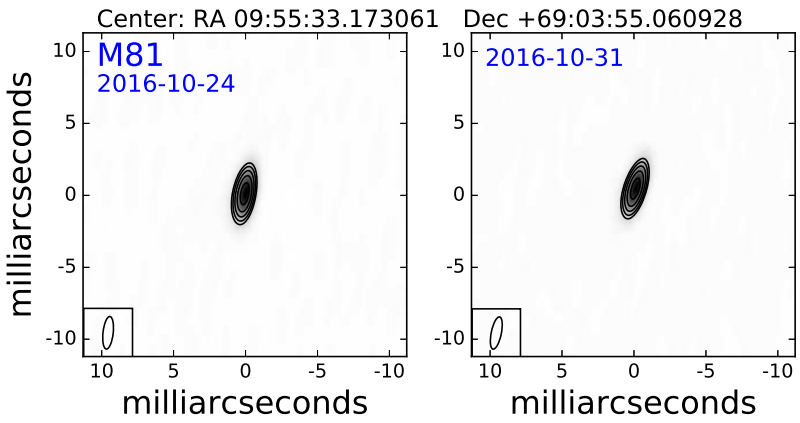
Center: RA 09:55:33.173061 Dec +69:03:55.060928
M81
2016-10-24
2016-10-31
milliarcseconds
milliarcseconds
milliarcseconds
milliarcseconds

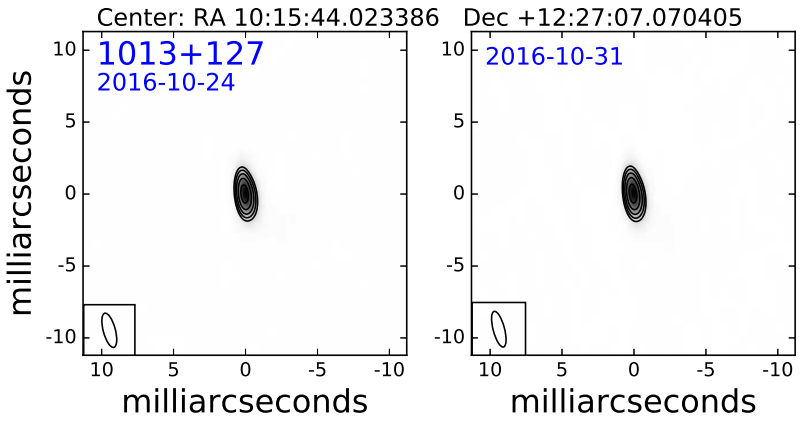
Center: RA 10:15:44.023386 Dec +12:27:07.070405
1013+127
2016-10-24
2016-10-31
milliarcseconds
milliarcseconds
milliarcseconds
milliarcseconds

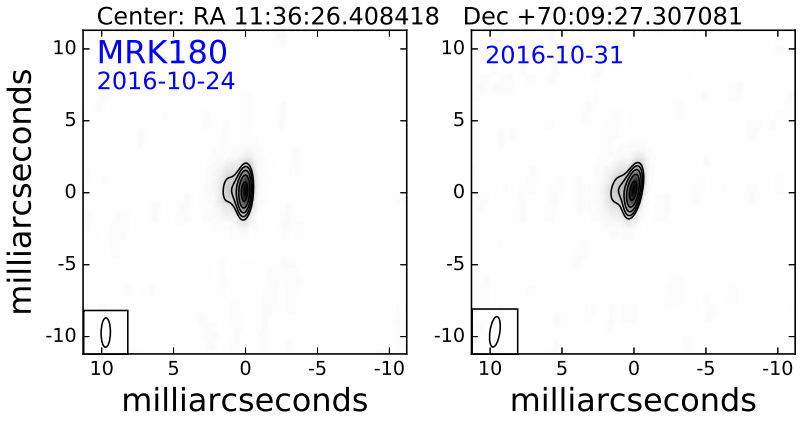
Center: RA 11:36:26.408418 Dec +70:09:27.307081
MRK180
2016-10-24
2016-10-31
milliarcseconds
milliarcseconds
milliarcseconds
milliarcseconds

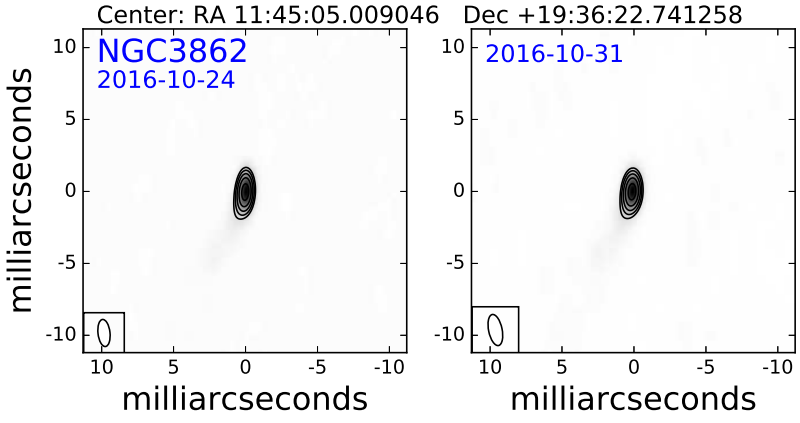
Center: RA 11:45:05.009046 Dec +19:36:22.741258
NGC3862
2016-10-24
2016-10-31
milliarcseconds
milliarcseconds
milliarcseconds
milliarcseconds

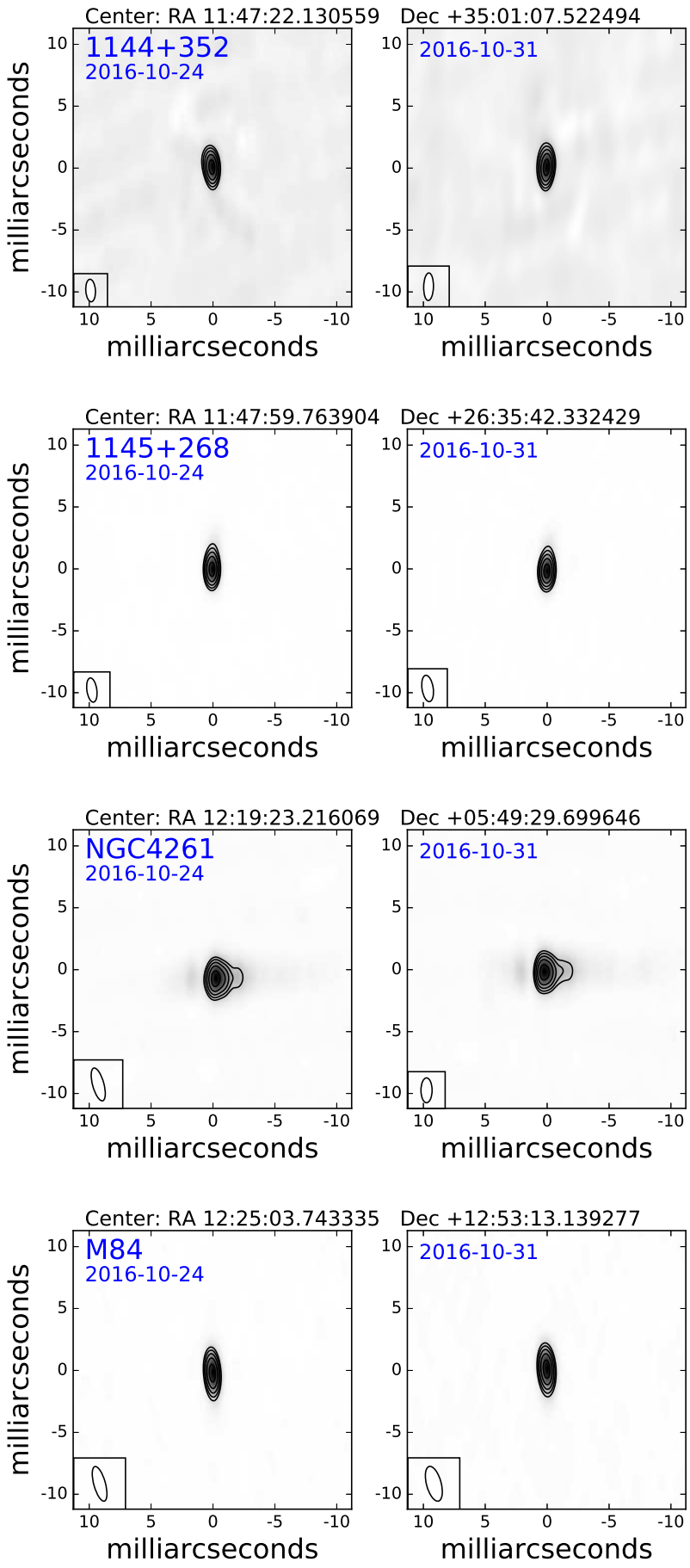
Center: RA 11:47:22.130559 Dec +35:01:07.522494
1144+352
2016-10-24
2016-10-31
Center: RA 11:47:59.763904 Dec +26:35:42.332429
1145+268
2016-10-24
2016-10-31
Center: RA 12:19:23.216069 Dec +05:49:29.699646
NGC4261
2016-10-24
2016-10-31
Center: RA 12:25:03.743335 Dec +12:53:13.139277
M84
2016-10-24
2016-10-31
milliarcseconds
10
5
0
-5
-10

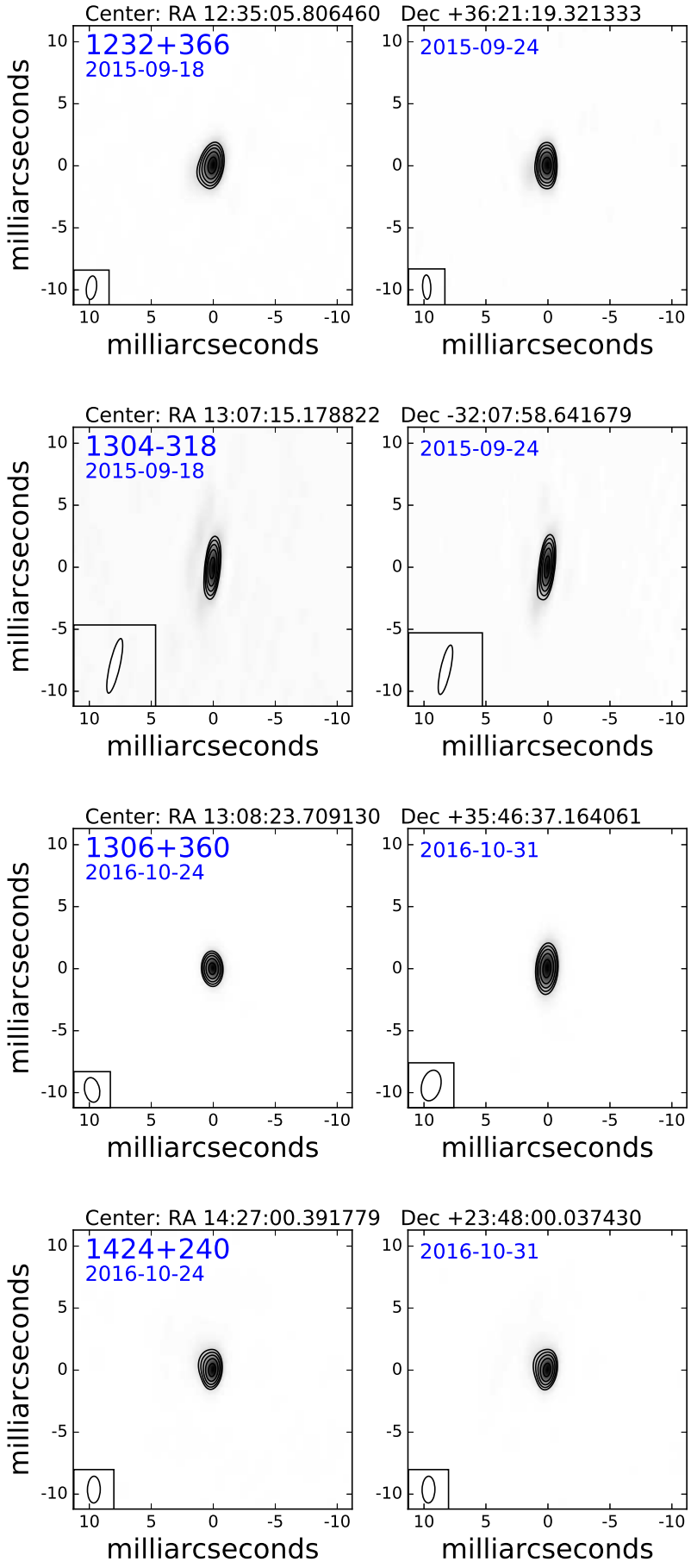
Center: RA 12:35:05.806460 Dec +36:21:19.321333
1232+366
2015-09-18
2015-09-24
Center: RA 13:07:15.178822 Dec -32:07:58.641679
1304-318
2015-09-18
2015-09-24
Center: RA 13:08:23.709130 Dec +35:46:37.164061
1306+360
2016-10-24
2016-10-31
Center: RA 14:27:00.391779 Dec +23:48:00.037430
1424+240
2016-10-24
2016-10-31
milliarcseconds
10
5
0
-5
-10

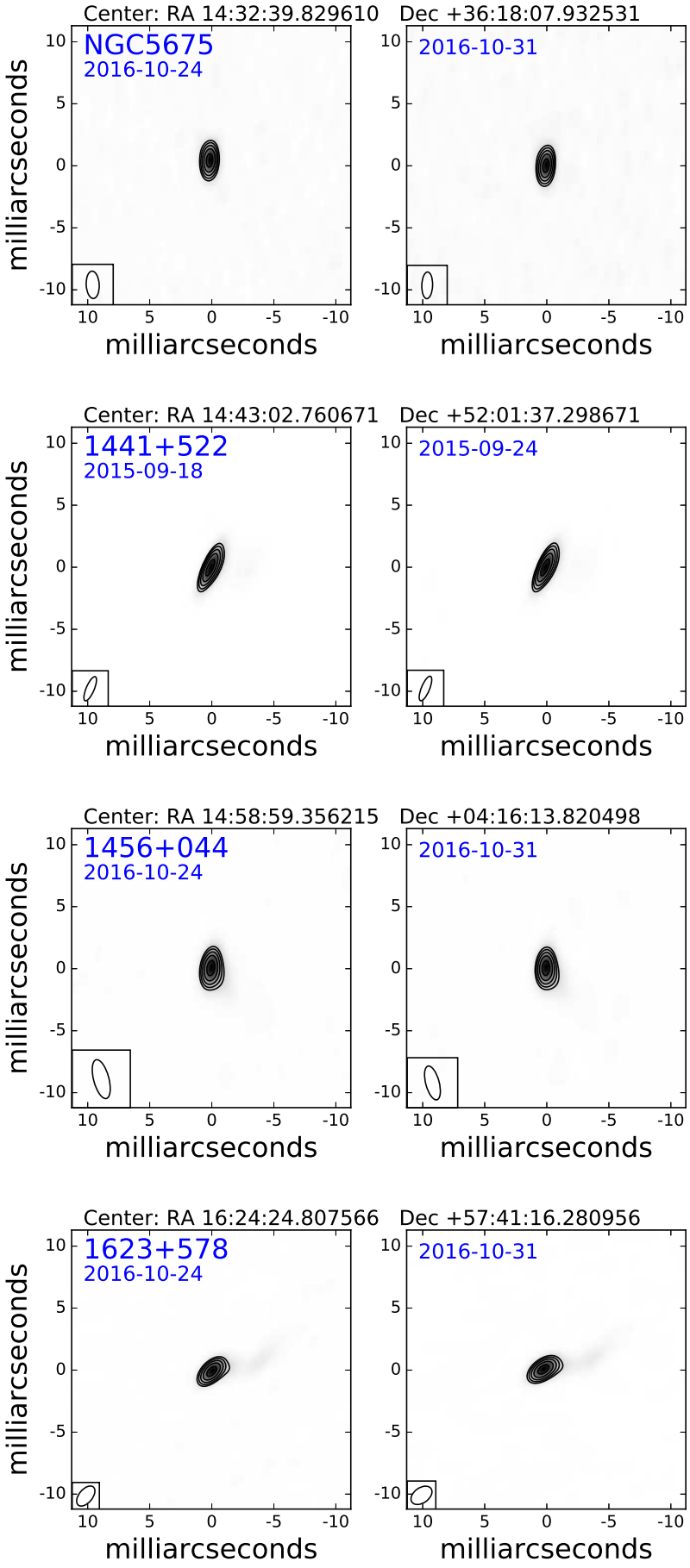
Center: RA 14:32:39.829610 Dec +36:18:07.932531
NGC5675
2016-10-24
2016-10-31
Center: RA 14:43:02.760671 Dec +52:01:37.298671
1441+522
2015-09-18
2015-09-24
Center: RA 14:58:59.356215 Dec +04:16:13.820498
1456+044
2016-10-24
2016-10-31
Center: RA 16:24:24.807566 Dec +57:41:16.280956
1623+578
2016-10-24
2016-10-31
milliarcseconds
10
5
0
-5
-10

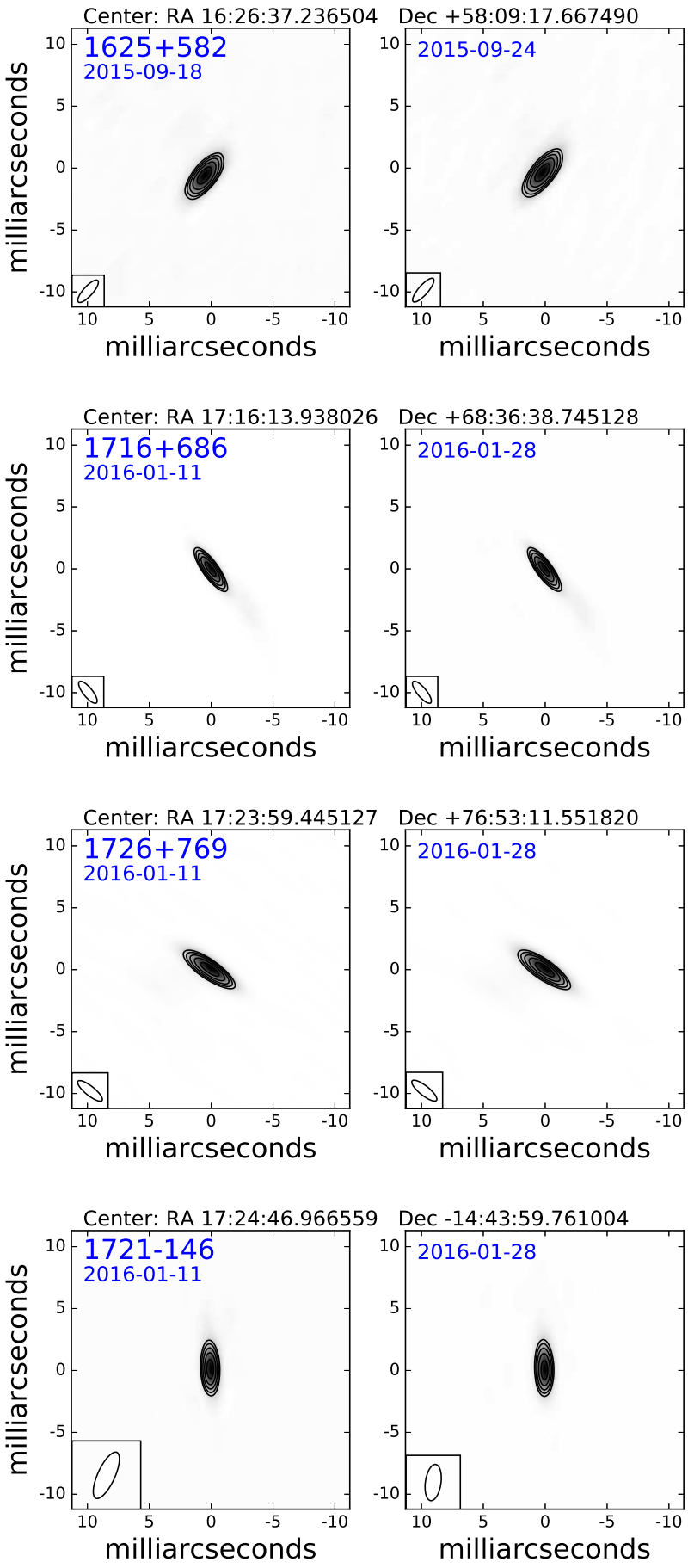
Center: RA 16:26:37.236504 Dec +58:09:17.667490
1625+582
2015-09-18
2015-09-24
Center: RA 17:16:13.938026 Dec +68:36:38.745128
1716+686
2016-01-11
2016-01-28
Center: RA 17:23:59.445127 Dec +76:53:11.551820
1726+769
2016-01-11
2016-01-28
Center: RA 17:24:46.966559 Dec -14:43:59.761004
1721-146
2016-01-11
2016-01-28
milliarcseconds
10
5
0
-5
-10

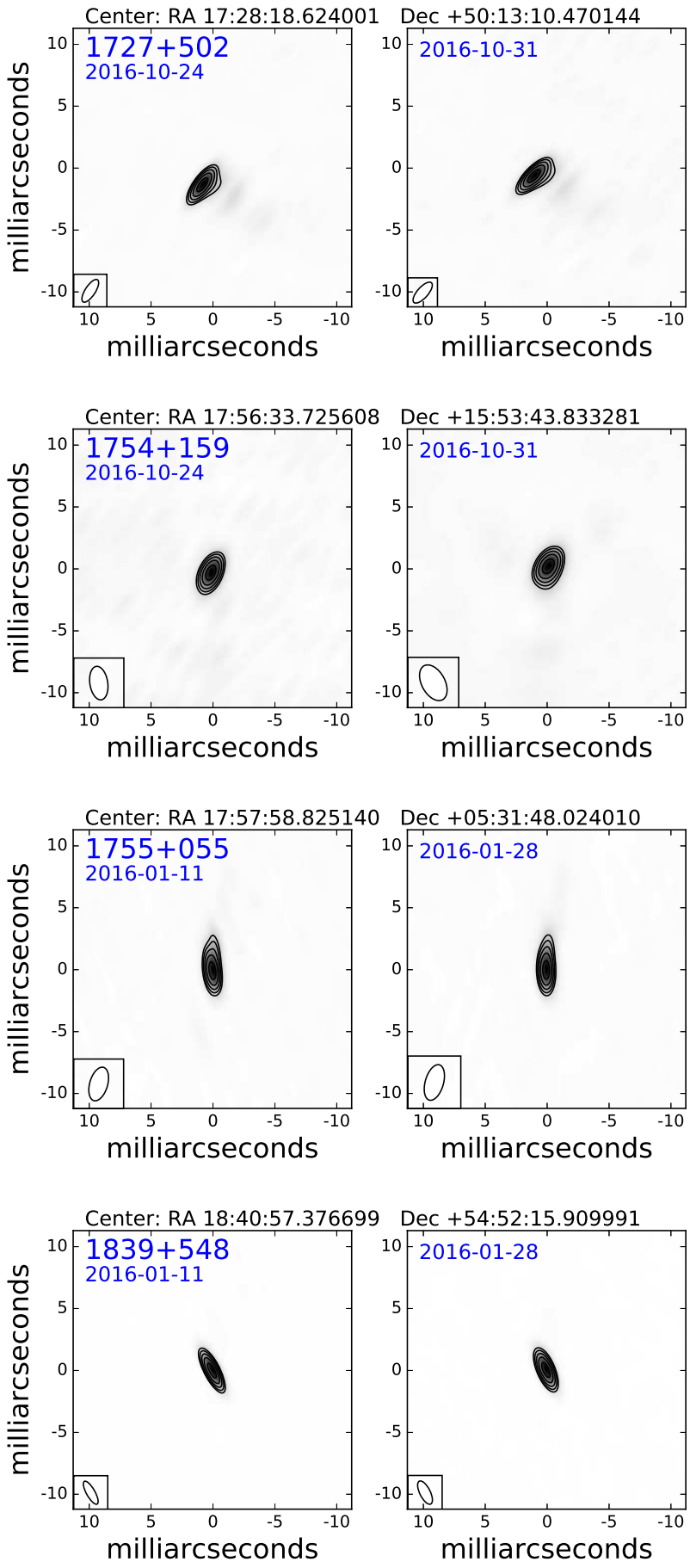
Center: RA 17:28:18.624001 Dec +50:13:10.470144
1727+502
2016-10-24
2016-10-31
Center: RA 17:56:33.725608 Dec +15:53:43.833281
1754+159
2016-10-24
2016-10-31
Center: RA 17:57:58.825140 Dec +05:31:48.024010
1755+055
2016-01-11
2016-01-28
Center: RA 18:40:57.376699 Dec +54:52:15.909991
1839+548
2016-01-11
2016-01-28
milliarcseconds
10
5
0
-5
-10

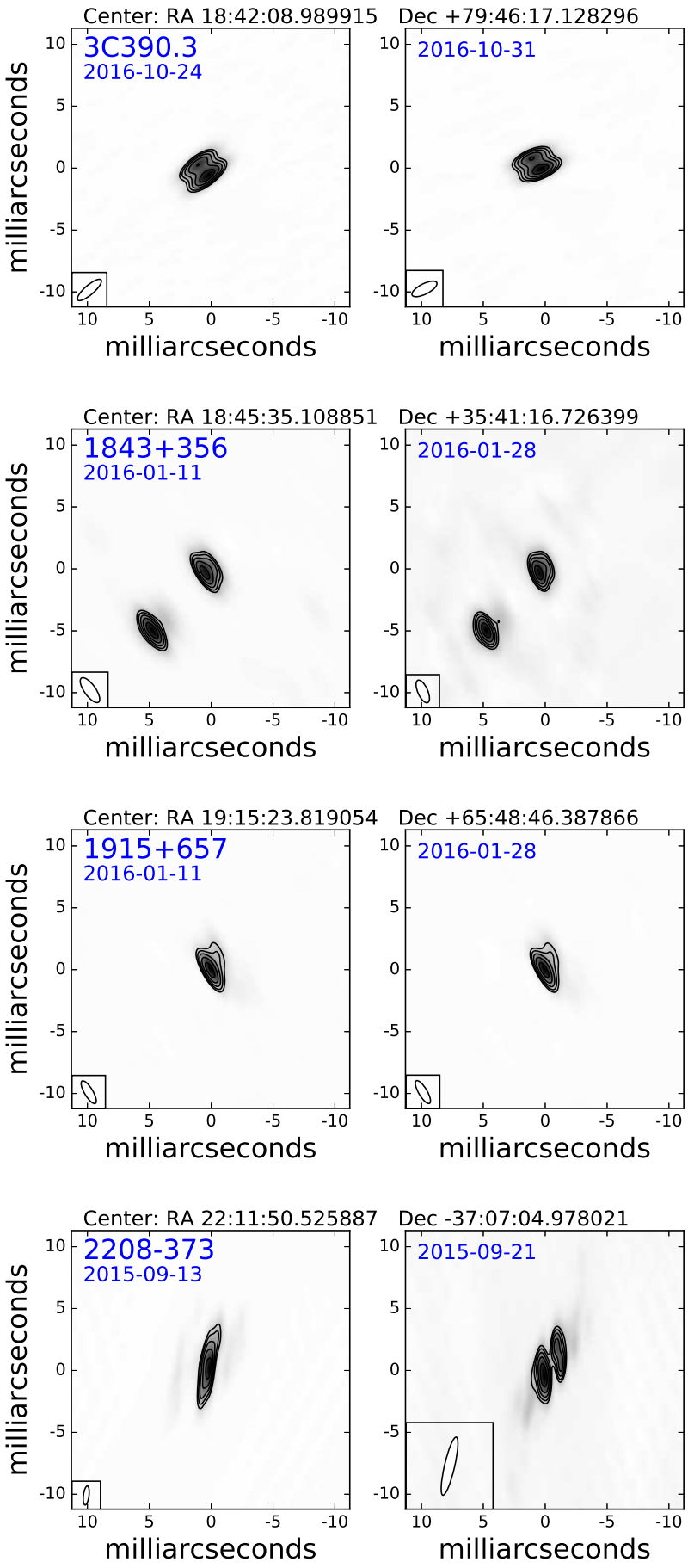
Center: RA 18:42:08.989915 Dec +79:46:17.128296
3C390.3
2016-10-24
2016-10-31
Center: RA 18:45:35.108851 Dec +35:41:16.726399
1843+356
2016-01-11
2016-01-28
Center: RA 19:15:23.819054 Dec +65:48:46.387866
1915+657
2016-01-11
2016-01-28
Center: RA 22:11:50.525887 Dec -37:07:04.978021
2208-373
2015-09-13
2015-09-21
milliarcseconds
10
5
0
-5
-10

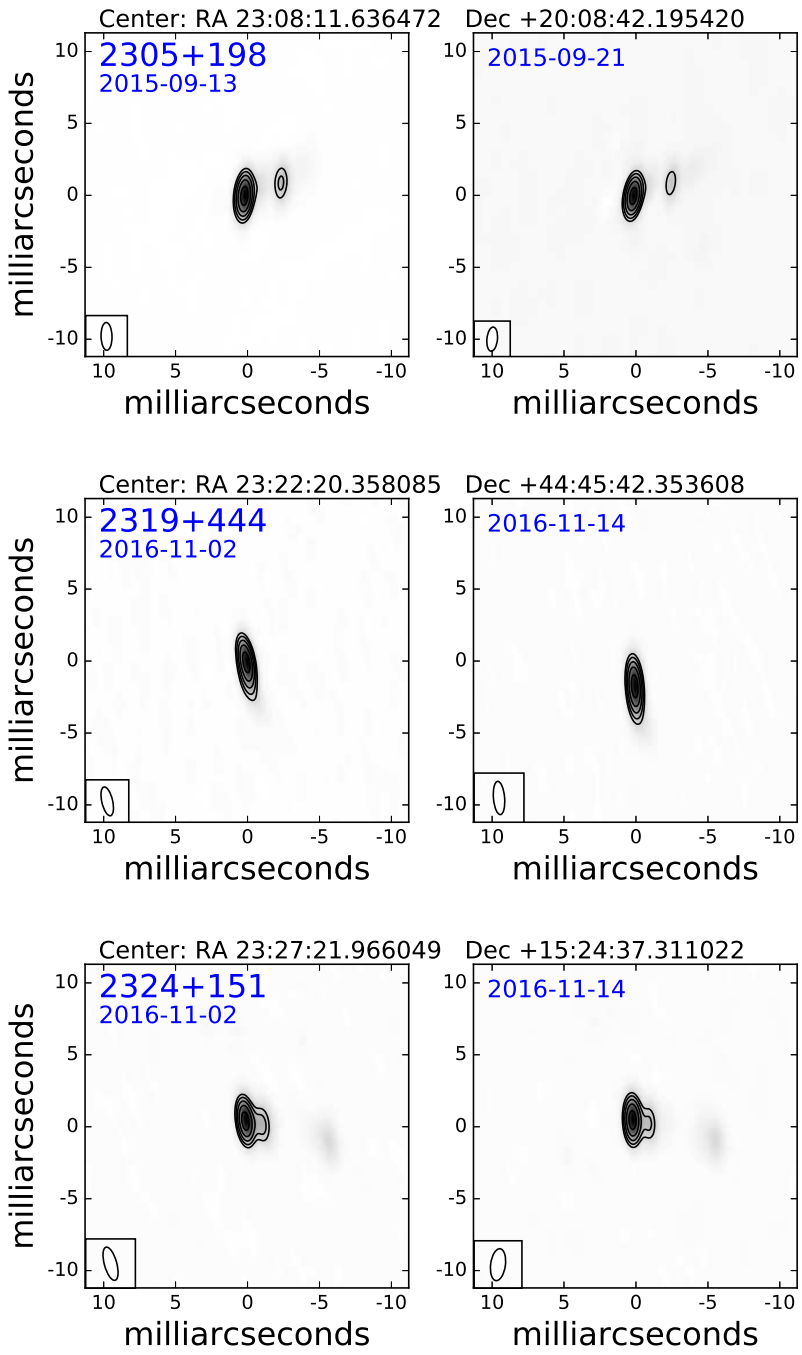

Figure 3.1 VLBA self-calibrated 8.3 GHz images. Each object is observed twice (within 3 – 24 days of each other) and the two epochs (A and B) are plotted side by side for each object. Each image has five logarithmically spaced contour levels ranging from 3σ to $0.8F_m$, where σ is the standard deviation of the image and F_m is the maximum pixel flux. Assuming $R = 0.8F_m/3\sigma$, the contour levels are $(1,R^{1/4},R^{1/2},R^{3/4},R)\times 3\sigma$. Relative positions in RA and Dec are shown on the X and Y axes, respectively. The center coordinates of each image are listed at the top of each plot – by design, these are the same for both epochs. The observing date for each image is listed in the top left corner of each image in yyyy-mm-dd format. The restored beam is shown at the lower left of each image.

CLEANed image. The benefit of this approach is that no assumptions must be made about the true source structure; one does not need to assume a gaussian or any other model. However, the precision of the measurement is resolution dependent – one can only know the position to within one pixel – and the peak brightness can be affected by blended, nearby objects that are not modeled by this approach. The second approach is to fit a series of two-dimensional gaussians in the image plane. This method is often preferred because an image has usually already been produced during self-calibration, making the final step of gaussian fitting simple and computationally inexpensive. Lastly, the centroid can be found by fitting the self-calibrated visibilities with gaussians. Often the initial guess for the gaussian shape is determined from a CLEANed image. This approach is often more accurate for determining the true angular size of the source and for mapping any extended complex structure. However, this approach is computationally more expensive because it requires several convolutions between the image plane and the uv-plane. Ultimately, we chose to fit gaussians in the image plane. Because we assume that all of the sources are point-like, we do not need to model the extended structures or true size of the objects, thereby making the advantages of fitting in the uv-plane inapplicable. Additionally, existing tasks in AIPS for fitting in the image plane are better developed than those for fitting in the uv-plane, enabling a better assessment of the quality of the final fit. Finally, fitting gaussians in the image plane is the typical approach for relative astrometry that has been used in many studies (e.g., Reid et al. 1999; Reid & Brunthaler 2004; Fomalont et al. 2011).

We fit a two-dimensional gaussian to the CLEANed final image for each object using the AIPS task `JMFIT`. For each image, we selected a small region approximately $10 - 20$ times the beam size containing the main object component. `JMFIT` makes an initial guess of a gaussian with a peak equal to the brightest pixel in the selected region and a width equal to the CLEAN beam. Then it performs a least-squares minimization until model convergence is achieved. `JMFIT` estimates the uncertainties of the fitted gaussian parameters using theoretical equations based on the image RMS from Condon (1997). If the object is a

point source (the beam area > 0.9 times the fitted gaussian area), $M = 1$. If the object is extended (the beam area < 0.1 times the fitted gaussian area), $M = \sqrt{8\ A_{\rm Beam}/A_{\rm Image}}$. For intermediate cases, $M = \sqrt{0.8 + 0.25(A_{\rm Beam}/A_{\rm Image} - 0.1)}$. Using the appropriate M, the uncertainties are estimated as follows,

$$\sigma_{\rm Fpeak} = M \times {\rm RMS}, \tag{3.1}$$

$$\sigma_{\rm Smaj} = S_{\rm Maj} * \frac{\sigma_{\rm Fpeak}}{\rm Fpeak}, \tag{3.2}$$

$$\sigma_{\rm Smin} = S_{\rm Min} * \frac{\sigma_{\rm Fpeak}}{\rm Fpeak}, \tag{3.3}$$

$$\sigma_{PA} = \sqrt{2}\ \frac{S_{\rm Maj} + S_{\rm Min}}{S^2_{\rm Maj} + S^2_{\rm Min}} \times \frac{\sigma_{\rm Fpeak}}{\rm Fpeak}, \tag{3.4}$$

$$\sigma_X = \sqrt{8\ln(2)\left(\sigma_{\rm Smaj}\sin({\rm PA})\right)^2 + \left(\sigma_{\rm Smin}\cos({\rm PA})\right)^2}, \tag{3.5}$$

$$\sigma_Y = \sqrt{8\ln(2)\left(\sigma_{\rm Smaj}\cos({\rm PA})\right)^2 + \left(\sigma_{\rm Smin}\sin({\rm PA})\right)^2}, \tag{3.6}$$

and

$$\sigma_{\rm Fint} = \sigma_{\rm Fpeak}\ \frac{A_{\rm Beam}}{A_{\rm Image}}\ \sqrt{1 + 2\frac{A_{\rm Beam}}{A_{\rm Image}}} \tag{3.7}$$

where $A_{\rm Beam} = B_{\rm Maj} \times B_{\rm Min}$, the major axis of the CLEAN beam times its minor axis ($A_{\rm Beam} \approx$ the area of the CLEAN beam divided by π), $A_{\rm Image} = S_{\rm Maj} \times S_{\rm Min}$, the major axis of the fitted gaussian in the image plane times its minor axis (note that this is the true object size convolved with the CLEAN beam), Fpeak is the peak flux density, PA is the position angle, X and Y are the center of the gaussian, and Fint is the integrated flux density. Table 3.1 lists the positions and associated uncertainties measured with `JMFIT`.

To calculate the proper motion of the target, we first found the centroid for both the target and its phase-reference in terms of the phase-reference coordinate system (the coordinates in the calibrated images are all in terms of the phase-reference coordinate system because we phase-referenced the visibilities during data reduction). The resulting position uncertainties are, on average, 4 μas. Then, we used use the centroids of the target and

phase-reference to find the separation between the two in right ascension and declination –

$$\Delta_\alpha = \alpha_{\rm target} - \alpha_{\rm phase} \tag{3.8}$$

and

$$\Delta_\delta = \delta_{\rm target} - \delta_{\rm phase}. \tag{3.9}$$

Uncertainties from `JMFIT` are added in quadrature to find the uncertainties in these separations. Next, we calculate the current location of the phase-reference using its proper motion;

$$\alpha_{\rm phase} = \frac{\mu_\alpha}{\cos\delta} t - \alpha_0, \tag{3.10}$$

and

$$\delta_{\rm phase} = \mu_\delta t - \delta_0, \tag{3.11}$$

where t is the date of our observation and α_0 and δ_0 are the y-intercepts of the least-squares fit to the object's time series in right ascension and declination, respectively. We remove the latitude correction for the proper motion in right ascension because we are calculating the angular change with time, not the absolute proper motion of the extragalactic object. The associated uncertainties for these equations are

$$\sigma_\alpha^2 = t^2 \frac{\sigma_{\mu_\alpha}^2}{\cos^2\delta} + \sigma_{\alpha_0}^2 + \frac{2t\sigma_{\mu,\alpha}}{\cos\delta}, \tag{3.12}$$

and

$$\sigma_\delta^2 = t^2\sigma_{\mu_\delta}^2 + \sigma_{\delta_0}^2 + 2t\sigma_{\mu,\delta}, \tag{3.13}$$

where $\sigma_{\mu,\alpha}$ and $\sigma_{\mu,\delta}$ are the covariances between μ_α and α_0 and μ_δ and δ_0, respectively. The covariances have units of μas^2 yr^{-1}. Finally, we use the separation between the target and phase-reference and the phase-reference's current location to calculate the current absolute position of the target;

$$\alpha_{\rm target} = \alpha_{\rm phase} + \Delta_\alpha \tag{3.14}$$

and

$$\delta_{\rm target} = \delta_{\rm phase} + \Delta_{\delta}. \tag{3.15}$$

Again the associated uncertainties are added in quadrature.

Using the above techniques, we measured the position of each target for both epochs of observation. In all cases, both positions were within 1σ of each other, indicating that the position measurements are robust and are not affected by atmospheric effects or calibration errors. To further increase the accuracy of our position measurements, we averaged the two position measurements together for each source. Then, we added the new position to the archival GSFC time series and derived a new proper motion using the same analytical least-squares parameter estimation described in Chapter 2. We did not include a bootstrap because these sources all have very few position measurements (often only three, including the new measurement). Figure 3.2 shows the time series and proper motion fits for our observed targets and Table 3.1 lists the results of the position measurements and the new derived proper motions. The new proper motions have a mean amplitude precision of 49.7 μas yr^{-1}. Although we were able to measure relative positions of our targets with accuracies of ~ 4 μas, our final proper motion uncertainties were dominated by the proper motion uncertainties of the phase-references and by the position uncertainties of previous astrometry epochs.

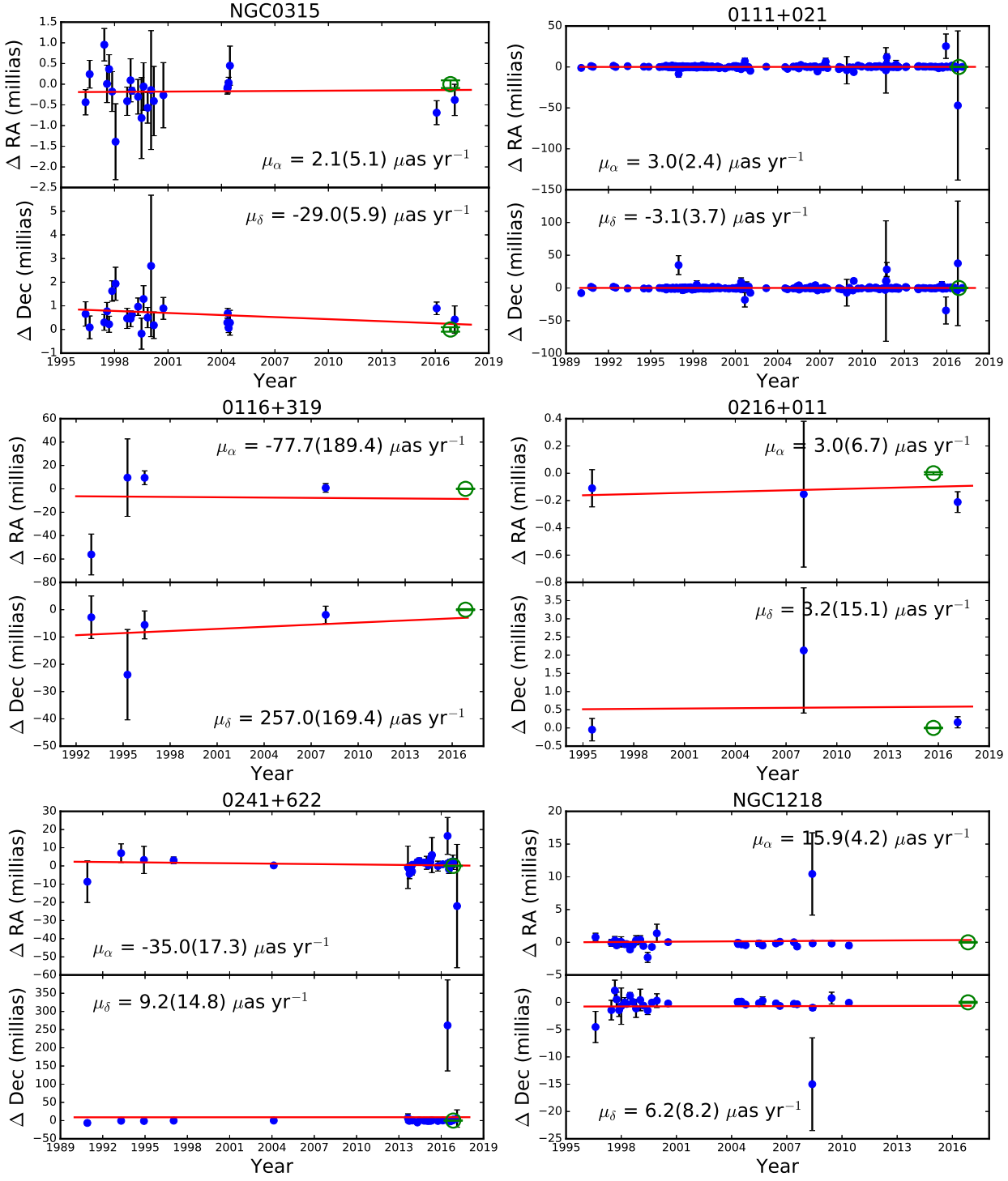
NGC0315
Δ RA (millias)
μ_α = 2.1(5.1) μas yr^{-1}
Δ Dec (millias)
μ_δ = -29.0(5.9) μas yr^{-1}
Year
0111+021
Δ RA (millias)
μ_α = 3.0(2.4) μas yr^{-1}
Δ Dec (millias)
μ_δ = -3.1(3.7) μas yr^{-1}
Year
0116+319
Δ RA (millias)
μ_α = -77.7(189.4) μas yr^{-1}
Δ Dec (millias)
μ_δ = 257.0(169.4) μas yr^{-1}
Year
0216+011
Δ RA (millias)
μ_α = 3.0(6.7) μas yr^{-1}
Δ Dec (millias)
μ_δ = 3.2(15.1) μas yr^{-1}
Year
0241+622
Δ RA (millias)
μ_α = -35.0(17.3) μas yr^{-1}
Δ Dec (millias)
μ_δ = 9.2(14.8) μas yr^{-1}
Year
NGC1218
Δ RA (millias)
μ_α = 15.9(4.2) μas yr^{-1}
Δ Dec (millias)
μ_δ = 6.2(8.2) μas yr^{-1}
Year

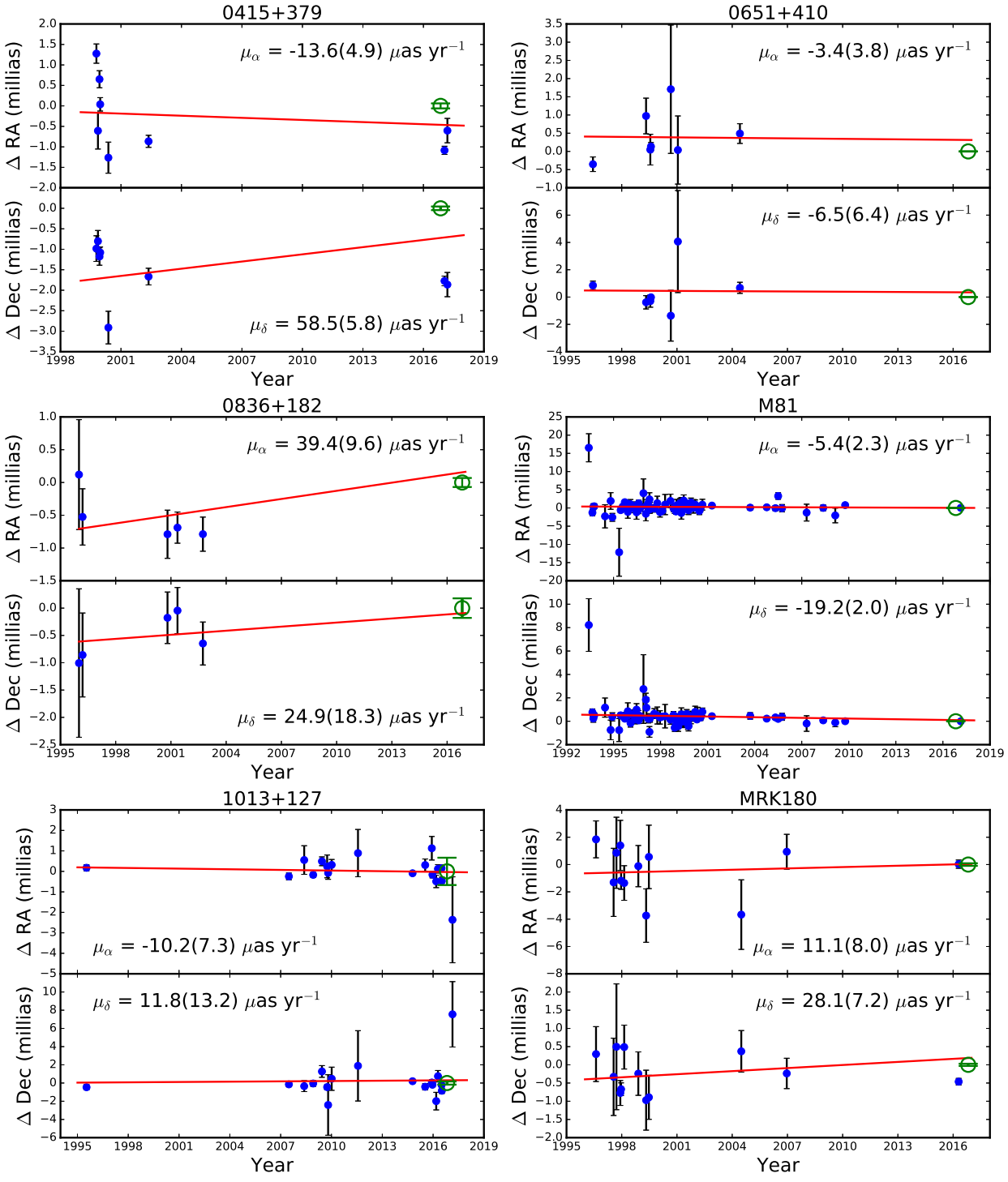
0415+379
μ_α = -13.6(4.9) μas yr^{-1}
μ_δ = 58.5(5.8) μas yr^{-1}
0651+410
μ_α = -3.4(3.8) μas yr^{-1}
μ_δ = -6.5(6.4) μas yr^{-1}
0836+182
μ_α = 39.4(9.6) μas yr^{-1}
μ_δ = 24.9(18.3) μas yr^{-1}
M81
μ_α = -5.4(2.3) μas yr^{-1}
μ_δ = -19.2(2.0) μas yr^{-1}
1013+127
μ_α = -10.2(7.3) μas yr^{-1}
μ_δ = 11.8(13.2) μas yr^{-1}
MRK180
μ_α = 11.1(8.0) μas yr^{-1}
μ_δ = 28.1(7.2) μas yr^{-1}
Δ RA (millias)
Δ Dec (millias)
Year

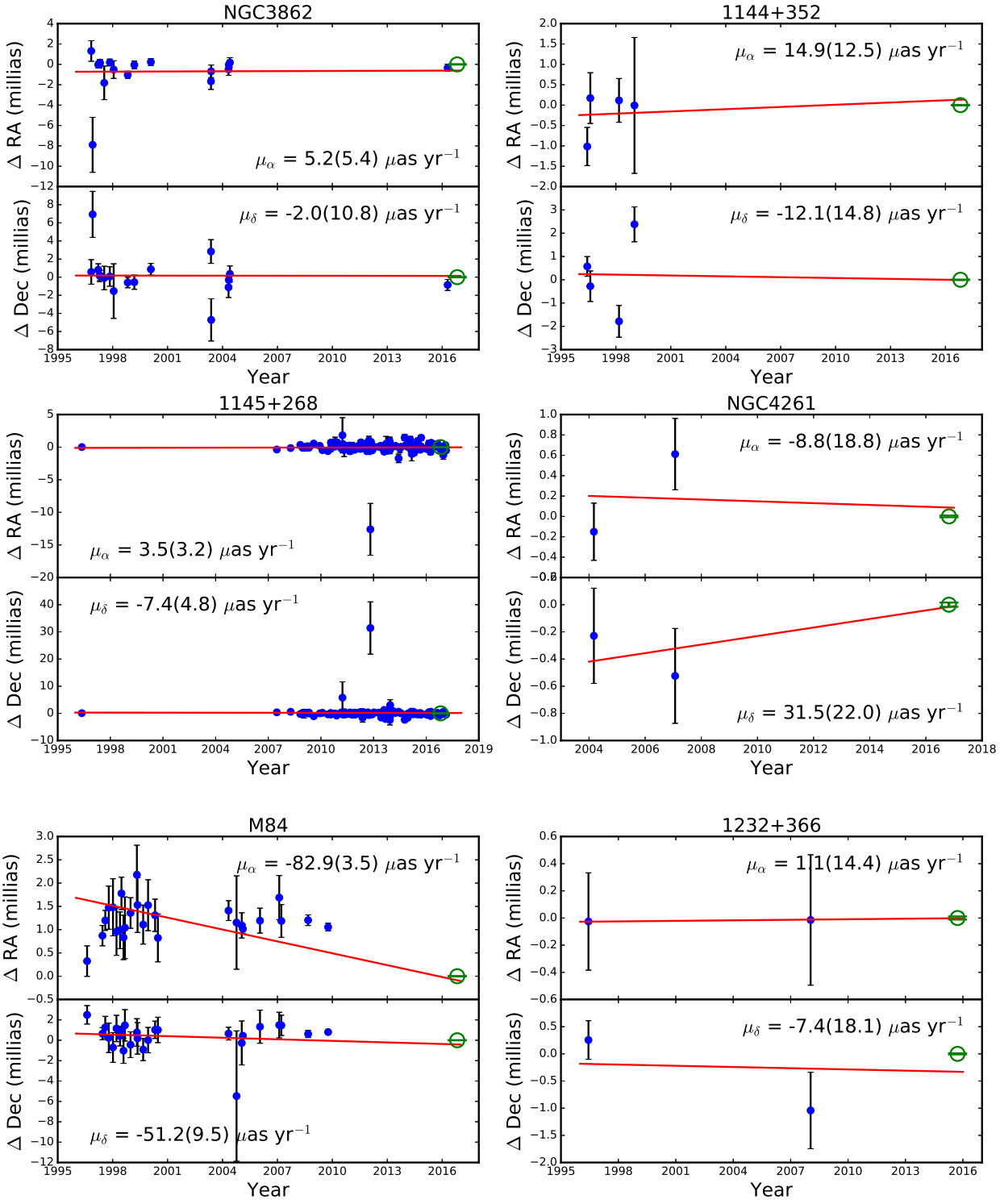
NGC3862
μ_α = 5.2(5.4) μas yr^{-1}
μ_δ = -2.0(10.8) μas yr^{-1}
1144+352
μ_α = 14.9(12.5) μas yr^{-1}
μ_δ = -12.1(14.8) μas yr^{-1}
1145+268
μ_α = 3.5(3.2) μas yr^{-1}
μ_δ = -7.4(4.8) μas yr^{-1}
NGC4261
μ_α = -8.8(18.8) μas yr^{-1}
μ_δ = 31.5(22.0) μas yr^{-1}
M84
μ_α = -82.9(3.5) μas yr^{-1}
μ_δ = -51.2(9.5) μas yr^{-1}
1232+366
μ_α = 1[illegible]1(14.4) μas yr^{-1}
μ_δ = -7.4(18.1) μas yr^{-1}
Δ RA (millias)
Δ Dec (millias)
Year

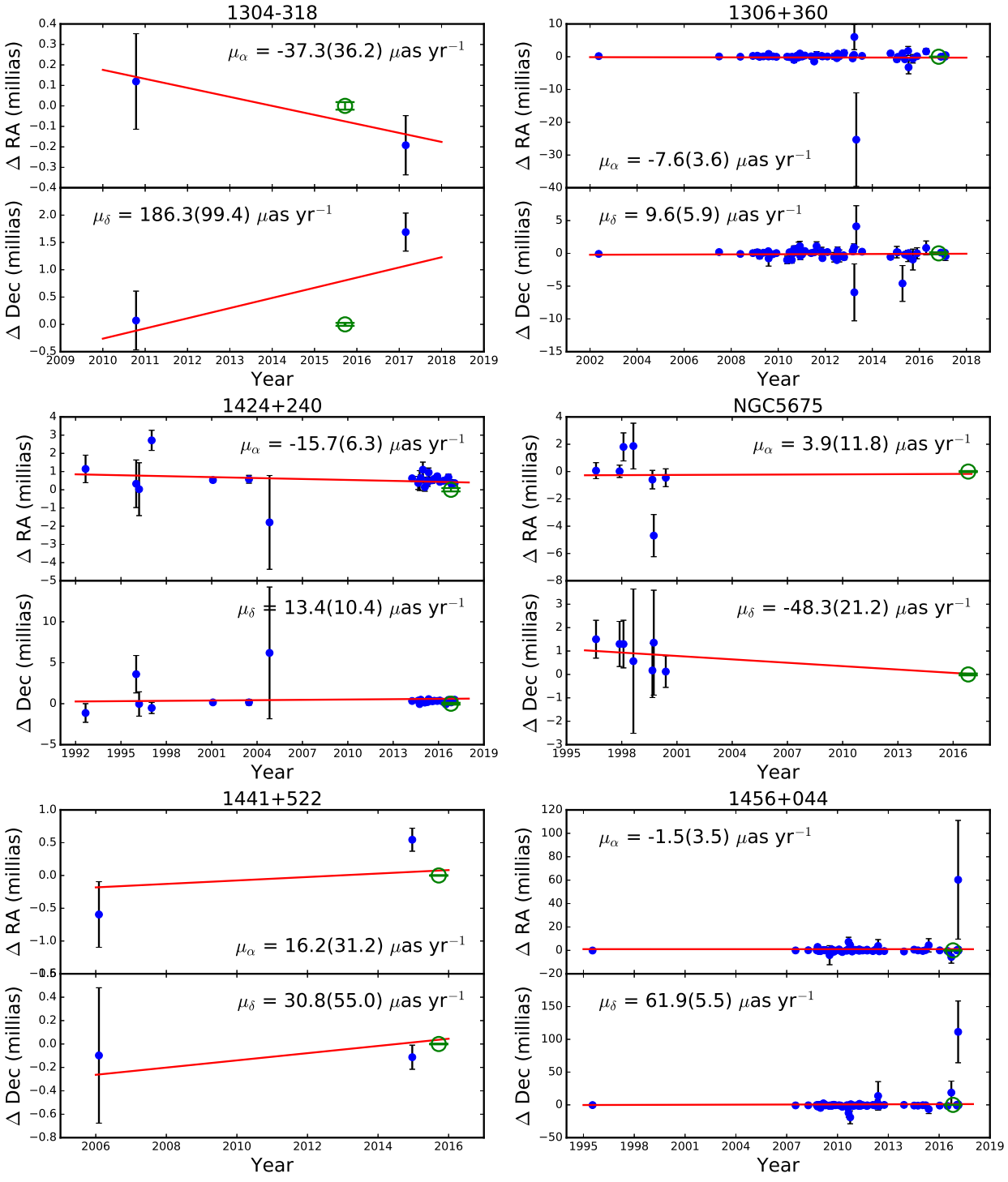
1304-318
μ_α = -37.3(36.2) μas yr^{-1}
μ_δ = 186.3(99.4) μas yr^{-1}
Δ RA (millias)
Δ Dec (millias)
Year
1306+360
μ_α = -7.6(3.6) μas yr^{-1}
μ_δ = 9.6(5.9) μas yr^{-1}
Δ RA (millias)
Δ Dec (millias)
Year
1424+240
μ_α = -15.7(6.3) μas yr^{-1}
μ_δ = 13.4(10.4) μas yr^{-1}
Δ RA (millias)
Δ Dec (millias)
Year
NGC5675
μ_α = 3.9(11.8) μas yr^{-1}
μ_δ = -48.3(21.2) μas yr^{-1}
Δ RA (millias)
Δ Dec (millias)
Year
1441+522
μ_α = 16.2(31.2) μas yr^{-1}
μ_δ = 30.8(55.0) μas yr^{-1}
Δ RA (millias)
Δ Dec (millias)
Year
1456+044
μ_α = -1.5(3.5) μas yr^{-1}
μ_δ = 61.9(5.5) μas yr^{-1}
Δ RA (millias)
Δ Dec (millias)
Year

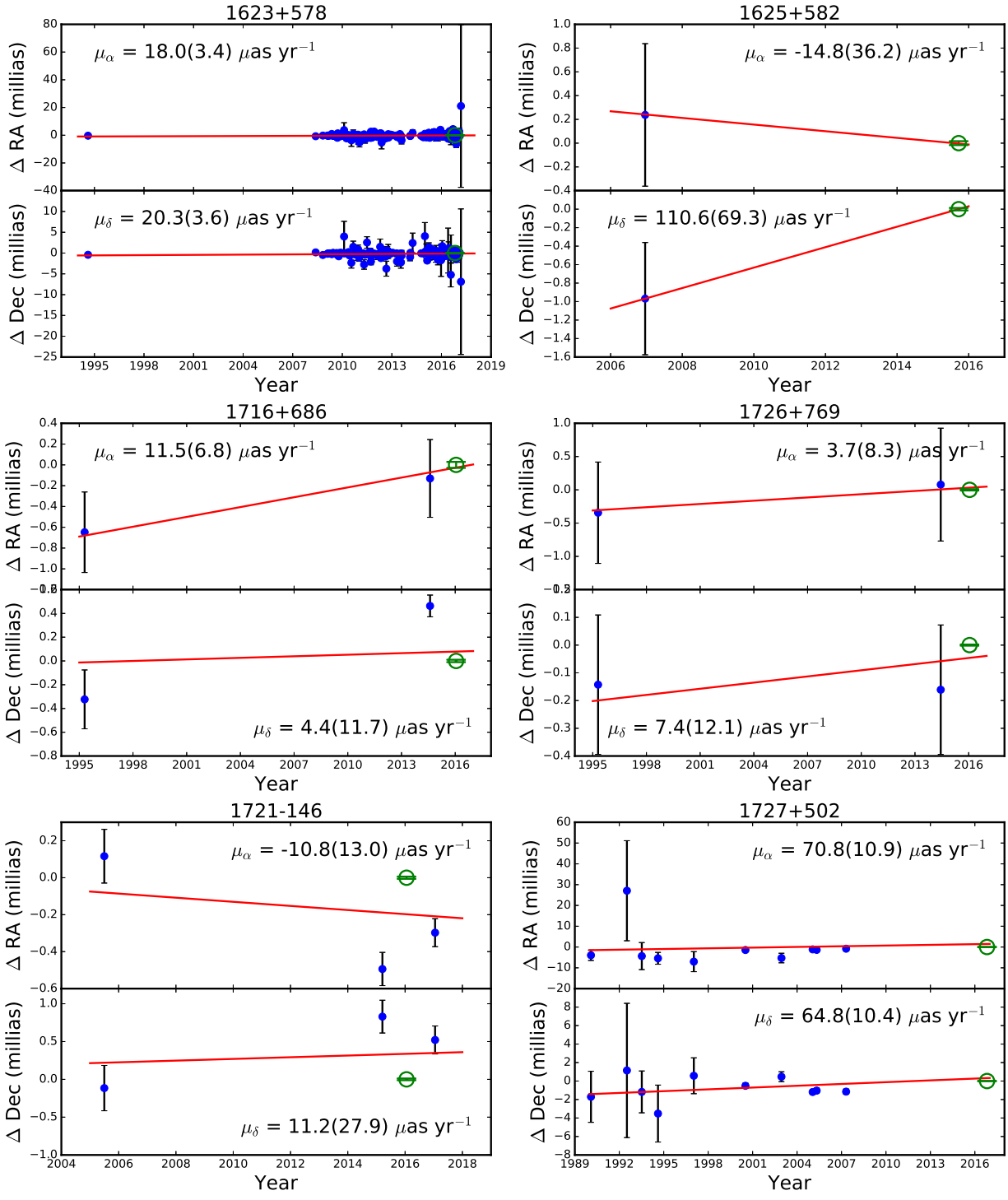
1623+578
μ_α = 18.0(3.4) μas yr^{-1}
μ_δ = 20.3(3.6) μas yr^{-1}
Δ RA (millias)
Δ Dec (millias)
Year
1625+582
μ_α = -14.8(36.2) μas yr^{-1}
μ_δ = 110.6(69.3) μas yr^{-1}
Δ RA (millias)
Δ Dec (millias)
Year
1716+686
μ_α = 11.5(6.8) μas yr^{-1}
μ_δ = 4.4(11.7) μas yr^{-1}
Δ RA (millias)
Δ Dec (millias)
Year
1726+769
μ_α = 3.7(8.3) μas yr^{-1}
μ_δ = 7.4(12.1) μas yr^{-1}
Δ RA (millias)
Δ Dec (millias)
Year
1721-146
μ_α = -10.8(13.0) μas yr^{-1}
μ_δ = 11.2(27.9) μas yr^{-1}
Δ RA (millias)
Δ Dec (millias)
Year
1727+502
μ_α = 70.8(10.9) μas yr^{-1}
μ_δ = 64.8(10.4) μas yr^{-1}
Δ RA (millias)
Δ Dec (millias)
Year

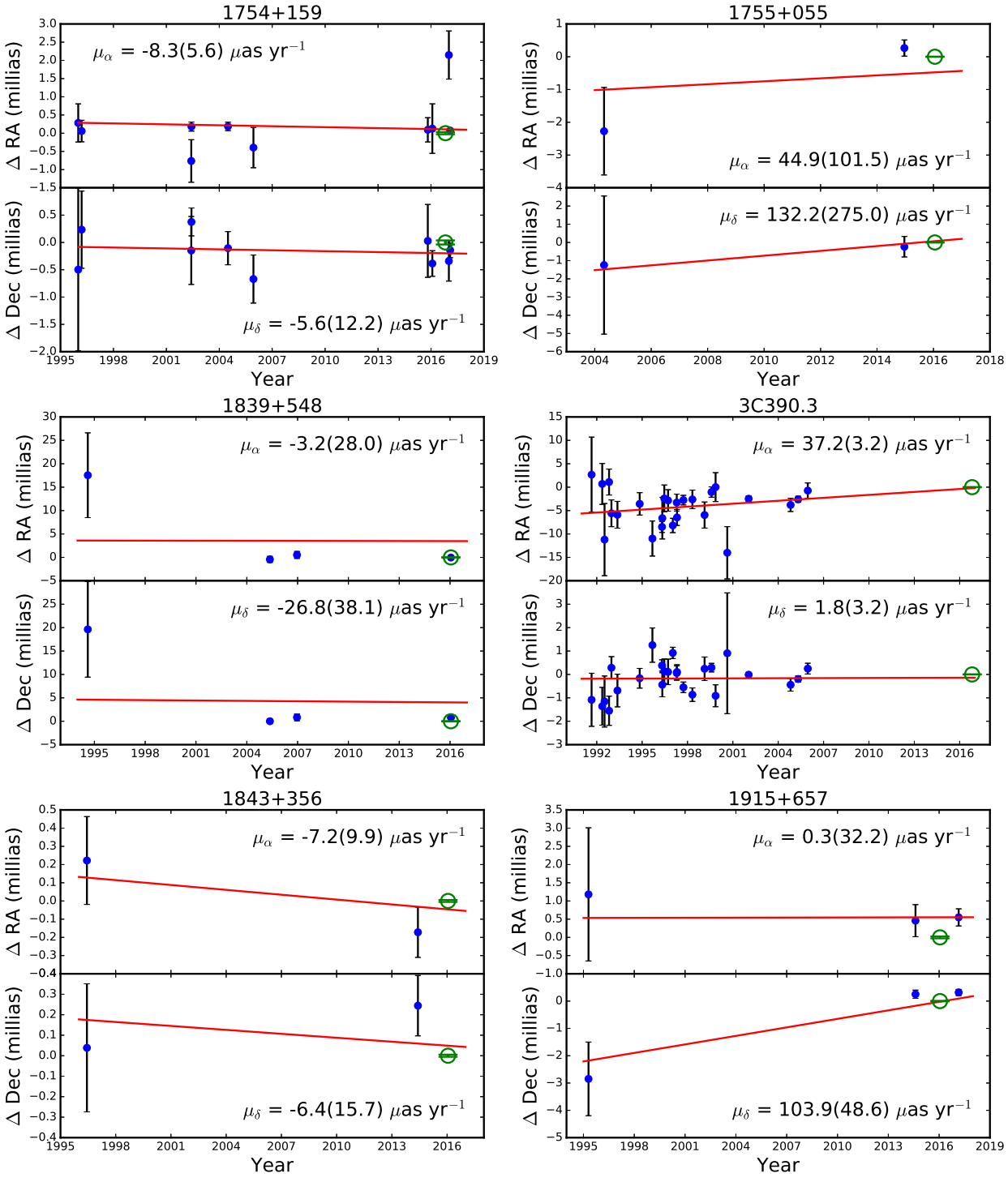
1754+159
μ_α = -8.3(5.6) μas yr^{-1}
μ_δ = -5.6(12.2) μas yr^{-1}
Δ RA (millias)
Δ Dec (millias)
Year
1755+055
μ_α = 44.9(101.5) μas yr^{-1}
μ_δ = 132.2(275.0) μas yr^{-1}
Δ RA (millias)
Δ Dec (millias)
Year
1839+548
μ_α = -3.2(28.0) μas yr^{-1}
μ_δ = -26.8(38.1) μas yr^{-1}
Δ RA (millias)
Δ Dec (millias)
Year
3C390.3
μ_α = 37.2(3.2) μas yr^{-1}
μ_δ = 1.8(3.2) μas yr^{-1}
Δ RA (millias)
Δ Dec (millias)
Year
1843+356
μ_α = -7.2(9.9) μas yr^{-1}
μ_δ = -6.4(15.7) μas yr^{-1}
Δ RA (millias)
Δ Dec (millias)
Year
1915+657
μ_α = 0.3(32.2) μas yr^{-1}
μ_δ = 103.9(48.6) μas yr^{-1}
Δ RA (millias)
Δ Dec (millias)
Year

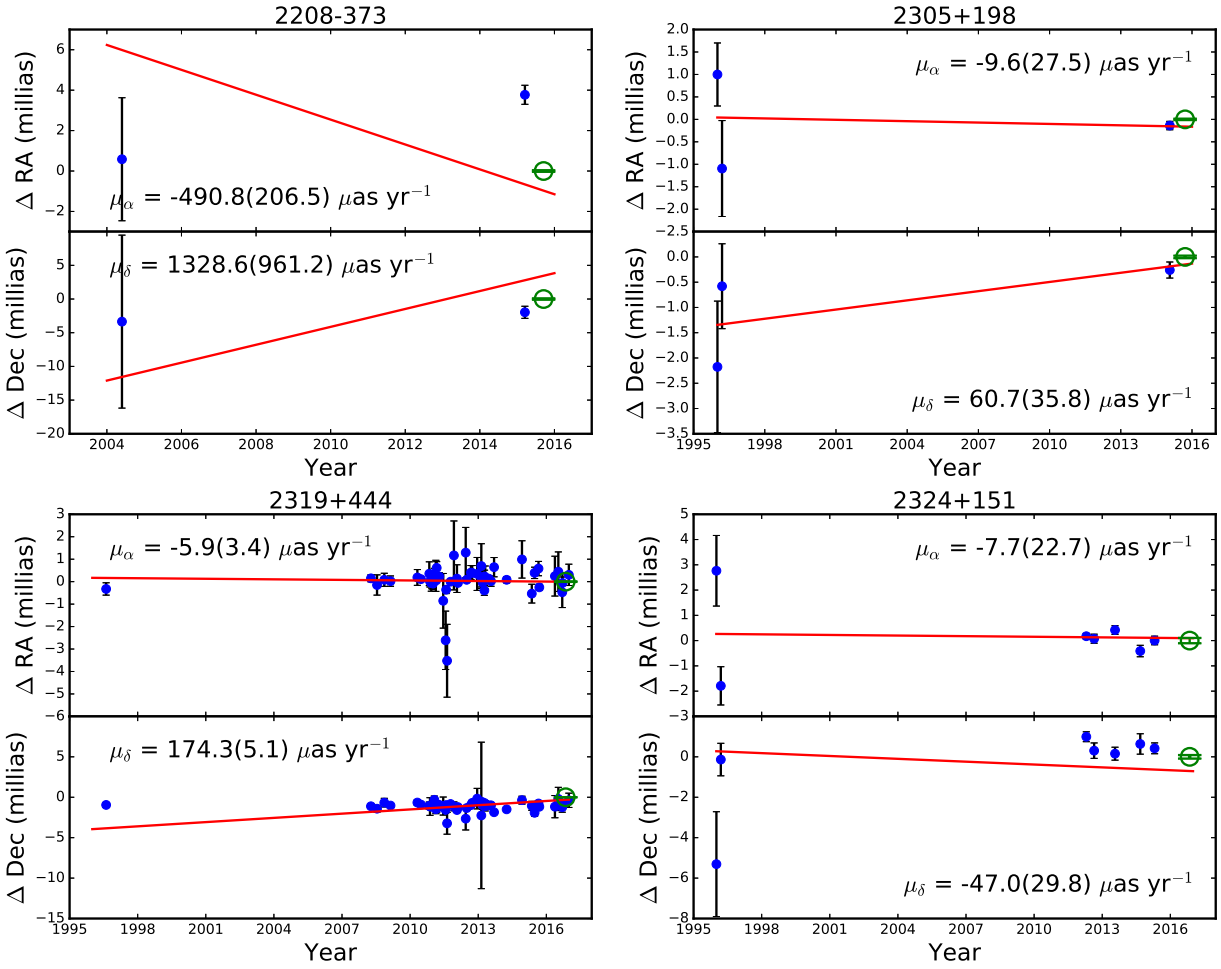

Figure 3.2 Time series for the extragalactic radio objects observed with the VLBA. The y-axis shows the change in right ascension or declination compared to the position measured from our VLBA observations. The blue points and associated error bars are from the GSFC 2017a time series. The green circle and associated error bar is our measurement of the object's radio position. The red line shows the maximum likelihood proper motion determined from the plotted points.

Table 3.1. Proper Motions Measured from VLBA Astrometry

IVS Name	RA[a] (J2000 h:m:s)	σ_α (μs)	Dec (J2000 d:m:s)	σ_δ (μas)	μ_α (μas/yr)	$\sigma_{\mu,\alpha}$ (μas/yr)	μ_δ (μas/yr)	$\sigma_{\mu,\delta}$ (μas/yr)	Phase Reference	MJD[b]
NGC0315	00:57:48.8833591	6.2	+30:21:08.8113827	94.8	2.1	5.1	-29.0	5.9	NGC0262	57700.0
0111+021	01:13:43.1449347	13.0	+02:22:17.3166440	272.5	3.0	2.4	-3.1	3.7	0056-001	57700.0
0116+319	01:19:35.0033968	8.0	+32:10:50.0580430	170.7	-77.7	189.4	257.0	169.4	0134+311	57700.0
0216+011	02:19:07.0245145	0.6	+01:20:59.8659918	10.0	3.0	6.7	3.2	15.1	0215+015	57282.0
0241+622	02:44:57.6966670	3.5	+62:28:06.5156963	29.8	-35.0	17.3	9.2	14.8	0302+625	57700.0
NGC1218	03:08:26.2238192	3.3	+04:06:39.3009211	102.3	15.9	4.2	6.2	8.2	0256+075	57700.0
0415+379	04:18:21.2772429	4.1	+38:01:35.8014697	44.6	-13.6	4.9	58.5	5.8	0420+417	57700.0
0651+410	06:55:10.0247270	0.3	+41:00:10.1598403	2.6	-3.4	3.8	-6.5	6.4	0642+449	57688.5
0836+182	08:39:30.7214128	4.6	+18:02:47.1430822	179.0	39.4	9.6	24.9	18.3	0839+187	57688.5
M81	09:55:33.1730490	1.3	+69:03:55.0606048	10.0	-5.4	2.3	-19.2	2.0	0954+658	57688.5
1013+127	10:15:44.0233882	44.5	+12:27:07.0703636	174.7	-10.2	7.3	11.8	13.2	1023+131	57688.5
MRK180	11:36:26.4084426	6.2	+70:09:27.3074967	29.8	11.1	8.0	28.1	7.2	1104+728	57688.5
NGC3862	11:45:05.0090524	1.7	+19:36:22.7412565	19.7	5.2	5.4	-2.0	10.8	1147+245	57688.5
1144+352	11:47:22.1305586	0.4	+35:01:07.5224176	10.0	14.9	12.5	-12.1	14.8	1128+385	57688.5
1145+268	11:47:59.7639062	1.7	+26:35:42.3324168	19.7	3.5	3.2	-7.4	4.8	1147+245	57688.5
NGC4261	12:19:23.2160634	0.6	+05:49:29.7000238	15.8	-8.8	18.8	31.5	22.0	1219+044	57688.5
M84	12:25:03.7432602	0.3	+12:53:13.1385898	5.6	-82.9	3.5	-51.2	9.5	3C274	57688.5
1232+366	12:35:05.8064618	0.8	+36:21:19.3212954	11.1	1.1	14.4	-7.4	18.1	1226+373	57286.0
1304-318	13:07:15.1788254	1.2	-32:07:58.64190010	27.4	-37.3	36.2	186.3	99.4	1313-333	57286.0
1306+360	13:08:23.7091270	3.6	+35:46:37.1639510	158.7	-7.6	3.6	9.6	5.9	OP326	57688.5
1424+240	14:27:00.3917388	6.1	+23:48:00.0371945	115.9	-15.7	6.3	13.4	10.4	1417+273	57688.5
NGC5675	14:32:39.8296178	2.7	+36:18:07.9320926	40.8	3.9	11.8	-48.3	21.2	1424+366	57688.5
1441+522	14:43:02.7606725	0.3	+52:01:37.2986544	3.1	16.2	31.2	30.8	55.0	1418+546	57286.0
1456+044	14:58:59.3562109	0.6	+04:16:13.8209655	8.3	-1.5	3.5	61.9	5.5	1502+036	57688.5
1623+578	16:24:24.8075814	1.2	+57:41:16.2810578	11.2	18.0	3.4	20.3	3.6	1637+574	57688.5
1625+582	16:26:37.2365501	1.1	+58:09:17.6680805	13.1	-14.8	36.2	110.6	69.3	1637+574	57286.0
1716+686	17:16:13.9380456	1.9	+68:36:38.7449705	10.1	11.5	6.8	4.4	11.7	1642+690	57406.5
1726+769	17:23:59.4451145	0.6	+76:53:11.5518107	2.0	3.7	8.3	7.4	12.1	1803+784	57406.5
1721-146	17:24:46.9665661	0.4	-14:43:59.76127900	11.4	-10.8	13.0	11.2	27.9	NRAO530	57406.5
1727+502	17:28:18.6240785	0.5	+50:13:10.4710557	5.8	70.8	10.9	64.8	10.4	1726+455	57688.5
1754+159	17:56:33.7256016	1.9	+15:53:43.8331315	37.4	-8.3	5.6	-5.6	12.2	1754+155	57688.5
1755+055	17:57:58.8251366	0.2	+05:31:48.0238501	3.6	44.9	101.5	132.2	275.0	1749+096	57406.5
1839+548	18:40:57.3766918	1.0	+54:52:15.9099683	10.9	-3.2	28.0	-26.8	38.1	1823+568	57406.5

Table 3.1 (cont'd)

IVS Name	RA[a] (J2000 h:m:s)	σ_α (μs)	Dec (J2000 d:m:s)	σ_δ (μas)	μ_α (μas/yr)	$\sigma_{\mu,\alpha}$ (μas/yr)	μ_δ (μas/yr)	$\sigma_{\mu,\delta}$ (μas/yr)	Phase Reference	MJD[b]
3C390.3	18:42:08.9901326	0.8	+79:46:17.1283321	2.3	37.2	3.2	1.8	3.2	1803+784	57688.5
1843+356	18:45:35.1088536	0.4	+35:41:16.7261975	5.3	-7.2	9.9	-6.4	15.7	1846+322	57406.5
1915+657	19:15:23.8190341	1.8	+65:48:46.3878479	9.5	0.3	32.2	103.9	48.6	1842+681	57406.5
2208-373	22:11:50.5258764	2.5	-37:07:04.97856310	97.4	-490.8	206.5	1328.6	961.2	2220-351	57282.0
2305+198	23:08:11.6364805	1.0	+20:08:42.1954031	25.0	-9.6	27.5	60.7	35.8	2250+194	57282.0
2319+444	23:22:20.3580790	0.7	+44:45:42.3545965	9.8	-5.9	3.4	174.3	5.1	2309+454	57700.0
2324+151	23:27:21.9660414	7.0	+15:24:37.3104954	87.0	-7.7	22.7	-47.0	29.8	2328+107	57700.0

[a]J2000 average positions derived from the two epochs of CLEANed VLBA images.

[b]Average Mean Julian Date of the two observation epochs.

Chapter 4

The VLBA Extragalactic Catalog and a Measurement of the Secular Aberration Drift

This chapter reproduces Sections 1 and 4 – 6 of Truebenbach & Darling (2017). Reproduced with permission of the AAS.

4.1 Context

We present a catalog of extragalactic proper motions created using archival VLBI data and our own VLBA astrometry. The catalog contains 713 proper motions, with average uncertainties of ~ 24 μas yr^{-1}, including 40 new or improved proper motion measurements using relative astrometry with the VLBA. The observations were conducted in X-band and yielded positions with uncertainties ~ 70 μas. We add 10 new redshifts using spectroscopic observations taken at Apache Point Observatory and Gemini North. With the VLBA Extragalactic Proper Motion Catalog, we detect the secular aberration drift – the apparent motion of extragalactic objects caused by the solar system's acceleration around the Galactic center – at a 6.3σ significance. We model the aberration drift as a spheroidal dipole, with the square root of the power equal to 4.89 ± 0.77 μas yr^{-1}, an amplitude of 1.69 ± 0.27 μas yr^{-1}, and an apex at $(275.2 \pm 10.0^\circ, -29.4 \pm 8.8^\circ)$. Our dipole model detects the aberration drift at a higher significance than some previous studies (e.g., Titov & Lambert 2013), but at a lower amplitude than expected or previously measured. The full aberration drift may be partially removed by the no-net-rotation constraint used when measuring archival

extragalactic radio source positions. Like the cosmic microwave background dipole, which is induced by the observer's motion, the aberration drift signal should be subtracted from extragalactic proper motions in order to detect cosmological proper motions, including the Hubble expansion, long-period stochastic gravitational waves, and the collapse of large-scale structure.

4.2 Introduction

Observations of extragalactic radio sources have been conducted with Very Long Baseline Interferometry (VLBI) since the 1970s with the purpose of measuring the Earth's orientation and monitoring the terrestrial and celestial reference frames. These observations have been conducted primarily by the United States Navy and the National Aeronautic and Space Administration (NASA), and, since 1998, have been coordinated by the International VLBI Service for Geodesy and Astrometry (IVS; Schlüter & Behrend 2007). By measuring group delays – the difference in arrival times of radio wave packets – at widely separated radio antennas, VLBI experiments can produce radio positions typically with milliarcsecond precision or better. These positions are used to determine the International Celestial Reference System (ICRS), a barycentric reference system standardized by the International Astronomical Union (IAU). Currently, the ICRS is defined by the second realization of the International Celestial Reference Frame (ICRF2; Ma et al. 1998; IERS Technical Note No. 35 2009). ICRF2 contains 3414 total sources, including 295 "defining" sources whose positions are used to fix the axes of the ICRS.

When point-like extragalactic radio sources such as quasars were selected to anchor the ICRF, it was assumed that these sources are approximately fixed on the sky and exhibit no measurable proper motion. However, as the precision of VLBI measurements have improved, it has become clear that quasars are *not* fixed over human timescales and have proper motions on the order of microarcseconds to milliarcseconds (e.g., Eubanks 1997; Gwinn et al. 1997; Feissel & Gontier 2000). The intrinsic radio proper motion of a quasar is predominately

due to the motion of plasma in relativistic jets produced by the quasars (e.g., Fey et al. 1997). These intrinsic proper motions are random in orientation on the sky. Quasars also show correlated proper motions from cosmological effects (e.g., Gwinn et al. 1997; Quercellini et al. 2009; Nusser et al. 2012; Darling 2013), as well as from observer-induced signatures such as the secular aberration drift (e.g., Fanselow 1983; Bastian 1995; Eubanks et al. 1995; Sovers et al. 1998; Mignard 2002; Kovalevsky 2003; Kopeikin & Makarov 2006; Titov et al. 2011; Titov & Lambert 2013; Xu et al. 2012, 2013). Both cosmological and observer-induced proper motions are often much smaller than the quasars' intrinsic proper motions, but the correlated nature of these effects allows a statistical detection if the sample size is large enough. Using a large sample of extragalactic proper motions, it is possible to obtain geometrical distances independent of canonical cosmological distance ladders (e.g., Ding & Croft 2009; Broderick et al. 2011), to measure or constrain the deflection of quasar light by a primordial gravitational wave background spanning $10^{-18} - 10^{-8}$ Hz (Gwinn et al. 1997; Book & Flanagan 2011), to test the isotropy of Hubble expansion (Darling 2014), and to measure the collapse of large-scale structure (e.g., Quercellini et al. 2009; Nusser et al. 2012; Darling 2013).

The secular aberration drift is an observer-induced effect caused by the acceleration of the solar system around the Galactic center. The observed signal can be modeled as a curl-free dipole with an apex at the Galactic center (266.4°, -28.9°) and has been detected by Titov et al. (2011) and confirmed by Xu et al. (2012), Titov & Lambert (2013) (hereafter TL13), and Xu et al. (2013). Using proper motions of masers associated with young massive stars, Reid et al. (2009) created a model of the Galactic plane to measure that the solar system is 8.4 ± 0.6 kpc from the Galactic center and has a barycentric circular rotation speed of 254 ± 16 km s^{-1}. This yields an acceleration of 0.79 ± 0.11 cm s^{-1} yr^{-1} and a dipole amplitude of 5.40 ± 0.78 μas yr^{-1}. In previous studies, extragalactic proper motions have been used to measure a solar acceleration of 0.93 ± 0.11 cm s^{-1} yr^{-1} (dipole amplitude of 6.4 ± 1.1 μas yr^{-1}; TL13) and 0.85 ± 0.05 cm s^{-1} yr^{-1} (dipole amplitude of 5.8 ± 0.3 μas

yr^{-1}; Xu et al. 2013).

Although the secular aberration drift signal is small compared to typical extragalactic proper motions, it is important that it be well measured. The detection of the secular aberration drift will give an independent estimate of the solar acceleration without reliance on Galactic objects. If not corrected for in geodetic experiments, the drift can cause a deformation of the celestial reference frame axes, which can lead to inaccurate estimates of other geodetic parameters (Titov 2010). Additionally, the secular aberration drift must be removed from extragalactic proper motions in order to detect and measure cosmological effects.

In this paper, we present the VLBA Extragalactic Proper Motion Catalog containing 713 proper motions created using ~ 30 years of archival VLBI data and our own NRAO Very Long Baseline Array (VLBA) observations. We then use the catalog to measure the secular aberration drift as a means of demonstrating one of the uses of a large, precise catalog of extragalactic proper motions. This catalog is 66% larger than previous catalogs used to measured the aberration drift – TL13 use 429 quasars – due both to geodetic VLBI observations conducted in the intervening years and to the addition of our own astrometric observations. In addition, we use an analytic least-squares bootstrap technique to determine the proper motions, which provides more accurate estimation of the proper motions and associated uncertainties than previous techniques. Section 4.3 presents the completed catalog, Section 4.4 measures the secular aberration drift, and Section 4.5 summarizes and suggests future additions to this work.

4.3 The VLBA Extragalactic Proper Motion Catalog

The final extragalactic proper motion catalog contains 713 proper motions. The complete catalog is shown in Appendix A. Figure 4.1 shows the sky distribution of our catalog, along with the proper motion of each object. Proper motions range from $0.01 - 1359.25$ μas yr^{-1}. On average, objects were observed for 21.9 years ($\sigma = 4.4$ years) and the proper motion

measurements were made based on an average of 249 group delays ($\sigma = 513$ delays). Figure 4.2 shows the catalog redshift distribution. The mean redshift is $z = 1.20$ and the standard deviation is $\sigma_z = 0.84$.

Figure 4.3 shows histograms of the catalog proper motions and errors, along with the equivalent histograms for the TL13 proper motion catalog. The median proper motion amplitude of our objects is 14.7 μas yr^{-1} and the standard deviation is 82.5 μas yr^{-1}. For the TL13 catalog, the median proper motion amplitude is 36.0 μas yr^{-1} with a standard deviation of 29.8 μas yr^{-1}. The large difference in standard deviations is primarily because TL13 remove large proper motions that deviate from their iteratively fit dipole by more than 7σ. For completeness, we have published all of our calculated proper motions without any clipping.

There is a large difference in the proper motion uncertainty distributions of the two catalogs – the mean proper motion uncertainty of our catalog is 26.8 μas yr^{-1}, while it is 51.8 μas yr^{-1} for the TL13 catalog. The lower uncertainty in our proper motions is due in part to the additional epochs of observations that have been added to the time series in the intervening years. It is also due to our new method of calculating the proper motions from the time series. Most curve-fitting programs use a non-linear parameter estimation, which arrives at the best-fit parameters through a series of guesses. Then the uncertainties of the best-fit parameters are estimated using a similar iterative approach. Instead of using this approximate technique, we derived the analytic equations for the maximum likelihood estimators. By directly calculating the best-fit line to the time series using an analytic calculation, we are also able to directly calculate the uncertainties of the best-fit parameters, rather than using an iterative method to approximate the uncertainties. However, due to the large variation in the uncertainties of individual positions within each time series, we report the standard deviation of a bootstrap distribution as the uncertainty of each proper motion (Section 2.1). These standard deviations are larger than the calculated uncertainties of the maximum likelihood estimators but are a better reflection of the true parameter

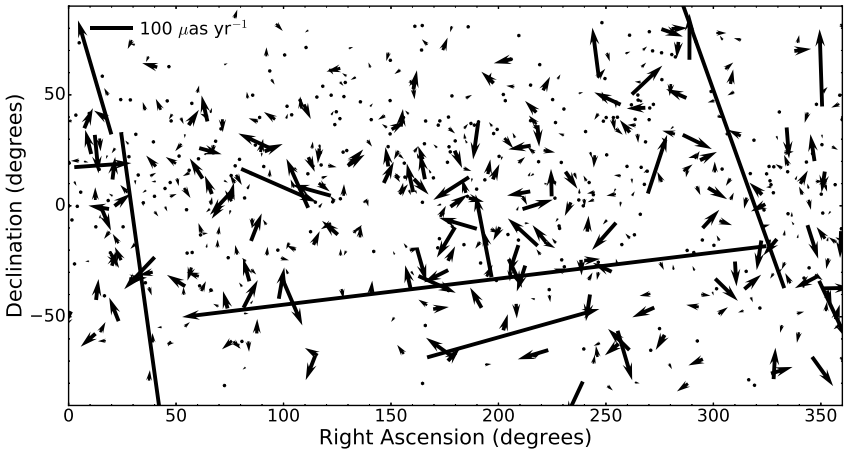

Figure 4.1 Proper motions and sky positions of all catalog objects. The arrow tails correspond to the object positions. A bar showing the size of a proper motion with amplitude 100 μas yr^{-1} is plotted at the top left.

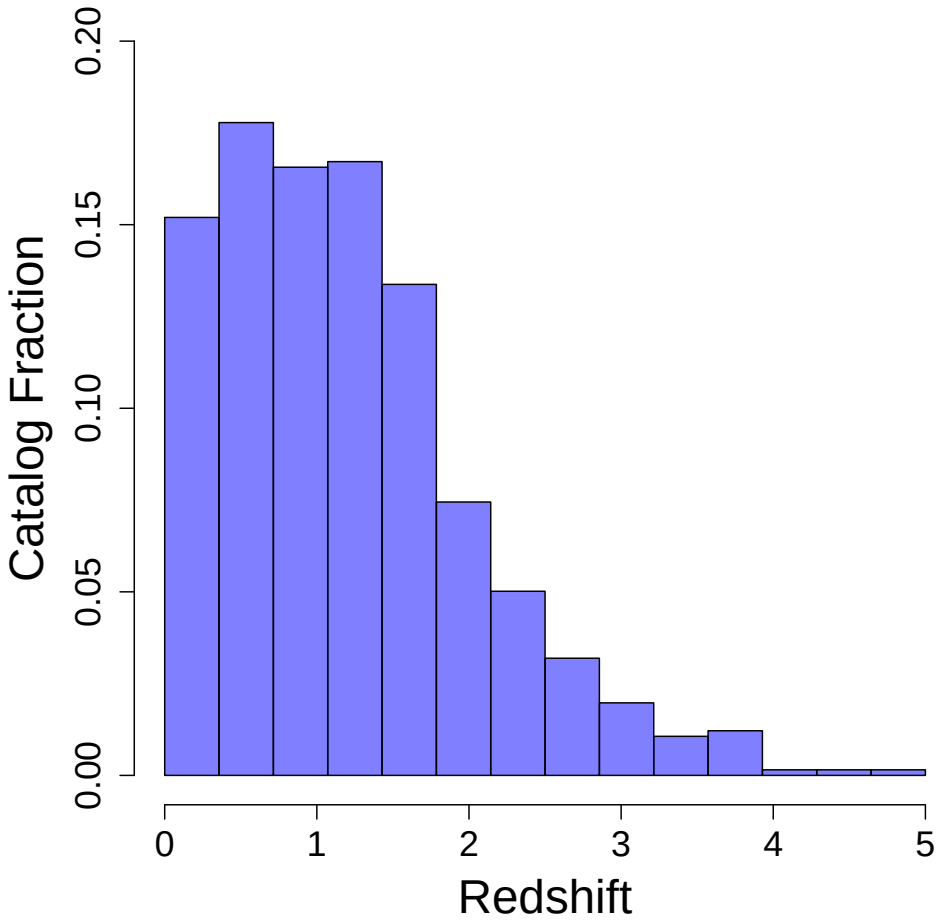

Figure 4.2 Redshift distribution of the VLBA Extragalactic Proper Motion Catalog. M81, which is blue-shifted, is excluded from the plot.

uncertainties. Despite this increase to the catalog proper motion uncertainties, our mean proper motion uncertainties remain significantly lower than those in TL13, demonstrating the significant effect our analytic calculations and additional epochs have on the proper motion uncertainties.

There are several systematic effects present in our catalog. First, there is a bias toward objects with positive declinations: 61% of the catalog objects lie above the celestial equator. This is due to the higher concentration of VLBI telescopes in the Northern Hemisphere than in the Southern Hemisphere. We find that this systematic does not have a significant effect on measuring the secular aberration drift (see Section 4.4). If this bias affected the measurement, we would expect to see a significant deviation in declination of the dipole apex from its expected location at the Galactic center. Section 4.4.1 shows that this is not the case and that our fitted apex is within 1σ of the Galactic center.

Second, the declination proper motions and associated uncertainties are systematically larger than those in right ascension. Figure 4.4 shows histograms illustrating this bias. The majority of our catalog was created using geodetic experiments conducted with the VLBA, which is more than twice as long in longitude than it is in latitude (East to West the VLBA is ~ 8600 km and North to South it is ~ 3400 km), causing the primary telescope beam to be an ellipse that is, on average, longer in declination than in right ascension. Thus, the ellipticity of the primary beam allows right ascensions to be measured more precisely than declinations for most point-like objects.

4.4 Secular Aberration Drift

Following the formalism in Mignard & Klioner (2012), the secular aberration drift can be expressed as the curl-free portion of a first-order vector spherical harmonic, resembling an electric (E) field dipole. The extragalactic proper motions due to the drift can then be

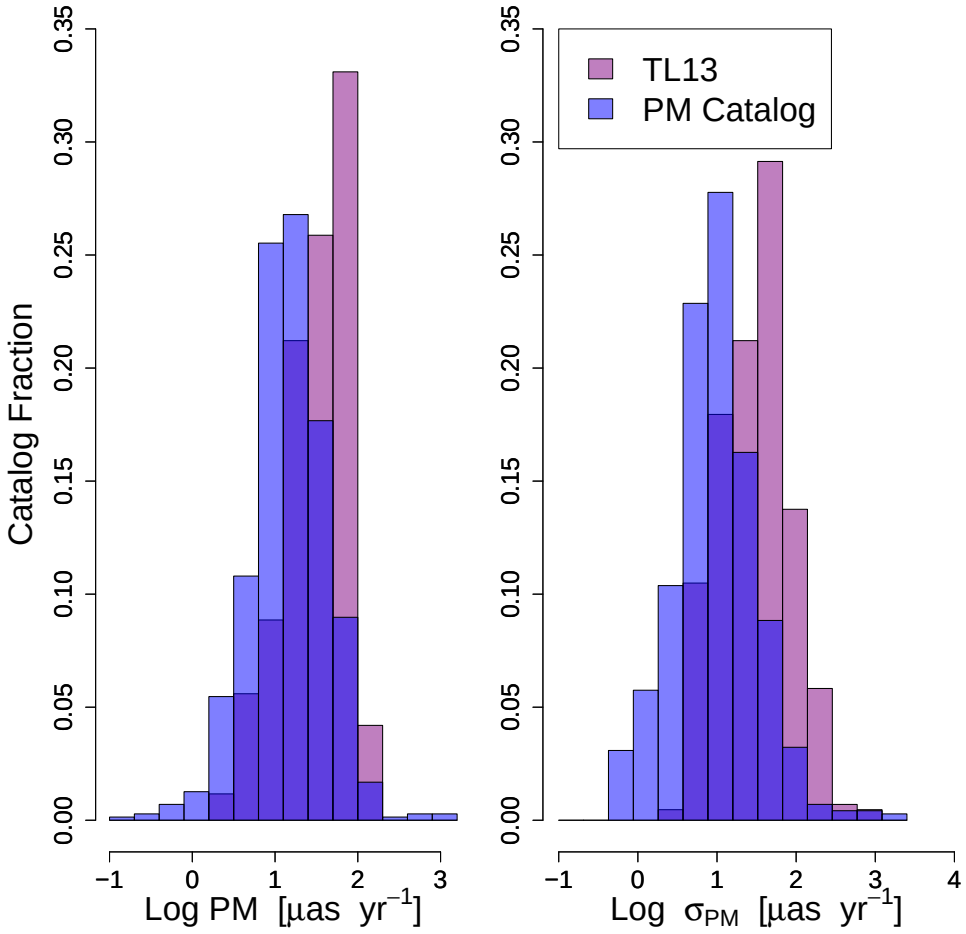

Figure 4.3 Proper motion amplitudes and associated uncertainties for our catalog (blue) and TL13 (purple). In both catalogs, the proper motions in right ascension and declination are calculated separately for each object, but here we show the total proper motion amplitude for illustrative purposes.

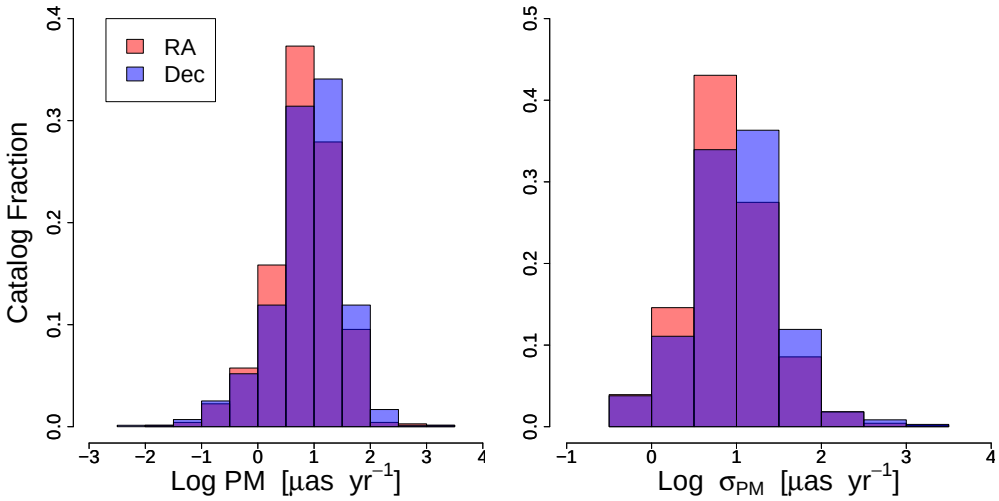

Figure 4.4 Proper motions and associated uncertainties for our catalog in right ascension (red) and declination (blue). The declination proper motions and uncertainties are systematically larger than those in right ascension.

expressed as an E-mode dipole as a function of sky position (α,δ) by

$$\mu_\alpha = \frac{1}{2}\sqrt{\frac{3}{\pi}}\ \left(s_{11}^{Re}\sin\alpha + s_{11}^{Im}\cos\alpha\right) \tag{4.1}$$

and

$$\mu_\delta = \frac{1}{2}\sqrt{\frac{3}{\pi}}\ \left(s_{10}\sqrt{\frac{1}{2}}\cos\delta + s_{11}^{Re}\cos\alpha\sin\delta - s_{11}^{Im}\sin\alpha\sin\delta\right), \tag{4.2}$$

where s_{lm} are the amplitudes of the "spheroidal" E-mode vector spherical harmonics of degree l and order m. These can be converted to the d_1, d_2, and d_3 amplitudes used in TL13 by

$$\begin{pmatrix} d_1 \\ d_2 \\ d_3 \end{pmatrix} = 2\sqrt{\frac{\pi}{3}}\ \begin{pmatrix} -\,s_{11}^{Re} \\ s_{11}^{Im} \\ \sqrt{2}\ s_{10} \end{pmatrix}. \tag{4.3}$$

In addition, a divergence-free first-order vector spherical harmonic, resembling a magnetic (B) field dipole can also be fit to the extragalactic proper motions using the equations

$$\mu_\alpha = \frac{1}{2}\sqrt{\frac{3}{\pi}}\ \left(t_{10}\sqrt{\frac{1}{2}}\cos\delta + t_{11}^{Re}\cos\alpha\sin\delta - t_{11}^{Im}\sin\alpha\sin\delta\right) \tag{4.4}$$

and

$$\mu_\delta = \frac{1}{2}\sqrt{\frac{3}{\pi}}\ \left(-t_{11}^{Re}\sin\alpha - t_{11}^{Im}\cos\alpha\right), \tag{4.5}$$

where t_{lm} are the "toroidal" B-mode vector spherical harmonic amplitudes and the conversion between these and the toroidal amplitudes used in TL13 is

$$\begin{pmatrix} r_1 \\ r_2 \\ r_3 \end{pmatrix} = 2\sqrt{\frac{\pi}{3}}\ \begin{pmatrix} t_{11}^{Re} \\ -\,t_{11}^{Im} \\ -\sqrt{2}\ t_{10} \end{pmatrix}. \tag{4.6}$$

4.4.1 Data Processing and Results

We simultaneously fit the E- and B-mode dipoles to our extragalactic proper motions using a Markov Chain Monte Carlo (MCMC) Bayesian sampling of the posterior probability

distribution function with the Python package `lmfit`[1] (Newville et al. 2014). The probability distributions for each dipole parameter are estimated through sampling of the log-likelihood functions where we assume the coefficients are drawn from a Gaussian distribution. Table 4.1 lists the maximum likelihood solution for each dipole E- and B-mode vector spherical harmonic coefficient and the 68% confidence interval spread of the probability distributions in both the spherical harmonic formalism and the TL13 formalism. Figure 4.5 shows the maximum likelihood secular aberration drift (E-mode dipole) model and Figure 4.6 shows the estimated posterior probability distributions. We detect the secular aberration drift at a 6.3σ significance level, with the square root of the power equal to 4.89 ± 0.77 μas yr^{-1}, an amplitude of 1.69 ± 0.27 μas yr^{-1}, and an apex of $(275.2 \pm 10.0^{\circ}, -29.4 \pm 8.8^{\circ})$. The apex of our E-mode dipole is within 1σ of the Galactic center (266.4°, -28.9°) and the amplitude is within 5σ of the predicted amplitude of 5.40 ± 0.78 μas yr^{-1}.

We do not detect the B-mode dipole at a 2.2σ significance level. We find that including the B-mode dipole increases the significance of the E-mode dipole by $\sim 0.63\sigma$ when compared to fitting just the E-mode dipole without a rotational component. The presence of a non-significant toroidal dipole indicates that we are detecting some residual Earth rotation that is not completely removed during data processing. Table 4.2 shows the correlations between the coefficients of our fit. There is a strong correlation between several coefficients of the E- and B-modes, which accounts for the necessary inclusion of the B-mode dipole.

Before fitting, we removed all objects with proper motion amplitudes greater than 500 μas yr^{-1} (three objects). The proper motions of these outliers are likely dominated by intrinsic radio jet motions and obscure the small signal from the secular aberration drift. To ensure that our choice of proper motion cut-off did not significantly affect the resulting dipole model, we fit the E- and B-mode dipoles for a wide range of cut-off values. Figure 4.7 shows the results of this experiment for proper motion cut-offs between 5 and 50 μas yr^{-1} (in steps of 1 μas yr^{-1}). We also performed the same experiment for cut-offs between 50

[1] https://lmfit.github.io/lmfit-py/

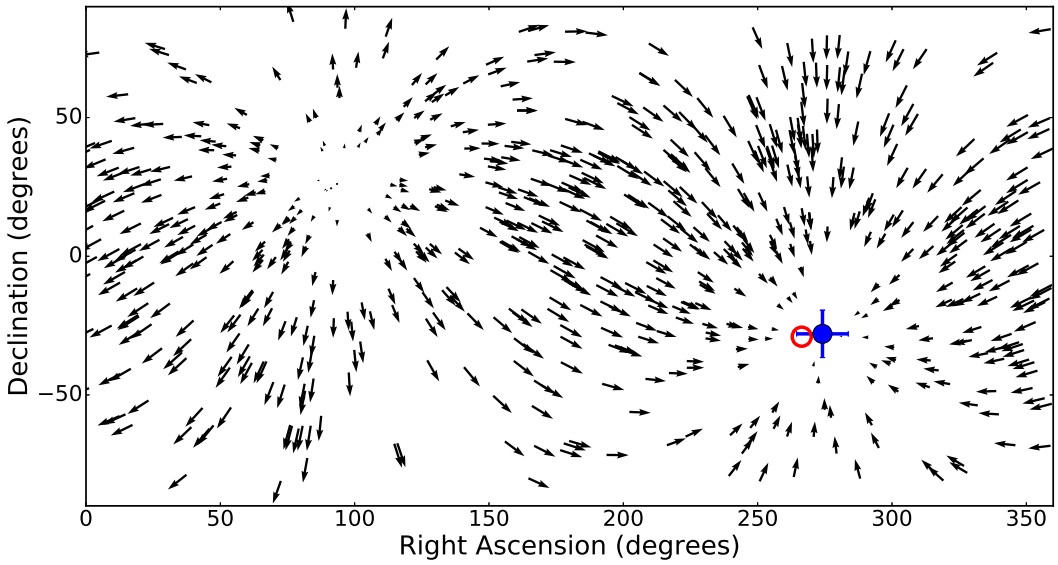

Figure 4.5 The maximum likelihood secular aberration drift (E-mode dipole) model estimated from the catalog proper motions. The apex of the dipole and its uncertainties are shown in blue, while the true location of the Galactic center is shown in red. The arrow tails correspond to the catalog object positions and the arrow amplitudes represent the modeled portion of the catalog proper motions due to the secular aberration drift.

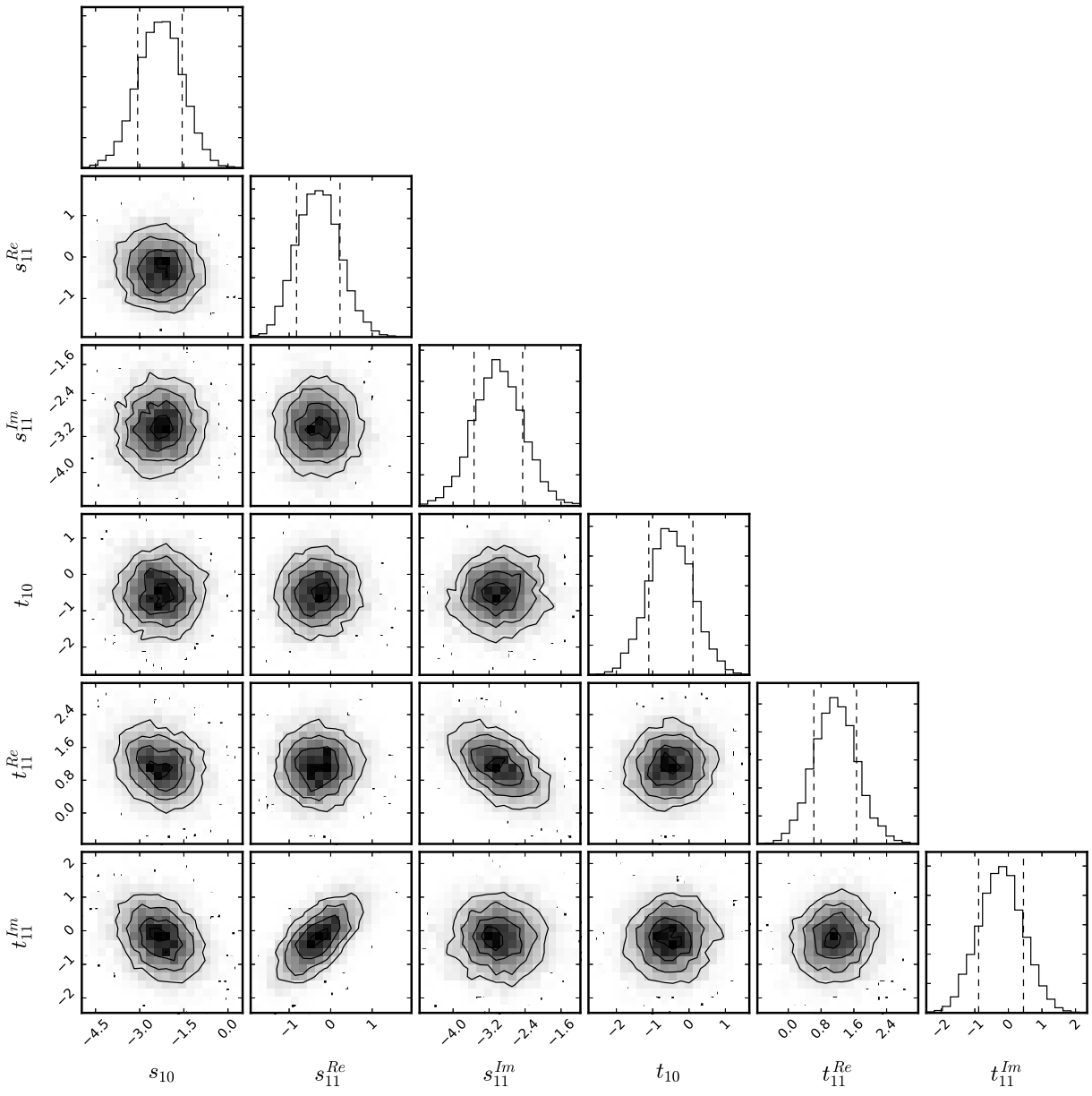

Figure 4.6 The two- and one-dimensional posterior probability distributions for the dipole coefficients plotted using the Python module `Corner` (Foreman-Mackey 2016). All coefficients are in units of μas yr^{-1}. The dashed lines on the one-dimensional histograms show the 68% confidence intervals for each parameter.

Table 4.1. Secular Aberration Drift Model

$\vec{Y}_{lm}$ Formalism[a]		TL13 Formalism[b]	
Order	Amplitude (μas yr^{-1})	Term	Amplitude (μas yr^{-1})
s_{10}	-2.40 ± 0.75	d_3	-6.94 ± 2.17
s_{11}^{Re}	-0.27 ± 0.52	$-d_1$	0.55 ± 1.06
s_{11}^{Im}	-3.00 ± 0.55	d_2	-6.13 ± 1.13
$\sqrt{P_1^s}$	4.89 ± 0.77	Amplitude	1.69 ± 0.27
t_{10}	-0.55 ± 0.59	$-r_3$	1.59 ± 1.71
t_{11}^{Re}	1.12 ± 0.54	r_1	2.29 ± 1.11
t_{11}^{Im}	-0.06 ± 0.65	$-r_2$	0.12 ± 1.33
$\sqrt{P_1^t}$	1.68 ± 0.75	Amplitude	0.58 ± 0.26
E-mode Apex	$(275.2 \pm 10.0°, -29.4 \pm 8.8°)$		

[a]Vector spherical harmonic coefficients using the formalism presented in Mignard & Klioner (2012).

[b]The same dipole model as presented in the left column, but converted into the formalism used in TL13 for comparison. See Sec. 4.4 for conversions between the two formalisms.

Note. — $\sqrt{P_1^s}$ and $\sqrt{P_1^t}$ are the square-root of the 1st order vector spherical harmonic powers. They can be converted to the TL13 amplitudes (right column) by dividing by $2\sqrt{2\pi/3}$.

Table 4.2. Correlations between Spherical Harmonic Coefficients

	B-mode Coefficients		
E-mode Coefficients	t_{10}	t_{11}^{Re}	t_{11}^{Im}
s_{10}	$\cdots$	-0.216	-0.282
s_{11}^{Re}	$\cdots$	$\cdots$	0.614
s_{11}^{Im}	$\cdots$	-0.502	$\cdots$

Note. — Unreported correlations are $<$ 0.150.

μas yr^{-1} and 1000 μas yr^{-1} (in steps of 50 μas yr^{-1}). We found that the Z-score (calculated following Mignard & Klioner (2012), Eqn. 85) is relatively constant and the fit remains statistically significant for all cut-offs greater than 9 μas yr^{-1}. Fits with cut-offs below 9 μas yr^{-1} include less than 226 proper motions and the decrease in significance can be attributed to the small number of data points. Additionally, we found that the apex remains within 2σ of the Galactic center for all cut-offs – all apex locations more than 1σ from the Galactic center were again for low cut-offs ($<$ 15 μas yr^{-1}) with a small number of data points. Combined, these factors indicate that our model of the dipole is robust and insensitive to our choice in maximum proper motion amplitude. Therefore, we chose to use a cut-off of 500 μas yr^{-1} to include the majority of the catalog in our fit.

The secular aberration drift has been measured by several previous studies, most notably TL13 and Xu et al. (2013). TL13 measured a spheroidal dipole with amplitude 6.4 ± 1.1 μas yr^{-1} pointed towards $(266 \pm 7°, -26 \pm 7°)$ and a toroidal component with amplitude 1.9 ± 0.8 μas yr^{-1}. Our model has a lower spheroidal dipole amplitude (1.7 ± 0.3 μas yr^{-1}) than that measured in TL13, making their amplitude a better match for the predicted amplitude (5.40 ± 0.78 μas yr^{-1}; see Section 4.2). However, our uncertainties are also much smaller, yielding a more significant detection. The apex of both fits are statistically consistent with the Galactic center.

One possible cause of our lower spheroidal dipole amplitude is the inclusion of a no-net-rotation (NNR) constraint in our catalog (see Section 2.1). To allow for some rotation of the radio source positions with respect to the ICRS axes, the NNR constraint was incrementally relaxed for subsets of the objects when creating the Goddard 2017a coordinate time series. On the other hand, TL13 used a more relaxed constraint that allowed sources to rotate by $<$ 2 arcseconds with respect to the ICRS axes. The difference in our E-mode amplitudes may be due, in part, to the different techniques used to handle the NNR constraint. The NNR constraint affects the toroidal dipole, which affects the spheroidal dipole because of the correlation between several of the E- and B-mode coefficients (Table 4.2). To this effect,

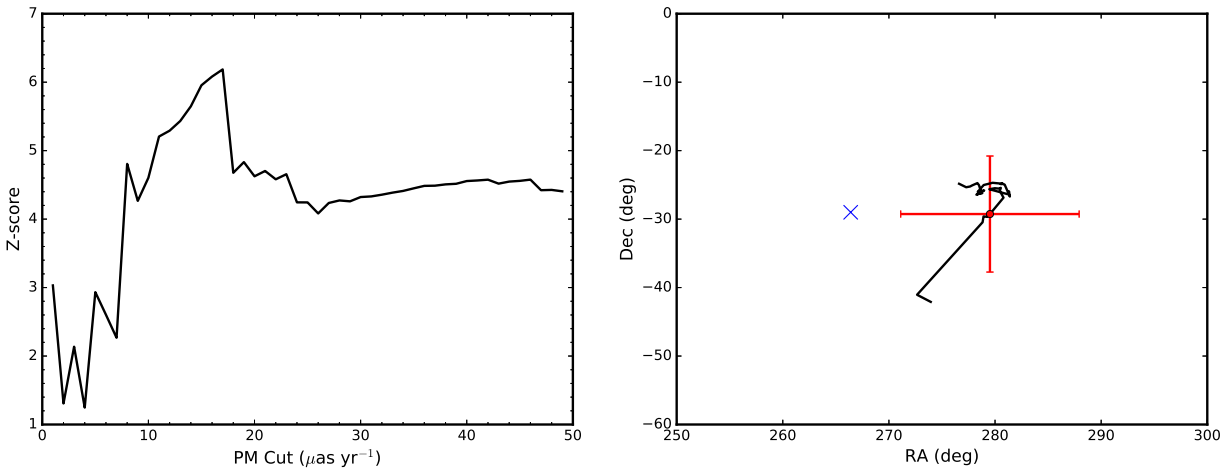

Figure 4.7 Left: The Z-score of our E-mode dipole model as a function of the maximum proper motion amplitude used in the fit. Z-score is calculated following Mignard & Klioner (2012), Eqn. 85. The fit remains significant ($> 5\sigma$) for all cut-offs greater than 9 μas yr^{-1}. Right: The location of the E-mode dipole apex of our model as a function of maximum proper motion amplitude for proper motion cut-offs between 5 and 50 μas yr^{-1} (in steps of 1 μas yr^{-1}). All apex locations are within 2σ of each other. The apex for our chosen cut-off (500 μas yr^{-1}) and its associated uncertainty is plotted in blue. The red dot marks the location of the Galactic center. Both of these plots demonstrate the robustness of our secular aberration drift model – both the location of the dipole apex and the significance of the fit are insensitive to our choice of maximum proper motion amplitude.

Titov et al. (2011) found that their spheroidal amplitude decreased and the E-mode apex shifted away from the Galactic center when sources were more closely fixed to the ICRS axes and only allowed to rotate by < 2 milliarcseconds. Our E-mode amplitude is lower than expected, but the associated apex is still in close alignment with the Galactic center, indicating that our model is only slightly affected by the NNR constraint and that the aberration drift is still detectable.

Xu et al. (2013) measured the secular aberration drift using a similar data set to TL13 but with a different estimation method. Instead of solving for individual proper motions and then fitting a dipole to these motions, Xu et al. (2013) added a three-dimensional solar acceleration vector to the global parameters in CALC/SOLVE and directly solved for this acceleration. They found a solar acceleration vector of $(7.47 \pm 0.46,\ 0.17 \pm 0.57,\ 3.95 \pm 0.47)$ mm s^{-1} yr^{-1}, which is equivalent to a dipole with root-power of 16.8 ± 0.8 μas yr^{-1} (5.8 ± 0.3 μas yr^{-1} using the convention in TL13) pointed towards $(243.0°,\ -11.5°)$. Their dipole is offset from the Galactic center by $\sim 18°$ north and $\sim 23°$ west. The offset equates to a significant acceleration component perpendicular to the Galactic plane. Our dipole model contains no significant out of plane acceleration (0.27 ± 0.51 mm s^{-1} yr^{-1}). Because our dipole apex is statistically consistent with the Galactic center, our solar acceleration vector does not contain a significant perpendicular component.

Since the secular aberration drift is a small component of the overall proper motion of many sources, there is a concern that individual large intrinsic proper motions with small uncertainties could have a significant effect on the dipole fit. Titov et al. (2011) used several subsets of their data, including only ICRF2 defining sources, sources with low structure indices, and sources with more than 1000 sessions, to assess the robustness of their fit. They found that the resulting dipole did not vary significantly for any of the data subsets. We performed a similar analysis to ensure that individual outliers in proper motion do not significantly influence our model. Figure 4.8 shows the results of a test where we clipped our data to only include objects whose proper motions were determined from a minimum

Table 4.3. Median Values of 1,000 Bootstrap Dipole Fits

	Median[a]	68% Confidence Interval
$\sqrt{P_1^s}$[b]	5.11	$3.61 - 6.71$
$\sqrt{P_1^t}$	2.85	$1.65 - 4.45$
E-mode Apex RA	284.6°	$274.1^\circ - 302.9^\circ$
E-mode Apex Dec	-29.2°	$-48.2^\circ - -9.1^\circ$

[a]All values are in units of μas yr^{-1}, except for the E-mode apex, which is in units of degrees.

[b]Square-root of the 1st order vector spherical harmonic power. Can be converted to the TL13 amplitude by dividing by $2\sqrt{2\pi/3}$.

number of observing sessions. We find that our model remains significant regardless of the number of observing sessions per object.

To further assess the effect of large intrinsic proper motions on our secular aberration drift model, we performed 1,000 bootstrap re-samplings of the fit. Table 4.4.1 lists the median values and 68% confidence intervals from the bootstrap distribution. We find a median root-power of 5.11 μas yr^{-1} with a 68% confidence interval of $3.61 - 6.71$ μas yr^{-1}. Our dipole model has a root-power of 4.89 ± 0.77 μas yr^{-1}, which is in good agreement with these values, indicating that our model is not significantly influenced by individual data points. Figure 4.9 shows the location of the E-mode apex for all bootstrap iterations. This plot demonstrates that the location of the E-mode apex is not significantly influenced by individual proper motions.

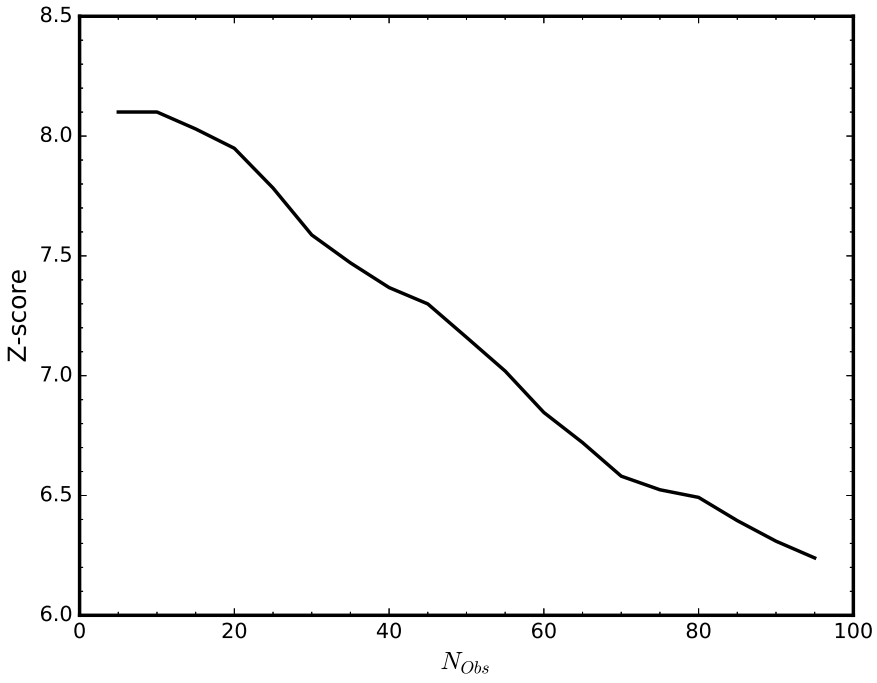

Figure 4.8 The Z-score of our E-mode dipole model as a function of the minimum number of observing sessions required for a proper motion to be included in the fit. Our model remains significant regardless of the number of observing sessions.

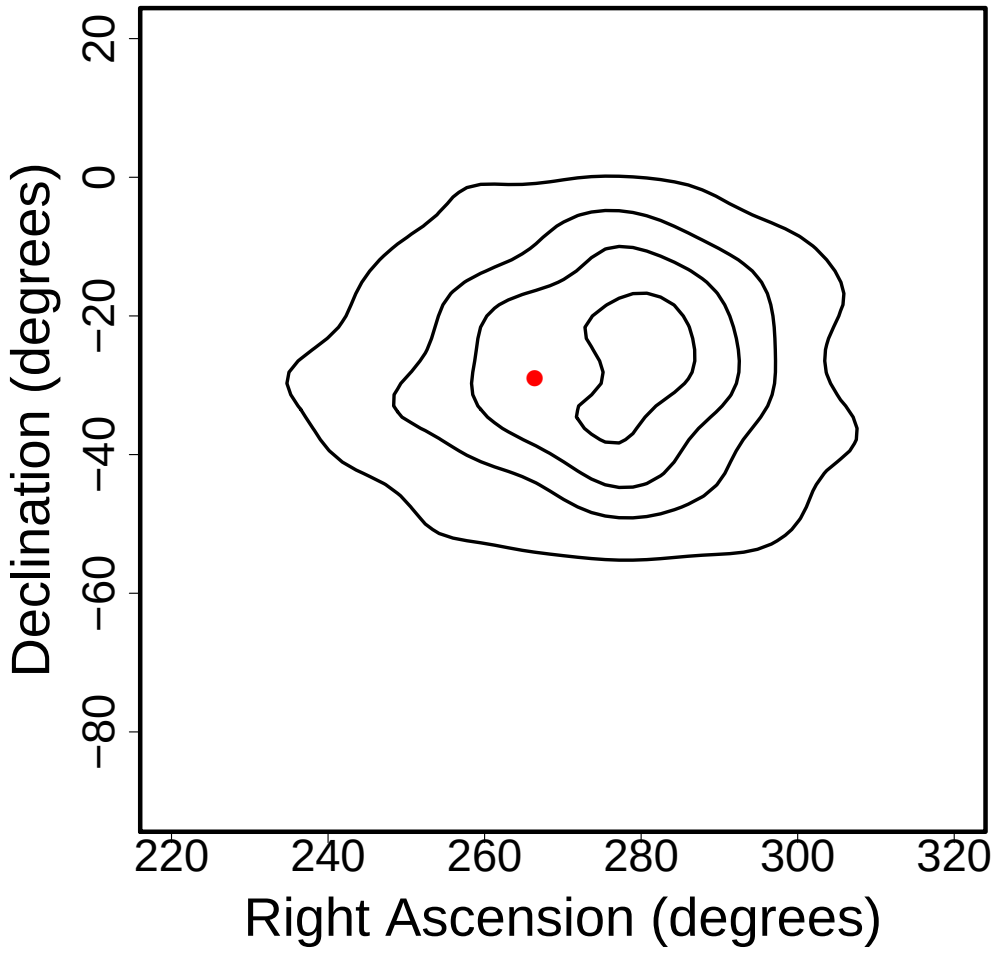

Figure 4.9 The location of the E-mode apex for each bootstrap re-sampling. The contours show the density of the bootstrap distribution. From the inner contour outward, the contours contain 10%, 30%, 60%, and 80% of the data. This shows that the apex of the E-mode dipole is insensitive to exclusion of subsets of the data. The Galactic center is marked in red.

4.5 Conclusions

In this paper we presented the VLBA Extragalactic Proper Motion Catalog containing 713 proper motions with average uncertainties of 24 μas yr^{-1}. The catalog is created primarily from archival Goddard VLBI data, with redshifts obtained from OCARS. In addition, we added or updated 40 extragalactic proper motions and 10 redshifts through our own VLBA and APO observations, respectively.

We used the resulting catalog to measure the secular aberration drift at a 6.3σ significance. An accurate measurement of the aberration drift is important so that it can be fully removed from extragalactic proper motions before using those proper motions to study cosmological effects. We detect a spherical dipole with a root-power of 4.89 ± 0.77 μas yr^{-1} and an apex at $(275.2 \pm 10.0^\circ, -29.4 \pm 8.8^\circ)$. We simultaneously fit a toroidal dipole with low significance (2.2σ) to increase the significance of the E-mode dipole. Overall, our model of the E-mode dipole proves robust to a number of tests and remains statistically significant for many subsets of the data.

Although the E-mode dipole is significant, its amplitude is much lower than expected. This difference may be caused by the NNR constraint used when the majority of our radio source positions were calculated. Even if the NNR constraint has prevented us from recovering the full dipole, our catalog can still be used for cosmological studies by removing the residual dipole.

In an upcoming paper, we subtract this dipole and use the remaining proper motions to search for relative proper motions between close separation extragalactic objects following Darling (2013). The relative proper motions of extragalactic objects contain signatures of both the Hubble expansion and the collapse of large-scale structure, enabling a detection or measurement of both effects. In a second paper, we fit a quadrupolar pattern to the catalog proper motions in order to obtain limits on the stochastic gravitational wave background (Darling et al. 2018 submitted).

With continued geodetic observations and new Goddard VLBI global solutions, the number of available extragalactic proper motions is expected to continue to increase in the coming years. Additional observing epochs of existing proper motions will also increase the overall accuracy of future catalogs. Both of these will contribute to more accurate measurements of the secular aberration drift and enable more detailed cosmological studies. In the near future, with the release of *Gaia* (Gaia Collaboration et al. 2016) proper motions, we expect to significantly expand our catalog. The *Gaia* proper motions will be less precise – astrometry of ~ 1.69 mas for objects in the secondary data set of DR1 (Lindegren et al. 2016) – than those produced by VLBI, but there will be $\sim 10^6$ new extragalactic proper motions (Robin et al. 2012). The dramatic increase in sample size should enable statistically significant detections of the secular aberration drift with relative precision of 10% (Mignard 2002) and cosmological effects despite the decrease in overall catalog proper motion accuracy. The *Gaia* proper motions will also be less affected by intrinsic proper motion, which will enable a higher significance detection of correlated motions like the secular aberration drift and cosmological effects (see Darling et al. 2018 submitted for further discussion). Additionally, the Next Generation Very Large Array (ngVLA) with VLBA baselines is expected to obtain proper motions of ~ 10 μas yr^{-1} (Bower et al. 2015). The addition of a central array with a large collecting area to be used in conjunction with the VLBA will enable rapid, high SNR detections of many radio sources within a single observing epoch and is expected to increase the number of epochs for many catalog objects, thereby increasing the overall proper motion precision of the catalog.

Chapter 5

Proper Motion Constraints on Large Scale Structure

Using the archival VLBI data and new optical and radio interferometry observations described in Chapters 2 and 3, we created the VLBA Extragalactic Proper Motion Catalog (presented in Chapter 4 and published in Truebenbach & Darling 2017). The catalog contains 713 proper motions, 596 of which have well measured redshifts. In this chapter, we removed the secular aberration drift signal measured in Truebenbach & Darling (2017) and used the residual proper motions to measure the pairwise proper motion for all catalog objects with physical separations less than 1500 comoving Mpc. We find a 3σ limit on the convergence rate of gravitationally-interacting objects with physical separations less than 100 Mpc of > -17.4 μas yr^{-1}. We also find that large-separation pairs (> 800 Mpc) are consistent with the expected null signal of Hubble expansion to within ~ 2.3 μas yr^{-1}. Finally, we created a simulated *Gaia* catalog with predicted end-of-mission proper motion uncertainties to test the significance at which *Gaia* proper motions will be able to detect the convergence of large-scale structure. We find that *Gaia* will detect the relative peculiar velocity of extragalactic objects caused by the mass distribution of large-scale structure on length scales < 50 Mpc (comoving) at a significance $> 9.8\sigma$. The shape and magnitude of the measured correlation of close-separation pairs with *Gaia* will constrain the mass power spectrum and provide a "distance ladder" independent verification of cosmological parameters that are derived from line-of-sight velocity surveys that rely on precise distance measurements.

We assume $H_0 = 70$ km s^{-1} Mpc^{-1} and a flat cosmology with $\Omega_\Lambda = 0.73$ and $\Omega_M =$

0.27.

5.1 Theoretical Predictions

The mass density distribution of large-scale structure (LSS) can be used to measure cosmological parameters, including the baryon and neutrino density (e.g., Eisenstein & Hu 1999; Eisenstein et al. 2005) and the spatial curvature (e.g., Eisenstein et al. 2005; Planck Collaboration et al. 2016d) through comparison of the observed distribution to that predicted by cosmological simulations. The observed LSS distribution is typically measured through redshift maps of visible galaxies (e.g., de Lapparent et al. 1986; York et al. 2000; Gott et al. 2005) or through line-of-sight peculiar velocity maps (e.g., Tully et al. 2014). However, both of these methods require redshifts or other model-dependent distance measures to either spatially place the galaxies or to translate the spectroscopic line shifts to peculiar velocities.

Extragalactic proper motions are an orthogonal measurement to line-of-sight velocities that do not require distances to measure the distribution of LSS. While line-of-sight velocities use distances to differentiate Hubble expansion from peculiar velocity, peculiar proper motions across the line-of-sight are separable from the Hubble expansion because gravitationally non-interacting objects entrained in the Hubble flow are expected to show no relative proper motion (Nusser et al. 2012; Darling 2013). Recall from Section 1.3.1 that for a "pair" of extragalactic objects[1] at the same angular diameter distance D_A, the relative proper motion of the two objects along a great circle, $\dot{\theta}$, is the fractional change in their angular separations –

$$\frac{\dot{\theta}}{\sin\theta} = \frac{-\dot{D_A}}{D_A} + \frac{\dot{l}}{l} = \frac{-H(z)}{1+z} + \frac{\dot{l}}{l}, \tag{5.1}$$

where

$$H(z) = H_0\sqrt{\Omega_{M,0}(1+z)^3 + \Omega_\Lambda}, \tag{5.2}$$

θ is the angular separation of the objects, l is the proper length separating the pair, $\dot{D_A}$ is

[1] "Pair" signifies any two randomly selected objects and does not denote any association between the two objects.

the change in angular diameter distance with time, and $\dot{l}$ is the change in proper length with time (Darling 2013).

If the pair of extragalactic objects are far enough apart that they do not interact gravitationally, then the space between the objects will expand with the Hubble expansion and no proper motion will be expected in a homogeneous expansion (see Eqn 1.32). On the other hand, if the objects are part of a static, gravitationally-bound structure (e.g., a virialized cluster), then $\dot{l}/l = 0$ and the objects will appear to contract as they move away from us with the Hubble flow. For objects at $z = 0$, static structures with no peculiar velocity will show a contraction of -15 μas yr^{-1}.

In reality, the majority of close physical separation pairs will show a relative proper motion that is a combination of the two signals; the pair will appear to converge as it moves away from us with the Hubble flow and it will have relative proper motion determined by the objects' gravitational interactions with their local mass density distribution. The average expected pair proper motion can be calculated using a two-point correlation statistic and a theoretical mass power spectrum. For a pair of objects with transverse velocities $\vec{v}_{\perp,1}$ and $\vec{v}_{\perp,2}$, respectively, we define a two-point correlation statistic,

$$\xi_{v,\perp}(\vec{x}_1, \vec{x}_2) = \langle (\vec{v}_{\perp,1} \cdot \hat{x})(\vec{v}_{\perp,2} \cdot \hat{x}) \rangle, \tag{5.3}$$

where $\vec{x}_1$ and $\vec{x}_2$ are the radial vectors to the objects and $\hat{x}$ is the unit space vector connecting the two radial vectors (Darling & Truebenbach 2018 in prep). To relate this statistic to the mass density of LSS, we assume linear growth of density perturbations $\delta = \delta\rho/\rho$. In the linear regime, peculiar velocity at low redshifts can be expressed in wavenumber $\vec{k}$ space as Fourier components

$$\vec{v}(\vec{k}) = i f H_0 \; \delta(\vec{k}) \frac{\vec{k}}{k^2}, \tag{5.4}$$

where f is the dimensionless linear growth rate approximated by $f = \Omega_m^{-0.6}$.

Following a similar derivation for line-of-sight peculiar velocities in Dodelson (2003),

Darling & Truebenbach (2018 in prep) find

$$\xi_{v,\perp}(\vec{x}_1,\vec{x}_2) = -f^2 H_0^2 \left(\sin^2\theta_1 \sin^2\theta_2 \int_0^\infty \frac{dk}{2\pi^2}\ P(k)\ j_0''(kx) \right. \\ \left. + \frac{1}{4}\sin 2\theta_1 \sin 2\theta_2 \int_0^\infty \frac{dk}{2\pi^2}\ P(k)\ \frac{j_0'(kx)}{kx} \right), \quad (5.5)$$

where $j_0(kx) = \sin(kx)/kx$ is the $l = 0$ spherical Bessel function and $j_0'(kx)$ and $j_0''(kx)$ are its first and second derivatives with respect to kx. $P(k)$ is the mass power spectrum in wavenumber space, $\cos\theta_1 = -\hat{x}_1 \cdot \hat{x}$, and $\cos\theta_2 = -\hat{x}_2 \cdot \hat{x}$. For pairs with small physical separations, distances will be similar. In the case where $|\vec{x}_1| = |\vec{x}_2|$, Equation 5.5 simplifies to

$$\xi_{v,\perp}(\vec{x}_1,\vec{x}_2) = -f^2 H_0^2 \left(\cos^4\frac{\Delta\theta}{2} \int_0^\infty \frac{dk}{2\pi^2}\ P(k)\ j_0''(kx) - \frac{1}{4}\sin^2\Delta\theta \int_0^\infty \frac{dk}{2\pi^2}\ P(k)\ \frac{j_0'(kx)}{kx} \right), \quad (5.6)$$

where $\Delta\theta = \theta_1 - \theta_2$ (Darling & Truebenbach 2018 in prep). Figure 5.1 shows Equation 5.6 – the two-point correlation statistic for close-separation pairs – as a function of comoving physical separation for a range of angular separations (Darling & Truebenbach 2018 in prep). The figure uses a theoretical mass power spectrum for $z = 0$ generated with Goddard Space Flight Center's Code for Anisotropies in the Microwave Background (CAMB) web interface[2] . The mass power spectrum was generated using the default parameters, including linear density perturbation growth, $H_0 = 70$ km s^{-1} Mpc^{-1}, and a flat cosmology with $\Omega_\Lambda = 0.73$ and $\Omega_M = 0.27$.

5.2 Pairwise Proper Motion Measurement

We measured the relative proper motion of extragalactic objects using the VLBA Extragalactic Proper Motion Catalog (Truebenbach & Darling 2017). The catalog contains 713 proper motions, 596 of which have well measured redshifts and are therefore usable for this measurement. We excluded all catalog objects with either no redshift or a flagged

[2] https://lambda.gsfc.nasa.gov/toolbox/tb_camb_form.cfm

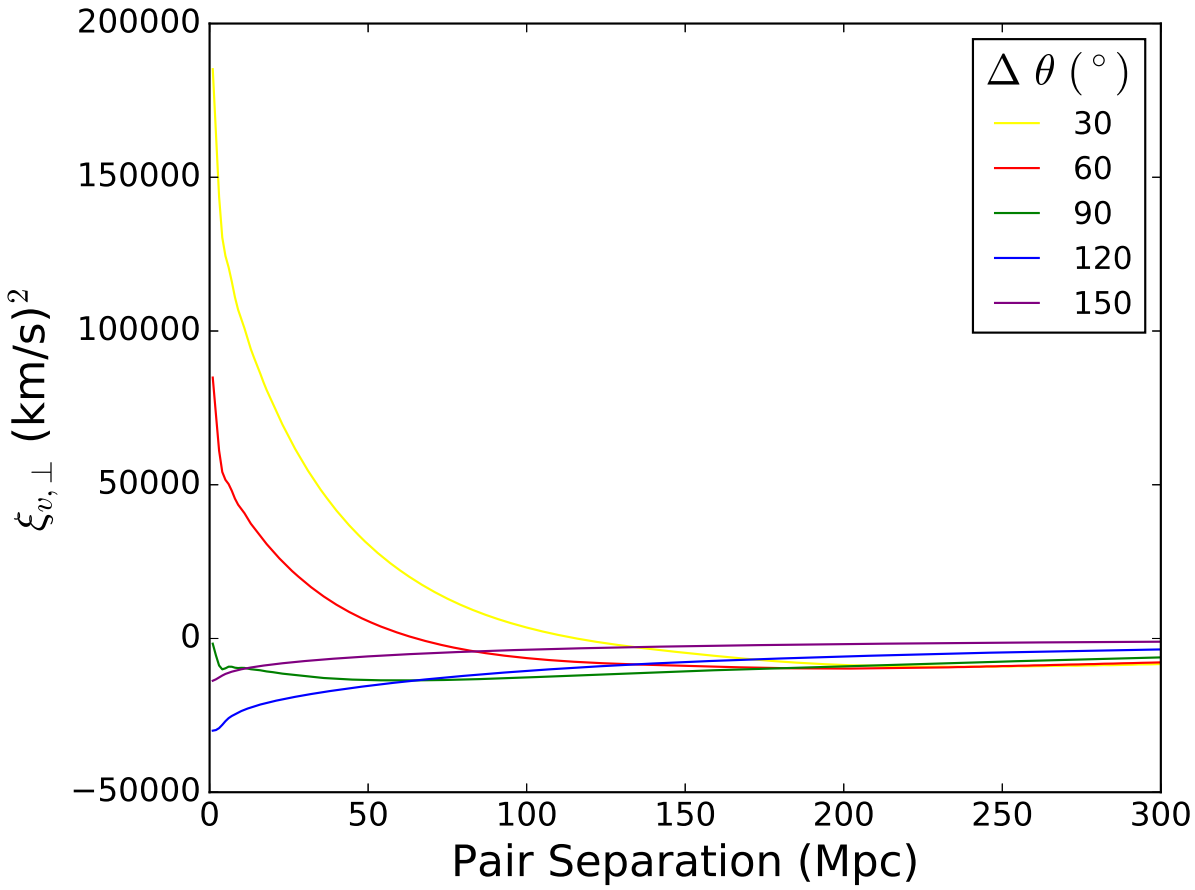

Figure 5.1 Transverse peculiar velocity two-point correlation statistic for close-separation pairs where $|\vec{x}_1| = |\vec{x}_2|$. Plotted for a range of angular separations. Reproduced from Darling & Truebenbach (2018 in prep).

redshift. Prior to calculating pairwise proper motions, we also removed the secular aberration drift signal measured in our catalog in Truebenbach & Darling (2017). The secular aberration drift, an apparent curl-free dipole motion of all extragalactic objects caused by the Solar System's acceleration towards the Galactic center, is not a real extragalactic motion and must be removed before analyzing any proper motions caused by cosmological effects. In Truebenbach & Darling (2017), we measured a partial dipole signal from the aberration drift with a square root power equal to 4.89 ± 0.77 μas yr^{-1} and an apex of ($275.2 \pm 10.0°$, $-29.4 \pm 8.8°$) in equatorial coordinates. Although we only detect a portion of the predicted dipole signal (expected square root power = 15.6 ± 2.3 μas yr^{-1}; derived from Reid et al. 2009) in our catalog, we still must remove this partial dipole before proceeding.

For all sources, we calculated their relative proper motion, $\dot{\theta}/\sin\theta$, with all other sources in the catalog. For two points on a sphere, the angular separation of the two points is

$$\theta_{ij} = \arccos(\sin\delta_i \ \sin\delta_j + \cos\delta_i \ \cos\delta_j \ \cos[\alpha_i - \alpha_j]), \tag{5.7}$$

where the points' equatorial coordinates are (α_i,δ_i), and the change in that separation due to the proper motion of those points is

$$\dot{\theta}_{ij} = -(\cos\delta_i \ \sin\delta_j[\mu_{\delta,i} - \mu_{\delta,j}\cos(\alpha_i - \alpha_j)] + \sin\delta_i \ \cos\delta_j[\mu_{\delta,j} - \mu_{\delta,i}\cos(\alpha_i - \alpha_j)] \\ - \cos\delta_i \ \ cos\delta_j \ \sin(\alpha_i - \alpha_j)[\mu_{\alpha,i} - \mu_{\alpha,j}])/\sin\theta_{ij}. \tag{5.8}$$

Comoving separation is calculated from the angular separation as

$$r_{ij}^2 = r_i^2 + r_j^2 - 2r_i r_j \cos\theta_{ij}, \tag{5.9}$$

where r_i and r_j are the comoving proper distances of the objects, calculated from their redshifts.

Several galaxies (M81, M84, 3C274, 1923+210, and NGC4261) are too nearby for redshift to be a good proxy for distance. For these, we used a median of various redshift-independent distances reported by the NASA/IPAC Extragalactic Database[3] (NED), in-

[3] https://ned.ipac.caltech.edu

cluding distances measured from Type 1a supernovae light curves (e.g., Colgate 1979; Riess et al. 1996; Perlmutter et al. 1999), globular cluster luminosity functions (e.g., Hanes 1977; Harris & Racine 1979), surface brightness fluctuations (Tonry & Schneider 1988; Tonry et al. 1990; Jensen et al. 1998; Blakeslee et al. 1999; Mei et al. 2005), and the Faber-Jackson relation (Faber & Jackson 1976). We did not include distance measurements from before 2000.

Figure 5.2 shows the relative proper motion of radio source pairs binned by comoving separation. The relative proper motions and error bars are the median and standard deviation of a bootstrap distribution (see below). The solid line at $\dot{\theta}/\sin\theta = -15$ μas yr^{-1} indicates the expected convergence of a static structure at $z = 0$. This represents the most extreme deviation from the null signal of Hubble expansion for pairs whose relative proper motion is not dominated by intrinsic motions (i.e., radio jets). The curved lines show the predicted relative proper motion from the transverse peculiar velocity two-point correlation function for close-separation pairs with an angular separation of 30 degrees (Eqn 5.6).

Table 5.1 lists the bin medians and uncertainties. As predicted, bins with comoving separations > 100 Mpc show no relative motion and are consistent with pure Hubble expansion. Despite the large scatter of relative proper motions within each bin due to the intrinsic proper motions from jets, we are still able to measure the expected cosmological behavior of large-separation pairs to high precision. Pairs with separations > 800 Mpc are consistent with Hubble expansion to within ~ 2.3 μas yr^{-1}, while pairs with separations $200 - 800$ Mpc are consistent to within ~ 5.7 μas yr^{-1}. This result is a strong verification of our method to place limits on small relative proper motion signals from a sample of large, uncorrelated intrinsic proper motions.

The bin with comoving separations < 100 Mpc is consistent with both Hubble expansion and the maximum convergence of static structures at $z = 0$. The predicted relative proper motion from the two-point correlation function lies between these two expected signals and is also consistent with the first bin. Overall, the < 100 Mpc bin contains too few

pairs to detect any significant deviation from pure Hubble expansion. Additionally, Figure 5.2 shows that the predicted two-point correlation function only deviates from zero for pairs with comoving separations $\lessapprox 50$ Mpc. There are only 8 pairs with separations < 50 Mpc, with an average relative proper motion of -11.5 μas yr^{-1} and a standard deviation of 22.2 μas yr^{-1}. Therefore, there are too few pairs with separations < 50 Mpc to statistically differentiate between pure Hubble expansion and the convergence expected for small-separation pairs.

The primary concern when calculating binned pairwise proper motion is the effect of individual objects with well-measured, large, intrinsic proper motions from relativistic jets. These intrinsic proper motions are often highly significant outliers in the bin and can dominate an error-weighted least-squares fit. This effect is particularly a concern for the first bin of pairs with comoving separations < 100 Mpc. Figure 5.3 shows the objects that comprise the first bin along the outer circle, while the connecting chords show the pairs. This figure demonstrates that many of the pairs in the first bin are composed of the same small number of galaxies. If one galaxy that is in many pairs has a significant intrinsic proper motion, it can have a large effect on the bin's average.

We use relative proper motions along a pair axis to somewhat mitigate this effect. Intrinsic proper motions are randomly oriented and are uncorrelated between objects, reducing the likelihood that the intrinsic proper motion will lie along the pair axis. However, Figure 5.4 shows the individual pairwise proper motions for all pairs with comoving separations < 100 Mpc and illustrates that the bin uncertainty is still dominated by significant individual pairwise proper motions. To quantify this scatter and reduce the influence of individual galaxies on the bin average, the bin averages and uncertainties in Figure 5.2 are the median and standard deviation of 1,000 iterations of a bootstrap distribution where subsets of the galaxies that comprise the bin are selected. We also reduce the influence of significant outliers by calculating the bin average of each bootstrap iteration through a maximum-likelihood "permissive fit" method (see Darling et al. 2018 submitted). For each

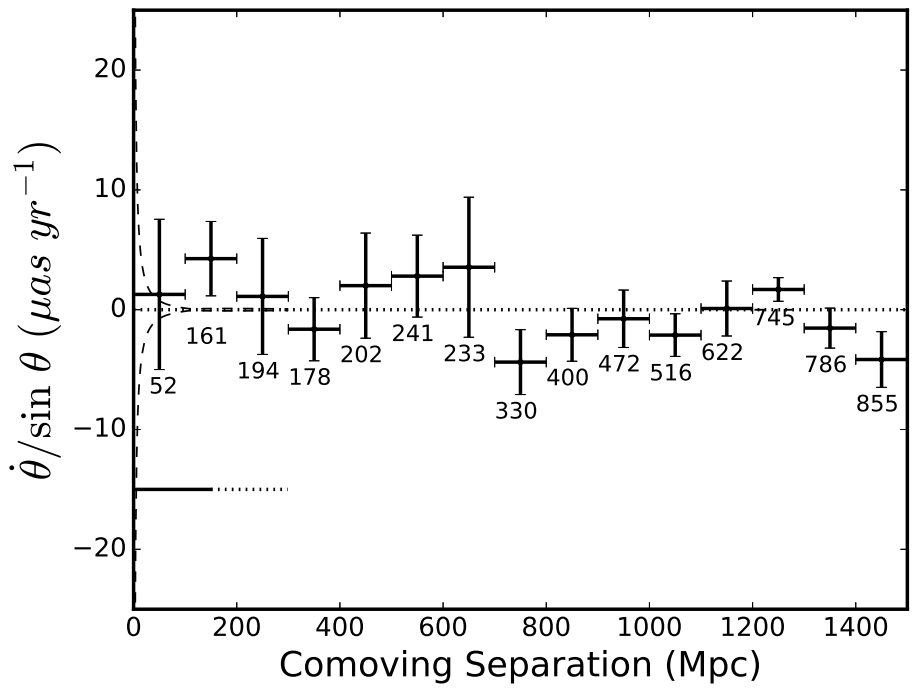

Figure 5.2 Measured pairwise divergence or convergence vs. comoving separation of radio sources in the proper motion catalog. Numbers beneath each data point indicate the number of pairs in each bin. The dotted line shows the null signal expected for gravitationally non-interacting pairs expanding with the Hubble flow, while the solid line at $\dot{\theta}/\sin\theta = -15$ μas yr^{-1} indicates the expected convergence of a static structure at $z = 0$. The dashed curved lines show the predicted relative proper motion of a pair with an angular separation of 30° derived from the transverse, peculiar velocity two-point correlation function (Eqn 5.6). We find a 3 sigma limit on the convergence rate of gravitationally-interacting objects (< 100 Mpc) of > -17.4 μas yr^{-1}. Large-separation pairs (> 800 Mpc) are consistent with the null signal expected for Hubble expansion to within ~ 2.3 μas yr^{-1}, while pairs with separations $200 - 800$ Mpc are consistent to within ~ 5.7 μas yr^{-1}.

Table 5.1. Binned Pairwise Proper Motions

Comoving Separation (Mpc)	$\langle z \rangle$	$\langle \dot{\theta} / \sin\theta \rangle$ (μas yr^{-1})	N
0–100	0.10	1.2 (6.2)	52
100–200	0.38	4.3 (3.0)	161
200–300	0.21	1.3 (5.0)	194
300–400	0.49	-1.7 (4.2)	178
400–500	0.62	1.7 (4.2)	202
500–600	0.57	2.6 (3.3)	241
600–700	0.65	3.7 (5.7)	233
700–800	0.67	-4.2 (2.7)	330
800–900	0.77	-2.0 (2.2)	400
900–1000	0.77	-0.9 (2.3)	472
1000–1100	0.83	-2.2 (1.7)	516
1100–1200	0.86	0.2 (2.2)	622
1200–1300	0.89	1.7 (0.9)	745
1300–1400	0.95	-1.3 (1.7)	786
1400–1500	0.96	-4.0 (2.3)	855

Note. — Columns from left to right: Pair comoving separation, average redshift of pairs within separation range, average relative proper motion, and number of pairs within separation range. Parenthetical values indicate 1σ uncertainties.

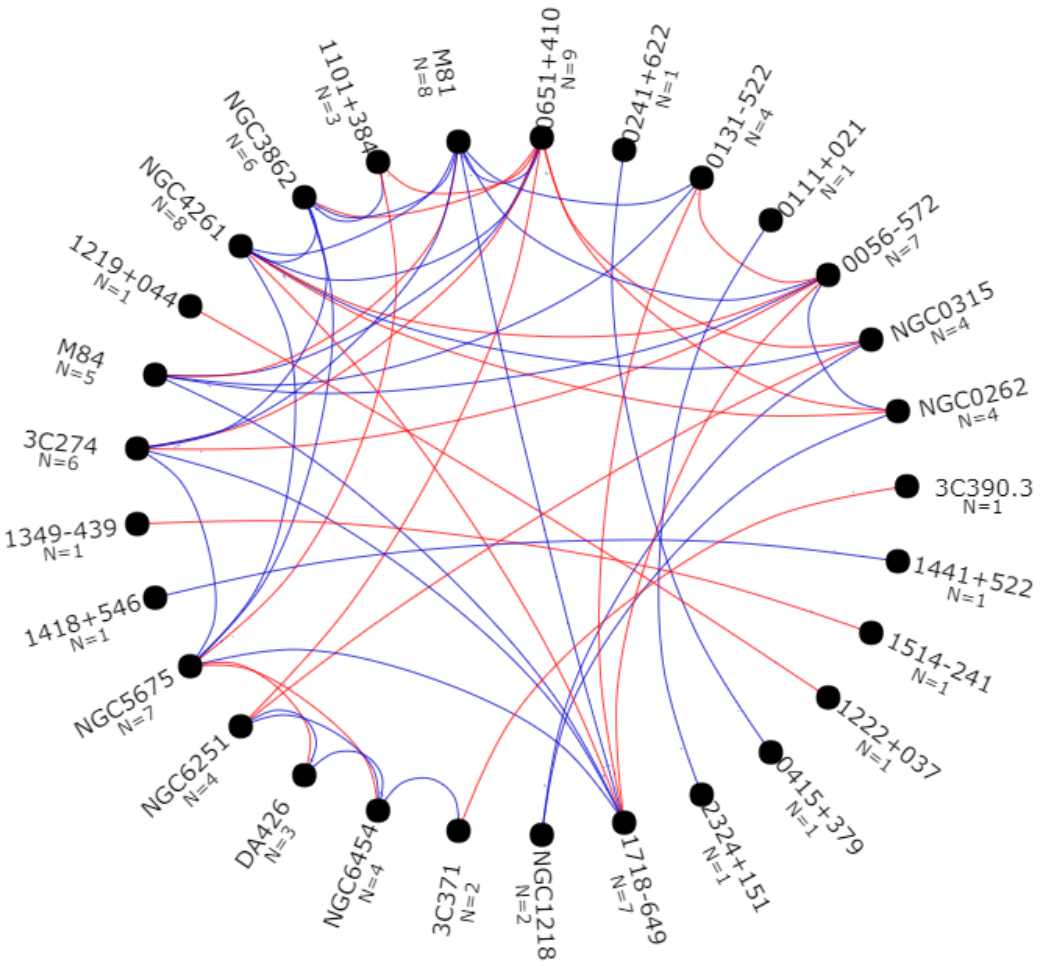

Figure 5.3 Chord diagram showing all objects that have pairs within 100 Mpc, comoving. The lines connect all objects that are pairs with each other. Blue lines indicate converging pairs ($\dot{\theta}/\theta < 0$), while red lines indicate diverging pairs ($\dot{\theta}/\theta > 0$). The number of pairs are also listed underneath each object. All pairs whose relative velocity is three times greater than the expected relative velocity of a static structure entrained in the Hubble flow (Eqn. 5.11) are removed from the plot.

iteration, we use a least-squares technique with `lmfit` (Newville et al. 2014) to obtain the bin average that minimizes the permissive fit residual.

Before we bootstrap and fit each bin, we clip all pairs whose relative velocity is greater than three times that expected for a static structure at the pair's redshift. For a pair at an average proper distance D, with relative velocity $v = (\dot{\theta}/\sin\theta)\ D$, the maximum convergence expected for a static pair that is entrained in the Hubble flow is

$$\frac{\dot{\theta}}{\sin\theta} = \frac{-H(z)}{1+z}, \tag{5.10}$$

which equates to a maximum expected relative velocity of

$$v_{\rm max} = \frac{-H(z)}{1+z}\ D. \tag{5.11}$$

We include in our bin averages all pairs whose relative velocity is within 1σ of the range $3v_{\rm max} < v < -3v_{\rm max}$, thereby removing all pairs who are contracting / expanding more than three times faster than the contraction expected for a static structure entrained in the Hubble flow. This clipping of large apparent relative velocities removes pairs whose relative proper motions are jet-dominated rather than dominated by peculiar velocities caused by the mass distribution of LSS. Figure 5.4 shows the clipped pairs from the first bin in red. This clipping criterion is preferable over simpler criteria (e.g., clipping objects with absolute proper motions or proper motion uncertainties > 100 μas yr^{-1}) because it is distance independent. If we clip objects with large absolute proper motions and proper motion uncertainties, we remove the most distant objects from our bin averages because the proper motion uncertainty is higher for more distant objects; these criteria bias the bin averages towards nearby pairs. On the other hand, our criterion clips using relative peculiar velocity, which is independent of distance.

Finally, we include three rounds of 5σ clipping of pairs that deviate from the bin median. On average, this iterative clipping removes < 1 pair from each bootstrap iteration for bins with separations < 500 Mpc. It removes $1-6$ pairs for bins with separations > 500 Mpc.

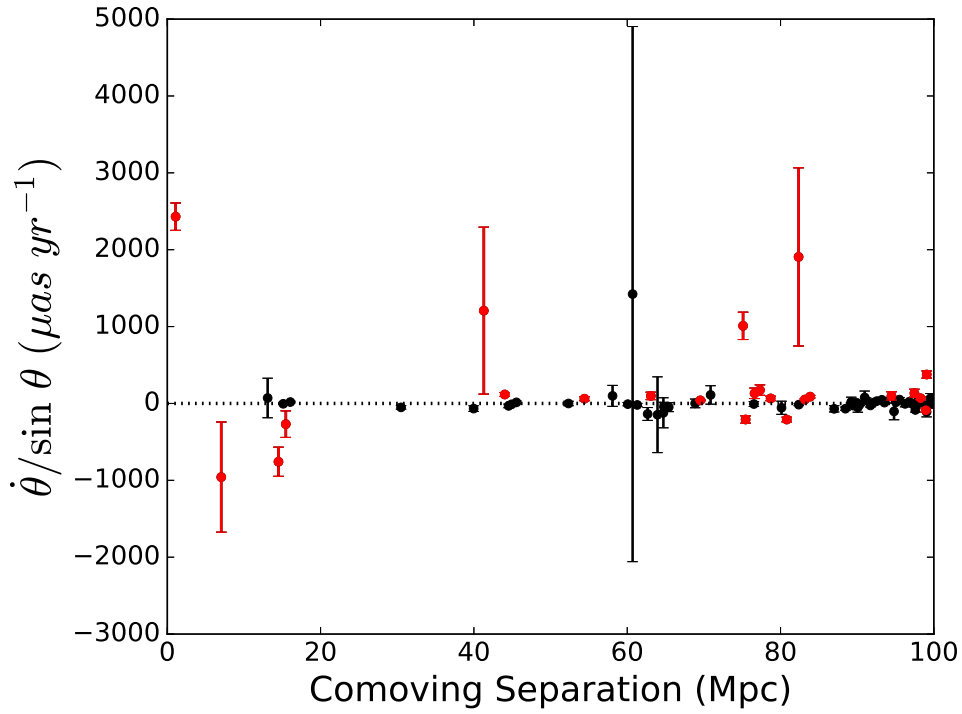

Figure 5.4 Measured pairwise divergence or convergence vs. comoving separation for all individual pairs with comoving separations < 100 Mpc. Black points are pairs included in the bin median, while red points are pairs that were clipped because their relative velocity is more than 1σ greater than three times the expected relative velocity for a static structure at the pair redshift. The dashed line shows the null signal expected for large-separation, gravitationally non-interacting pairs expanding with the Hubble flow.

5.2.1 Extragalactic Parallax

In addition to the secular aberration drift, the barycenter motion with respect to the CMB can also add a secular parallax to extragalactic objects that is not due to large-scale structure evolution or Hubble expansion. From the *Wilkinson Microwave Anisotropy Probe* (WMAP) sky survey, this dipole signal has an amplitude of 3.355 ± 0.008 mK and an apex of $(263.99 \pm 0.14°, 48.26 \pm 0.03)$ in Galactic coordinates, equivalent to a Solar System peculiar velocity of 369.0 ± 0.9 km s^{-1} or 0.3771 ± 0.0001 mpc yr^{-1} with respect to the CMB rest frame (Hinshaw et al. 2009). The barycenter peculiar motion adds an apparent proper motion away from the CMB apex for all extragalactic objects, modulated by the angle β between the object and the CMB apex and by the comoving distance of the object:

$$\mu = \frac{\pi}{D} |\sin \beta|, \tag{5.12}$$

where $\pi = 77.8$ μas yr^{-1}, the angular amplitude of the apparent CMB dipole motion, and D is the comoving distance in Mpc. The parallax effect is largest for nearby galaxies (20.8 μas yr^{-1} for M81; $D = 3.6$ Mpc), but can also be statistically detected in large samples of more distant objects (Ding & Croft 2009). Figure 5.5 shows the predicted parallax effect for all catalog objects.

To ensure that the barycenter motion with respect to the CMB rest frame does not have a significant effect on our pairwise proper motion measurements, we performed the pairwise measurement both with and without removing the parallax. On average, the dipole motion adds a proper motion of < 0.01 μas yr^{-1} to the catalog objects. For the four closest galaxies at comoving distances < 32 Mpc, extragalactic parallax adds a proper motion of ~ 1 μas yr^{-1}, with the exception of M81, which is noted above. Because the barycenter motion with respect to the CMB rest frame is strongly dependent on distance, it only significantly affects a very small number of catalog objects. Therefore, we found that removing this effect had no significant effect on our pairwise proper motion measurements.

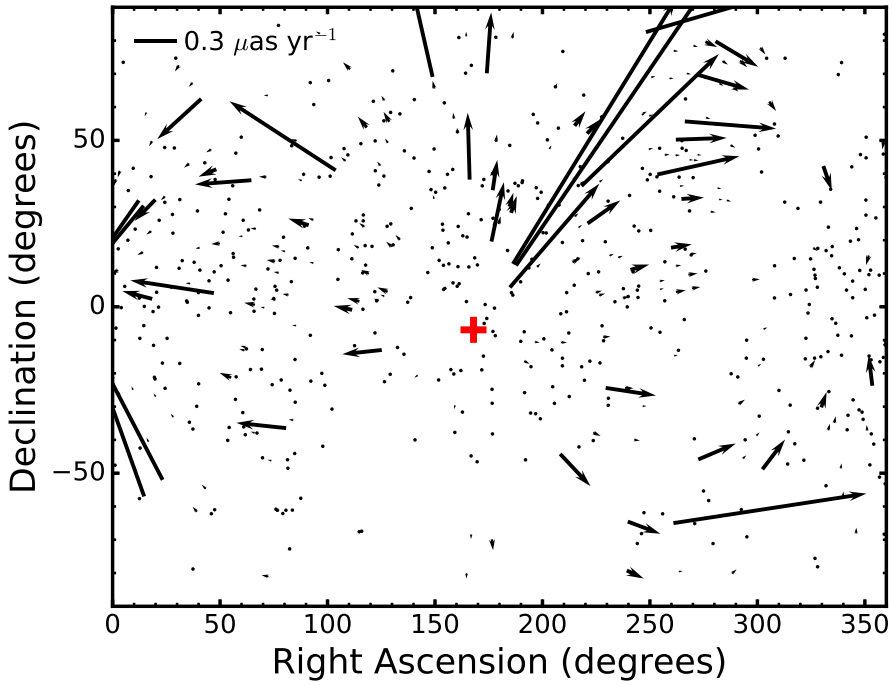

Figure 5.5 Secular parallax of catalog objects from the barycenter motion with respect to the CMB. Arrow tails correspond to catalog object locations. The red cross shows the location of the CMB apex. Scale in upper left corner.

5.3 Limit on Large-Scale Structure Growth

As discussed in Section 5.2 and shown in Figure 5.2, the bin of pairs with comoving separations < 100 Mpc is consistent with both pure Hubble expansion and the expected convergence of a static structure at $z = 0$. It is also consistent with the predicted relative proper motion of a pair with an angular separation of 30° derived from the transverse peculiar velocity two-point correlation function (Eqn 5.6). Based on the < 100 Mpc bin median, we find a 3 sigma range on the convergence rate of gravitationally-interacting objects of $19.8 < \dot{\theta}/\sin\theta < -17.4$ μas yr^{-1}. Large-separation pairs (> 800 Mpc) are consistent with the null signal expected for Hubble expansion to within ~ 2.3 μas yr^{-1}, while pairs with separations $200 - 800$ Mpc are consistent to within ~ 5.7 μas yr^{-1}.

The curved line representing the expected signal from the correlation function in Figure 5.2 is a rough approximation meant to aid in the reader's interpretation of the plot. To more accurately compare our pairwise proper motions to the expected signal derived from the mass power spectrum, we calculated the transverse peculiar velocity two-point correlation, ξ_i, for each individual pair. For two objects in flat space at locations (α_1,δ_1,D_1) and (α_2,δ_2,D_2) in spherical coordinates, the vector connecting the two objects, converted to Cartesian coordinates, is

$$\vec{x} = \begin{pmatrix} D_1 \cos\alpha_1 \cos\delta_1 - D_2 \cos\alpha_2 \cos\delta_2 \\ D_1 \sin\alpha_1 \cos\delta_1 - D_2 \sin\alpha_2 \cos\delta_2 \\ D_1 \sin\delta_1 - D_2 \sin\delta_2 \end{pmatrix}, \tag{5.13}$$

where D_1 and D_2 are the proper distances of the two objects.

The transverse velocity of each object, in equatorial coordinates, is

$$\vec{v}_\perp = D\ (\mu_\alpha\ \hat{e}_\alpha + \mu_\delta\ \hat{e}_\delta), \tag{5.14}$$

where $\hat{e}_\alpha$ and $\hat{e}_\delta$ are the unit vectors along the right ascension and declination axes. Using the conversion of $\hat{e}_\alpha$ and $\hat{e}_\delta$ to Cartesian coordinates from Mignard & Klioner (2012) (Eqns

5 and 6),

$$\vec{v}_\perp = D \begin{pmatrix} -\mu_\alpha \sin\alpha - \mu_\delta \cos\alpha \sin\delta \\ \mu_\alpha \cos\alpha - \mu_\delta \sin\alpha \sin\delta \\ \mu_\delta \cos\delta \end{pmatrix}, \tag{5.15}$$

with associated uncertainty

$$\sigma^2_{\vec{v}_\perp} = D^2 \begin{pmatrix} \sigma^2_{\mu_\alpha} \sin^2\alpha + \sigma^2_{\mu_\delta} \cos^2\alpha \sin^2\delta \\ \sigma^2_{\mu_\alpha} \cos^2\alpha + \sigma^2_{\mu_\delta} \sin^2\alpha \sin^2\delta \\ \sigma^2_{\mu_\delta} \cos^2\delta \end{pmatrix}. \tag{5.16}$$

We assume that the proper motion uncertainties are significantly larger than those in $\vec{x}$, α, δ, and D. In cases where the fractional proper motion uncertainty is less than 1, the uncertainty of D may be significant. Unfortunately, redshift uncertainties are not reported in the source catalog (nor many other redshift catalogs), so we are unable to account for distance uncertainties in our calculations.

For each object, we compute $\vec{v}_\perp \cdot \hat{x}$ through a normal Cartesian dot product –

$$\vec{v}_\perp \cdot \hat{x} = \frac{1}{|\vec{x}|} \left(v_{\perp,x}\ x_x + v_{\perp,y}\ x_y + v_{\perp,z}\ x_z \right). \tag{5.17}$$

The uncertainty for the dot product is

$$\sigma^2_{\vec{v}_\perp \cdot \hat{x}} = \frac{1}{|\vec{x}|^2} \left(\sigma^2_{v_{\perp,x}}\ x_x^2 + \sigma^2_{v_{\perp,y}}\ x_y^2 + \sigma^2_{v_{\perp,z}}\ x_z^2 \right), \tag{5.18}$$

assuming negligible uncertainty in $\vec{x}$. Therefore, the correlation statistic for two individual objects is

$$\xi_i = (\vec{v}_{\perp,1} \cdot \hat{x})(\vec{v}_{\perp,2} \cdot \hat{x}), \tag{5.19}$$

with associated uncertainty

$$\sigma^2_{\xi_i} = \xi_i^2 \left(\frac{\sigma^2_{\vec{v}_{\perp,1} \cdot \hat{x}}}{(\vec{v}_{\perp,1} \cdot \hat{x})^2} + \frac{\sigma^2_{\vec{v}_{\perp,2} \cdot \hat{x}}}{(\vec{v}_{\perp,2} \cdot \hat{x})^2} \right). \tag{5.20}$$

Figure 5.6 shows the average individual two-point correlation statistic (Eqn 5.19) for all pairs of objects with comoving separations < 1500 Mpc. The pairs are selected and clipped in the same manner as was used to create Figure 5.2. Again, the bin centers and error bars are the median and standard deviation of a 1000 iteration bootstrap distribution. The expected correlation statistic from the theoretical mass power spectrum is also plotted for several angular separations. Like Figure 5.2, this figure also shows that the bin with comoving separations < 100 Mpc is consistent with both pure Hubble expansion and the predicted convergence of close-separation pairs from the mass power spectrum at several angular separations.

5.4 Future Limits on Large-Scale Structure Growth

Our current data set of extragalactic proper motions is not sufficiently large to detect the average motion caused by the mass distribution of LSS. Specifically, we lack sufficient pairs with comoving separations < 50 Mpc, where the predicted correlation of LSS deviates from the null signal predicted on large length scales. If we roughly expect the error bars in Figure 5.6 to decrease by N, then we would need ~ 30 more close-separation pairs to significantly detect the relative proper motion from LSS growth.

Gaia (Gaia Collaboration et al. 2016) proper motions, coming in the next few months, will significantly increase the sample of pairs with separations < 50 Mpc. However, *Gaia* proper motions have much higher uncertainties ($\sim 20 - 200$ μas yr^{-1}; Paine et al. 2018 submitted) than those produced through VLBI observations (10's of μas yr^{-1}; Titov & Lambert 2013; Truebenbach & Darling 2017). To assess the contribution of *Gaia* proper motions to our measurement of the mass distribution of LSS, we created a simulated catalog of proper motions from *Gaia* DR1 (Lindegren et al. 2016). We cross-matched the DR1 catalog with the Large Quasar Astrometric Catalog DR3 (LQAC3; Souchay et al. 2009, 2015) to select a large sample of extragalactic objects and to obtain redshifts. Using the `pyGaia`[4]

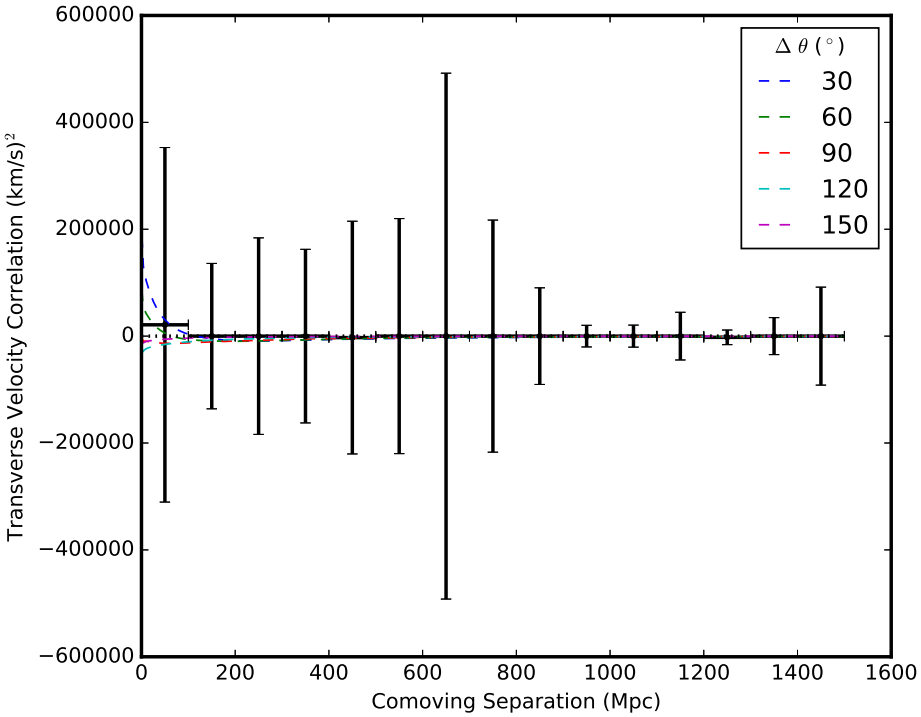

Figure 5.6 The average individual transverse peculiar velocity two-point correlation statistic (Eqn 5.19) for all pairs of objects with comoving separations < 1500 Mpc. The expected correlation statistic from the theoretical mass power spectrum is plotted for several angular separations as dashed colored lines. The dotted black line is the expected null signal for pure Hubble expansion. The number of pairs per bin is the same as for Figure 5.2.

package, we gave each quasar a predicted *Gaia* end-of-mission proper motion uncertainty based on its ecliptic angle and optical G-band magnitude. Then, we gave each quasar a proper motion randomly drawn from the distribution of predicted proper motion uncertainties. Our total simulated catalog roughly follows the Sloan Digital Sky Survey (SDSS; York et al. 2000) footprint with additional coverage across the entire sky and contains $\sim 1.9 \times 10^5$ objects with an average proper motion uncertainty of ~ 210 μas yr^{-1}.

We found $\sim$ 100,000 pairs with comoving separations < 50 Mpc. For each pair with a separation < 100 Mpc, we added the predicted correlation statistic from the mass distribution of LSS (Eqn 5.19) to the pair's randomly generated correlation. Then we attempted to recover the expected signal from LSS to predict whether *Gaia* proper motions will be able to detect the mass distribution of LSS for close-separation pairs. Figure 5.7 shows the binned correlation statistic for our simulated *Gaia* catalog. The blue stars show the bin averages for the catalog with the expected correlation statistic added to the randomly generated proper motions, while the black dots show the bin averages for the catalog with no signal added. We performed the same pairs search and ξ_i binning for both simulated *Gaia* catalogs as we did for our proper motion catalog. However, because of the large sample size, we did not include a bootstrap. Instead, the plotted bin values and uncertainties are the maximum likelihood solutions for the bin averages and the 68% confidence intervals of the probability distributions.

Figure 5.7 demonstrates that even a subset of $\sim 100,000$ *Gaia* extragalactic proper motion pairs will be able to detect a deviation from pure Hubble expansion for close-separation pairs. The first two bins with comoving separations $0-25$ and $25-50$ Mpc are 9.8σ and 8.9σ detections, respectively. Therefore, although *Gaia* proper motions will be much less precise than VLBI proper motions, the two orders of magnitude increase in the number of available extragalactic proper motions will allow a significant detection of the transverse, peculiar velocity two-point correlation function at physical separations < 50 Mpc. The shape and

[4] https://pypi.python.org/pypi/PyGaia

magnitude of the measured correlation will allow a means to test the shape of the theoretical mass power spectrum that is independent of any distance ladder.

5.5 Conclusions

In this Chapter, we measured the relative proper motion of all pairs of objects from the VLBA Extragalactic Proper Motion Catalog (Truebenbach & Darling 2017) with comoving separations less than 1500 Mpc. We found that large-separation pairs with separations > 200 Mpc are consistent with the null signal expected for Hubble expansion to within ~ 5.7 μas yr^{-1}. This result demonstrates that our method of measuring the average relative proper motion of pairs is able to extract small proper motion signals to high precision despite the large scatter of individual pairs due to the intrinsic proper motions from jets.

We also found that we have too few close-separation pairs (< 100 Mpc) to statistically detect the expected convergence predicted by the peculiar, transverse velocity two-point correlation function. We found a 3σ limit on the convergence rate of close-separation pairs of > -17.4 μas yr^{-1}. Additionally, we estimated that we would need ~ 30 more pairs with separations < 50 Mpc to make a 3σ detection of this effect.

Finally, we created a simulated *Gaia* proper motion catalog of $\sim 100,000$ extragalactic proper motion pairs with separations < 50 Mpc to estimate how well *Gaia* end-of-mission proper motions will be able to detect the relative velocity of close-separation pairs caused by the mass distribution of LSS. We found that the subset is able to detect the predicted correlation of close-separation pairs at a significant of 9.8σ. Therefore, although our current sample of close-separaion pairs is too small to statistically detect the net convergence of gravitationally-interacting pairs, *Gaia* proper motions will be able to make a highly signficant detection of the mass distribution of LSS on small scales. Comparison of the measured peculiar, transverse two-point correlationstatistic to that predicted by the theoretical mass power spectrum will allow a means to test the cosmological principles that contribute to the shape and magnitude of the power spectrum without a reliance on precise distance

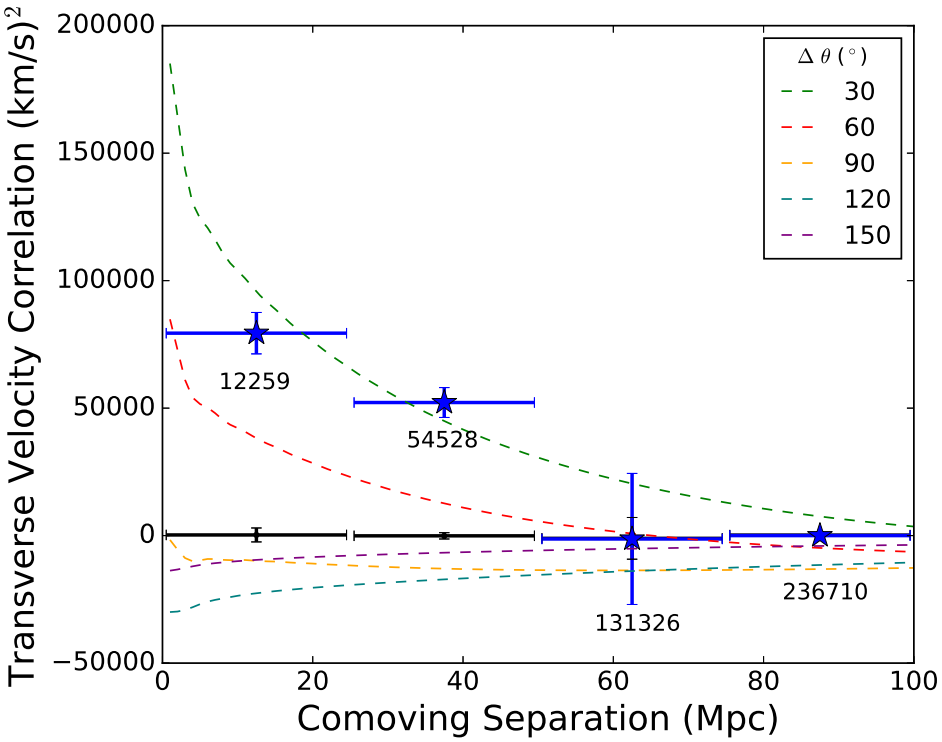

Figure 5.7 The transverse peculiar velocity two-point correlation statistic (Eqn 5.19) for the simulated *Gaia* catalog. The blue stars show the bin averages for the catalog with the expected correlation statistic added to the randomly generated proper motions, while the black dots show the bin averages for the catalog with no signal added. The two black bins with separations > 50 Mpc coincide with the blue bins for the same separations. The expected correlation statistic from the theoretical mass power spectrum is plotted for several angular separations as dashed colored lines. The number of pairs per bin is listed beneath each blue bin.

measurements.

Chapter 6

Conclusions

In this thesis, I have presented a new catalog of extragalactic proper motions and used that catalog to statistically measure or limit two small, correlated signals from the secular aberration drift and the mass distribution of LSS. I created the catalog using archival VLBI data, new astrometry from the VLBA, and a new method of calculating proper motions that produces lower uncertainties than those found by previous studies. I also developed a pipeline to calibrate and produce high signal-to-noise VLBA images. The final VLBA Extragalactic Proper Motion Catalog contians 713 proper motions with average uncertainties of ~ 24 μas yr^{-1}.

I measured the secular aberration drift as a curl-free dipole with an amplitude of 1.69 ± 0.27 μas yr^{-1} and an apex consistent with the Galactic Center ($275.2 \pm 10.0^{\circ}$, $-29.4 \pm 8.8^{\circ}$). Unlike previous studies, which use a priori knowledge of the expected signal to clip their data (e.g., Titov et al. 2011; Titov & Lambert 2013), I used a bootstrap MCMC parameter estimation to measure this small statistical signal without any assumptions about the expected signal or any significant data clipping. The measured dipole has a lower amplitude than that predicted by the solar acceleration (5.40 ± 0.78 μas yr^{-1}), possibly because it is diluted by the no-net-rotation constraint used in the archival astrometry. However, the measured signal is still a significant, real signal that must be removed before the proper motions can be used to measure cosmological effects.

Finally, I used the extragalactic proper motion catalog to place limits on the expected

relative proper motion of extragalactic object pairs due to the mass distribution of LSS. I find that there are too few pairs with comoving separations < 50 Mpc to detect the deviation from pure Hubble expansion that is predicted by a peculiar, transverse velocity two-point correlation statistic and a theoretical mass power spectrum. Additional close-separation pairs are needed in order for this method to be competitive with analogous line-of-sight velocity studies.

The best source for additional extragalactic proper motions is very long baseline interferometry because of its uniquely high angular resolution. From the uncertainties in Figure 5.6, we predict that we would need ~ 30 additional pairs with comoving separations < 50 Mpc to measure the expected signal from the mass distribution of LSS. However, in order to achieve the proper motion precisions in our catalog, astrometry was obtained for all quasars more than three times over at least a 10 year timespan. Therefore, addition of new close-separation pairs would be a long-term project that would require significant VLBI use.

The Next Generation Very Large Array (ngVLA) provides another avenue for measuring new extragalactic proper motions. The ngVLA will provide ten times the effective collecting area and ten times longer baselines (300 km) than the current Karl Jansky Very Large Array (JVLA; Carilli et al. 2015). The larger collecting area will enable faster astrometry of fainter sources than is currently possible with the VLBA. In one hour of observation time, the ngVLA will detect objects with flux densities of a few tenths of a mJy or brighter (Butler et al. 2018).

If additional ngVLA antennas are installed at VLBA sites, the collecting power of the ngVLA could be combined with the astrometric precision of the VLBA to quickly create a large sample of close-separation pairs. For example, if 10,000 objects were monitored on a yearly basis to obtain 10 μas yr^{-1} astrometry per object, this would enable global detection of 0.1 μas yr^{-1} correlated signals at 5σ significance (Bower et al. 2015). At this precision, we could constrain isotropy to 0.1% of H_0 (Bower et al. 2015). If objects are selected to be in close-separation pairs, a new proper motion catalog with the ngVLA and VLBA would

contain more than enough objects to detect the mass distribution of LSS; we predict that we need only ~ 30 pairs with separations < 50 Mpc for a 3σ detection of this effect (Section 5.4).

However, it is uncertain whether the ngVLA will include long baselines > 1000 km. For observations at 3.6 cm with a maximum baseline of 1000 km, the ngVLA will achieve a spatial resolution of ~ 7 mas. If objects are observed yearly for 10 years, then we expect to detect proper motions > 700 μas yr^{-1}. Therefore, unless the ngVLA includes baselines on order of VLBA baselines or can be used in conjunction with existing VLBI networks, the ngVLA will not be an effective tool to expand our sample of close-separation pairs.

With the limitations of current VLBA catalogs and ngVLA baselines, *Gaia* proper motions remain the best avenue for increasing our sample of close-separation pairs. As discussed in Sections **??** and 5.4, *Gaia* will produce $\sim 10^6$ new extragalactic proper motions (Robin et al. 2012) with astrometric precisions of ~ 1.69 mas (Lindegren et al. 2016). Although *Gaia* proper motions are much less precise (uncertainties $\sim 20 - 200$ μas yr^{-1}; Paine et al. 2018 submitted) than those produced through VLBI observations (tens of μas yr^{-1}; Titov & Lambert 2013; Truebenbach & Darling 2017), the large number of additional proper motions will allow a statistical detection of correlated signals. Additionally, optical proper motions typically have a smaller contribution from intrinsic proper motions than those measured in the radio because the optical source more frequently traces the galaxy core, rather than tracing a jet driven by the active galactic nucleus (Darling et al. 2018 submitted).

The significant increase in sample size, combined with reduced intrinsic proper motions, will enable a detection of the secular aberration drift with relative precision of 10% (Mignard 2002), constrain the gravitational wave background to $\Omega_{gw}h^2 < 2 \times 10^{-4}$ (Darling et al. 2018 submitted), and constrain the anisotropy of Hubble expansion to $\sim 2\%$ (Paine et al. 2018 submitted). Finally, we find in Section 5.4 that a subset of $\sim 100,000$ *Gaia* extragalactic proper motion pairs will detect a 9.8σ peculiar, transverse velocity correlation for close-separation pairs. Therefore, although current proper motions are unable to measure the

relative peculiar velocity of extragalactic objects from the mass distribution of LSS, this technique will produce significant results with the impending incorporation of *Gaia* data.

Bibliography

Aasi, J., Abbott, B. P., Abbott, R., et al. 2014, Physical Review Letters, 113, 231101

Ade, P. A. R., Ahmed, Z., Aikin, R. W., et al. 2016, Phys. Rev. Lett., 116, 031302

Alam, S., Albareti, F. D., Allende Prieto, C., et al. 2015, ApJS, 219, 12

Altamimi, Z., Rebischung, P., Mãtivier, L., & Collilieux, X. 2016, J. Geophys. Res. Solid Earth, 121, 6109

Associated Universities, I. 1999, AIPS: Astronomical Image Processing System, Astrophysics Source Code Library, , , ascl:9911.003

Backer, D. C., & Hellings, R. W. 1986, ARA&A, 24, 537

Bardeen, J. M., Bond, J. R., Kaiser, N., & Szalay, A. S. 1986, ApJ, 304, 15

Bastian, U. 1995, in ESA Special Publication, Vol. 379, Future Possibilities for bstrometry in Space, ed. M. A. C. Perryman & F. van Leeuwen, 99

Battye, R. A., & Moss, A. 2006, Phys. Rev. D, 74, 041301

BICEP2 Collaboration, Ade, P. A. R., Aikin, R. W., et al. 2014, Physical Review Letters, 112, 241101

BICEP2/Keck and Planck Collaborations, Ade, P. A. R., Aghanim, N., et al. 2015, Physical Review Letters, 114, 101301

Blakeslee, J. P., Ajhar, E. A., & Tonry, J. L. 1999, in Astrophysics and Space Science Library, Vol. 237, Post-Hipparcos Cosmic Candles, ed. A. Heck & F. Caputo, 181

Blumenthal, G. R., Faber, S. M., Primack, J. R., & Rees, M. J. 1984, Nature, 311, 517

Book, L. G., & Flanagan, É. É. 2011, Phys. Rev. D, 83, 024024

Bower, G. C., Demorest, P., Braatz, J., et al. 2015, ArXiv e-prints, arXiv:1510.06432

Braginsky, V. B., Kardashev, N. S., Polnarev, A. G., & Novikov, I. D. 1990, Nuovo Cimento B Serie, 105, 1141

Bridle, A. H., & Perley, R. A. 1984, ARA&A, 22, 319

Broderick, A. E., Loeb, A., & Reid, M. J. 2011, ApJ, 735, 57

Brout, R., Englert, F., & Gunzig, E. 1978, Annals of Physics, 115, 78

Butler, B., Grammer, W., Selina, R., Murphy, E. J., & Carilli, C. 2018, in American Astronomical Society Meeting Abstracts, Vol. 231, American Astronomical Society Meeting Abstracts, 342.09

Carilli, C. L., McKinnon, M., Ott, J., et al. 2015, ArXiv e-prints, arXiv:1510.06438

Chimento, L. P., & Forte, M. 2006, Phys. Rev. D, 73, 063502

Clark, B. G. 1980, A&A, 89, 377

Coles, P. 1993, MNRAS, 262, 1065

Colgate, S. A. 1979, ApJ, 232, 404

Condon, J. J. 1997, PASP, 109, 166

Cooray, A., Holz, D. E., & Caldwell, R. 2010, JCAP, 11, 015

Courtois, H. M., Hoffman, Y., Tully, R. B., & Gottlöber, S. 2012, ApJ, 744, 43

Cruz, M., Martínez-González, E., Vielva, P., & Cayón, L. 2005, MNRAS, 356, 29

Cutri, R. M., Wright, E. L., Conrow, T., et al. 2013, Explanatory Supplement to the AllWISE Data Release Products, Tech. rep.

D'Abrusco, R., Massaro, F., Paggi, A., et al. 2014, ApJS, 215, 14

Darling, J. 2013, ApJL, 777, L21

—. 2014, MNRAS, 442, L66

Darling, J., & Truebenbach, A. E. 2018 in prep, Connecting Proper Motions to the Matter Power Spectrum: Theory, ,

Darling, J., Truebenbach, A. E., & Paine, J. 2018 submitted, ApJ

Dawson, K. S., Schlegel, D. J., Ahn, C. P., et al. 2013, AJ, 145, 10

de Lapparent, V., Geller, M. J., & Huchra, J. P. 1986, ApJL, 302, L1

Dekel, A., Bertschinger, E., Yahil, A., et al. 1993, ApJ, 412, 1

Demorest, P. B., Ferdman, R. D., Gonzalez, M. E., et al. 2013, ApJ, 762, 94

Detweiler, S. 1979, ApJ, 234, 1100

Dicke, R. H., Peebles, P. J. E., Roll, P. G., & Wilkinson, D. T. 1965, ApJ, 142, 414

Ding, F., & Croft, R. A. C. 2009, MNRAS, 397, 1739

Dodelson, S. 2003, Modern Cosmology (Academic Press)

Doumler, T., Courtois, H., Gottlöber, S., & Hoffman, Y. 2013, MNRAS, 430, 902

Efstathiou, G., & Gratton, S. 2009, JCAP, 6, 011

Eisenstein, D. J., & Hu, W. 1999, ApJ, 511, 5

Eisenstein, D. J., Zehavi, I., Hogg, D. W., et al. 2005, ApJ, 633, 560

Eubanks, T. M. 1997, IERS Technical Note, 23

Eubanks, T. M., Matsakis, D. N., Josties, F. J., et al. 1995, in IAU Symposium, Vol. 166, Astronomical and Astrophysical Objectives of Sub-Milliarcsecond Optical Astrometry, ed. E. Hog & P. K. Seidelmann, 283

Faber, S. M., & Jackson, R. E. 1976, ApJ, 204, 668

Fanselow, J. L. 1983, Observation Model and parameter partial for the JPL VLBI parameter Estimation Software"MASTERFIT-V1.0", Tech. rep.

Feissel, M., & Gontier, A.-M. 2000, in International VLBI Service for Geodesy and Astrometry 2000 General Meeting Proceedings, ed. F. Takahashi, 280

Feissel-Vernier, M., Ray, J., Altamimi, Z., Dehant, V., & de Viron, O. 2004, in International VLBI Service for Geodesy and Astrometry 2004 General Meeting Proceedings, ed. N. R. Vandenberg & K. D. Baver, 22

Fey, A. L., Eubanks, M., & Kingham, K. A. 1997, AJ, 114, 2284

Flesch, E. W. 2015, PASA, 32, e010

Foltz, C. B., Chaffee, Jr., F. H., Hewett, P. C., et al. 1987, AJ, 94, 1423

Fomalont, E., Johnston, K., Fey, A., et al. 2011, AJ, 141, 91

Fomalont, E. B. 1999, in Astronomical Society of the Pacific Conference Series, Vol. 180, Synthesis Imaging in Radio Astronomy II, ed. G. B. Taylor, C. L. Carilli, & R. A. Perley, 463

Fomalont, E. B., & Perley, R. A. 1999, in Astronomical Society of the Pacific Conference Series, Vol. 180, Synthesis Imaging in Radio Astronomy II, ed. G. B. Taylor, C. L. Carilli, & R. A. Perley, 79

Fontanini, M., West, E. J., & Trodden, M. 2009, Phys. Rev. D, 80, 123515

Foreman-Mackey, D. 2016, The Journal of Open Source Software, 24, doi:10.21105/joss.00024

Fry, J. N. 1996, ApJL, 461, L65

Gaia Collaboration, Prusti, T., de Bruijne, J. H. J., et al. 2016, A&A, 595, A1

Gontier, A.-M., Le Bail, K., Feissel, M., & Eubanks, T. M. 2001, A&A, 375, 661

Gott, III, J. R., Jurić, M., Schlegel, D., et al. 2005, ApJ, 624, 463

Grishchuk, L. P. 1975, Soviet Journal of Experimental and Theoretical Physics, 40, 409

Gwinn, C. R., Eubanks, T. M., Pyne, T., Birkinshaw, M., & Matsakis, D. N. 1997, ApJ, 485, 87

Halpern, J. P., Eracleous, M., & Mattox, J. R. 2003, AJ, 125, 572

Hanes, D. A. 1977, RAS, Memoirs, 84, 45

Harris, W. E., & Racine, R. 1979, ARA&A, 17, 241

Hawking, S. W. 1982, Physics Letters B, 115, 295

Hazard, C., Morton, D. C., Terlevich, R., & McMahon, R. 1984, ApJ, 282, 33

Hellings, R. W., & Downs, G. S. 1983, ApJL, 265, L39

Hildebrand, R. H., Dotson, J. L., Dowell, C. D., Schleuning, D. A., & Vaillancourt, J. E. 1999, ApJ, 516, 834

Hinshaw, G., Weiland, J. L., Hill, R. S., et al. 2009, ApJS, 180, 225

Hofmann-Wellenhof, B., Legat, K., Wieser, M., & Lichtenegger, H. 2003, Navigation (Springer)

Högbom, J. A. 1974, A&AS, 15, 417

Hook, I. M., Jørgensen, I., Allington-Smith, J. R., et al. 2004, PASP, 116, 425

Hu, W., Spergel, D. N., & White, M. 1997, Phys. Rev. D, 55, 3288

Hu, W., & White, M. 1996a, Physical Review Letters, 77, 1687

—. 1996b, ApJ, 471, 30

Hughes, P. A., Aller, H. D., & Aller, M. F. 1992, ApJ, 396, 469

IERS Technical Note No. 35. 2009, in The Second Realization of the International Celestial Reference Frame by Very Long Baseline Interferometry, ed. A. Fey, D. Gordon, & C. Jacobs

Jensen, J. B., Tonry, J. L., & Luppino, G. A. 1998, ApJ, 505, 111

Kaiser, N. 1984, ApJL, 284, L9

Kelley, L. Z., Blecha, L., Hernquist, L., Sesana, A., & Taylor, S. R. 2017, MNRAS, 471, 4508

Kim, D.-H., & Trippe, S. 2016, ApJ, 830, 161

Kitaura, F.-S., Erdoğdu, P., Nuza, S. E., et al. 2012, MNRAS, 427, L35

Koivisto, T., & Mota, D. F. 2008a, JCAP, 6, 018

—. 2008b, ApJ, 679, 1

Kopeikin, S. M., & Makarov, V. V. 2006, AJ, 131, 1471

Kovalevsky, J. 2003, A&A, 404, 743

Krauss, L. M., & Wilczek, F. 2014, Phys. Rev. D, 89, 047501

Lambert, S. B., & Gontier, A.-M. 2009, A&A, 493, 317

Lentati, L., Taylor, S. R., Mingarelli, C. M. F., et al. 2015, MNRAS, 453, 2576

Lindegren, L., Lammers, U., Bastian, U., et al. 2016, A&A, 595, A4

Ma, C., Arias, E. F., Eubanks, T. M., et al. 1998, AJ, 116, 516

MacMillan, D. S. 1995, Geophys. Res. Lett., 22, 1041

MacMillan, D. S. 2005, in Astronomical Society of the Pacific Conference Series, Vol. 340, Future Directions in High Resolution Astronomy, ed. J. Romney & M. Reid, 477

MacMillan, D. S., & Ma, C. 1997, Geophys. Res. Lett., 24, 453

Malkin, Z. 2004, in Proceedings of the Journées 2003 "Systèmes deréférence spatio-temporels": Astrometry, Geodynamics and Solar System Dynamics: from milliarcseconds to microarcseconds, held at IAA, St.Petersburg, Russia, 22-25 September 2003, A. Finkelstein & N.Capitaine (eds.), ISBN 5-93197-019-3 & ISBN 2-901057-50-0, p. 24-31, ed. A. Finkelstein & N. Capitaine, 24–31

Malkin, Z. M. 2016, Astronomy Reports, 60, 996

Manchester, R. N., Hobbs, G., Bailes, M., et al. 2013, PASA, 30, e017

McCarthy, D. D., & Petit, G. 2004, IERS Technical Note, 32

Mei, S., Blakeslee, J. P., Tonry, J. L., et al. 2005, ApJS, 156, 113

Mignard, F. 2002, in EAS Publications Series, Vol. 2, EAS Publications Series, ed. O. Bienayme & C. Turon, 327–339

Mignard, F., & Klioner, S. 2012, A&A, 547, A59

Moodley, K., Bucher, M., Dunkley, J., Ferreira, P. G., & Skordis, C. 2004, Phys. Rev. D, 70, 103520

Mukhanov, V. F. 1985, ZhETF Pisma Redaktsiiu, 41, 402

Mukhanov, V. F., & Chibisov, G. V. 1981, ZhETF Pisma Redaktsiiu, 33, 549

Newville, M., Stensitzki, T., Allen, D. B., & Ingargiola, A. 2014, LMFIT: Non-Linear Least-Square Minimization and Curve-Fitting for Python, , , doi:10.5281/zenodo.11813

Noll, C. E. 2010, Advances in Space Research, 45, 1421

Nusser, A., Branchini, E., & Davis, M. 2012, ApJ, 755, 58

Pagano, L., Salvati, L., & Melchiorri, A. 2016, Physics Letters B, 760, 823

Paine, J., Darling, J., & Truebenbach, A. E. 2018 submitted, ApJS

Peiris, H. V., Komatsu, E., Verde, L., et al. 2003, ApJS, 148, 213

Penzias, A. A., & Wilson, R. W. 1965, ApJ, 142, 419

Perley, R. A., & Butler, B. J. 2013, ApJS, 204, 19

Perlmutter, S., Aldering, G., Goldhaber, G., et al. 1999, ApJ, 517, 565

Planck Collaboration, Adam, R., Ade, P. A. R., et al. 2016a, A&A, 594, A1

Planck Collaboration, Ade, P. A. R., Aghanim, N., et al. 2016b, A&A, 594, A13

—. 2016c, A&A, 594, A20

—. 2016d, A&A, 594, A14

Polnarev, A. G. 1985, Soviet Astronomy, 29, 607

Pyne, T., Gwinn, C. R., Birkinshaw, M., Eubanks, T. M., & Matsakis, D. N. 1996, ApJ, 465, 566

Quercellini, C., Quartin, M., & Amendola, L. 2009, Physical Review Letters, 102, 151302

Ransom, S. M. 2013, in IAU Symposium, Vol. 291, Neutron Stars and Pulsars: Challenges and Opportunities after 80 years, ed. J. van Leeuwen, 3–10

Reid, M. J., & Brunthaler, A. 2004, ApJ, 616, 872

Reid, M. J., Readhead, A. C. S., Vermeulen, R. C., & Treuhaft, R. N. 1999, ApJ, 524, 816

Reid, M. J., Menten, K. M., Zheng, X. W., et al. 2009, ApJ, 700, 137

Riess, A. G., Press, W. H., & Kirshner, R. P. 1996, ApJ, 473, 88

Riess, A. G., Filippenko, A. V., Challis, P., et al. 1998, AJ, 116, 1009

Riess, A. G., Nugent, P. E., Gilliland, R. L., et al. 2001, ApJ, 560, 49

Riess, A. G., Macri, L., Casertano, S., et al. 2011, ApJ, 730, 119

Robin, A. C., Luri, X., Reylé, C., et al. 2012, A&A, 543, A100

Rubakov, V. A., Sazhin, M. V., & Veryaskin, A. V. 1982, Physics Letters B, 115, 189

Saastamoinen, J. 1972, in Washington DC American Geophysical Union Geophysical Monograph Series, Vol. 15, The Use of Artificial Satellites for Geodesy, ed. S. W. Henriksen, A. Mancini, & B. H. Chovitz, 247

Sato, K. 1981, MNRAS, 195, 467

Schlüter, W., & Behrend, D. 2007, Journal of Geodesy, 81, 379

Seljak, U. 1997, ApJ, 482, 6

Shaw, M. S., Romani, R. W., Cotter, G., et al. 2013, ApJ, 764, 135

Smoot, G., Bennett, C., Weber, R., et al. 1990, ApJ, 360, 685

Smoot, G. F., Bennett, C. L., Kogut, A., et al. 1992, ApJL, 396, L1

Souchay, J., Andrei, A. H., Barache, C., et al. 2009, A&A, 494, 799

—. 2015, A&A, 583, A75

Sovers, O. J., Fanselow, J. L., & Jacobs, C. S. 1998, Reviews of Modern Physics, 70, 1393

Sowards-Emmerd, D., Romani, R. W., Michelson, P. F., Healey, S. E., & Nolan, P. L. 2005, ApJ, 626, 95

Starobinsky, A. A. 1980, Physics Letters B, 91, 99

—. 1982, Physics Letters B, 117, 175

Strauss, M. A., Davis, M., Yahil, A., & Huchra, J. P. 1992, ApJ, 385, 421

Tegmark, M., & Peebles, P. J. E. 1998, ApJL, 500, L79

Thompson, A. R. 1999, in Astronomical Society of the Pacific Conference Series, Vol. 180, Synthesis Imaging in Radio Astronomy II, ed. G. B. Taylor, C. L. Carilli, & R. A. Perley, 11

Titov, O. 2009, in 19th European VLBI for Geodesy and Astrometry Working Meeting, ed. G. Bourda, P. Charlot, & A. Collioud, 14–18

Titov, O. 2010, MNRAS, 407, L46

Titov, O., & Lambert, S. 2013, A&A, 559, A95

—. 2016, ArXiv e-prints, arXiv:1603.09416

Titov, O., Lambert, S. B., & Gontier, A.-M. 2011, A&A, 529, A91

Tonry, J., & Schneider, D. P. 1988, AJ, 96, 807

Tonry, J. L., Ajhar, E. A., & Luppino, G. A. 1990, AJ, 100, 1416

Truebenbach, A. E., & Darling, J. 2017, ApJS, 233, 3

Tully, R. B., Courtois, H., Hoffman, Y., & Pomarède, D. 2014, Nature, 513, 71

van Haasteren, R., Levin, Y., Janssen, G. H., et al. 2011, MNRAS, 414, 3117

Walker, R. C. 1999, in Astronomical Society of the Pacific Conference Series, Vol. 180, Synthesis Imaging in Radio Astronomy II, ed. G. B. Taylor, C. L. Carilli, & R. A. Perley, 433

Walker, R. C. 2000, in International VLBI Service for Geodesy and Astrometry 2000 General Meeting Proceedings, ed. F. Takahashi, 42

Walker, R. C. 2014, VLBA Scientific Memos 37

Wenger, M., Ochsenbein, F., Egret, D., et al. 2000, A&AS, 143, 9

Weymann, R. J., Morris, S. L., Foltz, C. B., & Hewett, P. C. 1991, ApJ, 373, 23

Xu, J., & Han, J. L. 2014, MNRAS, 442, 3329

Xu, M. H., Wang, G. L., & Zhao, M. 2012, A&A, 544, A135

—. 2013, MNRAS, 430, 2633

York, D. G., Adelman, J., Anderson, Jr., J. E., et al. 2000, AJ, 120, 1579

Zhang, B. R., Childress, M. J., Davis, T. M., et al. 2017, MNRAS, 471, 2254

Appendix A

The VLBA Extragalactic Proper Motion Catalog

Table A.1 lists the complete the VLBA Extragalactic Proper Motion Catalog. The catalog contains 713 radio sources. From left to right, the columns are the IVS name of the source, the source's right ascension and associated uncertainty (in milliseconds) from the most recent VLBA observing epoch, the declination and associated uncertainty (in milliarcseconds) from the most recent VLBA observing epoch, the proper motion in right ascension and associated uncertainty (both in μas yr^{-1}), the number of sessions used to determine the source's proper motion in right ascension, the reduced χ^2 of the derived proper motion in right ascension, the same quantities for the proper motion in declination, the number of years of VLBI observations used in determining the proper motion, the Modified Julian Date of the most recent VLBI session used to measure the object's position, a flag to indicate proper motions added or updated by this paper, the redshift of the source, a flag indicating the quality of the reported redshift, and the source from which the redshift data were obtained. The redshift flag is obtained from the OCARS catalog (Malkin 2016) and indicates the following potential limitations to the reported redshift: "(a) photometric, (b) unreliable or doubtful identification, (c) substantially different estimates in the literature, (d) lower limit, and (e) imaging." See the OCARS catalog for more information about the redshift of a particular source.

Table A.1. The VLBA Extragalactic Proper Motion Catalog

IVS	RA (J2000 h:m:s)	σ_α (ms)	Dec (J2000 d:′:″)	σ_δ (mas)	μ_α (μas/yr)	$\sigma_{\mu,\alpha}$ (μas/yr)	N_α	χ^2_α	μ_δ (μas/yr)	$\sigma_{\mu,\delta}$ (μas/yr)	N_δ	χ^2_δ	Length (years)	Last Obs. (MJD)	New PM	z	z flag	z Source
2358+189	00:01:08.621513	0.608	+19:14:33.800894	1.93	5.59	8.49	97	1.5	-1.12	9.45	97	1.1	21.2	57819.9		3.10		OCARS
0002-478	00:04:35.655473	0.015	-47:36:19.604493	0.26	-24.75	13.45	45	1.4	-47.34	20.18	45	1.1	22.8	57659.8		0.88		OCARS
0003+380	00:05:57.175296	0.172	+38:20:15.157041	17.96	-13.99	9.58	29	2.4	-2.21	11.12	29	1.7	22.9	57102.7		0.23		OCARS
0003-066	00:06:13.892882	0.003	-06:23:35.335489	0.05	0.27	1.29	1437	2.0	3.64	1.80	1437	2.2	23.5	57840.9		0.35		OCARS
IIIZW2	00:10:31.005918	0.029	+10:58:29.504257	1.35	5.17	12.17	62	2.8	-10.08	12.58	62	1.7	26.7	57776.2		0.09		OCARS
0007+171	00:10:33.991756	0.522	+17:24:18.762349	0.49	132.71	26.67	26	3.8	9.21	14.77	26	1.3	20.0	55244.7		1.60		OCARS
0008-264	00:11:01.246780	0.017	-26:12:33.377442	0.23	0.43	7.31	180	1.9	0.26	9.41	180	2.0	24.6	57840.9		1.10		OCARS
0010+405	00:13:31.130193	0.008	+40:51:37.144086	0.12	-3.90	3.06	67	1.2	7.63	4.64	67	1.6	25.6	57784.9		0.26		OCARS
0013-005	00:16:11.088362	0.095	-00:15:12.449356	2.57	1.61	5.51	59	1.4	3.95	7.81	59	1.3	23.7	57751.0		1.58		OCARS
0017+200	00:19:37.854481	0.003	+20:21:45.644651	0.03	-19.24	9.99	214	2.7	-0.74	4.25	214	2.2	21.2	57840.9				OCARS
0016+731	00:19:45.786374	0.009	+73:27:30.017554	0.04	-5.58	1.07	787	6.4	5.06	0.69	787	3.0	27.2	57840.9		1.78		OCARS
0019+058	00:22:32.441157	0.028	+06:08:04.268929	0.28	-3.79	4.61	209	1.5	-1.60	7.58	209	1.3	22.4	57837.0		2.86	d	APO
0025+197	00:28:29.818488	0.010	+20:00:26.744174	0.58	10.65	6.09	63	1.4	-2.15	10.63	63	0.9	21.0	57767.0		1.55		OCARS
0026+346	00:29:14.242539	0.184	+34:56:32.247728	1.44	19.89	64.22	10	3.2	45.42	57.51	10	1.3	26.5	57764.9		0.52		OCARS
0035-252	00:38:14.735497	0.006	-24:59:02.235519	0.17	-9.17	10.81	105	1.6	-0.35	19.07	105	1.6	19.2	57646.8		0.50	c	OCARS
0035+413	00:38:24.843626	0.026	+41:37:06.000322	0.18	-6.38	5.38	48	1.9	-3.02	11.28	48	1.5	22.9	57791.9		1.35		OCARS
0039+230	00:42:04.545160	0.010	+23:20:01.062033	0.16	-13.96	10.05	24	2.7	54.43	24.56	24	3.9	17.3	55250.7		1.43		OCARS
NGC0262	00:48:47.141490	0.004	+31:57:25.083955	0.08	8.64	10.34	24	1.4	-86.82	47.90	24	4.1	13.6	55168.8		0.01		OCARS
0047+023	00:49:43.235644	0.248	+02:37:03.796716	13.61	-0.15	12.15	25	1.4	28.59	21.96	25	1.2	21.6	57806.9		1.44	a	OCARS
0047-579	00:49:59.472946	0.035	-57:38:27.338886	1.33	-34.41	14.28	32	1.5	-29.40	26.80	32	1.0	19.9	55420.6		1.80		OCARS
0048-097	00:50:41.317407	0.023	-09:29:05.210140	0.14	-3.54	1.29	1675	1.8	-5.30	1.24	1675	1.5	27.1	57802.0		0.63	c	OCARS
0048-427	00:51:09.501827	0.014	-42:26:33.293332	0.55	5.71	11.56	118	1.8	47.16	18.49	118	2.1	15.1	57810.1		1.75	c	OCARS

Table A.1 (cont'd)

IVS	RA (J2000 h:m:s)	σ_α (ms)	Dec (J2000 d:′:″)	σ_δ (mas)	μ_α (μas/yr)	$\sigma_{\mu,\alpha}$ (μas/yr)	N_α	χ^2_α	μ_δ (μas/yr)	$\sigma_{\mu,\delta}$ (μas/yr)	N_δ	χ^2_δ	Length (years)	Last Obs. (MJD)	New PM	z	z flag	z Source
0054+161	00:56:55.294323	0.006	+16:25:13.340964	0.13	3.99	7.63	115	1.4	0.67	10.47	115	1.3	20.9	57786.0		0.21		OCARS
NGC0315	00:57:48.883334	0.025	+30:21:08.811804	0.57	2.07	5.07	24	1.2	-28.98	5.93	24	1.6	20.7	57788.0	*	0.02		OCARS
0055-059	00:58:05.066329	0.017	-05:39:52.278051	1.20	1.21	7.64	106	1.4	8.83	25.67	106	2.3	19.9	57837.0		1.25		OCARS
0056-572	00:58:46.581171	0.023	-56:59:11.470110	0.41	12.34	19.70	13	0.4	23.07	43.39	13	0.9	24.8	57151.7		0.02		OCARS
0056-001	00:59:05.515020	0.111	+00:06:51.620322	0.36	24.77	52.02	16	3.3	-56.62	48.10	16	1.9	26.7	57777.9		0.72		APO
0059+581	01:02:45.762395	0.012	+58:24:11.136572	0.08	-7.52	0.45	2441	2.9	-2.84	0.46	2441	3.1	25.0	57833.9		0.64		OCARS
0104-408	01:06:45.107967	0.008	-40:34:19.960315	0.12	-0.10	1.91	1284	2.1	-2.06	2.30	1284	2.4	26.6	57840.9		0.58		OCARS
0107-610	01:09:15.475256	0.044	-60:49:48.459134	0.45	-18.28	9.24	39	0.8	-1.06	26.58	39	1.2	13.3	57717.0				OCARS
0108+388	01:11:37.316792	0.011	+39:06:28.104611	0.15	-30.32	54.98	11	36.7	18.97	19.34	11	5.5	23.6	57707.9		0.67		OCARS
0109+224	01:12:05.824687	0.028	+22:44:38.786042	0.32	-3.34	3.83	102	2.1	-8.21	5.39	102	1.3	25.5	57735.9		0.27	b	OCARS
0110+495	01:13:27.006809	0.016	+49:48:24.043140	0.24	-9.11	5.49	55	2.2	16.37	6.49	55	1.8	22.7	57715.9		0.39		OCARS
0111+021	01:13:43.144944	0.039	+02:22:17.316734	1.65	3.04	2.41	231	1.3	-3.14	3.75	231	1.3	27.0	57788.0	*	0.05		OCARS
0112-017	01:15:17.099944	0.045	-01:27:04.577203	0.69	-47.90	38.25	14	9.5	7.61	19.37	14	2.0	24.4	57731.0		1.36	c	OCARS
0113-118	01:16:12.522047	0.038	-11:36:15.435046	0.46	-12.80	8.75	13	1.6	-16.68	19.78	13	2.3	23.4	57731.0		0.67		OCARS
0115-214	01:17:48.779917	0.243	-21:11:06.632879	2.57	7.19	4.75	270	1.4	-4.62	7.49	270	1.5	19.7	57816.0		1.49		OCARS
0116-219	01:18:57.262170	0.012	-21:41:30.140245	0.10	18.77	8.23	59	1.5	-31.86	13.26	59	1.5	19.6	57788.0		1.16		OCARS
0116+319	01:19:35.003397	0.008	+32:10:50.058043	0.17	-77.68	189.41	5	4.3	256.98	169.36	5	0.5	23.9	57700.0	*	0.06		OCARS
0118-272	01:20:31.663904	0.234	-27:01:24.594316	24.30	12.30	58.97	25	2.0	34.91	70.80	25	2.1	16.9	55810.1		0.56	d	OCARS
0119+115	01:21:41.595048	0.004	+11:49:50.413674	0.27	6.23	1.01	1449	1.9	50.85	2.50	1449	2.5	27.1	57837.0		0.57		OCARS
0119+041	01:21:56.861652	0.050	+04:22:24.734613	1.38	-8.55	1.86	1648	1.9	5.59	1.95	1648	1.4	27.2	57840.9		0.64		OCARS
0122-003	01:25:28.843871	0.043	-00:05:55.931391	0.66	37.27	390.91	10	1.2	27.73	500.66	10	1.1	17.3	56897.1		1.07		OCARS
0123+257	01:26:42.792712	0.184	+25:59:01.322263	40.00	-8.17	4.94	33	0.9	-11.59	16.12	33	2.2	23.9	57102.7		2.36		OCARS

Table A.1 (cont'd)

IVS	RA (J2000 h:m:s)	σ_α (ms)	Dec (J2000 d:′:″)	σ_δ (mas)	μ_α (μas/yr)	$\sigma_{\mu,\alpha}$ (μas/yr)	N_α	χ^2_α	μ_δ (μas/yr)	$\sigma_{\mu,\delta}$ (μas/yr)	N_δ	χ^2_δ	Length (years)	Last Obs. (MJD)	New PM	z	z flag	z Source
0130-171	01:32:43.487424	0.030	-16:54:48.522039	0.44	-13.25	10.68	35	1.0	21.05	15.21	35	0.8	13.5	55545.5		1.02		OCARS
0131-522	01:33:05.762524	0.025	-52:00:03.945460	0.54	-21.86	8.81	194	2.0	53.18	12.77	194	1.9	26.5	57837.0		0.02		OCARS
0133+476	01:36:58.594813	0.006	+47:51:29.100417	0.09	-1.58	0.69	1777	2.7	1.92	0.71	1777	2.3	27.2	57826.9		0.86		OCARS
0134+311	01:37:08.733675	0.031	+31:22:35.855439	0.39	6.16	4.12	303	1.4	9.57	8.82	303	1.2	20.7	57781.0		1.72		OCARS
0135-247	01:37:38.346431	0.056	-24:30:53.885476	0.39	-14.45	22.71	36	1.6	29.70	15.41	36	0.9	20.0	57102.7		0.84		OCARS
3C48	01:37:41.299616	0.149	+33:09:35.124473	8.73	100.83	447.99	12	2.7	-703.82	834.43	12	3.2	25.7	57595.6		0.37		OCARS
0138-097	01:41:25.832112	0.014	-09:28:43.674070	0.42	-6.30	10.36	66	2.9	4.24	10.38	66	2.4	21.4	57776.2		0.73	c	OCARS
0146+056	01:49:22.370895	0.025	+05:55:53.567986	0.84	-16.53	12.60	44	1.4	17.26	22.95	44	1.0	23.4	56641.8		2.35		OCARS
0148+274	01:51:27.146166	0.017	+27:44:41.793806	0.19	-7.42	17.47	21	3.7	8.36	16.23	21	2.2	18.0	55306.6		1.26		OCARS
0149+218	01:52:18.059046	0.009	+22:07:07.699858	0.11	0.09	2.90	57	1.7	3.88	4.77	57	2.1	27.1	57809.0		1.32		OCARS
0150-334	01:53:10.121790	0.107	-33:10:25.859623	6.07	40.96	46.42	24	0.8	3.95	35.85	24	1.0	20.2	55545.5		0.61		OCARS
0151+474	01:54:56.289884	0.013	+47:43:26.540020	0.20	-3.00	3.77	106	1.6	6.02	4.08	106	1.4	22.2	57840.9		1.03		OCARS
0153+744	01:57:34.967170	0.638	+74:42:43.220735	2.13	-9.50	16.57	21	2.7	-20.11	21.25	21	4.6	18.7	55306.6		2.34		OCARS
0159+723	02:03:33.384946	0.013	+72:32:53.667298	0.06	-11.15	5.11	54	1.5	1.99	4.60	54	1.4	25.4	57777.9		0.39	e	NED
0201+113	02:03:46.657052	0.019	+11:34:45.409948	0.30	0.76	1.78	734	1.6	-10.49	2.92	734	1.7	26.7	57777.9		3.64		OCARS
0202-172	02:04:57.674305	0.170	-17:01:19.840406	0.85	-12.50	4.31	88	1.7	-12.06	13.44	88	2.9	21.5	57464.4		1.74		OCARS
0202+319	02:05:04.925353	0.004	+32:12:30.095709	0.06	4.27	1.98	392	2.4	1.99	3.25	392	2.4	27.2	57837.0		1.47		OCARS
0206+136	02:09:35.998348	0.026	+13:52:00.751894	0.15	2.51	5.90	38	1.1	-0.72	16.42	38	0.8	21.1	57795.0		0.63		OCARS
0215+015	02:17:48.954751	0.004	+01:44:49.698899	0.05	1.73	3.29	238	2.6	-9.89	4.66	238	3.1	24.4	57819.9		1.72		OCARS
0216+011	02:19:07.024500	0.005	+01:20:59.866147	0.15	3.03	6.68	4	4.1	3.20	15.11	4	1.3	21.6	57805.1	*	1.62		OCARS
0219+428	02:22:39.611497	0.006	+43:02:07.799136	0.09	-5.85	9.97	21	1.6	18.61	12.25	21	1.0	17.9	55201.7		0.37	b	OCARS
0220-349	02:22:56.401755	0.058	-34:41:28.730136	0.59	-3.21	9.14	57	1.7	8.00	8.97	57	1.4	21.1	57102.7		1.49		OCARS

Table A.1 (cont'd)

IVS	RA (J2000 h:m:s)	σ_α (ms)	Dec (J2000 d:′:″)	σ_δ (mas)	μ_α (μas/yr)	$\sigma_{\mu,\alpha}$ (μas/yr)	N_α	χ^2_α	μ_δ (μas/yr)	$\sigma_{\mu,\delta}$ (μas/yr)	N_δ	χ^2_δ	Length (years)	Last Obs. (MJD)	New PM	z	z flag	z Source
0221+067	02:24:28.428189	0.007	+06:59:23.341508	0.22	-8.87	4.32	73	1.4	-5.78	6.66	73	1.8	21.5	57805.1		0.51		OCARS
4C67.05	02:28:50.051492	0.089	+67:21:03.030030	0.42	-5.98	3.80	33	1.3	-12.79	8.64	33	2.8	25.7	57464.4		0.52		OCARS
0227-369	02:29:28.449064	0.048	-36:43:56.821351	2.21	6.58	11.87	54	1.7	-18.34	13.82	54	1.1	14.8	57728.9		2.12		OCARS
0230-790	02:29:34.946700	0.105	-78:47:45.601059	0.26	2.18	6.14	98	1.1	23.64	9.55	98	1.4	24.7	57784.9		1.07		OCARS
0229+131	02:31:45.894077	0.006	+13:22:54.716144	0.08	13.87	0.72	2159	1.9	7.37	0.79	2159	1.7	27.2	57837.0		2.06		OCARS
0234-301	02:36:31.169424	0.007	-29:53:55.541140	0.26	-32.36	14.57	40	2.0	-7.13	18.29	40	1.5	12.8	57810.1		2.10		OCARS
0235-618	02:36:53.245718	0.064	-61:36:15.183750	0.33	-1.05	16.27	30	1.0	21.28	19.80	30	1.2	12.8	57525.4		0.47		OCARS
0234+285	02:37:52.405697	0.006	+28:48:08.989832	0.13	4.73	1.10	878	2.0	-2.23	1.58	878	1.8	27.1	57805.1		1.21		OCARS
0237-027	02:39:45.472266	0.006	-02:34:40.914460	0.09	9.15	3.92	335	1.8	-11.10	7.16	335	1.8	23.5	57837.0		1.12		OCARS
0237+040	02:39:51.263043	0.009	+04:16:21.411580	0.16	0.33	5.61	36	1.5	-0.80	6.25	36	1.0	26.2	57758.0		0.98		OCARS
0237-233	02:40:08.174936	0.250	-23:09:15.732949	1.58	-70.82	57.42	38	7.7	-72.38	51.28	38	5.2	20.8	55728.4		2.22		OCARS
0239+175	02:42:24.268262	0.006	+17:42:58.849222	0.14	-22.51	9.87	26	1.3	24.64	15.51	26	0.8	20.5	57576.6		0.55		OCARS
0239+108	02:42:29.171319	0.644	+11:01:00.719648	11.19	-10.39	4.37	83	1.4	-1.17	7.79	83	1.2	24.1	56925.1		2.68		OCARS
0241+622	02:44:57.695195	2.260	+62:28:06.521326	23.78	-34.96	17.32	28	1.8	9.20	14.84	28	3.1	26.2	57798.9	*	0.04		OCARS
0248+430	02:51:34.536731	0.010	+43:15:15.829319	0.14	-11.58	9.05	27	4.8	24.75	11.20	27	3.2	20.1	55264.7		1.31		OCARS
0252-549	02:53:29.180410	0.039	-54:41:51.437118	1.37	-10.73	14.49	24	0.6	-0.89	37.09	24	0.8	19.3	55420.6		0.54		OCARS
0256+075	02:59:27.076625	0.004	+07:47:39.643218	0.12	8.65	8.47	44	1.9	0.39	19.63	44	1.8	19.1	55112.8		0.89		OCARS
0256-005	02:59:28.516113	0.028	-00:19:59.975013	0.58	5.26	8.06	176	1.9	-11.07	6.79	176	1.6	19.8	57823.0		2.00		OCARS
0300+470	03:03:35.242216	0.005	+47:16:16.275439	0.06	-1.50	0.81	628	1.3	0.42	1.05	628	1.5	27.0	57758.0		0.47	b	OCARS
0302-623	03:03:50.631367	0.034	-62:11:25.550060	0.15	15.49	5.47	82	1.6	1.81	4.80	82	1.2	26.2	57717.0		1.35		OCARS
0302+625	03:06:42.659541	0.043	+62:43:02.024257	0.35	3.24	4.34	49	1.2	0.16	7.74	49	2.1	22.4	57802.0				OCARS
NGC1218	03:08:26.223819	0.003	+04:06:39.300921	0.10	15.86	4.21	33	1.3	6.16	8.19	33	1.4	20.2	57700.0	*	0.03		OCARS

Table A.1 (cont'd)

IVS	RA (J2000 h:m:s)	σ_α (ms)	Dec (J2000 d:′:″)	σ_δ (mas)	μ_α (μas/yr)	$\sigma_{\mu,\alpha}$ (μas/yr)	N_α	χ^2_α	μ_δ (μas/yr)	$\sigma_{\mu,\delta}$ (μas/yr)	N_δ	χ^2_δ	Length (years)	Last Obs. (MJD)	New PM	z	z flag	z Source
0306+102	03:09:03.623481	0.009	+10:29:16.341050	0.08	-4.48	5.78	90	0.9	-0.36	5.38	90	1.2	23.2	57725.0		0.86		OCARS
0308-611	03:09:56.099182	0.044	-60:58:39.056547	0.36	-6.06	2.33	703	2.3	-12.10	2.90	703	2.0	26.9	57840.9		1.48		OCARS
0307+380	03:10:49.879930	0.011	+38:14:53.838068	0.14	-6.34	4.41	213	1.6	4.83	7.11	213	1.6	21.6	57837.0		0.82		OCARS
0309+411	03:13:01.962114	0.006	+41:20:01.183507	0.06	-7.98	4.08	51	1.7	-11.93	6.31	51	2.7	26.3	57786.0		0.13		OCARS
0317+188	03:19:51.256693	0.020	+19:01:31.291658	0.45	-23.82	7.29	43	1.5	14.78	11.62	43	1.7	21.0	57679.8		0.30		OCARS
0319+121	03:21:53.103484	0.024	+12:21:13.953369	0.57	3.77	3.18	71	1.2	-17.20	22.35	71	3.4	26.0	57421.3		2.66		OCARS
0322+222	03:25:36.814429	0.029	+22:24:00.364426	0.40	-4.62	3.02	483	2.1	6.73	2.30	483	1.6	21.2	57837.0		2.06		OCARS
0325+395	03:28:50.312089	0.006	+39:40:44.566342	0.08	6.47	37.95	28	2.1	-14.27	43.16	28	2.1	20.5	57723.9				OCARS
0326+278	03:29:57.669326	0.019	+27:56:15.498382	0.41	-14.45	52.88	14	4.2	-16.71	18.82	14	0.9	27.0	57777.9		1.53		OCARS
0332-403	03:34:13.654460	0.011	-40:08:25.397879	0.12	-0.44	4.30	661	2.8	17.70	5.02	661	2.7	26.5	57833.9		1.45		OCARS
0332+078	03:34:53.316650	0.016	+08:00:14.418207	1.08	14.94	14.37	127	1.1	-22.46	11.75	127	1.5	21.6	57806.9		1.98		OCARS
0334-546	03:35:53.924843	0.019	-54:30:25.114865	0.21	12.22	9.07	37	0.6	10.35	18.03	37	1.0	24.4	57659.8				OCARS
NRAO140	03:36:30.107403	0.424	+32:18:29.345299	4.76	-0.61	4.88	116	1.8	-9.07	4.91	116	1.2	25.8	57520.5		1.26		OCARS
0335-364	03:36:54.023435	0.014	-36:16:06.224168	0.52	-42.28	31.33	17	1.5	25.51	31.65	17	1.3	18.8	57786.0		1.54		OCARS
CTA26	03:39:30.937787	0.006	-01:46:35.804020	0.06	1.14	1.23	2244	2.8	-1.78	0.90	2244	2.0	26.9	57837.0		0.85		OCARS
0338-214	03:40:35.607603	0.299	-21:19:31.177442	4.12	-7.20	5.33	157	1.9	2.42	7.07	157	1.4	23.0	57816.0		0.22		OCARS
0340+362	03:43:28.952416	0.024	+36:22:12.429882	0.31	23.67	6.90	74	1.3	34.44	14.50	74	1.2	20.7	57809.0		1.48	b	OCARS
0341+158	03:44:23.172097	0.044	+15:59:43.368877	0.48	-8.45	12.62	17	1.0	2.42	32.98	17	1.2	22.2	57784.9		2.28		OCARS
0342+147	03:45:06.416524	0.008	+14:53:49.558018	0.20	-15.62	5.68	51	1.5	-7.52	7.08	51	1.2	26.3	57810.1		1.56		OCARS
0346-279	03:48:38.144561	0.009	-27:49:13.565558	0.28	-9.22	7.52	135	1.6	-29.50	12.30	135	1.8	19.5	57810.1		0.99		OCARS
0345+460	03:49:18.741537	0.048	+46:09:59.656979	0.80	4.07	3.70	207	2.4	-3.08	5.26	207	1.5	20.6	57840.9		1.85		OCARS
0347-211	03:49:57.826682	0.012	-21:02:47.741612	0.14	-0.29	6.34	117	1.9	-7.23	6.44	117	1.3	19.7	57837.0		2.94		OCARS

Table A.1 (cont'd)

IVS	RA (J2000 h:m:s)	σ_α (ms)	Dec (J2000 d:′:″)	σ_δ (mas)	μ_α (μas/yr)	$\sigma_{\mu,\alpha}$ (μas/yr)	N_α	χ^2_α	μ_δ (μas/yr)	$\sigma_{\mu,\delta}$ (μas/yr)	N_δ	χ^2_δ	Length (years)	Last Obs. (MJD)	New PM	z	z flag	z Source
NRAO150	03:59:29.747222	0.114	+50:57:50.162138	1.01	4.24	4.09	313	1.5	16.28	6.28	313	1.8	27.2	57833.9		1.52		OCARS
0358+210	04:01:45.166086	0.010	+21:10:28.587310	0.33	5.24	6.14	53	1.3	0.23	8.54	53	1.6	21.1	57805.1		0.83		OCARS
0400-319	04:02:21.266397	0.325	-31:47:25.977414	20.03	-28.28	11.29	78	1.8	9.01	16.13	78	2.0	24.3	57626.8		1.29		OCARS
0400+258	04:03:05.586194	0.084	+26:00:01.505456	1.09	52.22	10.18	65	2.5	-13.89	9.59	65	1.2	26.3	57520.5		2.11		OCARS
0402-362	04:03:53.749928	0.009	-36:05:01.913097	0.28	5.30	2.64	632	2.1	6.52	3.50	632	2.3	27.1	57810.1		1.42		OCARS
0403-132	04:05:34.003373	0.024	-13:08:13.690974	0.46	1.01	3.61	92	1.7	-7.77	7.97	92	1.8	22.4	57840.9		0.57		OCARS
0405-385	04:06:59.035349	0.014	-38:26:28.042033	0.43	10.69	4.10	320	2.2	22.28	6.90	320	2.4	26.4	57805.1		1.28		OCARS
0405-123	04:07:48.429880	0.591	-12:11:36.580317	43.53	-7.71	10.81	40	1.5	22.00	21.56	40	2.2	22.8	57102.7		0.57		OCARS
0406-127	04:09:05.769497	0.195	-12:38:48.160994	14.86	12.73	5.99	52	1.3	1.69	11.97	52	1.3	21.8	57751.0		1.56		OCARS
0406+121	04:09:22.008686	0.017	+12:17:39.848053	0.37	-29.83	19.23	32	1.9	45.26	32.22	32	2.4	20.1	55250.7		0.50	c	OCARS
0409+229	04:12:43.666895	0.025	+23:05:05.452830	0.37	7.92	12.20	19	1.0	4.37	13.55	19	0.9	21.1	57806.9		1.22		OCARS
0414-189	04:16:36.544449	0.008	-18:51:08.340230	0.29	1.54	4.67	147	1.4	9.57	6.18	147	1.4	21.9	57805.1		1.54	c	OCARS
0415+379	04:18:21.277203	0.020	+38:01:35.799607	0.30	-13.61	4.85	9	24.1	58.51	5.84	9	37.3	17.4	57823.0	*	0.05		OCARS
0415+398	04:19:22.549542	0.021	+39:55:28.977324	0.19	-18.26	7.89	95	2.1	7.95	7.01	95	1.2	20.8	57837.0				OCARS
0420+022	04:22:52.214645	0.006	+02:19:26.930732	0.07	3.21	4.72	151	1.9	-11.19	7.27	151	2.1	21.5	57774.0		2.28		OCARS
0420-014	04:23:15.800721	0.006	-01:20:33.065804	0.07	-9.26	0.70	1194	1.9	-8.03	1.01	1194	2.0	27.1	57809.0		0.92		OCARS
0420+417	04:23:56.010000	0.238	+41:50:02.714658	1.18	3.48	11.28	45	2.0	11.53	8.80	45	1.2	25.6	57520.5				OCARS
0422-380	04:24:42.243663	0.021	-37:56:20.784086	0.31	-0.74	7.03	75	1.9	2.82	7.94	75	1.6	26.3	57764.9		0.78		OCARS
0422+004	04:24:46.842063	0.068	+00:36:06.329062	0.93	2.62	4.67	112	1.9	16.82	9.24	112	2.0	27.0	57777.9		0.27		APO
0423+051	04:26:36.604072	0.026	+05:18:19.872465	1.13	-16.18	23.56	18	1.8	41.22	16.99	18	0.7	18.5	54937.9		1.33		OCARS
0423+233	04:26:55.734812	0.004	+23:27:39.633401	0.08	9.34	13.47	11	1.2	-0.22	51.22	11	2.7	20.7	57646.8		0.55		OCARS
0426-380	04:28:40.424361	0.063	-37:56:19.580476	0.47	-10.37	9.32	101	1.2	-6.04	12.53	101	1.7	25.0	57291.6		1.11		OCARS

Table A.1 (cont'd)

IVS	RA (J2000 h:m:s)	σ_α (ms)	Dec (J2000 d:′:″)	σ_δ (mas)	μ_α (μas/yr)	$\sigma_{\mu,\alpha}$ (μas/yr)	N_α	χ^2_α	μ_δ (μas/yr)	$\sigma_{\mu,\delta}$ (μas/yr)	N_δ	χ^2_δ	Length (years)	Last Obs. (MJD)	New PM	z	z flag	z Source
0426+273	04:29:52.960768	0.008	+27:24:37.876096	0.17	-2.52	2.62	67	1.0	-20.57	6.06	67	1.5	20.8	57810.1				OCARS
0430+289	04:33:37.829853	0.028	+29:05:55.477241	0.42	2.15	2.41	162	1.1	7.88	2.97	162	1.4	21.3	57805.1		0.97	b	OCARS
0434-188	04:37:01.482699	0.082	-18:44:48.621640	3.65	0.51	5.71	217	1.7	17.85	16.27	217	2.1	27.0	57791.9		2.70		OCARS
0436-129	04:38:35.021007	0.016	-12:51:03.359295	0.27	2.60	9.11	75	1.5	18.36	15.13	75	1.6	19.7	57774.0		1.28		OCARS
0437-454	04:39:00.854581	0.028	-45:22:22.561704	2.18	-12.37	10.22	113	1.8	5.94	10.77	113	1.5	24.8	57810.1		2.02	b	OCARS
NRAO190	04:42:38.660931	0.156	-00:17:43.421434	1.63	-20.37	9.96	134	2.0	-27.71	3.99	134	1.4	26.9	57759.0		0.84		OCARS
0440+345	04:43:31.635207	0.009	+34:41:06.664235	0.22	-1.55	2.59	62	1.9	-4.20	3.60	62	1.8	22.8	57810.1				OCARS
0442+389	04:46:11.494121	0.123	+39:00:17.099162	1.29	0.80	15.20	35	1.2	-29.21	26.51	35	1.2	20.1	57598.7		0.41		OCARS
0446+112	04:49:07.671096	0.007	+11:21:28.596431	0.22	9.19	4.14	289	2.0	-4.46	4.70	289	1.7	22.5	57776.2		2.15		OCARS
0444+634	04:49:23.310601	0.009	+63:32:09.434116	0.07	8.31	21.99	11	2.1	3.43	35.11	11	2.3	22.8	57743.9		0.78		OCARS
0454-810	04:50:05.440358	0.103	-81:01:02.231420	0.18	1.06	5.83	152	2.3	-3.21	6.64	152	1.3	26.4	57816.0		0.44		OCARS
0454-463	04:55:50.772471	0.029	-46:15:58.679593	0.19	-10.63	20.01	129	2.8	39.05	18.84	129	1.9	23.9	57733.0		0.85		OCARS
0454-234	04:57:03.179213	0.009	-23:24:52.020340	0.08	-3.78	0.72	2932	2.0	-7.07	0.80	2932	1.8	27.2	57837.0		1.00		OCARS
0457+024	04:59:52.050649	0.018	+02:29:31.176717	0.32	9.82	11.20	63	1.9	39.89	11.13	63	1.5	19.7	55118.8		2.38		OCARS
0458-020	05:01:12.809878	0.008	-01:59:14.256443	0.09	-2.63	0.87	2329	2.0	-10.37	0.79	2329	1.6	26.7	57837.0		2.29		OCARS
0458+138	05:01:45.270809	0.011	+13:56:07.219323	0.35	3.72	8.56	22	1.9	-9.73	23.07	22	2.2	21.8	57805.1				OCARS
0459+060	05:02:15.445852	0.031	+06:09:07.493101	0.33	-48.98	37.11	10	1.8	-51.02	31.54	10	0.4	21.8	57666.8		1.11		OCARS
0459+135	05:02:33.219523	0.008	+13:38:10.958704	0.12	0.29	11.32	11	2.1	0.33	12.16	11	1.7	20.9	57715.9		0.35		APO
0500+019	05:03:21.197148	0.005	+02:03:04.676648	0.13	-15.35	25.88	13	6.4	24.70	21.64	13	3.3	26.7	57786.0		0.58	c	OCARS
0503-608	05:04:01.701072	0.234	-60:49:52.539881	0.90	-23.22	87.64	15	1.1	-19.33	38.73	15	0.2	20.0	55420.6		1.04		OCARS
0502+049	05:05:23.184675	0.010	+04:59:42.723811	0.20	-4.30	15.81	27	2.9	-16.00	18.07	27	2.5	18.2	55285.6		0.95		OCARS
0506-612	05:06:43.988777	0.025	-61:09:40.994207	0.23	16.94	7.02	95	1.0	-16.45	10.19	95	0.9	26.3	57717.0		1.09		OCARS

Table A.1 (cont'd)

IVS	RA (J2000 h:m:s)	σ_α (ms)	Dec (J2000 d:′:″)	σ_δ (mas)	μ_α (μas/yr)	$\sigma_{\mu,\alpha}$ (μas/yr)	N_α	χ^2_α	μ_δ (μas/yr)	$\sigma_{\mu,\delta}$ (μas/yr)	N_δ	χ^2_δ	Length (years)	Last Obs. (MJD)	New PM	z	z flag	z Source
0454+844	05:08:42.363585	0.191	+84:32:04.543811	0.31	6.53	4.71	322	1.5	19.32	3.09	322	1.4	26.3	57795.0		1.34		OCARS
0506+101	05:09:27.456942	0.123	+10:11:44.601331	1.70	-11.16	5.06	99	1.5	18.19	8.43	99	1.8	22.1	57816.0		0.62		OCARS
0507+179	05:10:02.369100	0.009	+18:00:41.581997	0.22	1.13	3.50	66	1.1	-3.75	5.29	66	1.3	26.3	57805.1		0.42		OCARS
0508+138	05:11:38.319347	0.180	+13:57:19.188447	2.77	13.46	16.92	11	2.1	-22.94	16.73	11	1.8	21.1	57798.9		1.70		OCARS
0511-220	05:13:49.114316	0.006	-21:59:16.091337	0.19	-4.70	9.32	13	1.5	21.46	17.87	13	2.1	23.4	57646.8		1.30		OCARS
0516-621	05:16:44.926129	0.016	-62:07:05.389517	0.14	-1.55	6.69	129	1.6	-10.43	7.55	129	1.1	24.8	57806.9		1.30		OCARS
0515+208	05:18:03.824664	0.038	+20:54:52.497558	0.41	3.21	10.83	65	2.8	8.05	14.45	65	1.7	20.9	57729.9		2.58		OCARS
3C138	05:21:09.886039	0.016	+16:38:22.051502	0.19	176.16	94.48	21	21.8	-74.97	42.70	21	2.4	20.2	55306.6		0.76		OCARS
0522-611	05:22:34.425527	0.066	-61:07:57.134080	1.10	1.18	10.00	43	0.6	2.54	9.91	43	0.6	25.5	57717.0		1.40		OCARS
0521-365	05:22:57.984655	0.019	-36:27:30.851168	0.19	-7.38	5.09	203	2.3	9.47	7.69	203	2.1	25.8	57520.5		0.06		OCARS
0524-460	05:25:31.400057	13.749	-45:57:54.685991	206.26	33.11	33.10	30	0.8	62.35	28.52	30	0.7	21.3	57525.4		1.48		OCARS
0524-485	05:26:16.671395	0.026	-48:30:36.794652	1.40	10.83	13.66	37	1.6	-0.47	21.20	37	2.0	12.3	57723.9		1.30		OCARS
0524+034	05:27:32.705432	0.024	+03:31:31.517775	0.85	1.93	7.80	96	1.9	-5.20	12.29	96	1.3	21.6	57810.1		0.51	c	OCARS
0530-727	05:29:30.042196	0.060	-72:45:28.507076	0.30	-7.06	4.15	154	1.4	-5.41	4.84	154	1.2	26.9	57837.0		1.34	a	OCARS
0528-250	05:30:07.962797	0.015	-25:03:29.899760	0.31	-9.64	7.29	38	1.6	7.53	12.18	38	1.7	24.7	57693.8		2.78		OCARS
0529+075	05:32:38.998447	0.048	+07:32:43.347047	1.05	5.89	169.49	14	2.3	11.67	115.36	14	2.5	26.2	57781.0		1.25		OCARS
0529+483	05:33:15.865796	0.004	+48:22:52.807829	0.05	-1.91	2.89	379	2.8	14.99	3.91	379	3.0	20.6	57840.9		1.16		OCARS
0534-611	05:34:35.772503	0.017	-61:06:07.073536	0.19	1.52	12.51	37	1.2	-23.61	11.92	37	0.7	12.9	57659.8		2.00		OCARS
0534-340	05:36:28.432373	0.009	-34:01:11.468199	0.31	-14.87	15.71	94	2.0	51.52	18.48	94	1.6	15.1	57810.1		0.68		OCARS
0537-441	05:38:50.361599	0.024	-44:05:08.935758	1.45	5.75	1.40	1827	2.3	7.42	1.46	1827	2.3	27.0	57837.0		0.89		OCARS
0537-158	05:39:32.009997	0.215	-15:50:30.326055	9.47	24.86	30.39	12	0.6	62.06	79.10	12	1.3	14.6	55810.1		0.95		OCARS
0536+145	05:39:42.365931	0.032	+14:33:45.562175	0.44	-1.80	4.46	167	1.7	4.92	4.49	167	1.6	22.4	57837.0		2.69		OCARS

Table A.1 (cont'd)

IVS	RA (J2000 h:m:s)	σ_α (ms)	Dec (J2000 d:′:″)	σ_δ (mas)	μ_α (μas/yr)	$\sigma_{\mu,\alpha}$ (μas/yr)	N_α	χ^2_α	μ_δ (μas/yr)	$\sigma_{\mu,\delta}$ (μas/yr)	N_δ	χ^2_δ	Length (years)	Last Obs. (MJD)	New PM	z	z flag	z Source
0537-286	05:39:54.281437	0.039	-28:39:55.948249	0.28	11.61	7.69	325	2.0	-11.62	5.64	325	1.7	25.4	57840.9		3.10		OCARS
0539-057	05:41:38.083387	0.020	-05:41:49.428390	0.28	-0.08	16.36	35	1.5	-22.21	27.37	35	1.5	17.4	55545.5		0.84		OCARS
3C147	05:42:36.137905	0.009	+49:51:07.233532	0.12	-0.75	10.28	22	2.3	-3.60	9.29	22	1.3	25.4	57805.1		0.55		OCARS
0544+273	05:47:34.148922	0.008	+27:21:56.842559	0.17	1.29	2.49	185	1.8	-7.24	3.86	185	1.7	22.4	57840.9				OCARS
0549-575	05:50:09.580101	0.030	-57:32:24.396850	0.25	1.16	14.39	45	1.4	32.56	17.09	45	0.9	12.5	57791.9		2.00		OCARS
0548+378	05:52:17.936895	0.009	+37:54:25.283260	0.30	-21.46	14.86	58	1.5	7.78	12.76	58	1.2	20.6	57767.0		0.81		OCARS
0552+398	05:55:30.805589	0.022	+39:48:49.165157	0.23	-0.23	0.38	3267	2.4	-3.59	0.44	3267	2.1	27.2	57816.0		2.37		OCARS
0554+242	05:57:04.713558	0.102	+24:13:55.299386	1.27	6.29	25.39	23	1.2	29.72	26.16	23	1.5	17.7	56524.8		3.23		OCARS
0556+238	05:59:32.033122	0.102	+23:53:53.927421	1.18	-0.54	1.37	708	1.5	-9.39	2.66	708	1.3	21.8	57809.0				OCARS
0600+177	06:03:09.130250	0.007	+17:42:16.810945	0.21	0.22	6.28	52	1.7	-1.00	8.47	52	1.2	22.2	57776.2		1.74		OCARS
0601+245	06:04:55.121427	0.009	+24:29:55.036636	0.09	41.92	84.21	20	3.0	16.84	26.94	20	1.8	14.7	57771.9		0.13		OCARS
0602+673	06:07:52.671429	0.172	+67:20:55.409110	0.99	0.49	0.85	916	1.7	20.39	1.21	916	2.0	22.2	57840.9		1.97		OCARS
0605-085	06:07:59.698891	2.361	-08:34:50.040654	72.28	-7.81	10.72	35	2.6	11.79	9.55	35	1.3	21.8	57520.5		0.87		OCARS
0606-223	06:08:59.686825	0.021	-22:20:20.956602	0.31	1.56	5.28	231	1.7	19.31	7.12	231	1.7	19.6	57791.9		1.93		OCARS
0610+260	06:13:50.139196	0.081	+26:04:36.720557	2.09	-72.35	37.20	14	1.9	32.65	23.89	14	0.5	20.7	57609.7		0.58		OCARS
0611+131	06:13:57.692794	0.073	+13:06:45.399920	1.51	0.91	9.60	24	1.9	17.07	19.43	24	1.9	18.6	56470.9		0.74		OCARS
0609+607	06:14:23.866187	0.030	+60:46:21.756003	0.23	5.07	5.78	26	1.5	-6.47	10.34	26	1.6	19.8	55138.7		2.70		OCARS
0613+570	06:17:16.922616	0.036	+57:01:16.422985	0.32	7.77	7.03	100	1.6	-11.98	7.42	100	1.3	22.6	57819.9				OCARS
0620+389	06:24:19.021267	0.022	+38:56:48.736537	0.55	-26.00	14.24	24	3.6	16.61	17.60	24	2.8	16.3	55334.6		3.47		OCARS
0615+820	06:26:03.008790	2.412	+82:02:25.568291	0.72	15.72	8.68	31	2.0	-16.25	12.67	31	1.6	26.2	57499.5		0.71		OCARS
0627-199	06:29:23.761861	0.031	-19:59:19.723574	0.24	-7.39	9.23	170	2.4	-3.01	8.26	170	1.9	19.7	57826.9		1.72	b	OCARS
0629-418	06:31:11.998052	0.014	-41:54:26.944879	0.42	12.73	30.96	27	1.0	70.73	99.91	27	1.6	24.7	57786.0		1.42		OCARS

Table A.1 (cont'd)

IVS	RA (J2000 h:m:s)	σ_α (ms)	Dec (J2000 d:′:″)	σ_δ (mas)	μ_α (μas/yr)	$\sigma_{\mu,\alpha}$ (μas/yr)	N_α	χ^2_α	μ_δ (μas/yr)	$\sigma_{\mu,\delta}$ (μas/yr)	N_δ	χ^2_δ	Length (years)	Last Obs. (MJD)	New PM	z	z flag	z Source
0632-235	06:34:59.000993	0.016	-23:35:11.956922	0.17	18.87	16.80	80	2.4	-4.87	14.40	80	1.9	11.6	57758.0		1.53		OCARS
0637-337	06:39:20.904615	0.128	-33:46:00.114895	1.24	44.65	57.55	20	0.6	-100.83	36.09	20	0.6	14.8	55810.1				OCARS
0636+680	06:42:04.257387	0.031	+67:58:35.620710	0.17	-6.91	6.35	72	2.0	2.90	4.03	72	1.4	25.9	57816.0		3.18		OCARS
0641+392	06:44:53.709518	0.159	+39:14:47.534502	0.85	3.78	16.64	219	1.8	11.40	8.75	219	1.4	20.8	57837.0		1.27		OCARS
0642+449	06:46:32.025943	0.011	+44:51:16.589671	0.10	-1.56	1.24	1474	4.9	-2.64	0.73	1474	1.9	25.6	57823.0		3.40		OCARS
0646-306	06:48:14.096500	0.097	-30:44:19.660417	1.26	-5.18	8.95	125	2.1	12.31	9.23	125	2.3	24.8	57833.9		1.15		OCARS
0648-165	06:50:24.581858	0.007	-16:37:39.725695	0.16	-6.80	5.43	370	2.0	-14.93	5.04	370	2.2	22.5	57823.0				OCARS
0651+410	06:55:10.024727	0.000	+41:00:10.159840	0.00	-3.38	3.75	8	2.0	-6.50	6.41	8	2.0	20.4	57688.5	*	0.02		OCARS
0656+082	06:59:17.995526	0.315	+08:13:30.946926	4.43	-7.57	2.94	793	1.5	18.16	5.43	793	1.3	21.6	57816.0		2.78		OCARS
0657+172	07:00:01.525540	0.007	+17:09:21.701419	0.09	7.41	1.36	458	2.2	-5.37	1.95	458	1.9	27.2	57837.0		1.08		OCARS
0700-197	07:02:42.900666	0.006	-19:51:22.035614	0.08	-21.41	6.25	161	1.4	9.94	12.99	161	2.2	11.7	57840.9				OCARS
0707+476	07:10:46.104889	0.013	+47:32:11.142612	0.10	0.55	4.47	58	1.6	1.40	7.83	58	1.9	27.0	57759.0		1.29		OCARS
0710+439	07:13:38.165547	12.855	+43:49:17.219601	79.45	-3.57	18.30	26	2.6	27.36	31.58	26	4.4	24.9	57291.6		0.52		OCARS
0714+457	07:17:51.852210	0.164	+45:38:03.306026	56.81	16.07	8.76	141	1.7	-32.74	7.90	141	1.8	20.5	57809.0		0.94		OCARS
0716+714	07:21:53.448458	0.014	+71:20:36.363339	0.07	3.81	1.61	418	2.7	0.64	2.02	418	3.0	27.1	57837.0		0.30	b	OCARS
0722+145	07:25:16.807775	0.013	+14:25:13.746673	0.08	4.93	3.31	72	1.7	-3.45	4.78	72	1.9	26.1	57735.9		1.04		OCARS
0723-008	07:25:50.639897	0.010	-00:54:56.543127	0.13	-50.55	6.88	150	2.9	110.64	13.78	150	4.4	24.6	57520.5		0.13		NED
0718+793	07:26:11.734155	0.675	+79:11:31.012729	1.02	-7.85	1.32	1351	1.8	-5.54	0.70	1351	1.4	26.3	57833.9				OCARS
0723+219	07:26:14.260808	0.024	+21:53:20.114152	0.34	14.84	7.46	88	1.4	-32.91	11.04	88	1.1	12.8	57819.9		1.86		OCARS
0727-115	07:30:19.112463	0.009	-11:41:12.600894	0.09	0.32	0.51	3764	2.3	-2.45	0.61	3764	1.9	27.2	57837.0		1.59		OCARS
0729+259	07:32:56.275257	0.007	+25:48:38.795777	0.11	1.98	5.76	78	1.2	15.68	8.71	78	1.6	20.7	57777.9		1.44		OCARS
0733-174	07:35:45.813132	1.392	-17:35:48.502214	1.65	14.44	24.79	26	1.0	30.81	59.30	26	1.8	18.1	55545.5				OCARS

Table A.1 (cont'd)

IVS	RA (J2000 h:m:s)	σ_α (ms)	Dec (J2000 d:′:″)	σ_δ (mas)	μ_α (μas/yr)	$\sigma_{\mu,\alpha}$ (μas/yr)	N_α	χ^2_α	μ_δ (μas/yr)	$\sigma_{\mu,\delta}$ (μas/yr)	N_δ	χ^2_δ	Length (years)	Last Obs. (MJD)	New PM	z	z flag	z Source
0735+178	07:38:07.393753	0.016	+17:42:18.998076	0.22	-12.52	3.75	497	2.2	5.03	3.02	497	1.4	19.8	55138.7		0.45		OCARS
0738-674	07:38:56.496305	0.095	-67:35:50.825340	1.16	-22.10	17.91	23	0.8	-54.97	35.31	23	1.1	21.0	55784.3		1.66		OCARS
0736+017	07:39:18.033894	0.016	+01:37:04.617810	0.17	-0.14	4.39	177	2.1	0.15	2.95	177	1.5	25.5	57826.9		0.19		OCARS
0738+491	07:42:02.748954	0.008	+49:00:15.608738	0.12	6.37	3.61	130	1.9	-2.97	3.47	130	1.8	22.1	57837.0		2.32		OCARS
0743-673	07:43:31.611719	0.079	-67:26:25.546767	0.47	-29.66	26.26	31	2.8	16.74	19.43	31	1.7	24.1	56897.1		1.51		OCARS
0742+103	07:45:33.059516	0.037	+10:11:12.691904	2.10	25.62	9.84	195	2.3	-18.63	9.57	195	1.9	23.9	56641.8		2.62		OCARS
0743-006	07:45:54.082341	0.008	-00:44:17.539576	0.24	8.20	4.03	92	1.5	10.36	6.74	92	2.2	26.5	57776.2		0.99		OCARS
0743+259	07:46:25.874219	0.132	+25:49:02.139112	1.53	-3.20	2.72	751	1.7	-33.28	3.46	751	1.7	25.9	57816.0		2.99		OCARS
0743+277	07:46:40.432298	0.033	+27:34:59.046453	0.65	2.29	5.74	108	1.8	-12.96	6.91	108	1.2	20.8	57812.9		1.70		OCARS
0745+241	07:48:36.109274	0.004	+24:00:24.109824	0.07	2.52	3.12	139	1.9	-0.15	3.07	139	1.3	27.1	57786.0		0.41		OCARS
0747+185	07:50:00.329955	0.011	+18:23:11.407392	0.28	1.95	8.92	49	1.3	-0.41	11.50	49	1.2	20.9	57725.0		1.16		OCARS
0748+126	07:50:52.045743	0.003	+12:31:04.828260	0.05	14.03	2.84	515	3.8	4.96	1.90	515	1.8	25.0	57840.9		0.89	c	OCARS
0749+540	07:53:01.384568	0.044	+53:52:59.636912	0.42	0.39	0.83	1064	2.0	2.96	0.79	1064	1.9	27.2	57840.9		0.20	b	OCARS
0754+100	07:57:06.642934	0.018	+09:56:34.852266	0.56	-2.83	5.12	52	1.5	-9.64	12.04	52	2.2	24.6	56886.8		0.27		OCARS
0759+183	08:02:48.031981	0.004	+18:09:49.248974	0.11	19.96	4.79	107	1.6	-3.75	8.57	107	1.4	21.1	57806.9		1.59		OCARS
0800+618	08:05:18.179316	0.393	+61:44:23.697229	2.59	9.09	3.67	338	2.1	-12.90	6.21	338	2.9	14.9	57833.9		3.03		OCARS
0805+046	08:07:57.538424	0.009	+04:32:34.531631	0.28	-90.24	18.45	29	5.0	24.36	12.93	29	1.8	21.5	57771.2		2.88		OCARS
0805-077	08:08:15.536097	0.028	-07:51:09.886279	0.38	-23.36	9.32	19	2.1	-13.49	5.13	19	0.9	22.3	57731.0		1.84		OCARS
0804+499	08:08:39.666257	0.015	+49:50:36.530510	0.19	3.70	0.77	1443	1.6	0.35	0.76	1443	1.6	26.8	57819.9		1.44		OCARS
0805+410	08:08:56.652032	0.004	+40:52:44.888977	0.08	5.42	1.07	684	1.5	9.32	1.33	684	1.3	24.9	57812.9		1.42		OCARS
0808+019	08:11:26.707300	0.011	+01:46:52.220384	0.19	-0.13	1.73	475	1.8	-0.89	1.92	475	1.8	26.4	57833.9		1.15		OCARS
0812+020	08:15:22.960834	0.018	+01:54:59.480861	0.32	-10.60	77.60	30	3.4	12.48	57.14	30	2.6	10.1	57798.9		0.40		OCARS

Table A.1 (cont'd)

IVS	RA (J2000 h:m:s)	σ_α (ms)	Dec (J2000 d:′:″)	σ_δ (mas)	μ_α (μas/yr)	$\sigma_{\mu,\alpha}$ (μas/yr)	N_α	χ^2_α	μ_δ (μas/yr)	$\sigma_{\mu,\delta}$ (μas/yr)	N_δ	χ^2_δ	Length (years)	Last Obs. (MJD)	New PM	z	z flag	z Source
0812+367	08:15:25.944858	0.005	+36:35:15.148870	0.06	5.45	4.39	61	2.0	-5.24	7.19	61	2.3	24.6	57723.9		1.03		OCARS
0814+425	08:18:15.999616	0.007	+42:22:45.414823	0.12	7.17	2.03	176	1.8	0.86	2.08	176	1.7	27.2	57833.9		0.53	b	OCARS
0818-128	08:20:57.447328	0.593	-12:58:59.170049	2.28	-36.61	18.45	29	1.2	30.87	15.89	29	1.1	15.8	55257.7		0.05		OCARS
0820+560	08:24:47.236365	0.009	+55:52:42.669407	0.09	8.50	5.31	79	3.2	-9.29	5.00	79	1.9	19.8	55250.7		1.42		OCARS
0821+394	08:24:55.483864	0.004	+39:16:41.903870	0.06	3.11	2.23	149	1.8	-0.13	2.91	149	1.9	26.4	57840.9		1.22		OCARS
0821+621	08:25:38.612125	0.028	+61:57:28.578962	0.17	-32.16	30.30	17	2.7	-7.25	12.94	17	1.0	22.7	57732.0		0.54		OCARS
0823+033	08:25:50.338339	0.005	+03:09:24.520847	0.42	-0.30	1.11	1550	2.0	3.10	1.52	1550	1.6	27.2	57837.0		0.51		OCARS
0823-223	08:26:01.572976	0.037	-22:30:27.203460	0.52	0.49	24.89	30	1.7	15.57	20.53	30	1.5	19.4	57731.0		0.91		OCARS
0826-373	08:28:04.780259	0.076	-37:31:06.280673	0.81	4.53	11.02	152	1.6	-22.28	13.10	152	1.6	25.0	57291.6				OCARS
0827+243	08:30:52.086194	0.005	+24:10:59.820238	0.09	-1.15	2.07	205	2.2	-1.93	2.25	205	1.7	25.6	57837.0		0.94		OCARS
0829+046	08:31:48.876971	0.011	+04:29:39.086021	0.63	0.91	7.04	38	1.6	26.36	9.01	38	0.9	18.3	55327.6		0.17		OCARS
0828+493	08:32:23.216702	0.011	+49:13:21.038176	0.09	-4.06	8.06	23	1.2	-0.05	13.22	23	1.7	19.7	55201.7		0.55	c	OCARS
0831+557	08:34:54.904169	0.049	+55:34:21.070599	0.48	0.36	43.93	21	3.2	0.66	26.27	21	1.8	19.8	55180.7		0.24		OCARS
0834-201	08:36:39.215232	0.010	-20:16:59.504243	0.12	-5.71	5.84	393	1.8	-10.91	9.52	393	2.0	23.0	57840.9		2.75		OCARS
0833+585	08:37:22.409724	0.107	+58:25:01.846948	0.95	-10.44	20.32	26	3.4	6.82	8.47	26	1.4	24.0	57520.5		2.10		OCARS
0834+250	08:37:40.245693	0.012	+24:54:23.121591	0.13	2.91	8.39	21	1.5	-6.91	4.96	21	1.2	20.7	57784.9		1.13		OCARS
0836+182	08:39:30.721413	0.005	+18:02:47.143082	0.18	39.39	9.58	6	0.7	24.88	18.32	6	0.4	20.8	57688.5	*	0.28	c	OCARS
0836+710	08:41:24.365414	0.051	+70:53:42.172961	0.55	10.23	6.42	27	3.0	3.39	9.07	27	4.2	24.1	57499.5		2.17		OCARS
0839+187	08:42:05.094193	0.006	+18:35:40.991753	0.24	32.83	8.31	34	2.6	34.13	35.73	34	3.1	18.9	54943.9		1.28		OCARS
0847-120	08:50:09.635642	0.006	-12:13:35.376331	0.10	12.33	8.89	146	2.0	12.50	6.40	146	1.5	12.9	57833.9		0.57		OCARS
0850+581	08:54:41.996391	0.016	+57:57:29.939639	0.15	-12.24	9.77	22	1.7	-5.92	17.84	22	2.8	18.0	55293.6		1.32		OCARS
OJ287	08:54:48.874920	0.003	+20:06:30.640793	0.04	-1.81	0.47	3102	2.4	0.17	0.45	3102	2.0	27.2	57840.9		0.31		OCARS

Table A.1 (cont'd)

IVS	RA (J2000 h:m:s)	σ_α (ms)	Dec (J2000 d:′:″)	σ_δ (mas)	μ_α (μas/yr)	$\sigma_{\mu,\alpha}$ (μas/yr)	N_α	χ^2_α	μ_δ (μas/yr)	$\sigma_{\mu,\delta}$ (μas/yr)	N_δ	χ^2_δ	Length (years)	Last Obs. (MJD)	New PM	z	z flag	z Source
0854-108	08:56:41.811734	4.323	-11:05:14.305829	69.58	11.57	8.92	175	1.7	12.07	8.89	175	1.5	11.7	57816.0				OCARS
0859-140	09:02:16.830933	0.022	-14:15:30.877068	0.92	1.87	8.25	30	2.9	26.84	33.20	30	9.9	19.8	56641.8		1.33		OCARS
0859+470	09:03:03.989734	0.221	+46:51:04.144686	4.47	-0.86	7.53	83	1.1	-2.12	5.75	83	0.8	24.7	56935.8		1.47		OCARS
0906+015	09:09:10.091593	0.005	+01:21:35.617595	0.14	9.04	7.40	20	1.8	9.79	11.98	20	1.7	26.2	57498.5		1.02		OCARS
0912+029	09:14:37.913044	0.390	+02:45:59.237814	6.18	3.98	3.14	459	1.8	-15.41	10.38	459	2.8	22.7	57833.9		0.43		OCARS
0912+297	09:15:52.401649	0.012	+29:33:24.042669	0.32	11.03	12.38	28	1.8	-14.44	19.34	28	1.7	26.2	57776.2		1.52		OCARS
0917+449	09:20:58.458560	0.075	+44:41:53.985139	1.85	6.72	7.38	48	2.0	7.35	9.12	48	1.9	22.5	56946.1		2.19		OCARS
0917+624	09:21:36.231226	0.045	+62:15:52.179407	0.95	-4.46	5.12	146	2.5	11.75	4.53	146	1.8	26.0	57499.5		1.45		OCARS
0920-397	09:22:46.418243	0.023	-39:59:35.068024	3.58	2.89	3.57	461	3.2	31.24	9.10	461	2.9	26.5	57840.9		0.59		OCARS
0920+390	09:23:14.452995	0.044	+38:49:39.909823	0.28	5.58	2.32	193	1.4	-0.06	3.10	193	1.2	22.2	57837.0				OCARS
0925-203	09:27:51.824366	0.024	-20:34:51.233128	0.24	4.21	6.65	366	1.9	-3.04	8.28	366	2.0	26.5	57837.0		0.35		OCARS
0943+105	09:46:35.070056	0.047	+10:17:06.135250	0.22	23.23	11.93	36	1.3	47.70	25.06	36	1.7	21.7	57837.0		1.00		OCARS
0945+408	09:48:55.337932	0.643	+40:39:44.597263	32.63	-16.11	16.71	58	5.7	-9.19	9.30	58	2.6	24.6	56921.9		1.25		OCARS
0949+354	09:52:32.026165	0.006	+35:12:52.403080	0.15	-11.79	6.13	29	2.2	8.05	12.78	29	2.3	20.6	57767.0		1.88		OCARS
0951+268	09:54:39.794008	2.551	+26:39:24.564873	18.48	-4.29	9.58	39	1.2	1.65	9.76	39	0.9	20.8	57806.9				OCARS
0952+179	09:54:56.823633	0.010	+17:43:31.222591	0.25	-6.54	6.20	49	1.8	43.55	13.14	49	2.3	19.0	55118.8		1.48		OCARS
M81	09:55:33.173052	0.037	+69:03:55.060599	0.14	-5.38	2.26	73	1.2	-19.22	2.01	73	1.1	23.7	57805.1	*	-0.0		OCARS
0955+476	09:58:19.671653	0.005	+47:25:07.842465	0.06	0.35	0.50	2475	3.0	-0.44	0.42	2475	1.6	25.0	57840.9		1.88		OCARS
0955+326	09:58:20.949629	0.007	+32:24:02.209786	0.16	1.61	3.21	64	1.8	0.26	5.85	64	1.9	26.6	57805.1		0.53		OCARS
0954+658	09:58:47.245109	0.012	+65:33:54.817943	0.07	-1.67	1.49	311	1.8	0.11	1.47	311	2.0	27.1	57810.1		0.37		OCARS
0958+346	10:01:11.949321	0.046	+34:24:50.460301	0.75	31.99	14.26	52	1.9	17.93	10.55	52	1.3	20.7	57774.0		0.95		OCARS
1004-500	10:06:14.009285	0.063	-50:18:13.470478	1.76	-7.49	12.05	82	1.0	-10.21	22.55	82	1.5	13.7	57837.0				OCARS

Table A.1 (cont'd)

IVS	RA (J2000 h:m:s)	σ_α (ms)	Dec (J2000 d:′:″)	σ_δ (mas)	μ_α (μas/yr)	$\sigma_{\mu,\alpha}$ (μas/yr)	N_α	χ^2_α	μ_δ (μas/yr)	$\sigma_{\mu,\delta}$ (μas/yr)	N_δ	χ^2_δ	Length (years)	Last Obs. (MJD)	New PM	z	z flag	z Source
1004-217	10:06:46.413693	0.007	-21:59:20.410434	0.22	-3.82	23.97	19	2.9	7.96	23.20	19	2.2	19.6	57786.0		0.33		OCARS
1004+141	10:07:41.498091	0.003	+13:56:29.600487	0.11	11.35	8.75	261	1.8	-16.43	8.17	261	1.5	19.1	55168.8		2.71		OCARS
1011+250	10:13:53.428774	0.005	+24:49:16.440635	0.08	-10.43	8.91	20	1.8	-19.94	7.27	20	0.8	15.2	55244.7		1.64		OCARS
1012+232	10:14:47.065442	0.008	+23:01:16.570914	0.16	11.26	3.59	79	3.2	-9.51	3.04	79	1.3	26.3	57810.1		0.57		OCARS
1013+127	10:15:44.023231	0.140	+12:27:07.077912	3.59	-10.22	7.27	19	1.8	11.79	13.25	19	1.8	21.6	57806.9	*	0.46	b	OCARS
1013+054	10:16:03.136494	0.006	+05:13:02.341371	0.16	19.42	8.99	78	1.8	22.38	13.62	78	1.5	21.4	57723.9		1.71		OCARS
1014+615	10:17:25.887513	0.021	+61:16:27.496410	0.14	-13.68	3.80	57	2.6	-9.46	3.34	57	1.9	23.0	57812.9		2.80		OCARS
1015+359	10:18:10.988099	0.007	+35:42:39.441153	0.11	5.09	6.50	114	1.6	39.63	14.91	114	2.1	20.6	57781.0		1.23		OCARS
1015+057	10:18:27.848316	0.022	+05:30:29.961916	1.55	5.13	10.43	94	1.5	24.34	17.59	94	1.5	21.5	57767.0		1.95		OCARS
1020+400	10:23:11.565657	0.010	+39:48:15.385436	0.14	-3.23	5.42	26	1.7	8.10	7.45	26	1.0	20.3	55320.6		1.25		OCARS
1022-665	10:23:43.533330	0.076	-66:46:48.717011	0.38	-15.25	14.81	45	1.3	20.41	13.01	45	1.0	13.3	57731.0				OCARS
1022+194	10:24:44.809587	0.017	+19:12:20.415690	0.30	-1.60	4.18	63	1.7	0.95	3.92	63	1.9	22.0	57693.8		0.83		OCARS
1023+131	10:25:56.285344	0.011	+12:53:49.022017	0.13	3.00	53.91	50	2.9	-7.32	28.09	50	2.1	16.7	56168.7		0.66		OCARS
1027-186	10:29:33.097942	0.871	-18:52:50.288125	3.25	-7.44	13.10	59	1.9	10.12	37.00	59	1.9	19.6	57802.0		1.78		OCARS
1030+415	10:33:03.707868	0.005	+41:16:06.233063	0.05	-8.42	3.94	147	2.8	8.44	4.08	147	2.6	27.1	57837.0		1.12		OCARS
1030+074	10:33:34.024306	0.035	+07:11:26.147459	0.17	4.18	8.57	120	1.5	-11.97	6.72	120	1.2	19.0	57791.9		1.53		OCARS
1032-199	10:35:02.155436	0.095	-20:11:34.358926	0.70	21.83	6.60	82	2.0	7.36	12.98	82	2.0	22.8	57102.7		2.20		OCARS
1031+567	10:35:07.040025	0.020	+56:28:46.795465	0.15	11.92	56.80	16	9.9	-14.88	27.27	16	2.5	25.8	57786.0		0.45		OCARS
1034-374	10:36:53.439637	0.078	-37:44:15.066834	3.61	-13.06	17.70	60	1.5	54.55	23.02	60	1.2	12.5	57805.1		1.82		OCARS
1034-293	10:37:16.079745	0.023	-29:34:02.813539	0.22	7.51	2.12	1997	2.2	-9.52	2.31	1997	2.3	27.2	57840.9		0.31		OCARS
1038+064	10:41:17.162096	0.187	+06:10:16.915853	4.13	-14.80	3.58	112	1.6	64.56	8.48	112	2.5	24.5	57499.5		1.27		OCARS
1038+52A	10:41:46.781666	0.010	+52:33:28.232142	0.10	8.13	2.01	212	1.6	42.61	3.07	212	2.6	25.4	57810.1		0.68		OCARS

Table A.1 (cont'd)

IVS	RA (J2000 h:m:s)	σ_α (ms)	Dec (J2000 d:′:″)	σ_δ (mas)	μ_α (μas/yr)	$\sigma_{\mu,\alpha}$ (μas/yr)	N_α	χ^2_α	μ_δ (μas/yr)	$\sigma_{\mu,\delta}$ (μas/yr)	N_δ	χ^2_δ	Length (years)	Last Obs. (MJD)	New PM	z	z flag	z Source
1038+52B	10:41:48.897688	0.076	+52:33:55.607807	0.55	2.58	306.43	11	1.6	-22.93	474.00	11	1.7	23.4	57723.9		2.30		OCARS
3C245	10:42:44.605282	0.008	+12:03:31.263610	0.24	34.04	31.87	16	2.3	-34.92	32.64	16	2.1	24.1	57776.2		1.03		OCARS
1040+244	10:43:09.035774	0.022	+24:08:35.410001	0.64	9.22	5.20	179	2.0	13.66	8.21	179	1.8	20.8	57826.9		0.56		OCARS
1039+811	10:44:23.062495	0.047	+80:54:39.442856	0.08	4.82	4.76	129	8.2	2.88	2.39	129	2.1	26.7	57823.0		1.26		OCARS
1042+071	10:44:55.911006	0.222	+06:55:38.275185	7.52	4.42	13.69	23	2.3	-7.92	13.86	23	2.0	22.3	57644.7		0.69		OCARS
1045-188	10:48:06.620613	0.050	-19:09:35.727046	0.85	21.96	4.53	132	1.8	-74.89	10.76	132	2.6	22.6	57665.8		0.59		OCARS
1048-313	10:51:04.777071	0.397	-31:38:14.305716	1.92	86.82	37.19	27	1.6	-37.91	40.38	27	1.4	15.5	55728.4		1.43		OCARS
1049+215	10:51:48.789175	0.037	+21:19:52.313566	0.46	-4.56	9.89	43	3.3	11.90	6.21	43	1.6	27.0	57805.1		1.30		OCARS
1053+704	10:56:53.617290	0.188	+70:11:45.916520	1.47	-4.00	3.45	253	2.5	-6.28	2.79	253	1.9	23.7	57809.0		2.49		OCARS
1053+815	10:58:11.534876	0.643	+81:14:32.675155	2.50	-7.23	1.40	741	1.8	1.88	1.63	741	2.0	26.9	57826.9		0.71		OCARS
1055+018	10:58:29.605226	0.010	+01:33:58.824206	0.30	1.74	3.14	174	1.7	5.79	3.11	174	1.5	27.0	57776.2		0.89		OCARS
1057-797	10:58:43.309786	0.026	-80:03:54.159719	0.07	0.50	1.40	1248	1.8	-7.70	1.11	1248	1.6	27.0	57840.9		0.58		OCARS
1056+212	10:59:39.042664	0.012	+20:57:21.956623	0.26	-11.53	7.62	14	0.8	29.64	35.77	14	2.5	19.7	57275.3		0.40		OCARS
1059+282	11:02:14.288549	0.026	+27:57:08.689869	0.12	3.72	13.99	48	1.7	4.81	11.99	48	1.3	20.9	57837.0		1.86		OCARS
1100+122	11:03:03.529885	0.063	+11:58:16.626862	3.46	-11.31	45.84	16	2.5	57.99	25.36	16	0.7	12.5	57707.9		0.91	c	OCARS
1101-536	11:03:52.221670	0.016	-53:57:00.697041	0.24	3.45	4.21	65	1.0	-2.07	6.76	65	1.0	26.1	57659.8				OCARS
1101+384	11:04:27.313997	0.099	+38:12:31.792694	3.04	2.02	1.33	522	1.4	-4.99	1.67	522	1.1	22.8	57840.9		0.03		OCARS
1104-445	11:07:08.694157	0.020	-44:49:07.618393	0.21	-20.09	3.26	514	3.0	12.61	3.32	514	2.7	27.0	57833.9		1.60		OCARS
1105-680	11:07:12.695107	0.113	-68:20:50.729964	0.85	400.83	236.70	20	14.2	109.16	124.45	20	6.4	19.2	55784.3		0.59		OCARS
1104+728	11:07:41.722583	0.030	+72:32:36.004897	0.11	-12.87	9.99	33	1.6	12.57	16.41	33	1.7	21.4	57646.8		2.10		OCARS
1111+149	11:13:58.695110	0.031	+14:42:26.952253	0.85	-5.02	6.24	143	1.6	9.05	6.61	143	1.4	27.1	57819.9		0.87		OCARS
1116-462	11:18:26.957661	0.032	-46:34:14.999925	1.27	36.44	46.33	22	1.3	4.80	59.28	22	1.3	20.0	55420.6		0.71		OCARS

Table A.1 (cont'd)

IVS	RA (J2000 h:m:s)	σ_α (ms)	Dec (J2000 d:′:″)	σ_δ (mas)	μ_α (μas/yr)	$\sigma_{\mu,\alpha}$ (μas/yr)	N_α	χ^2_α	μ_δ (μas/yr)	$\sigma_{\mu,\delta}$ (μas/yr)	N_δ	χ^2_δ	Length (years)	Last Obs. (MJD)	New PM	z	z flag	z Source
1116+128	11:18:57.301406	0.127	+12:34:41.717462	0.54	-1.80	14.13	33	2.4	0.43	22.29	33	1.6	23.0	57102.7		2.13		OCARS
1123+264	11:25:53.711926	0.004	+26:10:19.978708	0.06	-8.78	2.72	206	2.2	7.54	2.54	206	1.6	27.1	57806.9		2.35		OCARS
1124-186	11:27:04.392450	0.005	-18:57:17.441958	0.06	1.78	1.15	1728	2.3	-6.86	1.16	1728	2.2	27.2	57840.9		1.05		OCARS
1125+366	11:27:58.870817	0.016	+36:20:28.351839	0.26	6.79	21.37	17	1.6	0.31	31.49	17	0.9	20.1	57589.6		0.88		OCARS
1127-145	11:30:07.052558	0.032	-14:49:27.388576	0.31	3.20	25.11	31	2.6	-3.03	19.38	31	1.6	18.1	55545.5		1.18		OCARS
1128+385	11:30:53.282610	0.003	+38:15:18.546915	0.04	-2.37	0.63	1526	1.7	1.70	0.75	1526	1.7	25.9	57786.0		1.74		OCARS
1128-047	11:31:30.516755	0.022	-05:00:19.656880	0.41	13.30	15.62	12	1.1	24.86	18.92	12	0.9	23.2	57583.6		0.27		OCARS
1130+009	11:33:20.055767	0.019	+00:40:52.837173	0.57	-10.29	7.00	64	1.5	-3.37	9.23	64	1.4	27.1	57805.1		1.64		OCARS
1133-032	11:36:24.576910	0.016	-03:30:29.496106	0.33	6.18	5.43	190	1.8	-1.39	7.25	190	1.4	19.9	57840.9		1.65		OCARS
MRK180	11:36:26.408443	0.006	+70:09:27.307497	0.03	11.08	7.97	13	1.1	28.13	7.25	13	2.8	20.2	57688.5	*	0.05		OCARS
NGC3862	11:45:05.009052	0.002	+19:36:22.741257	0.02	5.24	5.39	18	1.7	-2.04	10.78	18	1.6	20.0	57688.5	*	0.02		OCARS
1143-696	11:45:53.624214	0.094	-69:54:01.797641	0.41	28.44	9.82	36	1.0	29.32	13.35	36	0.9	13.3	57731.0		0.24		OCARS
1143-245	11:46:08.103521	0.267	-24:47:32.897733	1.35	16.48	17.29	42	1.1	32.62	22.02	42	1.6	16.0	55728.4		1.94		OCARS
1143-287	11:46:26.188545	0.064	-28:59:18.504188	0.53	-56.62	81.47	19	1.1	-27.57	72.34	19	0.8	13.3	55545.5		0.45		OCARS
1144+402	11:46:58.297864	0.025	+39:58:34.304831	0.31	-3.65	2.19	466	2.3	-3.80	2.50	466	2.5	26.9	57833.9		1.09		OCARS
1144-379	11:47:01.370711	0.005	-38:12:11.023489	0.07	3.94	1.65	1466	2.4	3.61	1.78	1466	2.3	26.6	57840.9		1.05		OCARS
1144+352	11:47:22.130559	0.000	+35:01:07.522418	0.01	14.92	12.53	5	1.2	-12.14	14.78	5	6.1	20.4	57688.5	*	0.06		OCARS
1145-071	11:47:51.554039	0.009	-07:24:41.141794	0.27	4.29	4.03	172	2.7	6.11	3.34	172	1.8	25.1	57810.1		1.34		OCARS
1145+268	11:47:59.763873	0.022	+26:35:42.331925	0.36	3.52	3.17	132	2.0	-7.45	4.77	132	2.0	20.8	57802.0	*	0.87		OCARS
1147+245	11:50:19.212176	0.013	+24:17:53.835406	0.14	2.55	4.89	55	1.8	-0.83	3.92	55	1.2	24.7	57758.0		0.21	d	APO
1148-001	11:50:43.870979	0.134	-00:23:54.211031	4.96	39.91	18.87	18	4.0	27.11	20.90	18	2.5	26.5	57694.9		1.98	c	OCARS
1148-671	11:51:13.426591	0.086	-67:28:11.091110	1.39	-57.61	64.54	10	1.8	39.97	64.15	10	1.0	17.2	54439.2				OCARS

Table A.1 (cont'd)

IVS	RA (J2000 h:m:s)	σ_α (ms)	Dec (J2000 d:′:″)	σ_δ (mas)	μ_α (μas/yr)	$\sigma_{\mu,\alpha}$ (μas/yr)	N_α	χ^2_α	μ_δ (μas/yr)	$\sigma_{\mu,\delta}$ (μas/yr)	N_δ	χ^2_δ	Length (years)	Last Obs. (MJD)	New PM	z	z flag	z Source
1149-084	11:52:17.209467	0.102	-08:41:03.314268	0.39	7.91	6.77	315	2.3	-13.81	4.19	315	2.4	19.8	57812.9		2.37		OCARS
1150+812	11:53:12.499048	0.028	+80:58:29.154384	0.07	-3.90	7.66	64	2.2	-13.70	5.89	64	2.4	19.4	55042.9		1.25		OCARS
1150+497	11:53:24.466123	0.286	+49:31:08.837998	4.41	2.30	10.80	38	2.5	8.12	12.39	38	2.8	24.6	56921.9		0.33		OCARS
1155+251	11:58:25.787565	0.033	+24:50:17.963641	0.69	17.33	34.68	17	2.0	-39.03	39.91	17	1.3	18.5	54937.9		0.20		OCARS
1156-094	11:59:12.711709	0.010	-09:40:52.049099	0.19	-42.25	33.57	11	1.5	-68.18	93.60	11	2.6	21.4	57498.5				OCARS
1156-663	11:59:18.305360	0.083	-66:35:39.427053	1.63	-0.95	25.67	27	1.3	-3.92	37.20	27	0.9	12.6	57485.5				OCARS
1156+295	11:59:31.833903	0.004	+29:14:43.826773	0.05	0.33	0.85	1443	1.8	4.59	1.47	1443	2.5	27.2	57840.9		0.72		OCARS
1212+171	12:15:03.978594	1.105	+16:54:37.954849	4.38	18.16	14.23	59	2.0	-6.31	16.93	59	1.8	20.9	57710.9		1.13		OCARS
1213-172	12:15:46.751772	0.016	-17:31:45.403452	0.48	-4.46	3.38	192	1.6	3.25	6.01	192	2.0	23.0	57805.1				OCARS
1213+350	12:15:55.601071	0.131	+34:48:15.217961	2.92	9.36	9.51	53	1.2	10.80	11.04	53	1.0	24.0	56946.1		0.86		OCARS
1215+303	12:17:52.081962	0.016	+30:07:00.636175	0.33	-2.33	4.99	50	1.5	13.18	6.83	50	1.0	25.4	57700.8		0.13		OCARS
1216+487	12:19:06.414749	0.011	+48:29:56.164821	0.14	14.55	6.78	26	1.7	7.37	7.04	26	1.0	20.3	55342.6		1.08		OCARS
NGC4261	12:19:23.216063	0.001	+05:49:29.700024	0.02	-8.83	18.79	3	3.4	31.45	21.95	3	0.6	12.6	57688.5	*	0.01		OCARS
1219+285	12:21:31.690504	0.010	+28:13:58.500201	0.29	-5.24	16.21	26	3.5	8.47	10.96	26	0.9	17.1	54739.8		0.10		OCARS
1219+044	12:22:22.549629	0.006	+04:13:15.776610	0.37	6.41	1.17	1302	1.6	-3.38	2.12	1302	1.5	25.9	57837.0		0.97		OCARS
1221+809	12:23:40.493761	0.079	+80:40:04.340304	0.20	0.98	2.44	71	1.2	2.81	3.53	71	1.4	26.7	57764.9		0.47		OCARS
1222+037	12:24:52.421952	0.021	+03:30:50.292481	0.28	34.94	38.04	35	1.7	-8.59	68.52	35	1.3	26.9	57735.9		0.95		OCARS
M84	12:25:03.743260	0.000	+12:53:13.138590	0.01	-82.89	3.54	27	4.1	-51.16	9.52	27	0.9	20.2	57688.5	*	0.00		OCARS
1226+373	12:28:47.423687	0.013	+37:06:12.095129	0.22	-5.45	4.50	194	2.1	5.62	4.33	194	1.6	25.8	57802.0		1.52		OCARS
3C274	12:30:49.423387	0.007	+12:23:28.043730	0.09	-1.16	0.94	1740	1.9	-8.74	1.10	1740	1.7	27.1	57840.9		0.00		OCARS
1232+366	12:35:05.806462	0.001	+36:21:19.321295	0.01	1.06	14.36	3	0.0	-7.44	18.08	3	2.5	19.3	57286.0	*	1.60		OCARS
1236+077	12:39:24.588365	0.020	+07:30:17.189401	0.12	2.98	4.88	85	2.1	-4.15	6.15	85	1.9	23.7	57759.0		1.37		OCARS

Table A.1 (cont'd)

IVS	RA (J2000 h:m:s)	σ_α (ms)	Dec (J2000 d:′:″)	σ_δ (mas)	μ_α (μas/yr)	$\sigma_{\mu,\alpha}$ (μas/yr)	N_α	χ^2_α	μ_δ (μas/yr)	$\sigma_{\mu,\delta}$ (μas/yr)	N_δ	χ^2_δ	Length (years)	Last Obs. (MJD)	New PM	z	z flag	z Source
1237-101	12:39:43.061482	0.052	-10:23:28.691540	0.93	-87.84	11.97	63	2.2	24.98	10.77	63	1.6	20.6	56935.8		0.75		OCARS
1239+376	12:42:09.812372	0.010	+37:20:05.691061	0.21	-11.78	35.56	11	1.4	-82.35	118.82	11	2.5	20.1	57500.5		3.82		OCARS
1240+381	12:42:51.369110	0.010	+37:51:00.025001	0.28	0.41	13.07	42	3.1	5.05	10.84	42	1.9	22.9	57806.9		1.32		OCARS
1243-160	12:45:53.742278	0.008	-16:16:45.705191	0.09	-11.45	11.23	92	2.0	-15.18	9.11	92	1.8	19.7	57819.9		0.20	a	OCARS
1243-072	12:46:04.232113	0.008	-07:30:46.574659	0.08	2.55	3.82	217	1.7	9.41	5.04	217	1.7	22.8	57840.9		1.29		OCARS
1244-255	12:46:46.802366	0.536	-25:47:49.287618	1.63	-3.69	4.67	249	2.1	-6.84	3.82	249	1.5	26.7	57840.9		0.63		OCARS
1245-454	12:48:28.494994	0.047	-45:59:47.181776	1.51	-26.58	45.59	16	1.4	45.77	77.08	16	0.8	12.9	57723.9		1.02		OCARS
1252+119	12:54:38.255631	0.030	+11:41:05.895830	0.88	4.60	8.87	68	5.0	3.40	6.03	68	2.1	25.5	57812.9		0.87		OCARS
1251-713	12:54:59.921722	0.189	-71:38:18.436272	0.41	14.60	5.22	62	1.4	1.55	6.30	62	1.0	26.3	57784.9				OCARS
1255-316	12:57:59.060843	0.015	-31:55:16.851336	0.22	13.74	2.34	824	2.2	26.64	3.84	824	2.2	26.5	57833.9		1.92		OCARS
1255-177	12:58:38.301767	0.030	-18:00:03.124640	0.39	-9.23	8.84	91	1.7	34.97	11.49	91	1.6	19.6	57795.0		1.96		OCARS
1257+145	13:00:20.918817	0.041	+14:17:18.532113	0.71	5.67	18.85	34	1.1	33.15	41.70	34	1.6	17.8	55293.6		1.11		OCARS
1300+580	13:02:52.465282	0.006	+57:48:37.609443	0.07	5.22	0.74	1212	1.8	11.31	0.80	1212	1.7	23.0	57840.9		1.09		OCARS
1302-102	13:05:33.015022	0.070	-10:33:19.428040	0.81	19.36	29.23	42	3.9	-8.79	39.92	42	2.6	19.6	56566.4		0.28		OCARS
1304-318	13:07:15.178813	0.010	-32:07:58.640211	0.35	-37.25	36.24	3	1.0	186.30	99.44	3	20.0	6.4	57810.1	*	1.21		OCARS
1306+360	13:08:23.709158	0.030	+35:46:37.163510	0.65	-7.60	3.64	58	2.2	9.65	5.87	58	1.7	14.7	57795.0	*	1.05		OCARS
1307+121	13:09:33.932464	1.015	+11:54:24.552045	30.72	15.21	13.08	70	1.4	34.43	34.63	70	1.3	21.9	57102.7		0.32	b	OCARS
1308+328	13:10:59.402733	0.031	+32:33:34.450325	0.34	-0.22	2.64	286	2.0	-2.75	2.15	286	1.5	22.1	57791.9		1.63	c	OCARS
1308+554	13:11:03.210825	0.061	+55:13:54.322447	0.47	-28.57	21.78	32	1.8	26.03	27.64	32	1.9	22.1	57661.8		0.92		OCARS
1313-333	13:16:07.985957	0.007	-33:38:59.171915	0.27	3.50	3.78	234	3.0	-2.82	8.32	234	3.4	26.6	57810.1		1.21		OCARS
OP326	13:17:36.494182	0.004	+34:25:15.932445	0.09	-6.00	11.20	24	1.5	-0.09	12.56	24	1.2	15.4	54943.9		1.06		OCARS
1318+225	13:21:11.202550	0.004	+22:16:12.108411	0.09	-7.12	132.01	10	1.0	5.11	273.05	10	1.7	20.0	57407.3		0.94		OCARS

Table A.1 (cont'd)

IVS	RA (J2000 h:m:s)	σ_α (ms)	Dec (J2000 d:′:″)	σ_δ (mas)	μ_α (μas/yr)	$\sigma_{\mu,\alpha}$ (μas/yr)	N_α	χ^2_α	μ_δ (μas/yr)	$\sigma_{\mu,\delta}$ (μas/yr)	N_δ	χ^2_δ	Length (years)	Last Obs. (MJD)	New PM	z	z flag	z Source
1319-093	13:22:36.912629	0.006	-09:37:37.800671	0.19	-15.29	91.12	12	0.8	-30.10	168.80	12	1.4	19.0	57498.5		1.86		OCARS
1324+224	13:27:00.861314	0.005	+22:10:50.162886	0.05	-3.19	2.82	520	2.3	-8.42	3.30	520	2.6	22.2	57837.0		1.40	b	OCARS
1325-558	13:29:01.145048	0.042	-56:08:02.663964	0.38	10.41	20.15	44	1.5	36.34	25.92	44	1.2	14.0	57777.9				OCARS
1327+504	13:29:05.802720	0.010	+50:09:26.400778	0.13	2.85	8.65	55	1.9	-5.16	12.30	55	1.8	22.6	57837.0		2.65		OCARS
3C286	13:31:08.288087	0.028	+30:30:32.958261	0.52	20.45	47.72	11	1.9	-22.72	37.22	11	1.3	24.6	57774.0		0.85		OCARS
1330+476	13:32:45.246405	0.010	+47:22:22.667696	0.19	7.44	8.78	19	3.3	3.85	7.18	19	1.8	20.5	57802.0		0.67		OCARS
1334-127	13:37:39.782779	0.005	-12:57:24.693343	0.08	-1.17	0.65	2904	2.1	-3.05	0.85	2904	2.2	27.2	57823.0		0.54		OCARS
1336-237	13:39:01.746415	0.007	-24:01:14.007057	0.25	31.18	142.68	11	0.4	-64.81	378.42	11	1.7	17.7	57099.0		0.66		OCARS
1339-287	13:42:15.345577	0.015	-29:00:41.833351	0.64	-1.34	22.80	13	1.7	-24.97	68.54	13	2.4	18.9	57576.6		1.44		OCARS
1342+662	13:43:45.959489	0.024	+66:02:25.744922	0.21	-3.69	8.27	192	2.9	6.46	4.48	192	1.9	26.8	57802.0		0.77		OCARS
1342+663	13:44:08.679622	0.028	+66:06:11.643539	0.10	-41.06	7.26	61	2.9	-9.35	2.69	61	1.8	26.7	57771.9		1.35		OCARS
1347+539	13:49:34.656615	0.013	+53:41:17.040074	0.17	-18.67	12.88	29	2.3	1.93	16.88	29	2.7	20.3	55349.6		0.98		OCARS
1348+308	13:50:52.736243	0.023	+30:34:53.590683	0.10	-5.73	12.29	56	1.2	11.80	10.23	56	1.1	20.3	57625.7		0.71		OCARS
1349-439	13:52:56.534877	0.048	-44:12:40.388724	0.97	1.49	8.85	57	1.5	-32.76	14.16	57	1.5	26.3	57717.0		0.05		OCARS
1351-018	13:54:06.895323	0.005	-02:06:03.189443	0.38	4.36	1.31	1214	1.8	9.47	2.71	1214	1.5	25.3	57837.0		3.71		OCARS
1352-104	13:54:46.518689	0.003	-10:41:02.656054	0.10	2.68	6.72	103	2.3	5.34	9.31	103	1.9	20.1	57786.0		0.33		OCARS
1354+195	13:57:04.436646	0.041	+19:19:07.370591	1.14	15.61	9.64	83	2.0	13.24	9.15	83	1.8	26.3	57520.5		0.72		OCARS
1354-174	13:57:06.074213	0.068	-17:44:01.903191	0.89	-22.99	26.13	32	1.4	-66.92	35.31	32	1.9	16.6	56524.8		3.15		OCARS
1354-152	13:57:11.245005	0.008	-15:27:28.787021	0.26	-1.97	4.45	182	1.9	1.15	5.99	182	1.8	27.1	57810.1		1.89		OCARS
1357+769	13:57:55.371534	0.073	+76:43:21.051280	0.94	2.39	0.48	2069	1.7	-1.65	0.53	2069	1.7	25.5	57837.0		1.58	b	OCARS
1402-012	14:04:45.895359	0.063	-01:30:21.947205	0.43	70.62	33.65	38	1.9	21.33	27.91	38	1.5	18.8	55545.5		2.52		OCARS
1402+044	14:05:01.119779	0.020	+04:15:35.818324	0.95	10.34	6.40	58	1.4	-19.42	12.05	58	1.5	21.2	56641.8		3.21		OCARS

Table A.1 (cont'd)

IVS	RA (J2000 h:m:s)	σ_α (ms)	Dec (J2000 d:′:″)	σ_δ (mas)	μ_α (μas/yr)	$\sigma_{\mu,\alpha}$ (μas/yr)	N_α	χ^2_α	μ_δ (μas/yr)	$\sigma_{\mu,\delta}$ (μas/yr)	N_δ	χ^2_δ	Length (years)	Last Obs. (MJD)	New PM	z	z flag	z Source
1406-076	14:08:56.481290	0.021	-07:52:26.665923	0.28	10.83	3.71	222	2.0	0.02	3.74	222	2.5	23.1	57833.9		1.49		OCARS
1406-267	14:09:50.169814	0.037	-26:57:36.980210	0.36	-19.74	15.27	144	2.3	-58.42	15.78	144	2.0	19.7	57823.0		2.43		OCARS
1413+135	14:15:58.817503	0.020	+13:20:23.712810	0.25	4.49	5.54	70	2.5	9.21	5.94	70	2.3	27.1	57826.9		0.25		OCARS
1416+067	14:19:08.180179	0.022	+06:28:34.803140	0.36	-53.96	48.16	15	0.6	-9.35	72.42	15	1.6	17.1	54440.3		1.44		OCARS
1418+546	14:19:46.597396	0.010	+54:23:14.787215	0.09	1.93	0.86	919	1.7	-1.83	0.92	919	1.8	27.2	57833.9		0.15		OCARS
1417+385	14:19:46.613786	0.017	+38:21:48.475400	0.18	-2.82	1.38	558	1.9	2.85	1.84	558	1.7	22.2	57840.9		1.83		OCARS
1417+273	14:19:59.297060	0.005	+27:06:25.552801	0.09	-51.80	17.35	20	2.9	-8.31	21.87	20	1.7	17.1	55112.8		0.54		OCARS
1420-679	14:24:55.557501	0.064	-68:07:58.094741	0.48	17.91	13.19	35	1.6	10.11	15.33	35	0.8	13.4	57758.0				OCARS
1423+146	14:25:49.018000	0.004	+14:24:56.901838	0.12	-8.50	7.49	45	1.6	-5.53	13.18	45	1.9	21.1	57786.0		0.78		OCARS
1424+366	14:26:37.087585	0.031	+36:25:09.572547	0.46	13.00	31.60	48	3.0	-16.83	8.29	48	1.2	19.1	57227.4		1.09		OCARS
1424+240	14:27:00.391763	0.005	+23:48:00.037679	0.07	-15.74	6.30	26	2.7	13.37	10.41	26	1.5	24.4	57777.9	*	0.60	b	OCARS
1424-418	14:27:56.297566	0.008	-42:06:19.437412	0.12	-9.90	1.56	1507	2.3	1.98	1.89	1507	2.3	26.9	57840.9		1.52		OCARS
1428+422	14:30:23.741610	0.034	+42:04:36.491338	0.24	-26.21	37.69	14	0.6	26.05	79.37	14	1.6	12.1	54664.7		4.71		OCARS
1428+370	14:30:40.583639	0.453	+36:49:03.888557	9.59	-17.48	10.25	33	0.8	19.29	7.55	33	1.0	12.8	57806.9		0.57	c	OCARS
NGC5675	14:32:39.829618	0.003	+36:18:07.932093	0.04	3.89	11.76	8	2.5	-48.27	21.18	8	0.4	20.2	57688.5	*	0.01		OCARS
1430-178	14:32:57.690682	0.058	-18:01:35.248715	1.07	-69.44	53.64	10	1.9	61.76	47.70	10	0.8	22.2	57491.4		2.33		OCARS
1432+200	14:34:39.793407	0.047	+19:52:00.734969	0.64	6.67	5.78	79	1.6	-3.82	7.42	79	1.4	24.5	57802.0		1.38		OCARS
1435+638	14:36:45.796067	12.585	+63:36:37.952577	61.13	-1.51	5.63	24	1.5	5.09	13.95	24	3.3	24.9	57291.6		2.07		OCARS
1435-218	14:38:09.469348	0.036	-22:04:54.748530	0.41	-9.57	8.55	20	1.6	12.48	15.17	20	2.0	23.4	57731.0		1.19		OCARS
1441+522	14:43:02.760672	0.000	+52:01:37.298654	0.00	16.23	31.23	3	253.9	30.80	55.04	3	314.2	9.6	57286.0	*	0.14		OCARS
1441+252	14:43:56.892193	0.020	+25:01:44.490813	0.24	26.72	8.25	90	2.3	-4.90	5.93	90	1.5	14.7	57795.0		0.06	c	OCARS
OQ172	14:45:16.465260	0.023	+09:58:36.073309	0.43	8.96	16.30	35	2.6	-1.13	19.15	35	2.1	18.5	55320.6		3.55		OCARS

Table A.1 (cont'd)

IVS	RA (J2000 h:m:s)	σ_α (ms)	Dec (J2000 d:′:″)	σ_δ (mas)	μ_α (μas/yr)	$\sigma_{\mu,\alpha}$ (μas/yr)	N_α	χ^2_α	μ_δ (μas/yr)	$\sigma_{\mu,\delta}$ (μas/yr)	N_δ	χ^2_δ	Length (years)	Last Obs. (MJD)	New PM	z	z flag	z Source
1443-162	14:45:53.376313	0.006	-16:29:01.619302	0.21	24.65	7.61	46	1.2	-12.87	12.08	46	1.1	20.5	57810.1				OCARS
1445-161	14:48:15.054114	0.195	-16:20:24.547101	3.69	-31.07	29.05	30	1.5	38.09	29.29	30	0.8	20.8	57514.5		2.41		OCARS
1448-648	14:52:39.679225	0.219	-65:02:03.433788	1.26	-70.91	26.13	21	0.8	-20.83	24.69	21	0.7	13.1	57659.8				OCARS
1451-375	14:54:27.409746	0.009	-37:47:33.145798	0.57	0.24	4.72	266	2.3	6.82	10.25	266	3.4	26.3	57723.9		0.31		OCARS
1451-400	14:54:32.912397	0.069	-40:12:32.514966	0.88	2.38	7.82	73	2.6	-16.02	15.11	73	3.4	24.5	57806.9		1.81		OCARS
1456+044	14:58:59.356194	0.010	+04:16:13.820349	0.31	-1.54	3.51	73	1.3	61.91	5.52	73	2.0	21.6	57805.1	*	0.39		OCARS
1459+480	15:00:48.654215	0.011	+47:51:15.537763	0.12	7.54	5.65	55	2.1	-1.80	5.42	55	1.9	27.0	57795.0		1.06		OCARS
1502+106	15:04:24.979774	0.007	+10:29:39.198465	0.08	0.61	1.42	456	1.4	3.13	2.12	456	1.4	27.2	57812.9		1.84		OCARS
1502+036	15:05:06.477148	0.018	+03:26:30.812583	0.20	-1.27	3.50	288	1.9	-0.34	3.67	288	1.6	24.6	57823.0		0.41		OCARS
1504+377	15:06:09.529966	0.007	+37:30:51.132340	0.12	7.41	3.35	115	2.2	2.66	3.34	115	1.8	25.4	57837.0		0.67		OCARS
1504-166	15:07:04.786952	0.013	-16:52:30.267517	0.51	-9.58	7.69	67	1.7	11.45	12.97	67	1.8	19.0	56641.8		0.88		OCARS
1508+572	15:10:02.922372	0.064	+57:02:43.375681	0.32	6.59	6.07	72	1.9	10.87	5.53	72	1.9	21.7	57465.4		4.31		OCARS
1508-055	15:10:53.591398	0.032	-05:43:07.417541	0.11	-5.90	7.52	29	1.3	-8.01	12.87	29	1.0	13.0	55313.6		1.19		OCARS
1510-089	15:12:50.532900	0.015	-09:05:59.829187	0.33	1.29	1.43	407	1.9	-7.63	3.71	407	2.3	27.1	57810.1		0.36		OCARS
1511-100	15:13:44.893434	0.018	-10:12:00.264832	0.38	8.17	8.59	56	3.2	-3.30	6.28	56	5.9	23.0	57810.1		1.51		OCARS
1514+197	15:16:56.796166	0.006	+19:32:12.991698	0.10	1.78	3.25	123	2.0	-7.98	4.71	123	1.6	25.7	57837.0		1.07	c	OCARS
1514-241	15:17:41.810474	3.664	-24:22:19.510185	51.82	-4.41	2.92	281	2.6	5.94	6.10	281	2.1	23.5	57464.4		0.05		OCARS
1520+437	15:21:49.613844	0.019	+43:36:39.267219	0.42	-4.63	3.02	265	1.6	6.17	5.12	265	1.6	20.8	57823.0		2.17		OCARS
1520+319	15:22:09.991711	0.020	+31:44:14.382191	0.56	-13.23	5.34	211	1.7	4.67	5.51	211	1.3	20.8	57798.9		1.49		OCARS
1519-294	15:22:25.486282	0.438	-29:36:25.231354	1.62	-24.69	29.03	43	2.4	6.41	15.96	43	1.4	19.3	57738.0		2.13		OCARS
1519-273	15:22:37.676004	0.006	-27:30:10.785550	0.08	6.92	1.37	1092	1.8	5.37	1.39	1092	1.9	26.7	57840.9		1.29		OCARS
1522+155	15:24:41.611519	0.042	+15:21:21.050924	1.75	27.94	18.80	30	1.4	-38.41	59.65	30	1.4	21.2	57833.9		0.63		OCARS

Table A.1 (cont'd)

IVS	RA (J2000 h:m:s)	σ_α (ms)	Dec (J2000 d:′:″)	σ_δ (mas)	μ_α (μas/yr)	$\sigma_{\mu,\alpha}$ (μas/yr)	N_α	χ^2_α	μ_δ (μas/yr)	$\sigma_{\mu,\delta}$ (μas/yr)	N_δ	χ^2_δ	Length (years)	Last Obs. (MJD)	New PM	z	z flag	z Source
1532+016	15:34:52.453660	0.013	+01:31:04.206826	0.79	-14.37	18.66	29	2.0	-30.47	15.72	29	0.9	20.2	55327.6		1.44		OCARS
1538+149	15:40:49.491511	0.013	+14:47:45.884521	0.11	6.39	4.60	123	2.1	-14.61	4.97	123	2.2	27.1	57809.0		0.60		OCARS
1547+507	15:49:17.468562	0.005	+50:38:05.788111	0.06	10.38	6.19	20	1.7	2.62	7.06	20	1.0	17.4	55112.8		2.17		OCARS
1546+027	15:49:29.436857	0.007	+02:37:01.163373	0.13	4.18	2.23	309	1.9	1.64	6.00	309	3.4	24.8	57833.9		0.41		OCARS
1548+056	15:50:35.269277	0.018	+05:27:10.447862	0.27	-0.31	1.72	204	1.4	12.04	4.24	204	2.4	27.2	57816.0		1.42		OCARS
1550-242	15:53:31.627806	0.010	-24:22:06.035328	0.33	1.49	16.73	18	1.2	-35.06	56.76	18	1.7	19.0	57576.6		0.33		OCARS
1549-790	15:56:58.870440	0.350	-79:14:04.281724	2.14	-39.81	27.85	21	1.8	-82.49	31.86	21	2.5	21.0	55784.3		0.15		OCARS
1555+001	15:57:51.433988	0.017	-00:01:50.413834	0.14	-1.75	2.85	238	1.4	0.59	3.92	238	1.4	27.1	57809.0		1.77		OCARS
1554-643	15:58:50.284359	0.085	-64:32:29.637286	2.09	-3.82	11.23	16	0.3	-4.01	34.94	16	0.7	13.1	57659.8		0.08		OCARS
1557+032	15:59:30.972631	0.044	+03:04:48.256033	0.76	0.99	4.19	72	1.6	-17.74	5.73	72	1.3	22.5	57776.2		3.89		OCARS
1556-245	15:59:41.409133	0.214	-24:42:38.832572	1.21	36.77	48.49	23	1.2	3.86	50.23	23	0.9	13.9	55700.4		2.81		OCARS
1600+335	16:02:07.263907	1.408	+33:26:53.082288	9.89	-0.70	7.02	52	2.5	3.68	10.73	52	2.0	19.9	56946.1		1.10		OCARS
1601+112	16:03:41.931253	0.009	+11:05:48.679018	0.20	-6.94	9.86	47	2.0	12.73	20.24	47	2.1	21.6	57798.9		0.14		OCARS
1602-115	16:05:17.531645	0.020	-11:39:26.830582	0.83	3.08	8.34	88	1.3	35.70	20.15	88	1.7	11.5	57767.0				OCARS
1604-333	16:07:34.762354	0.019	-33:31:08.912748	0.61	9.29	13.75	56	1.3	17.38	21.26	56	1.8	22.0	57810.1				OCARS
1606+106	16:08:46.203176	0.013	+10:29:07.775740	0.17	5.33	0.91	2396	2.1	0.11	0.83	2396	1.7	27.1	57823.0		1.23		OCARS
1606-398	16:10:21.879141	0.049	-39:58:58.329456	0.49	-9.51	122.22	12	2.5	-60.03	90.99	12	1.9	14.9	57731.0		0.52		OCARS
1608+243	16:10:42.026754	0.022	+24:14:49.011805	0.24	3.74	8.96	58	1.6	-12.88	5.51	58	1.1	20.7	57795.0		1.45		OCARS
1611-710	16:16:30.641504	0.050	-71:08:31.454063	0.30	3.58	24.24	24	0.9	19.62	20.05	24	0.4	13.1	57659.8		2.27		OCARS
1614+051	16:16:37.556849	0.015	+04:59:32.736591	0.07	5.93	3.64	153	1.3	-6.50	3.54	153	1.3	25.1	57735.9		3.21		OCARS
1615+029	16:17:49.909430	0.587	+02:46:43.079755	9.21	-14.88	10.91	72	1.0	-5.78	30.15	72	1.5	21.6	57791.9		1.34		OCARS
1616+063	16:19:03.687674	0.036	+06:13:02.242524	0.32	-17.81	7.69	81	1.5	-3.47	11.47	81	1.4	24.5	57738.0		2.09		OCARS

Table A.1 (cont'd)

IVS	RA (J2000 h:m:s)	σ_α (ms)	Dec (J2000 d:′:″)	σ_δ (mas)	μ_α (μas/yr)	$\sigma_{\mu,\alpha}$ (μas/yr)	N_α	χ^2_α	μ_δ (μas/yr)	$\sigma_{\mu,\delta}$ (μas/yr)	N_δ	χ^2_δ	Length (years)	Last Obs. (MJD)	New PM	z	z flag	z Source
1617+229	16:19:14.824598	0.021	+22:47:47.850324	0.41	-2.52	4.33	284	1.9	-27.82	6.93	284	1.6	21.2	57819.9		1.99		OCARS
1619-680	16:24:18.437016	0.090	-68:09:12.498015	0.94	-3.71	15.22	55	1.8	25.14	18.86	55	1.7	26.3	57784.9		1.36		OCARS
1623+578	16:24:24.808987	3.911	+57:41:16.274174	17.50	17.96	3.41	159	1.6	20.30	3.60	159	1.3	22.6	57819.9	*	0.79		OCARS
1622-253	16:25:46.892006	0.082	-25:27:38.327596	0.31	-0.47	1.08	2246	2.1	8.01	1.38	2246	2.2	27.2	57837.0		0.79		OCARS
1624+416	16:25:57.669704	0.010	+41:34:40.629209	0.11	-9.52	8.27	30	1.6	-14.27	8.30	30	1.0	20.1	55264.7		2.55		OCARS
1622-297	16:26:06.020805	0.025	-29:51:26.971595	0.32	-3.63	6.39	78	2.5	-17.95	8.40	78	2.1	22.6	56886.8		0.81		OCARS
1625+582	16:26:37.236550	0.001	+58:09:17.668081	0.01	-14.76	36.16	2	inf	110.64	69.33	2	inf	8.8	57286.0	*	0.75		OCARS
1624-617	16:28:54.689806	0.042	-61:52:36.398351	0.34	-14.71	11.82	42	0.8	-6.16	18.55	42	1.6	13.3	57728.9		2.58		OCARS
NGC6251	16:32:31.969801	0.138	+82:32:16.400841	0.69	0.16	3.24	200	1.6	-1.58	2.54	200	1.5	19.6	57833.9		0.02		OCARS
1633+38	16:35:15.493006	0.013	+38:08:04.500380	0.05	2.42	1.91	321	2.6	0.50	3.36	321	1.8	26.3	57499.5		1.81		OCARS
1636+473	16:37:45.130542	0.020	+47:17:33.831251	0.37	-6.86	5.27	142	2.1	21.02	6.26	142	1.6	20.6	57840.9		0.74		OCARS
1637+574	16:38:13.456291	0.008	+57:20:23.979023	0.07	5.88	1.75	149	1.6	-1.23	2.36	149	2.4	26.9	57798.9		0.75		OCARS
NRAO512	16:40:29.632767	0.020	+39:46:46.028564	0.15	-1.19	0.61	1467	2.0	-2.77	0.57	1467	1.9	26.4	57833.9		1.66		OCARS
1639+230	16:41:25.227553	0.009	+22:57:04.032877	0.15	0.32	2.68	341	1.8	-7.31	4.76	341	2.2	21.2	57837.0		2.06		OCARS
1639-062	16:42:02.177707	0.007	-06:21:23.694946	0.12	-9.66	3.94	324	1.9	-10.41	2.85	324	1.7	12.9	57833.9		1.51		OCARS
1642+690	16:42:07.848540	0.008	+68:56:39.756414	0.04	6.29	1.71	149	1.9	-19.43	3.17	149	3.5	27.1	57786.0		0.75		OCARS
1633-810	16:42:57.345787	0.183	-81:08:35.069762	1.59	12.42	18.41	21	0.8	-10.54	24.03	21	1.0	12.9	57590.7				OCARS
1647-296	16:50:39.544209	0.215	-29:43:46.960744	10.88	-43.69	29.62	24	0.9	19.94	33.12	24	0.9	19.7	57102.7				OCARS
1651+391	16:52:58.509548	0.041	+39:02:49.818367	1.77	4.49	5.98	76	1.6	-25.46	8.02	76	2.3	20.5	57729.9		1.30		OCARS
DA426	16:53:52.216673	0.007	+39:45:36.608832	0.10	-1.59	1.93	319	1.5	3.22	2.70	319	1.4	25.2	57759.0		0.03		OCARS
1656+348	16:58:01.419092	0.174	+34:43:28.401917	0.47	16.82	17.98	19	1.1	-13.41	23.88	19	1.3	17.7	55306.6		1.94		OCARS
1656+477	16:58:02.779597	0.009	+47:37:49.230378	0.17	0.74	10.82	23	2.0	-18.13	18.89	23	4.2	16.8	55313.6		1.62		OCARS

Table A.1 (cont'd)

IVS	RA (J2000 h:m:s)	σ_α (ms)	Dec (J2000 d:′:″)	σ_δ (mas)	μ_α (μas/yr)	$\sigma_{\mu,\alpha}$ (μas/yr)	N_α	χ^2_α	μ_δ (μas/yr)	$\sigma_{\mu,\delta}$ (μas/yr)	N_δ	χ^2_δ	Length (years)	Last Obs. (MJD)	New PM	z	z flag	z Source
1655+077	16:58:09.011159	0.417	+07:41:27.552104	15.25	-4.64	9.68	53	1.2	-7.62	11.24	53	1.2	25.1	57102.7		0.62		OCARS
1656+053	16:58:33.446879	4.144	+05:15:16.416395	197.15	-22.02	16.04	76	2.0	-3.58	10.61	76	1.4	26.2	57464.4		0.88		OCARS
1656-075	16:58:44.061935	0.012	-07:39:17.694281	0.20	-55.90	26.16	109	2.3	-61.35	20.70	109	1.8	15.1	57806.9		3.74		OCARS
1657-261	17:00:53.154070	0.048	-26:10:51.725470	0.17	-2.88	3.63	438	2.4	11.59	6.62	438	2.4	26.6	57840.9				OCARS
1659+399	17:01:24.634800	0.045	+39:54:37.091975	0.70	-2.86	11.82	42	1.8	-3.60	10.27	42	0.9	11.7	57809.0		0.51	c	OCARS
1657-562	17:01:44.858107	0.060	-56:21:55.901462	0.96	33.89	10.04	48	1.1	-111.25	18.20	48	1.9	13.6	57735.9				OCARS
1659-621	17:03:36.541222	0.032	-62:12:40.008739	0.22	-31.97	8.94	46	1.0	-26.01	13.07	46	1.0	13.5	57791.9		1.75		OCARS
1705+456	17:07:17.753328	0.028	+45:36:10.553109	0.25	-61.32	21.67	21	2.4	27.64	16.42	21	1.4	18.9	55342.6		0.65		OCARS
1705+018	17:07:34.415278	0.006	+01:48:45.699180	0.06	-1.59	2.84	236	2.0	-11.98	5.01	236	2.2	26.0	57840.9		2.57		OCARS
1705+135	17:07:45.637258	0.011	+13:31:05.232934	0.17	-16.01	23.20	10	3.5	1.41	22.40	10	1.5	20.9	57707.9		0.94		OCARS
1706-174	17:09:34.345372	0.022	-17:28:53.364852	0.42	-3.32	6.82	130	1.4	-0.34	7.15	130	1.2	21.7	57819.9				OCARS
1716+686	17:16:13.938046	0.002	+68:36:38.744970	0.01	11.49	6.81	3	0.1	4.37	11.75	3	27.0	20.8	57406.5	*	0.78		OCARS
1717+178	17:19:13.048378	0.048	+17:45:06.438476	0.53	-5.86	2.92	71	1.8	-0.75	3.66	71	2.3	27.1	57805.1		0.14	b	NED
1718-649	17:23:41.029468	0.032	-65:00:36.611083	0.19	-49.67	103.33	17	8.0	47.65	120.86	17	7.1	25.8	57548.6		0.01		OCARS
1726+769	17:23:59.445114	0.001	+76:53:11.551811	0.00	3.70	8.31	3	4.9	7.40	12.07	3	39.8	20.8	57406.5	*	0.68		OCARS
1722+330	17:24:14.197829	0.043	+33:03:03.938287	1.11	-22.98	10.48	63	2.1	28.20	25.97	63	2.2	20.6	57753.0		1.87	c	OCARS
1721-146	17:24:46.966546	0.005	-14:43:59.760758	0.19	-10.76	13.01	4	24.1	11.18	27.92	4	11.2	11.5	57771.2	*	0.90		OCARS
1726+455	17:27:27.650784	0.008	+45:30:39.730808	0.16	-4.35	1.01	1413	1.9	-2.98	0.95	1413	1.7	24.9	57805.1		0.72		OCARS
1725+123	17:28:07.051144	0.041	+12:15:39.485552	0.77	0.85	10.11	45	2.0	-11.23	20.16	45	2.0	21.6	57802.0		0.59		OCARS
1727+502	17:28:18.624078	0.000	+50:13:10.471056	0.01	70.75	10.87	11	3.2	64.76	10.40	11	2.1	26.7	57688.5	*	0.06		OCARS
1725+044	17:28:24.952721	0.011	+04:27:04.913880	0.22	6.44	8.36	30	1.2	10.31	16.78	30	1.9	20.1	55271.7		0.30		OCARS
NRAO530	17:33:02.705793	0.004	-13:04:49.548303	0.12	5.98	1.59	432	1.9	5.85	2.67	432	2.1	27.1	57810.1		0.90		OCARS

Table A.1 (cont'd)

IVS	RA (J2000 h:m:s)	σ_α (ms)	Dec (J2000 d:′:″)	σ_δ (mas)	μ_α (μas/yr)	$\sigma_{\mu,\alpha}$ (μas/yr)	N_α	χ^2_α	μ_δ (μas/yr)	$\sigma_{\mu,\delta}$ (μas/yr)	N_δ	χ^2_δ	Length (years)	Last Obs. (MJD)	New PM	z	z flag	z Source
1725-795	17:33:40.700355	0.061	-79:35:55.716478	0.38	11.31	13.15	28	0.6	-2.05	28.25	28	0.7	13.1	57659.8		0.88		OCARS
1732+389	17:34:20.578531	0.006	+38:57:51.442954	0.10	-5.16	3.06	102	2.6	4.66	4.20	102	2.6	27.1	57810.1		0.97		OCARS
1734+363	17:35:48.086598	0.016	+36:16:45.611611	0.14	-19.67	13.04	10	1.6	0.80	10.93	10	1.2	21.6	57840.9		0.80	c	OCARS
1736+324	17:38:40.501749	0.035	+32:24:09.024946	0.58	1.69	12.18	30	2.1	-19.99	19.26	30	1.2	20.8	57802.0		0.13		OCARS
1738+499	17:39:27.390529	0.043	+49:55:03.368281	0.26	-0.40	6.23	59	2.7	-0.86	5.52	59	1.7	22.9	57791.9		1.54		OCARS
1738+476	17:39:57.129049	0.016	+47:37:58.361914	0.14	-5.19	5.11	57	2.6	2.91	5.34	57	1.4	26.3	57700.8		0.95		OCARS
1741-038	17:43:58.856143	0.008	-03:50:04.616613	0.08	1.05	0.45	3797	2.0	-0.90	0.52	3797	2.2	27.2	57837.0		1.05		OCARS
NGC6454	17:44:56.607057	0.010	+55:42:17.161215	0.10	-14.06	11.10	27	1.4	1.15	9.62	27	0.6	12.7	54943.9		0.03		OCARS
1743+173	17:45:35.208168	0.007	+17:20:01.423484	0.11	6.50	4.37	56	1.5	-0.01	11.85	56	2.0	25.3	57819.9		1.70		OCARS
1745+624	17:46:14.034142	0.019	+62:26:54.737878	0.22	10.81	1.44	821	1.5	10.42	2.17	821	1.5	24.3	57810.1		3.89		OCARS
1746+470	17:47:26.647190	0.250	+46:58:50.921256	13.73	-13.51	6.30	59	1.7	5.27	3.61	59	0.8	22.2	57514.5		1.48	b	OCARS
1749+701	17:48:32.851984	5.415	+70:05:50.723398	23.83	10.03	10.90	28	1.7	8.60	6.52	28	0.9	24.4	57464.4		0.77		OCARS
1749+096	17:51:32.818576	0.007	+09:39:00.728510	0.06	0.49	0.44	3075	1.8	-0.06	0.46	3075	1.7	27.2	57837.0		0.32		OCARS
1751+441	17:53:22.647881	0.006	+44:09:45.686064	0.06	-43.30	8.68	25	2.4	-1.64	11.73	25	2.5	19.8	55168.8		0.87		OCARS
1751+288	17:53:42.473623	0.009	+28:48:04.938784	0.06	-5.76	3.88	388	3.1	-1.43	3.25	388	2.6	23.5	57837.0		1.11		OCARS
1754+159	17:56:33.725606	0.004	+15:53:43.832989	0.14	-8.33	5.62	11	1.7	-5.59	12.19	11	1.0	21.1	57786.0	*	0.55		OCARS
1754+155	17:56:53.101525	0.292	+15:35:20.824205	1.32	8.53	9.76	180	1.6	0.59	6.60	180	1.3	15.1	57809.0		2.06		APO
1755+055	17:57:58.825137	0.000	+05:31:48.023850	0.00	44.90	101.54	3	160569.5	132.22	274.99	3	2456.2	11.7	57406.5	*	0.34		OCARS
1758+388	18:00:24.765342	0.007	+38:48:30.697413	0.08	-1.61	2.28	121	1.6	2.52	4.54	121	1.8	22.9	57806.9		2.09		OCARS
1803+784	18:00:45.683929	0.019	+78:28:04.018211	0.07	-0.34	0.46	1908	1.8	-0.88	0.45	1908	1.8	27.2	57837.0		0.68		OCARS
1800+440	18:01:32.314816	0.007	+44:04:21.900329	0.09	-3.16	4.10	98	3.1	-4.50	6.70	98	2.5	26.2	57777.9		0.66		OCARS
1759-396	18:02:42.680087	0.114	-39:40:07.901575	7.30	-25.10	10.13	426	2.0	-4.71	12.22	426	1.9	15.2	57840.9		1.32		OCARS

Table A.1 (cont'd)

IVS	RA (J2000 h:m:s)	σ_α (ms)	Dec (J2000 d:′:″)	σ_δ (mas)	μ_α (μas/yr)	$\sigma_{\mu,\alpha}$ (μas/yr)	N_α	χ^2_α	μ_δ (μas/yr)	$\sigma_{\mu,\delta}$ (μas/yr)	N_δ	χ^2_δ	Length (years)	Last Obs. (MJD)	New PM	z	z flag	z Source
1758-651	18:03:23.496592	0.037	-65:07:36.761274	0.24	3.01	6.31	198	1.3	-0.73	7.59	198	1.2	24.9	57840.9		1.20		OCARS
3C371	18:06:50.680682	0.044	+69:49:28.108642	0.19	6.82	0.73	1181	2.1	-0.24	0.59	1181	1.6	26.4	57823.0		0.05		OCARS
1806+456	18:08:21.885884	0.012	+45:42:20.866229	0.20	-0.67	3.46	264	1.9	8.32	5.79	264	2.4	23.0	57823.0		0.83		OCARS
1806-458	18:09:57.871690	0.016	-45:52:41.014652	0.30	-51.20	23.14	50	1.5	-21.98	25.41	50	1.5	15.3	57659.8		0.07		OCARS
1815-553	18:19:45.399574	0.043	-55:21:20.745071	0.32	-5.66	5.70	260	1.5	-5.71	6.57	260	1.6	26.7	57717.0		1.63		OCARS
1817-254	18:20:57.848788	0.045	-25:28:12.584578	0.59	8.63	14.84	20	1.5	-17.40	23.43	20	1.1	24.4	57731.0				OCARS
1826+796	18:23:14.108983	0.097	+79:38:49.001654	0.21	49.88	37.64	15	9.3	-16.96	23.24	15	3.4	26.3	57679.8		0.22		OCARS
1823+689	18:23:32.853945	0.080	+68:57:52.613150	0.62	4.39	6.10	68	1.1	-0.27	9.00	68	1.2	21.7	57764.9		2.14		APO
1821+107	18:24:02.855191	0.107	+10:44:23.774173	3.23	-10.51	4.99	35	1.0	23.13	11.35	35	1.4	26.0	57520.5		1.36		OCARS
1823+568	18:24:07.068367	0.007	+56:51:01.490896	0.10	-4.73	1.31	187	1.6	2.33	1.95	187	1.9	27.1	57812.9		0.66		OCARS
1824-582	18:29:12.402387	0.051	-58:13:55.161987	0.48	-20.73	13.26	28	1.4	-33.83	22.49	28	1.9	12.6	57809.0		1.53		OCARS
1830+285	18:32:50.185629	0.006	+28:33:35.955233	0.14	-11.75	7.95	29	2.4	11.03	10.35	29	1.4	18.5	55112.8		0.59		OCARS
1831-711	18:37:28.714975	0.021	-71:08:43.554581	0.17	6.66	4.71	44	1.2	-12.57	5.74	44	1.1	26.7	57717.0		1.36		OCARS
1839+548	18:40:57.376690	0.024	+54:52:15.910749	0.17	-3.23	28.00	5	2.2	-26.83	38.08	5	8.2	21.4	57407.3	*	0.65		OCARS
3C390.3	18:42:08.990133	0.001	+79:46:17.128332	0.00	37.20	3.21	26	2.1	1.80	3.24	26	2.6	25.2	57688.5	*	0.06		OCARS
1842+681	18:42:33.641666	0.015	+68:09:25.228007	0.09	1.13	3.91	74	1.9	-1.76	4.03	74	3.4	26.5	57840.9		0.47		OCARS
1843+356	18:45:35.108854	0.000	+35:41:16.726197	0.01	-7.23	9.89	3	1.9	-6.41	15.70	3	2.6	19.6	57406.5	*	0.76		OCARS
1842-289	18:45:51.368266	0.040	-28:52:40.276471	0.56	-1.42	828.46	11	4.3	11.83	1294.18	11	3.2	10.3	56897.1				OCARS
1846+322	18:48:22.088575	0.004	+32:19:02.603731	0.07	-29.28	5.06	541	3.8	7.61	5.38	541	4.0	20.9	57840.9		0.80		OCARS
1849+670	18:49:16.072301	0.015	+67:05:41.680532	0.12	-0.94	1.10	279	2.6	-4.17	1.56	279	3.8	25.1	57833.9		0.66		OCARS
1856+736	18:54:57.299954	0.050	+73:51:19.906419	0.25	-4.17	11.30	25	1.5	-36.58	14.10	25	1.8	18.2	55216.7		0.46		OCARS
3C395	19:02:55.938805	0.101	+31:59:41.699293	1.35	67.84	9.50	65	3.0	-32.23	7.13	65	1.6	24.9	57520.5		0.64		OCARS

Table A.1 (cont'd)

IVS	RA (J2000 h:m:s)	σ_α (ms)	Dec (J2000 d:′:″)	σ_δ (mas)	μ_α (μas/yr)	$\sigma_{\mu,\alpha}$ (μas/yr)	N_α	χ^2_α	μ_δ (μas/yr)	$\sigma_{\mu,\delta}$ (μas/yr)	N_δ	χ^2_δ	Length (years)	Last Obs. (MJD)	New PM	z	z flag	z Source
1901+155	19:04:14.361135	0.007	+15:36:38.451226	0.15	21.34	34.45	10	1.0	15.21	66.47	10	0.7	20.5	57576.6				OCARS
1908+484	19:09:46.562714	0.023	+48:34:31.820159	0.20	-47.36	83.14	22	1.9	20.25	48.46	22	0.9	20.1	57646.8		0.51	b	OCARS
1908-201	19:11:09.652907	0.011	-20:06:55.108381	0.27	4.58	1.51	966	1.9	-5.27	2.91	966	2.1	23.9	57840.9		1.12		OCARS
1909+161	19:11:58.257456	0.029	+16:11:46.865161	0.31	-3.85	6.80	241	1.5	-16.90	9.63	241	1.4	21.1	57806.9				OCARS
1903-802	19:12:40.020801	1.910	-80:10:05.951280	3.01	-25.63	14.73	19	0.6	-17.53	14.31	19	0.6	19.3	55229.7		0.50	c	OCARS
1915+657	19:15:23.819071	0.016	+65:48:46.388165	0.11	0.35	32.24	4	3.4	103.89	48.60	4	11.4	21.9	57810.1	*	0.49		OCARS
1920-211	19:23:32.189827	0.006	-21:04:33.333036	0.09	-6.61	3.61	246	1.7	-1.00	5.65	246	1.7	21.1	57806.9		0.87		OCARS
1921-293	19:24:51.055948	0.010	-29:14:30.120773	0.19	-4.72	1.02	1836	2.7	10.52	1.53	1836	2.9	27.2	57833.9		0.35		OCARS
1923+210	19:25:59.605378	0.017	+21:06:26.162281	0.16	10.43	2.30	955	2.4	17.79	1.41	955	1.7	27.2	57837.0		0.00		OCARS
1928+738	19:27:48.495149	0.035	+73:58:01.570235	0.21	-3.37	3.78	100	1.8	-7.88	12.85	100	5.6	26.2	57464.4		0.30		OCARS
1926+087	19:28:40.855481	0.016	+08:48:48.412859	0.32	8.83	19.05	11	1.0	-19.98	47.91	11	1.6	14.1	54854.0				OCARS
1925-610	19:30:06.160085	0.046	-60:56:09.183063	0.43	-0.62	13.36	50	1.4	8.28	15.57	50	1.8	26.4	57745.0		3.25		OCARS
1929+226	19:31:24.916760	0.015	+22:43:31.258579	0.23	-22.47	3.74	122	1.8	-5.85	6.77	122	2.1	22.7	57819.9				OCARS
1929-457	19:32:44.887832	0.052	-45:36:37.929008	0.53	-28.98	88.86	12	1.5	4.79	256.81	12	1.0	11.8	57548.6		0.65		OCARS
1932+204	19:35:10.472964	0.036	+20:31:54.154282	0.26	39.21	21.06	25	2.1	18.79	16.84	25	1.5	21.3	56568.8				OCARS
1933-400	19:37:16.217395	0.029	-39:58:01.548505	1.55	21.59	6.27	94	1.2	-2.76	12.77	94	1.2	26.3	57776.2		0.96	c	OCARS
1936-155	19:39:26.657754	0.009	-15:25:43.058441	0.11	8.04	2.18	196	1.8	2.65	4.07	196	1.7	23.9	57826.9		1.66		OCARS
1937-101	19:39:57.256601	0.007	-10:02:41.520233	0.22	38.74	11.89	29	1.1	41.26	17.05	29	1.1	19.2	55112.8		3.79		OCARS
1935-692	19:40:25.528099	0.027	-69:07:56.972174	0.29	-33.68	7.50	52	1.0	-14.15	12.45	52	1.1	26.1	57659.8		3.15		OCARS
1947+079	19:50:05.540114	0.041	+08:07:13.980023	0.41	44.37	72.79	17	7.7	-25.72	169.11	17	11.4	26.9	57764.9		0.30		OCARS
1954+513	19:55:42.738293	0.012	+51:31:48.546123	0.17	-0.29	8.79	77	9.6	-2.43	4.66	77	3.6	27.0	57776.2		1.22		OCARS
1954-388	19:57:59.819266	0.028	-38:45:06.356168	0.18	3.18	1.25	1261	2.1	-8.51	1.79	1261	2.5	24.8	57840.9		0.63		OCARS

Table A.1 (cont'd)

IVS	RA (J2000 h:m:s)	σ_α (ms)	Dec (J2000 d:′:″)	σ_δ (mas)	μ_α (μas/yr)	$\sigma_{\mu,\alpha}$ (μas/yr)	N_α	χ^2_α	μ_δ (μas/yr)	$\sigma_{\mu,\delta}$ (μas/yr)	N_δ	χ^2_δ	Length (years)	Last Obs. (MJD)	New PM	z	z flag	z Source
1958-179	20:00:57.090441	0.010	-17:48:57.672777	0.12	-7.63	1.00	1515	1.8	-3.78	1.41	1515	1.8	26.3	57823.0		0.65		OCARS
2000+472	20:02:10.418293	0.016	+47:25:28.773666	0.25	-16.00	3.91	353	4.1	-4.25	3.01	353	2.1	20.6	57833.9		2.27		OCARS
2000+148	20:02:41.999223	0.035	+15:01:14.573680	1.04	-0.27	6.42	33	1.3	24.52	15.19	33	2.1	20.5	57581.6				OCARS
2000-330	20:03:24.115751	0.442	-32:51:45.119635	9.75	52.74	17.65	31	1.1	-50.01	48.28	31	1.9	22.6	57102.7		3.77		OCARS
2007+777	20:05:30.998861	0.233	+77:52:43.245748	1.37	23.25	3.42	266	3.0	-0.04	1.37	266	1.6	26.0	57499.5		0.34		OCARS
2002-375	20:05:55.070917	0.008	-37:23:41.478989	0.32	-4.15	14.19	52	1.5	3.47	31.22	52	1.8	15.1	57810.1				OCARS
2005+403	20:07:44.945068	0.464	+40:29:48.609553	7.55	14.79	114.24	12	0.8	-5.00	96.80	12	1.4	25.5	57520.5		1.74		OCARS
2005-489	20:09:25.390896	0.285	-48:49:53.724291	2.51	21.94	65.72	51	2.5	15.63	32.23	51	1.9	24.2	56932.6		0.07		OCARS
OW-015	20:11:14.216404	0.204	-06:44:03.530287	11.06	29.19	33.17	21	1.9	-10.03	35.62	21	1.4	16.8	55545.5		0.55		OCARS
2008-159	20:11:15.710925	0.006	-15:46:40.253704	0.06	-6.55	2.40	580	1.8	12.28	3.22	580	1.8	27.2	57840.9		1.18		OCARS
2013+163	20:16:13.860043	0.012	+16:32:34.113289	0.17	-3.08	5.16	171	1.6	6.05	7.48	171	1.7	21.2	57837.0				OCARS
2017+743	20:17:13.079406	0.051	+74:40:48.000289	0.24	-6.63	10.26	25	3.5	10.14	6.19	25	1.0	23.4	56470.9		2.19		OCARS
2021+614	20:22:06.681807	0.023	+61:36:58.804746	0.13	18.60	9.51	31	4.2	14.89	12.61	31	5.2	25.6	57520.5		0.23		OCARS
2021+317	20:23:19.016484	0.225	+31:53:02.287368	7.27	12.00	15.56	42	4.4	11.38	14.86	42	3.3	24.4	57102.7				OCARS
2029+024	20:31:47.251128	0.006	+02:39:37.283509	0.16	7.60	54.31	14	2.0	16.49	120.49	14	1.6	11.0	57786.0		0.86		OCARS
2030+547	20:31:47.958712	0.195	+54:55:03.138309	1.89	6.28	20.63	18	3.0	32.68	51.60	18	5.8	17.5	55229.7		1.26		OCARS
2029+121	20:31:54.994268	0.006	+12:19:41.340146	0.09	-10.93	3.11	99	1.6	-16.81	4.37	99	1.8	24.8	57798.9		1.22		OCARS
3C418	20:38:37.034660	0.004	+51:19:12.661988	0.04	-15.52	1.29	1794	4.4	-7.80	1.55	1794	4.8	27.2	57840.9		1.69		OCARS
2037-253	20:40:08.772802	0.235	-25:07:46.663329	1.00	3.63	18.67	44	1.0	-55.92	17.29	44	1.1	16.6	55700.4		1.57		OCARS
CL4	20:50:51.131535	0.136	+31:27:27.375375	10.06	-28.73	26.63	17	0.5	13.45	56.76	17	2.8	18.3	54882.0		3.18		OCARS
2051+745	20:51:33.734493	0.043	+74:41:40.498349	0.12	-16.80	35.28	14	2.5	4.26	28.86	14	1.1	25.2	57776.2		0.92		APO
2052-474	20:56:16.359799	0.014	-47:14:47.627221	0.19	-12.97	2.85	970	2.1	-4.21	3.24	970	2.0	26.5	57833.9		1.49		OCARS

Table A.1 (cont'd)

IVS	RA (J2000 h:m:s)	σ_α (ms)	Dec (J2000 d:′:″)	σ_δ (mas)	μ_α (μas/yr)	$\sigma_{\mu,\alpha}$ (μas/yr)	N_α	χ^2_α	μ_δ (μas/yr)	$\sigma_{\mu,\delta}$ (μas/yr)	N_δ	χ^2_δ	Length (years)	Last Obs. (MJD)	New PM	z	z flag	z Source
2054-377	20:57:41.603508	0.010	-37:34:02.990149	0.40	38.96	19.86	14	1.8	32.56	28.59	14	1.9	25.6	57498.5		1.07		OCARS
2058-297	21:01:01.660025	0.045	-29:33:27.835698	0.65	-1.77	75.84	20	1.1	-7.52	70.77	20	0.9	13.3	55545.5		1.49	c	OCARS
2059+034	21:01:38.834159	0.007	+03:41:31.320773	0.09	-5.71	3.29	638	1.9	-25.12	3.85	638	2.0	25.7	57837.0		1.01		OCARS
2059-786	21:05:44.961715	0.147	-78:25:34.546725	1.64	1.83	41.24	17	0.9	-4.97	36.04	17	0.9	20.0	55420.6				OCARS
2106+143	21:08:41.032144	0.004	+14:30:27.012621	0.06	-3.69	4.05	38	1.0	6.48	6.27	38	1.1	21.2	57840.9		2.02		OCARS
2106-413	21:09:33.188649	0.019	-41:10:20.606878	0.63	4.89	9.75	78	2.1	-11.47	10.25	78	1.4	26.6	57810.1		1.06		OCARS
2113+293	21:15:29.413405	0.011	+29:33:38.365904	0.32	0.01	1.08	1106	1.7	0.15	1.77	1106	1.6	27.2	57840.9		1.51		OCARS
2109-811	21:16:30.845842	0.166	-80:53:55.223832	0.45	1.68	12.18	26	0.7	7.25	14.67	26	0.9	18.2	55420.6				OCARS
2123-463	21:26:30.704253	0.013	-46:05:47.891991	0.24	-3.33	18.95	28	1.3	-3.94	34.86	28	0.7	12.3	57717.0		1.67	c	OCARS
2126-158	21:29:12.175845	0.054	-15:38:41.037987	2.03	-10.82	2.32	741	1.7	-66.77	5.00	741	1.9	25.4	57840.9		3.27		OCARS
2127-096	21:30:19.087229	0.399	-09:27:37.410108	10.46	18.65	8.08	90	1.8	4.89	11.43	90	1.5	19.7	57781.0		0.78	b	OCARS
2128+048	21:30:32.877320	0.047	+05:02:17.476724	0.65	-29.37	53.47	14	2.3	27.04	49.15	14	2.0	26.4	57673.8		0.99		OCARS
2131-021	21:34:10.309602	0.008	-01:53:17.238646	0.25	-4.75	6.11	178	1.6	-4.97	7.41	178	1.6	27.1	57805.1		1.28		OCARS
2134+00	21:36:38.586260	0.037	+00:41:54.211377	0.48	-33.42	8.41	386	1.9	-16.29	6.93	386	1.7	26.9	57743.9		1.94		OCARS
2135-184	21:38:41.926828	0.200	-18:10:44.380046	3.65	-1359.25	1927.45	13	5.9	-159.81	1716.43	13	4.1	19.0	57576.6		0.19		OCARS
2136+141	21:39:01.309285	0.006	+14:23:35.992178	0.06	2.60	1.85	1095	2.3	1.62	2.01	1095	1.8	26.8	57806.9		2.43		OCARS
2141+175	21:43:35.544552	0.014	+17:43:48.787675	0.16	6.39	4.76	226	2.1	-5.67	4.36	226	1.9	12.9	57826.9		0.21		OCARS
2142+110	21:45:18.775072	0.004	+11:15:27.312417	0.10	-2.97	10.62	35	1.5	-5.98	12.26	35	1.3	21.2	57646.8		0.55		OCARS
2143-156	21:46:22.978976	0.340	-15:25:43.888751	3.04	-8.66	7.83	161	1.9	-7.87	11.74	161	1.6	21.6	57816.0		0.70		OCARS
2144+092	21:47:10.162969	0.006	+09:29:46.671977	0.08	5.38	5.98	116	2.2	-5.60	5.12	116	1.6	26.7	57774.0		1.11		OCARS
2142-758	21:47:12.730783	0.029	-75:36:13.224790	0.11	50.22	16.07	109	1.8	14.81	9.81	109	1.4	26.1	57659.8		1.14		OCARS
2145+082	21:47:55.219374	0.106	+08:30:11.896806	0.32	-12.31	45.27	25	1.6	-0.63	160.11	25	1.1	21.1	57625.7		2.61		OCARS

Table A.1 (cont'd)

IVS	RA (J2000 h:m:s)	σ_α (ms)	Dec (J2000 d:′:″)	σ_δ (mas)	μ_α (μas/yr)	$\sigma_{\mu,\alpha}$ (μas/yr)	N_α	χ^2_α	μ_δ (μas/yr)	$\sigma_{\mu,\delta}$ (μas/yr)	N_δ	χ^2_δ	Length (years)	Last Obs. (MJD)	New PM	z	z flag	z Source
2149+056	21:51:37.875555	0.108	+05:52:12.956192	0.91	-0.19	2.95	476	1.6	-0.27	5.55	476	1.5	26.8	57816.0		0.74		OCARS
2149-306	21:51:55.523924	0.022	-30:27:53.698173	0.18	-7.95	8.52	149	1.6	-12.00	7.31	149	1.7	25.6	57520.5		2.35	c	OCARS
2146-783	21:52:03.154460	0.274	-78:07:06.638483	1.69	4.22	59.15	12	1.5	70.64	32.91	12	0.5	21.0	55784.3		4.00		OCARS
2150+173	21:52:24.819384	0.010	+17:34:37.795020	0.32	-7.52	3.48	68	1.4	3.23	3.75	68	1.6	25.5	57805.1		0.87		OCARS
2155+312	21:57:28.823919	0.009	+31:27:01.351373	0.09	3.29	7.63	101	1.8	-9.39	10.72	101	2.0	20.7	57788.0		1.49		OCARS
2155-152	21:58:06.281879	0.015	-15:01:09.328765	0.20	-31.38	6.47	56	3.2	-36.72	7.04	56	2.7	22.0	57733.0		0.67		OCARS
2155-304	21:58:52.065128	0.026	-30:13:32.118144	0.20	11.44	7.76	40	0.9	9.37	20.76	40	1.7	24.7	57777.9		0.12		OCARS
VR422201	22:02:43.291372	0.016	+42:16:39.979442	0.26	2.26	2.41	344	2.4	-1.53	5.68	344	6.1	26.4	57520.5		0.07		OCARS
2204-540	22:07:43.733273	0.029	-53:46:33.821003	0.47	-4.63	6.98	71	1.2	-17.34	9.37	71	1.3	26.6	57840.9		1.21		OCARS
2205+166	22:07:52.865693	0.041	+16:52:17.815783	1.44	-15.15	15.59	23	1.4	9.44	29.58	23	0.8	20.9	57707.9		1.64		OCARS
2208-137	22:11:24.099463	0.005	-13:28:09.723597	0.17	2.26	18.33	48	1.2	12.88	43.89	48	1.4	19.6	57723.9		0.39		OCARS
2208-373	22:11:50.525876	0.003	-37:07:04.978563	0.10	-490.79	206.50	3	60.3	1328.64	961.15	3	3.2	11.3	57282.0	*	0.32		OCARS
2209+236	22:12:05.966303	0.025	+23:55:40.543896	0.16	21.76	1.94	427	2.3	2.38	1.84	427	1.9	26.4	57823.0		1.13		OCARS
2210-257	22:13:02.497922	0.060	-25:29:30.081449	2.27	-7.41	17.40	29	1.2	-15.94	50.81	29	1.9	16.7	55810.1		1.83		OCARS
2214+350	22:16:20.009959	0.099	+35:18:14.179648	1.01	5.61	3.13	470	2.1	-69.90	4.93	470	2.1	22.2	57840.9		0.51		OCARS
2215+150	22:18:10.913912	0.004	+15:20:35.717363	0.06	5.52	4.46	128	2.0	1.44	4.72	128	2.1	11.7	57837.0		2.33		OCARS
2216-038	22:18:52.037718	0.010	-03:35:36.881573	0.72	3.05	2.60	258	1.4	-0.19	5.75	258	1.6	24.6	56879.9		0.90		OCARS
2216+178	22:19:14.092472	0.006	+18:06:35.581192	0.24	-9.63	31.01	10	2.4	24.09	24.16	10	0.4	17.9	56638.8		1.07		OCARS
2220-351	22:23:05.930531	0.014	-34:55:47.178003	0.47	-11.77	13.71	41	1.2	22.93	36.13	41	1.2	12.6	57810.1		0.30		OCARS
3C446	22:25:47.259303	0.003	-04:57:01.390762	0.04	0.35	1.25	1342	2.4	10.97	1.13	1342	2.1	23.5	57840.9		1.40		OCARS
2227-088	22:29:40.084337	0.005	-08:32:54.435554	0.06	-5.22	2.83	419	2.0	7.56	3.44	419	2.4	22.5	57837.0		1.56		OCARS
2229+695	22:30:36.469709	0.031	+69:46:28.077534	0.31	39.16	3.33	603	5.4	4.73	1.58	603	2.0	27.1	57833.9		1.41		OCARS

Table A.1 (cont'd)

IVS	RA (J2000 h:m:s)	σ_α (ms)	Dec (J2000 d:′:″)	σ_δ (mas)	μ_α (μas/yr)	$\sigma_{\mu,\alpha}$ (μas/yr)	N_α	χ^2_α	μ_δ (μas/yr)	$\sigma_{\mu,\delta}$ (μas/yr)	N_δ	χ^2_δ	Length (years)	Last Obs. (MJD)	New PM	z	z flag	z Source
CTA102	22:32:36.408871	0.011	+11:43:50.903673	0.27	4.34	3.94	208	2.3	9.37	5.16	208	2.4	26.4	57520.5		1.04		OCARS
2232-488	22:35:13.236545	0.029	-48:35:58.795036	0.44	17.01	11.78	188	2.2	4.37	10.02	188	1.8	26.3	57784.9		0.51		OCARS
2233-148	22:36:34.087048	0.447	-14:33:22.186790	3.24	1.71	42.92	12	0.8	8.94	32.45	12	1.8	20.8	57694.9		0.33	c	OCARS
2235+731	22:36:38.596740	0.321	+73:22:52.662598	1.39	3.78	10.19	86	1.2	17.68	11.35	86	1.4	15.1	55342.6		1.34		OCARS
2236-572	22:39:12.075920	0.024	-57:01:00.839318	0.30	-4.74	10.30	49	1.5	-23.67	15.54	49	1.4	12.5	57788.0		0.57		OCARS
2239+096	22:41:49.717305	0.011	+09:53:52.445254	0.09	17.29	31.47	29	2.3	30.02	26.80	29	2.2	21.6	57802.0		1.71		OCARS
2243+047	22:45:53.654085	0.012	+05:00:56.963384	0.83	-8.09	11.73	44	1.3	18.16	27.22	44	1.4	21.5	57753.0		1.09		OCARS
2244-372	22:47:03.917312	0.020	-36:57:46.304790	0.71	3.01	18.33	62	2.2	10.63	17.99	62	1.4	14.1	57810.1		2.25		OCARS
2245-328	22:48:38.685718	0.010	-32:35:52.187210	0.36	-5.21	12.11	49	2.0	-2.38	16.16	49	1.7	26.5	57805.1		2.27		OCARS
2250+194	22:53:07.369173	0.005	+19:42:34.628548	0.14	3.47	3.69	125	1.6	-8.03	8.30	125	1.6	21.2	57810.1		0.28		OCARS
2252-089	22:55:04.239704	0.051	-08:44:04.022190	0.69	25.01	13.96	25	1.2	-75.66	30.97	25	1.4	16.1	55545.5		0.61		OCARS
2253+417	22:55:36.703345	13.215	+42:02:52.676979	148.49	-7.22	9.82	37	1.3	-23.22	11.60	37	1.5	25.7	57291.6		1.48		OCARS
2254+074	22:57:17.303113	0.019	+07:43:12.302651	0.21	-3.13	3.29	103	1.5	11.52	4.18	103	1.3	26.4	57819.9		0.19		OCARS
2254+024	22:57:17.563295	0.297	+02:43:17.509005	2.97	5.36	9.32	27	1.4	-22.70	18.83	27	1.7	25.8	57625.7		2.08		OCARS
2255-282	22:58:05.962900	0.013	-27:58:21.256366	0.14	-4.05	1.16	2125	2.0	1.88	2.17	2125	2.4	27.2	57840.9		0.93		OCARS
2300-683	23:03:43.564515	0.087	-68:07:37.443382	0.49	48.89	12.88	180	1.9	-65.74	13.99	180	1.9	13.3	57823.0		0.52		OCARS
2302+232	23:04:36.436400	0.006	+23:31:07.611353	0.14	-2.69	6.29	17	0.9	7.21	17.66	17	1.6	21.1	57786.0		1.24		OCARS
2305+198	23:08:11.636481	0.001	+20:08:42.195403	0.02	-9.60	27.49	4	2.6	60.66	35.75	4	1.5	19.7	57282.0	*	0.23		OCARS
2306-312	23:09:14.331428	0.024	-30:59:12.584337	0.35	17.55	32.47	13	0.4	-12.62	91.79	13	0.7	12.2	57583.6		1.38		OCARS
2307+106	23:10:28.517802	0.029	+10:55:30.695988	0.19	16.89	14.65	108	1.7	0.82	20.25	108	1.6	21.6	57795.0		0.49	c	OCARS
2309+454	23:11:47.408974	0.019	+45:43:56.016160	0.12	0.52	5.49	225	2.1	-6.78	6.93	225	1.9	20.6	57837.0		1.45		OCARS
2312-319	23:14:48.500505	0.043	-31:38:39.526808	0.60	-53.96	28.62	34	1.2	-27.44	50.77	34	2.0	20.4	55545.5		1.32	c	OCARS

Table A.1 (cont'd)

IVS	RA (J2000 h:m:s)	σ_α (ms)	Dec (J2000 d:′:″)	σ_δ (mas)	μ_α (μas/yr)	$\sigma_{\mu,\alpha}$ (μas/yr)	N_α	χ^2_α	μ_δ (μas/yr)	$\sigma_{\mu,\delta}$ (μas/yr)	N_δ	χ^2_δ	Length (years)	Last Obs. (MJD)	New PM	z	z flag	z Source
2314-340	23:16:43.386413	0.111	-33:49:12.486227	2.65	64.15	112.76	15	0.7	-131.48	100.45	15	0.8	11.5	56524.8		3.10	c	OCARS
2318+049	23:20:44.856585	0.003	+05:13:49.952461	0.04	-5.05	1.74	977	1.7	-1.24	1.57	977	1.6	26.9	57840.9		0.62		OCARS
2319+317	23:21:54.955984	0.013	+32:04:07.622647	0.21	1.13	3.26	294	1.8	-8.67	4.88	294	1.6	12.9	57837.0		1.49		OCARS
2319+272	23:21:59.862218	0.038	+27:32:46.441240	1.36	-1.88	8.97	31	1.8	5.12	13.15	31	1.5	22.2	56641.8		1.25		OCARS
2319+444	23:22:20.358099	0.032	+44:45:42.354218	0.88	-5.88	3.37	53	1.1	174.27	5.08	53	7.4	20.4	57751.0	*	1.31	b	OCARS
2320+506	23:22:25.982456	0.145	+50:57:51.962244	0.92	12.49	5.00	51	1.9	12.83	15.57	51	2.5	24.1	57520.5		1.28		OCARS
2320-035	23:23:31.953833	0.413	-03:17:05.025106	2.90	-5.78	13.73	58	1.4	0.74	12.81	58	1.0	18.8	55728.4		1.41		OCARS
2321-375	23:24:07.111732	0.080	-37:14:22.455629	0.50	67.12	60.63	18	1.4	1.48	36.72	18	0.7	14.4	57583.6		0.37		OCARS
2324+151	23:27:21.966041	0.007	+15:24:37.310495	0.09	-7.71	22.71	8	3.3	-46.97	29.77	8	3.2	20.8	57700.0	*	0.05		OCARS
2325+093	23:27:33.580578	0.024	+09:40:09.462492	0.13	4.97	27.61	30	0.9	-16.40	19.69	30	1.6	21.5	57759.0		1.84		OCARS
2325-150	23:27:47.964463	0.343	-14:47:55.746758	9.59	-19.69	40.16	26	1.5	26.11	33.24	26	1.1	17.2	55810.1		2.46		OCARS
2326-477	23:29:17.704338	0.014	-47:30:19.114240	0.15	2.52	8.16	121	1.7	21.28	10.38	121	1.5	26.9	57791.9		1.30		OCARS
2328+107	23:30:40.852193	0.039	+11:00:18.710907	0.76	-18.06	13.30	12	1.6	-6.92	45.02	12	3.1	26.8	57700.8		1.49		OCARS
2329-162	23:31:38.652296	0.038	-15:56:57.020307	3.44	2.82	17.35	36	3.8	9.59	20.73	36	2.3	19.1	56641.8		1.15		OCARS
2329-384	23:31:59.476171	0.017	-38:11:47.650806	0.19	9.88	9.22	60	1.2	-28.29	13.56	60	1.4	26.6	57833.9		1.20		OCARS
2331-240	23:33:55.237812	0.055	-23:43:40.657962	0.58	-5.13	12.07	17	1.5	-23.84	17.23	17	1.6	23.4	57731.0		0.05		OCARS
2333-415	23:36:33.985127	0.039	-41:15:21.987293	2.75	-14.00	10.66	43	1.0	0.30	35.33	43	1.5	12.6	57810.1		1.41		OCARS
2335-027	23:37:57.339020	0.063	-02:30:57.629706	0.65	-5.54	4.71	194	1.7	-7.24	6.67	194	1.6	22.6	57794.0		1.07		OCARS
2337+264	23:40:29.029464	0.012	+26:41:56.804836	0.19	14.09	41.82	18	3.6	-7.33	57.04	18	2.1	25.7	57745.0		0.37		OCARS
2344+09A	23:46:36.838493	0.042	+09:30:45.513949	0.63	1.65	19.50	20	3.3	-2.55	20.23	20	3.1	26.3	57520.5		0.68		OCARS
2344-514	23:47:19.864039	0.111	-51:10:36.065102	0.60	9.82	16.22	28	1.2	33.34	32.78	28	1.9	12.3	57731.0		1.75		OCARS
2345-167	23:48:02.608488	0.006	-16:31:12.021713	0.21	-16.31	8.13	62	2.0	11.50	17.76	62	2.4	24.4	56839.2		0.58		OCARS

Table A.1 (cont'd)

IVS	RA (J2000 h:m:s)	σ_α (ms)	Dec (J2000 d:′:″)	σ_δ (mas)	μ_α (μas/yr)	$\sigma_{\mu,\alpha}$ (μas/yr)	N_α	χ^2_α	μ_δ (μas/yr)	$\sigma_{\mu,\delta}$ (μas/yr)	N_δ	χ^2_δ	Length (years)	Last Obs. (MJD)	New PM	z	z flag	z Source
2351+456	23:54:21.680255	0.012	+45:53:04.236529	0.11	-18.83	18.73	32	4.2	-8.24	11.53	32	1.4	18.6	55320.6		1.99		OCARS
2351-154	23:54:30.195177	0.008	-15:13:11.213004	0.26	-9.35	6.21	54	1.8	5.22	11.03	54	1.8	22.2	57810.1		2.67		OCARS
2352+495	23:55:09.458042	0.043	+49:50:08.339740	0.59	-2.06	73.38	11	3.4	-4.22	60.19	11	4.1	27.0	57759.0		0.24		OCARS
2353-686	23:56:00.681569	0.088	-68:20:03.472339	0.32	9.84	8.78	58	1.2	-9.00	9.31	58	1.3	26.2	57731.0		1.72	c	OCARS
2353+816	23:56:22.793947	0.091	+81:52:52.254816	0.17	13.83	15.65	32	1.7	-13.71	15.94	32	1.9	19.2	57700.8		1.34	b	OCARS
2354-117	23:57:31.197524	0.111	-11:25:39.177273	1.36	-2.33	301.19	13	0.9	-60.41	706.74	13	0.7	17.6	57009.1		0.96		OCARS
2355-534	23:57:53.266047	0.026	-53:11:13.689105	0.25	-17.81	6.93	132	1.1	-12.25	12.26	132	1.7	26.9	57809.0		1.01		OCARS
2355-106	23:58:10.882383	0.010	-10:20:08.611543	0.12	-7.88	3.27	555	2.0	-0.49	3.40	555	1.8	27.1	57837.0		1.64		OCARS
2356+385	23:59:33.180798	0.008	+38:50:42.318185	0.14	3.96	1.48	1022	1.4	-5.97	2.30	1022	1.5	22.7	57810.1		2.70		OCARS

[a]The complete VLBA Extragalactic Proper Motion Catalog. See Appendix A for a description of the columns.